ANALYSIS OF FLOW INDUCED VIBRATIONS USING THE FINITE ELEMENT METHOD

by

Sukhdeep Raj GOSSAIN, BSc

A thesis submitted for the degree of Doctor of Philosophy of the University of London and for the Diploma of Membership of Imperial College

Department of Aeronautics
Imperial College of Science and Technology
London SW7 2BY

ABSTRACT

The fluid-structure interaction problem is defined by the governing equations of motion of fluid and structure, and by interface boundary conditions. For the structural model standard finite element techniques are used. The fluid element is based on a displacement formulation in terms of the velocity degrees of freedom at the element nodes. A reduced selective integration method is used to obtain the penalty function formulation of the incompressibility constraint. The algorithms used to solve for the transient response is a one step "linearly implicit" predictor-corrector method. Velocities obtained from the solution of the fluid problem are used to calculate the surface forces acting on the structure. The response of the structure under these forces is calculated from the equations of motion of the structure using an implicit technique (Newmark Method). The resulting structural velocities are used as the interface boundary conditions for the next time step. The process is repeated for a series of time steps until the final steady state solution or total time response solution is achieved. A nine-noded parabolic element is used for the fluid, thus making it simple to model curved or complicated geometries. The solution technique does not involve any of the much criticised upwinding, and has been found to be stable for relatively high Reynolds numbers. Results are available for the cross-flow vibrational analysis of a circular cylinder for a range of Reynolds numbers. Some results are also presented for the flow-induced vibrations of a column of tubes.

ACKNOWLEDGEMENTS

I wish to express my sincere thanks to my supervisor, Dennis Hitchings for his invaluable and inspirational guidance, assistance and encouragement throughout the course of this research.

I would like to offer my gratitude to Babcock Power Limited for their sponsorship of this project, and in particular, to John Wharmby and the staff at MSD for their help and guidance.

I would like to thank my friends and colleagues in the Department, for their constructive criticism, and R. Desai for his help with computing. I would also like to thank Ferdous for her help during the preparation of this thesis.

Finally, I dedicate this work to my father for his continuous encouragement and guidance throughout my life.

TABLE OF CONTENTS

NOMENCLATURE

a	acceleration
$a_0 - a_7$	integration constants
A	cross-sectional area
c	constant depending on computer word length
$\underline{C}$	Stokes flow matrix
$\underline{C}_{DIL}$	dilatational part of C
$\underline{C}_{DEV}$	deviatoric part of C
C_L	lift coefficient
C_D	drag coefficient
cn	convergence factor
d	radius
D	drag
D'	cylinder width
E	Young's modulus of elasticity
Ec	euclidean norm
$\underline{F}$	force vector
f	frequency of vortex shedding
h	channel height upstream of step
H	channel height downstream of step
h', g'	given boundary data
I	moment of inertia
J	Jacobian operator
k	stiffness
K	$1/(1-2\nu)$, ν is the Poissons ratio
l	element length
L	length of body on which Reynolds number is based
l'	length of channel upstream of step
L'	length of channel downstream of step

m	mass per unit length
$\underline{M}_F$	mass matrix (fluid)
$\underline{M}_S$	mass matrix (structure)
n	number of timesteps
ne	number of elements
ni	number of interface nodes
$\underline{N}$	non-linear convective matrix
NE	number of equations
p	pressure
$\underline{r}$	displacement vector
$\underline{R}$	load vector
Re	Reynolds number
r	distance in radial direction
S	Strouhal number
t	time
Δt	timestep
T	total time
$\underline{T}$	transformation matrix
t'	thickness
t_{ij}	Cauchy stress tensor
u	horizontal velocity component
v	vertical velocity component
$\bar{u},\bar{v}$	virtual velocity
w	weighting function
$\underline{w}$	interpolation function matrix
Δx	distance between two element nodes
z	distance in axial direction

Greek

$\underline{\alpha}$	strain-velocity matrix
$\underline{\alpha}_{DIL}$	dilatational part of $\underline{\alpha}$
$\underline{\alpha}_{DEV}$	deviatoric part of $\underline{\alpha}$
α'	number of points of reduced quadrature
β'	number of parameters describing the variation in velocity
γ	positive parameter governing the stability and accuracy of algorithm
ε	strain
σ	stress
τ	shear stress
η, δ	parameters governing the accuracy and stability of fluid-structure interaction solution
δ_{ij}	Kronecker delta
ξ_1, ξ_2	intrinsic coordinates of basic square
$\underline{\chi}$	material property matrix
Ω	bounded region
Γ	boundary of bounded region
ν	Poissons ratio
μ	dynamic viscosity
λ	penalty function
ρ	density
∇, ∂	differential operators

Vectors and Tensors

x_i	ith component of the position vector x
u_i	ith component of the velocity vector u
$u_{i,j}$	$\partial u_i / \partial x_j$, the velocity gradient
u(i,j)	$(u_{ij} + u_{ji})/2$, symmetric part of velocity gradient
t_{ii}	$t_{11} + t_{22} + \cdots\cdots + t_{nn}$

LIST OF FIGURES

Page

CHAPTER 8.

1. INTRODUCTION

1.1 General Introduction and Previous Studies

The problem of fluid-structure interaction is likely to exist wherever relative motion of a solid and fluid occurs. The fluid flow and structure are coupled systems and their interaction is usually time varying. The coupling occurs between the forces that the fluid exerts on the structure and the dynamic response of the structure giving time varying boundary conditions to the fluid. The fluid structure interaction problem can be classified as:

(i) The fluid internal to the structure, for example the instability of fluid conveying pipes and seismic response of ground supported liquid storage tanks.

(ii) The fluid external to the structure as for example the transient motion of submerged or partially submerged structures, and flow induced vibrations.

Various techniques have been used to solve the problem of fluid structure interaction. Most of these problems are of such complex nature that the method of analysis must be numerical. The Finite Element Method is one technique for the modelling of such complicated problems and techniques that have previously been developed for the analysis of fluid-solid systems can be categorized into the following three basic approaches:

1.1.1 Added mass approximation

In the added mass approach some fraction of the fluid mass is added to the structural model at the fluid-structure interface. Normally the assumption used to evaluate the added mass is based on a flexible structure and incompressible fluid. This approach neglects the stiffness effects in the fluid and, in general, leads to conservative results. It is a relatively simple approach which has been used to obtain practical engineering results for both two and three dimensional cases (2,3).

In the early 1930's, Westergaard (1) proposed a method for computing the hydrodynamic pressures induced on gravity dams by earthquakes, utilising the equivalent added mass concept. The approach is based on the assumption that the dam is rigid, the ground motion harmonic and the effects of water compressibility and surface waves are negligible. Since this pioneering effort, many authors (4,5) have studied seismic interaction between dam and reservoir, and their results indicate that the Westergaard added mass concept is a good approximation where his basic assumptions of dam rigidity and water incompressibility are valid.

The hydrodynamic mass matrix for a vibrating ship has been evaluated using a three dimensional finite element discretisation of the surrounding water in reference (7), which includes several other references on this approach for investigating ship vibrations. Solution for the hydroelastic vibrations of tanks partially filled with an inviscid fluid, was obtained by directly determining the added mass matrix by Sayhi and Ousset (6). The effect of the fluid-structure interaction leads to the calculation of a fully populated added mass matrix which is computed from the impedence matrix relating the pressure to the displacement on the interaction surface. An eigenvalue problem is then solved and the natural frequencies of the coupled system are predicted. Similar approximate methods have been used for the analysis of liquid filled tanks (10). Added mass coefficients of large offshore structures subject to ground excitation were calculated by Buragohain and Agarwal (15) using this approach.

The added mass method is widely used to analyse the flow induced vibrations of ship structures. The increase in the flexibility of ship structures accompanied by the increase in propulsion power, has resulted in high levels of vibration with various annoying consequences. In the conventional approach, the ship is assumed to be a slender body, concentrated added masses are then introduced at various sections of the ship. Such a method is compatible

with a hull girder theory for the structural behaviour of the ship (7), which yields good results concerning the first few vibration modes. The influence of the dynamically varying pressures acting on the submerged surface of the vibrating hull were taken into account by introducing an additional mass term in the equations of motion of the structure (7). For the first few modes of the hull girder, finite element results for added mass agree with the results obtained from conventional semi-empirical formulas. However, with higher, more complex modes, the discrepency increases. Also free surface effects are generally neglected in the frequency range of interest(8,9). The radiation condition certainly influences the hydrodynamic mass matrix in a way which is difficult to assess. Infinite elements (8,9) may prove useful to deal with the problems of an infinite boundary and with wave radiation effects. This radiates energy and appears to the structure as an apparent damping with a magnitude often greater than any inherent damping within the structure itself.

The added mass method is often applicable to a class of practical problems where the structural vibration is of small amplitude and low frequency, and the fluid motion can be described as an ideal fluid flow. Such assumptions are used by Yu and Vanburen (131) to perform an added mass fluid-structure interaction analysis of a submerged

four-tube array. The hydrodynamic mass matrix for the tube array is generated using a substructure technique of a finite element code. By combining the substructural hydrodynamic mass with the structure, many dynamic characteristics such as normal modes, shock spectrum and time history analysis were computed.

1.1.2 Lagrangian formulation

In the Lagrangian approach, the behaviour of the fluid is expressed in terms of displacements at the finite element nodes in the same manner as in structure. The fluid is treated as an elastic medium with a small but finite shear modulus. Hence, compatibility and equilibrium are automatically satisfied at the nodes along the interface between the fluid and the structure. The major advantage of this approach is that the fluid finite elements that are generated can be readily incorporated into a general purpose computer program for structural analysis, since special interface equations are not required.

The transient response of fluid-structure system using this approach has been presented by Shantaram et al (18) and Wilson (19). The finite element displacement formulations for coupled fluid-structure system pose the difficulty of zero energy deformation modes with non-zero

frequencies (4,6). Zienkiewicz et al (3) have suggested the use of penalty-type finite element formulation for avoiding the zero energy deformation modes in the fluid domain. However, at low values of penalty coefficient zero energy modes were observed, which disappeared as the value of penalty coefficient was increased, and only the true frequencies appeared in the free vibration analysis of the system. Similiar findings were observed by Hamdi et al (25). In the case of examples with top free surface, it was observed that some zero energy frequencies were still present, even when a high value of penalty coefficient was used. The number of these zero energy frequencies increased with an increase in the number of elements in the fluid domain. Deshpande et al (26) solved the coupled problem of a real, compressible but inviscid fluid and an elastic structure. A constraint of irrotationality on the displacements in the fluid was imposed and a penalty-type finite element formulation for the coupled fluid-structure system was obtained. The fluid-structure boundary was represented using interface finite elements in an attempt to reduce the zero energy modes and the equations that were finally obtained were banded and symmetric. The cost of the modal analysis was reduced by the suppression of zero energy modes. Numerical results for free and forced response of a coupled fluid-structure system were presented.

A constraint of zero fluid rotation at the integration points is introduced by Wilson and Khalvati (24) to selectively eliminate zero energy modes and produce a fluid element with optimum behaviour. A nine-noded Lagrangian element with 2X2 integration and four rotational constraints at the integration points is produced. The mode shapes and frequencies of a rectangular tank of fluid were evaluated using this element and some suggestions are given to develop a three-dimensional element.

A transient finite element formulation for incompressible viscous flow in a arbitrarily mixed Lagrangian-Eulerian (ALE) description is presented by Hughes et al (27). Arbitrary Lagrangian-Eulerian finite element methods were recently developed in response to the need of very versatile modelling techniques for treating transient fluid-structure systems. Such methods combine the basic attributes of the finite element technique and the freedom of moving the fluid mesh offered by the ALE description, and thus have considerable potential for application to a wide variety of fluid-structure interaction and free surface flow problems. Such an approach is used by Donea and Giuliani (28) to solve the problem of fluid-structure interaction with interfaces involving sharp corners. Problems of this type are encountered, in the analysis of clusters of fast reactor subassemblies. Liu and Belytschko

(29) have used ALE methods and direct time integration to solve the problem of fluid-structure interaction with sloshing. The ALE approach is suitable when surface displacements are large. Analogous finite element ALE formulations for compressible fluids are presented in (30,31).

The technique of fixed-interface modal synthesis sub-structure methods, used to solve large structural eigenvalue problems was extended to the fluid-structure eigenvalue problem with a view to obtaining an efficient solution to problems involving localised modifications (32). The three cases considered in this reference are;

(i) Fluid or fluid-structure vibration problems directly analogous to structural case.

(ii) The modification of the fluid model of a structure enclosing a compressible fluid.

(iii) The modification of fluid and structural models of a structure enclosing an incompressible fluid.

1.1.3 Eulerian formulation

In the Eulerian approach the behaviour of the fluid is characterised by a single pressure (or potential) variable and the coupling is achieved by consideration of interface forces. The behaviour of the fluid can be expressed in

terms of analytic functions (for certain geometries) or a mesh of finite elements with the pressure as the unknown nodal variable. The solution of the coupled system can be accomplished by solving the two systems separately with the interaction effects found by iteration (11,12). It is also possible to couple both systems and solve them as one without the need to iterate but this leads to unsymmetrical equations (13,14). The Eulerian formulation requires only a single pressure or potential variable to describe the fluid motion, whereas the Lagrangian formulation, requires pressure as well as velocities to describe the fluid motion. The method thus has the advantage that in general a smaller number of variables are involved to describe the fluid motion and is widely used in the fluid-structure interaction problems. A considerable disadvantage is that the coupled equations at the interface cause the finite element equations to have a large bandwidth. The computational cost can thus be considerable, but the process is effective, particularly if the compressibility effects are negligible. The special coupling equations and the lack of symmetry usually means that this approach requires a special purpose computer program.

In fluid-structure interaction problems, it is sometimes convenient to describe the motion of the fluid in Eulerian system and motion of the solid in Lagrangian system. That is, the fluid motion is described using a single pressure

(or potential) variable, whereas the behaviour of the structure is expressed in terms of displacements at the finite element nodes. The finite element displacement representation of the structure is standard. The method is classified as the Eulerian-Lagrangian formulation. Such an approach is used (16) to solve for the transient dynamic analysis of reservoir-dam interaction. The Staggered solution scheme was adopted in (17) to make the solution procedure more efficient.

1.2 Scope of Present Investigation

The present work deals with the development of a general finite element procedure which can be used to solve fluid-structure interaction problems, it can be included in any general purpose modular finite element package. The development has been carried out using the general purpose finite element package FINEL (33). A Lagrangian formulation has been used, where the fluid element has velocities as nodal variables. The major advantage of this approach is that the fluid element can be readily incorporated into a general purpose computer program used for structural analysis, since the coefficient matrix has the same properties as a structure stiffness matrix, that is, it is symmetric and positive definite. The Navier-Stokes equations are used to describe the fluid motion and are solved using a penalty function formulation with selective reduced integration. This method has been used successfully in the solution of incompressible orthotropic elasticity problems (34,35). The method used for the orthotropic elasticity can be directly applied to solve incompressible Stokes flow. The penalty function approach leads to the simplest effective finite element implementation of incompressibility and is achieved by making the effective Poissons ratio of the fluid ν very

nearly 0.5. The consequences of imposing this form of incompressibility constraint and value of Poissons ratio required have been found by studying axisymmetric flows between two parallel plates. This is discussed in chapter 6. A considerable loss in mass flow rate results if the incompressibility constraint is not fully satisfied. This chapter also include tests to define the maximum value of element aspect ratio that can be used in regions of fully developed flow.

Pressure is eliminated from the finite element equations since the incompressibility constraint ensures no volume change and hence no virtual work is done by the pressure. This means that the pressure term is present in the Navier Stokes equations but it is not present in the discretised finite element equations because its weighted residual value is always identically zero (or very small in this case since the Poissons ratio term is just slightly less than 0.5). However, it is shown in section 2.10 that the pressure can be easily recovered from the results. The unsteady non-linear equations that are formed require a time stepping algorithm in order to obtain a solution. This has been an area of much research and many ideas have been proposed (36-39). In this work a one-step linearly implicit predictor-corrector method has been employed (40). The theory for the fluid element formulation is covered in chapter 2. Based on the previous studies

carried out in this field at Imperial College (51), a nine-noded fluid element is selected and formulated (section 2.8). The superior behaviour of the nine-noded element formulated using selective reduced integration has been confirmed numerically (51,53). A very simple structure model is used (chapter 3). A more complicated general finite element model of the structure can, however, easily be incorporated into the method. The theory for fluid-structure interaction is considered in chapter 4. The fluid and structural systems are solved independently and the interaction is achieved by use of interface force and velocity boundary conditions. Within each time step the fluid equation of motion is solved first, assuming that the interface velocities are defined by the structural response in the previous step. The structural equations of motion are then solved, where the forces acting on the structure are the fluid pressure forces calculated from the solution of the fluid equation for this step. For the following time step a new set of velocity boundary conditions found from the structure response are applied to the interface boundary. Thus, at every time step the effect of the structure's motion on the fluid is taken into account as are the fluid forces acting on the structure. Only a small amplitude response has been considered. The computer implementation of the entire procedure inside the finite element package FINEL is briefly discussed in chapter 5.

Since the finite element method is well developed for structural analysis, more emphasis is placed upon the development and testing of the fluid elements. The associated computer program FINEL already has an extensive library of structural elements. The examples of flow in a channel, flow over a step, flow in a cavity, flow over a backward step, flow over a circular cylinder and vortex shedding are considered to check the validity of the fluid element (chapter 6,7). These are all well-known test cases and many experimental and numerical results are available for comparision.

A simple problem of fluid-structure interaction is considered in chapter 8. Firstly the flow induced vibration of a single rigid cylinder on elastic supports is considered (section 8.1). The results obtained are compared with the available experimental results. This is further extended to analyse the flow around a column of three rigid cylinders in section 8.2.

Finally, in chapter 9, the present developments are summarised and suggestions for further work are made.

2 THE FLUID IDEALISATION

2.1 Fluid Equations

The fluid environment surrounding the structure is assumed to be incompressible and viscous. Consequently, the behaviour of the fluid is defined by the Navier-Stokes equations and the continuity equation. The tensor notation is used throughout and the repeated indices summation convention is also employed.

a) Conservation of mass

$$u_{i,i} = 0 \tag{2.1}$$

This is the continuity equation for an incompressible medium.

b) Conservation of momentum

$$\rho(u_{i,t} + u_j u_{i,j}) - t_{ij,j} = 0 \tag{2.2}$$

The Cauchy stress tensor t_{ij} is

$$t_{ij} = -p\delta_{ij} + 2\mu u(i,j) \tag{2.3}$$

p is the pressure

δ_{ij} is the Kronecker =1 for i=j

Delta =0 for i≠j

and $u(i,j) = (u_{ij} + u_{ji})/2$ is the symmetric part of the velocity gradients.

The density (ρ) and dynamic viscosity (μ) are physical properties of the fluid.

Equation (2.2) is the Navier Stokes equation for incompressible and viscous flow. In rectangular coordinates the complete equation can also be written as

x-component

$$\rho\left[\frac{\partial u}{\partial t} + u\frac{\partial u}{\partial x} + v\frac{\partial u}{\partial y} + w\frac{\partial u}{\partial z}\right] + \frac{\partial p}{\partial x} - \mu\left[\frac{\partial^2 u}{\partial x^2} + \frac{\partial^2 u}{\partial y^2} + \frac{\partial^2 u}{\partial z^2}\right] = 0$$

y-component

$$\rho\left[\frac{\partial v}{\partial t} + u\frac{\partial v}{\partial x} + v\frac{\partial v}{\partial y} + w\frac{\partial v}{\partial z}\right] + \frac{\partial p}{\partial y} - \mu\left[\frac{\partial^2 v}{\partial x^2} + \frac{\partial^2 v}{\partial y^2} + \frac{\partial^2 v}{\partial z^2}\right] = 0$$

z-component

$$\rho\left[\frac{\partial w}{\partial t} + u\frac{\partial w}{\partial x} + v\frac{\partial w}{\partial y} + w\frac{\partial w}{\partial z}\right] + \frac{\partial p}{\partial z} - \mu\left[\frac{\partial^2 w}{\partial x^2} + \frac{\partial^2 w}{\partial y^2} + \frac{\partial^2 w}{\partial z^2}\right] = 0$$

Omission of the unsteady term ($u_{i,t}$) in equation (2.2) leads to the steady Navier-Stokes equation for incompressible, viscous flow. Furthermore, if the non-linear convective or inertia term ($u_j u_{i,j}$) is eliminated, the Stokes equation for incompressible flow is obtained. For small Reynolds number that is, slow velocity, large viscosity or small bodies the solution of Stokes equations provides a good approximation to the solution of equation (2.1) and (2.2).

In order to solve equations 2.1 and 2.2 specific initial and boundary conditions must be defined. Let Ω be a bounded region in $R^{\bar{n}}$, $\bar{n} \geq 1$ with piecewise smooth boundary $\partial\Omega$.

The mixed initial boundary value problem consists of finding a vector velocity field u(x,t) and a scalar pressure field p(x,t) which satisfy the Navier-Stokes equations for all $x \in \Omega$ and $t \in (0,T), T>0$, such that

$$\underline{u}(x,0) = \underline{u}_0(x), \quad x \in \Omega \tag{2.5a}$$

$$\underline{u}(x,t) = \underline{g}'(x,t), \quad x \in \partial\Omega_1, t \in (0,T) \tag{2.5b}$$

$$\underline{n}'(x).\underline{T}(x,t) = \underline{h}'(x,t), x \in \partial\Omega_2, t \in (0,T) \tag{2.5c}$$

where $\underline{u}_0$ is the given initial data, $\underline{g}'$ and $\underline{h}'$ are the given boundary data, and $\underline{n}'$ is the unit outward normal vector to $\partial\Omega$. $\partial\Omega_1$ and $\partial\Omega_2$ are subregions of $\partial\Omega$ satisfying $\partial\Omega_1 \cup \partial\Omega_2 = \partial\Omega$ and $\partial\Omega_1 \cap \partial\Omega_2 = 0$.

When ρ is formally set to zero in equation 2.2 and the initial conditions are ignored, then the boundary value problem becomes one of Stokes flow. The resulting equations are identical to those of isotropic, incompressible linear elastostatics.

Different methods have been used in the past to solve the Navier Stokes equation and the continuity equation. Much of the initial work employed the stream function-vorticity formulation which has the advantage of satisfying incompressibility identically (41). However, the difficulties encountered in applying boundary conditions and extending the approach to the solution of three-dimensional problems have led to an increasing interest in solving the Navier Stokes equations and the continuity equation in terms of the primitive variables of pressure and velocity. The principal problem with the primitive variable approach is the imposition of the incompressibility constraint. Three distinct approaches to imposing the constraint are found in the finite element literature.

(i) The interpolation function for the pressure are used as the weighting functions for the continuity equation in a Galerkin or virtual work formulation (42). In the case of the Stokes flow where a variational principal exists,

this approach corresponds to the method of Lagrange multipliers.

(ii) The interpolation functions for the velocity are chosen such that the incompressibility constraint is satisfied in an integral sense for each element (43). As a consequence, the pressure is eliminated from the equations, although it is retained in the boundary conditions.

(iii) The incompressibility constraint is imposed through the addition of a constrainted term to the Galerkin formulation. The pressure is eliminated as a dependent variable. This latter approach is called the "Penalty Function Method" (40).

The Penalty Function Method was first applied in the context of finite element analysis with solution of elasticity problems for incompressible solids by considering the limit of compressible solution as Poissons ratio approaches 0.5 (44). There is an analgous problem in Stokes flow (45). The first effort to apply the penalty function method to problems where the acceleration terms are significant in the Navier Stokes equations was that of Hughes et al (46).

2.2 The Penalty Function Formulation

Here the Navier-Stokes equations are replaced by an auxiliary system of equations whose solution is "close" to the required solution (40). This auxiliary system of equations serves as the basis of the finite element approximations.

The equation for the stress-tensor (2.3) can be re-written as

$$\overset{\lambda}{t}_{ij} = -\overset{\lambda}{p}\delta_{ij} + 2\mu\overset{\lambda}{u}(i,j) \qquad (2.6)$$

where $\overset{\lambda}{p} = -\lambda u_{k,k}$ (2.7)

For isotropic solids $\mu = E/2(1+\nu)$

and $\lambda = 2\mu\nu/(1-2\nu)$. (2.8)

The lamé parameter λ and μ are assumed to be independent of rates of strain.

In order to solve equation (2.2) with the stress tensor (2.6) using the finite element method, an equivalent variational equation is required. This is obtained using the Galerkin formulation (49,50). Physically, the Galerkin formulation can be interpreted as the virtual energy obtained if a virtual velocity is applied to the forces corresponding to the terms of equation (2.2). However, the pressure will only give rise to a virtual work if a volume change occurs. As the flow is assumed to be

incompressible, no volumetric changes occur, and pressure's contribution to virtual energy equilibrium is zero. The incompressibility is enforced by taking the value of Poissons ratio very close to 0.5. Thus equation (2.6) can be rewritten as

$$t_{ij} = \lambda \delta_{ij} u_{k,k} + 2\mu u(i,j) \qquad (2.9)$$

(In equation (2.9) the subscripts (λ) have been dropped.)

Provided λ is a large parameter, the incompressibility condition will be satisfied and need not be included as a separate equation

$$u_{k,k} = -p/\lambda \rightarrow 0 \quad \text{as} \quad \lambda \rightarrow \infty \qquad (2.10)$$

We attain this by making Poissons ratio ν just less than 0.5 in equation (2.8). The value of λ approaching infinity leads to certain computational difficulties which are overcome by the use of Selective Reduced Integration when the element is formed (section 2.9).

Equations (2.9 and 2.10) do not correspond to any physical problem unless λ is large. They are not the equations of compressible flow. However, similar limit arguments may be used to derive the incompressible equations from those for compressible flow (39). The convergence of the

penalty-function solution to the Stokes flow equations has been proved by Temam (39). From the proof in ref.39 it follows that as $\lambda \to \infty$, $u^{\lambda} \to u$ and $p^{\lambda} \to p$. If λ is selected sufficiently large then u^{λ} and p^{λ} differ negligibly from u and p, respectively. The equations of Stokes flow are identical to the equations of classical, isotropic, incompressible elasticity, where u is the displacement vector. The use of penalty methods in solid mechanics is widespread. The penalty equations used here are identical to classical, isotropic, compressible elasticity in which λ and μ are interpreted as Lame parameters. Thus the penalty approach in elasticity amounts to approximating an incompressible medium by a slightly compressible one. In fluids it is slightly different in that it is the continuity equation which is approximated and the associated errors amount to a net fluid loss or gain.

When selecting the constraint parameter λ various factors have to be considered. It must be large enough so that the compressibility and pressure errors are negligible, yet not so large that numerical ill-conditioning ensues. It has been suggested (40) that λ could be picked according to the relation

$$\lambda = c\mu \qquad (2.11)$$

Equation (2.11) applies to Stokes flow calculations whilst

for the solution of complete non-linear equation we can approximate the value from (40)

$$\lambda = c \max(\mu, \mu Re) \qquad (2.12)$$

where μ is the dynamic viscosity, $Re \left(= \frac{\rho u L}{\mu}\right)$ is the Reynolds number and c is a constant which depends only on the computer word length. Numerical studies reveal that for a floating-point word length of 60-64 bits, a suitable choice of value for c is 10^7.

Generally it is not necessary to be very precise about the selection of the actual value for λ and it may vary over several orders of magnitude with an insignifcant effect on results. However, for certain flow geometries where compressibility effects are important, a selection of the value of λ is important and highest possible value is required (48).

2.3 The Finite Element Discretisation

To apply the finite element method approximate variational equations corresponding to equation (2.2) with stress tensor as in equation (2.9) are required which are valid for whole of the domain under consideration. The Galerkin Method is used (49,50). Assume u_i^* to be the weighting function, the value of which is arbitrary everywhere on

the domain Ω except on the boundary Γ where u_i^* is assumed to be zero. Applying the Galerkin approximation and rewriting equation (2.2) gives

$$\rho\int_\Omega u_i^* u_{i,t}\,d\Omega + \rho\int_\Omega u_i^* u_j u_{ij}\,d\Omega - \int_\Omega u_i^* t_{ij,j}\,d\Omega = 0 \qquad (2.13)$$

Using Green's Theorem on the third term of equation (2.13) to reduce the order of differentiation of the term $t_{ij,j}$ then:

$$\rho\int_\Omega u_i^* u_{i,t}\,d\Omega + \rho\int_\Omega u_i^* u_j u_{i,j}\,d\Omega + \int_\Omega \frac{\partial u_i^*}{\partial x_j} t_{ij}\,d\Omega - \int_\Gamma u_i^* t_{i,j} n_j\,d\Gamma = 0 \qquad (2.14)$$

where n_j signifies the outward normal to the boundary of the fluid domain. Using the boundary condition as in equation (2.5c), equation (2.14) becomes

$$\rho\int_\Omega u_i^* u_{i,t}\,d\Omega + \rho\int_\Omega u_i^* u_j u_{i,j}\,d\Omega + \int_\Omega \frac{\partial u_i^*}{\partial x_j} t_{ij}\,d\Omega - \int_\Gamma u_i^* t_i\,d\Gamma = 0 \qquad (2.15)$$

Substituting for the stress tensor from equation (2.9).

$$\rho\int_\Omega u_i^* u_{i,t}\,d\Omega + \rho\int_\Omega u_i^* u_j u_{i,j}\,d\Omega + \int_\Omega \frac{\partial u_i^*}{\partial x_j}\left(\lambda u_{k,k}\delta_{ij} + 2\mu u(i,j)\right)d\Omega = \int_\Gamma u_i^* t_i\,d\Gamma \qquad (2.16)$$

We will expand equation (2.16) in its two-dimensional

form only, in order to keep the derivation of the matrix simple. The three-dimensional form follows in exactly the same fashion.

Equation (2.16) in the x-direction is

$$\rho\int_\Omega u_1^* \frac{\partial u}{\partial t}\,d\Omega + \rho\int_\Omega u_1^*\left(u\frac{\partial u}{\partial x}+v\frac{\partial u}{\partial y}\right)d\Omega + \int_\Omega \frac{\partial u_1^*}{\partial x}\left(\lambda\left(\frac{\partial u}{\partial x}+\frac{\partial v}{\partial y}\right)+2\mu\frac{\partial u}{\partial x}\right)d\Omega$$

$$+\int_\Omega \frac{\partial u_1^*}{\partial y}\mu\left(\frac{\partial u}{\partial x}+\frac{\partial v}{\partial y}\right)d\Omega = \int_\Gamma u_1^* t_1\,d\Gamma \qquad (2.17)$$

and in the y-direction

$$\rho\int_\Omega u_2^*\frac{\partial v}{\partial t}\,d\Omega + \rho\int_\Omega u_2^*\left(u\frac{\partial v}{\partial x}+v\frac{\partial v}{\partial y}\right)d\Omega + \int_\Omega \frac{\partial u_2^*}{\partial y}\mu\left(\frac{\partial u}{\partial y}+\frac{\partial v}{\partial x}\right)d\Omega$$

$$+\rho\int_\Omega \frac{\partial u_2^*}{\partial y}\left(\lambda\left(\frac{\partial u}{\partial x}+\frac{\partial v}{\partial y}\right)+2\mu\frac{\partial v}{\partial y}\right)d\Omega = \int_\Gamma u_2^* t_2\,d\Gamma \qquad (2.18)$$

where t_1 and t_2 are the components of t_i in the x and y direction respectively.

Rearranging equation (2.17) and (2.18) gives

$$\rho\int_\Omega u_1^*\frac{\partial u}{\partial t}\,d\Omega + \rho\int_\Omega u_1^*\left(u\frac{\partial u}{\partial x}+v\frac{\partial u}{\partial y}\right)d\Omega + \int_\Omega \frac{\partial u_1^*}{\partial x}\left((2\mu+\lambda)\frac{\partial u}{\partial x}+\lambda\frac{\partial v}{\partial y}\right)d\Omega$$

$$+\int_\Omega \frac{\partial u_1^*}{\partial y}\mu\left(\frac{\partial u}{\partial y}+\frac{\partial v}{\partial x}\right)d\Omega = \int_\Gamma u_1^* t_1\,d\Gamma \qquad (2.19)$$

and

$$\rho\int_\Omega u_2^*\frac{\partial v}{\partial t}\,d\Omega + \rho\int_\Omega u_2^*\left(u\frac{\partial v}{\partial x}+v\frac{\partial v}{\partial y}\right)d\Omega + \int_\Omega \frac{\partial u_2^*}{\partial y}\mu\left(\frac{\partial u}{\partial y}+\frac{\partial v}{\partial x}\right)d\Omega$$

$$+\int_\Omega \frac{\partial u_2^*}{\partial y}\left(\lambda\frac{\partial u}{\partial x}+(2\mu+\lambda)\frac{\partial v}{\partial y}\right)d\Omega = \int_\Gamma u_2^* t_2\,d\Gamma \qquad (2.20)$$

2.4 Matrix Problem

The domain Ω is discretised into non-overlapping elements. The nth element is denoted by e_n and its boundary is denoted by Γ_n (fig.2.1). Associated with the discretisation is a set of nodal points. The position vector of the nth node is denoted by x_n. The "interpolation function" associated with node n is denoted by w_n. These interpolation functions are used to interpolate element geometry and displacements. These are evaluated in section (2.8) for a nine-noded element and the strain-velocity matrix α is evaluated. The solution of the Galerkin problem may be expressed in terms of the interpolation functions.

In the finite element method both the real velocities $\underline{U}$ and the virtual velocities $\bar{\underline{U}}$ can be interpolated from the nodal values. In the matrix form the interpolations are

$$\underline{U} = \underline{w}\ \underline{u} \tag{2.21}$$

$$\underline{U} = \begin{bmatrix} U \\ V \end{bmatrix} = \begin{bmatrix} w_1\ 0\ w_2\ 0\ w_3\ 0\ w_4\ 0\ w_5\ 0 \cdots \\ 0\ w_1\ 0\ w_2\ 0\ w_3\ 0\ w_4\ 0\ w_5 \cdots \end{bmatrix} \begin{bmatrix} u_1 \\ v_1 \\ u_2 \\ v_2 \\ - \\ - \\ - \end{bmatrix} \tag{2.22}$$

Similiarly

$$\bar{\underline{U}} = \underline{w}\ \bar{\underline{u}} \qquad (2.23)$$

w = interpolation functions (section 2.9)

u = vector of nodal velocities

$\bar{u}$ = vector of nodal velocities of the weighting function u_i^* .

These are arbitrary and non-zero everywhere except at the boundary Γ , where they become zero.

Grouping equations (2.19) and (2.20) into a matrix form, and using the above defined interpolation function gives

$$\rho\int_\Omega \underline{\bar{u}}^{*t}\underline{\omega}^t\underline{\omega}\,\dot{u}\,d\Omega + \rho\int_\Omega \underline{\bar{u}}^{*t}\underline{\omega}^t\left[\underline{\nabla}^t(\underline{\omega}u)^t\right]^t\omega.u\,d\Omega + \int_\Omega \underline{\bar{u}}^{*t}\omega\underline{\partial}\chi\underline{\partial}\underline{\omega}\,\underline{u}\,d\Omega$$

$$= \int_\Gamma \underline{\bar{u}}^{*t}\underline{\omega}^t\underline{F}\,d\Gamma \qquad (2.24)$$

where $\underline{\partial}$ and $\underline{\nabla}$ are the differential operators given as

$$\underline{\partial} = \begin{bmatrix} \frac{\partial}{\partial x} & 0 \\ 0 & \frac{\partial}{\partial y} \\ \frac{\partial}{\partial y} & \frac{\partial}{\partial x} \end{bmatrix} \quad \text{and} \quad \underline{\nabla} = \begin{bmatrix} \frac{\partial}{\partial x} \\ \frac{\partial}{\partial y} \end{bmatrix} \qquad (2.25)$$

$\underline{\chi}$ is the material property matrix and is derived from

$$\underline{\chi} = \begin{bmatrix} 2\mu+\lambda & \lambda & 0 \\ \lambda & 2\mu+\lambda & 0 \\ 0 & 0 & \mu \end{bmatrix} = \begin{bmatrix} 2\mu+\frac{2\mu\nu}{1-2\nu} & \frac{2\mu\nu}{1-2\nu} & 0 \\ \frac{2\mu\nu}{1-2\nu} & 2\mu+\frac{2\mu\nu}{1-2\nu} & 0 \\ 0 & 0 & \mu \end{bmatrix}$$

$$= \mu \begin{bmatrix} \frac{2(1-\nu)}{1-2\nu} & \frac{2\nu}{1-2\nu} & 0 \\ \frac{2\nu}{1-2\nu} & \frac{2(1-\nu)}{1-2\nu} & 0 \\ 0 & 0 & 1 \end{bmatrix} = \mu \begin{bmatrix} 2(1-\nu)K & 2\nu K & 0 \\ 2\nu K & 2(1-\nu)K & 0 \\ 0 & 0 & 1 \end{bmatrix}$$

where $K = 1/(1-2\nu)$

and F = force vector

The expression for $\underline{\chi}$ is the same as in the case of plain strain, isotropic material.

The virtual velocities $\underline{\bar{u}}$ are non-zero and arbitrary. Equating the terms containing these, the following equations are obtained

$$\rho\int_{\Omega} \underline{w}^t \underline{w}\, \underline{\dot{u}}\, d\Omega + \rho\int_{\Omega} \underline{w}^t \left[\underline{\nabla}(\underline{w}\,\underline{u})^t\right]^t \underline{w}\, \underline{u}\, d\Omega + \int_{\Omega} \underline{\alpha}^t \underline{\chi}\, \underline{\alpha}\, \underline{u}\, d\Omega = \int_{\Gamma} \underline{w}^t \underline{F}\, d\Gamma \qquad (2.27)$$

where $\underline{\alpha} = \underline{\partial}\,\underline{w}$

Equation (2.27) applies to a single finite element and a small portion of the continuum it represents. The entire continuum region of interest is represented by assembling these elements such that the inter-element continuity of

the velocities is enforced. The following matrix equation is obtained as a result of this assembly process.

$$\underline{M}\dot{\underline{u}} + \underline{C}\underline{u} + \underline{N}(\underline{u})\underline{u} = \underline{F} \qquad (2.28)$$

Equation (2.28) forms the basic numerical description of the finite element analysis of problems in fluid flow. In a finite element computer program, it is most convenient to form the arrays $\underline{M}, \underline{C}, \underline{N}$ and $\underline{F}$ in a element-by-element fashion, such that

$$\underline{M} = \sum_{1}^{ne} \underline{M}_e \ , \ \underline{C} = \sum_{1}^{ne} \underline{C}_e, \quad \underline{N} = \sum_{1}^{ne} \underline{N}_e \quad \text{and} \quad \underline{F} = \sum_{1}^{ne} \underline{F}_e \qquad (2.29)$$

where $\sum$ denotes an "assembly operator" whose function is to add elemental contributions $\underline{M}_e$, $\underline{C}_e$, $\underline{N}_e$, $\underline{F}_e$ to the appropriate locations of $\underline{M}$, $\underline{C}$, $\underline{N}$ and $\underline{F}$, and ne is the number of elements. The matrices are identified as

a) The Mass Matrix

$$\underline{M}_e = \rho \int_{\Omega} \underline{w}^t \underline{w} \, d\Omega \qquad (2.30)$$

$\underline{M}_e$ is usually approximated to a diagonal matrix.

b) The Stokes Flow Matrix

$$\underline{C}_e = \int_{\Omega} \underline{\alpha}^t \underline{\chi} \underline{\alpha} \, d\Omega \tag{2.31}$$

$\underline{C}_e$ is symmetric, positive definite and possess a band profile structure (fig.2.2).

c) The Non-Linear Convective Matrix

$$\underline{N}_e = \rho \int_{\Omega} \underline{w}^t \left[\underline{\nabla} . (\underline{w} . \underline{u})^t \right]^t \underline{w} \, d\Omega \tag{2.32}$$

d) The Force Vector

$$\underline{F}_e = \int_{\Gamma} \underline{w}^t \underline{f} \, d\Gamma \tag{2.33}$$

These matrices are integrated using numerical integration (50).

2.5 Selective Reduced Integration

In the analysis of a three-dimensional or plane strain elastic body, as Poissons ratio tends towards 0.5 the equations become ill-conditioned because of the high bulk stiffness. Taking ν too close to 0.5 can either ruin the discretisation accuracy or produce an excessively ill-conditioned stiffness matrix. If the Poissons ratio is not sufficiently close to 0.5 then the solution is no longer incompressible.

For incompressible flow problems then, when λ is chosen to be sufficiently large that the flow is incompressible, other problems can arise, most especially element locking. When the element is integrated numerically an incompressibility constraint is introduced at every integration point. If a large number of integration points are chosen then there will be more constraints than there are degrees of freedom and the element will "lock". It is important, therefore, that only a sufficient number of constraints are introduced to enforce incompressibility. This is achieved by only enforcing the constraint at a selected number of points within the element, usually at fewer points than are used to integrate the element matrices. Thus in integrating the element matrices the Stokes flow component are sampled at a sufficient number of integration points to integrate them exactly, but the incompressible constraints are only enforced at sufficient points to obtain a non-singular matrix. This process is termed selective reduced integration and it has been used extensively in this work.

To implement the selective reduced integration the Stokes Flow coefficient matrix $\underline{C}$ is segregated into two components, the dilatational (volumetric) and the deviatoric (shear) contributions.

$$C = \int_{\Omega} \underline{\alpha}^{t} \underline{K} \underline{\alpha} \, d\Omega = \underline{C}_{DIL} + \underline{C}_{DEV} \qquad (2.34)$$

$\underline{\chi}$ is the material property matrix containing the terms $1/(1-2\nu)$ which becomes infinite as ν approaches 0.5. The strain-velocity matrix is split into two components in a way such that when the product $\underline{\alpha}^t\underline{\chi}\underline{\alpha}$ is performed, only the terms of $\underline{C}$ which give rise to volumetric changes, retain the infinite terms of $\underline{\chi}$.

A typical nodal element submatrix of 'α' is

$$\underline{\alpha}_n = \begin{bmatrix} \frac{\partial \omega_n}{\partial x} & 0 \\ 0 & \frac{\partial \omega_n}{\partial y} \\ \frac{\partial \omega_n}{\partial y} & \frac{\partial \omega_n}{\partial x} \end{bmatrix} \qquad (2.35)$$

Let α_{DIL} denote the dilatational part of α_n(34).

$$\alpha_{DIL} = \frac{1}{2}\begin{bmatrix} \frac{\partial \omega_n}{\partial x} & \frac{\partial \omega_n}{\partial y} \\ \frac{\partial \omega_n}{\partial x} & \frac{\partial \omega_n}{\partial y} \\ 0 & 0 \end{bmatrix} \qquad (2.36)$$

Then the deviatoric component $\underline{\alpha}_{DEV}$ is

$$\underline{\alpha}_{DEV} = \underline{\alpha}_n - \underline{\alpha}_{DIL}$$

$$\underline{\alpha}_{DEV} = \begin{bmatrix} \frac{1}{2}\frac{\partial w_n}{\partial x} & -\frac{1}{2}\frac{\partial w_n}{\partial y} \\ -\frac{1}{2}\frac{\partial w_n}{\partial x} & \frac{1}{2}\frac{\partial w_n}{\partial y} \\ \frac{\partial w_n}{\partial y} & \frac{\partial w_n}{\partial x} \end{bmatrix} \qquad (2.37)$$

The expression for $\underline{C}$ then becomes

$$\underline{C} = \int_{\Omega} \left(\underline{\alpha}^t_{DEV} + \underline{\alpha}^t_{DIL}\right) \underline{X} \left(\underline{\alpha}_{DEV} + \underline{\alpha}_{DIL}\right) d\Omega \qquad (2.38)$$

If the multiplication is carried out the equation (2.38) becomes

$$\underline{C} = \int_{\Omega} \underline{\alpha}^t_{DEV} \underline{X} \underline{\alpha}_{DEV} d\Omega + \int_{\Omega} \underline{\alpha}^t_{DIL} \underline{X} \underline{\alpha}_{DIL} d\Omega \qquad (2.39)$$

The terms $\int_{\Omega} \underline{\alpha}^t_{DEV} \underline{X} \underline{\alpha}_{DIL} d\Omega$ and $\int_{\Omega} \underline{\alpha}^t_{DIL} \underline{X} \underline{\alpha}_{DEV} d\Omega$ are identically zero for an isotropic media.

Volumetric part is

$$\underline{\alpha}_{DIL}^{t}\underline{X}\,\underline{\alpha}_{DIL} = \begin{bmatrix} \frac{1}{2}\frac{\partial \omega_n}{\partial x} & \frac{1}{2}\frac{\partial \omega_n}{\partial x} & 0 \\ \frac{1}{2}\frac{\partial \omega_n}{\partial y} & \frac{1}{2}\frac{\partial \omega_n}{\partial y} & 0 \end{bmatrix} \mu \begin{bmatrix} 2(1-\nu)K & 2K\nu & 0 \\ 2K\nu & 2(1-\nu)K & 0 \\ 0 & 0 & 1 \end{bmatrix} \begin{bmatrix} \frac{1}{2}\frac{\partial \omega_n}{\partial x} & \frac{1}{2}\frac{\partial \omega_n}{\partial y} \\ \frac{1}{2}\frac{\partial \omega_n}{\partial x} & \frac{1}{2}\frac{\partial \omega_n}{\partial y} \\ 0 & 0 \end{bmatrix}$$

$$= \mu \begin{bmatrix} \frac{\partial \omega_n}{\partial x}\cdot\frac{K}{4}(1+2\nu)\frac{\partial \omega_n}{\partial x} & \frac{\partial \omega_n}{\partial x}\cdot\frac{K}{4}(1+2\nu)\frac{\partial \omega_n}{\partial y} \\ \frac{\partial \omega_n}{\partial y}\cdot\frac{K}{4}(1+2\nu)\frac{\partial \omega_n}{\partial x} & \frac{\partial \omega_n}{\partial y}\cdot\frac{K}{4}(1+2\nu)\frac{\partial \omega_n}{\partial y} \end{bmatrix} \qquad (2.40)$$

$K = 1/(1-2\nu)$ approaches infinity as $\nu \rightarrow 0.5$. Thus the matrix $\underline{C}_{DIL}$ contains all the infinite terms.

Deviatoric part is

$$\underline{\alpha}_{DEV}^{t}\underline{X}\,\underline{\alpha}_{DEV} = \begin{bmatrix} \frac{1}{2}\frac{\partial \omega_n}{\partial x} & -\frac{1}{2}\frac{\partial \omega_n}{\partial x} & \frac{\partial \omega_n}{\partial y} \\ -\frac{1}{2}\frac{\partial \omega_n}{\partial y} & \frac{1}{2}\frac{\partial \omega_n}{\partial y} & \frac{\partial \omega_n}{\partial x} \end{bmatrix} \mu \begin{bmatrix} 2(1-\nu)K & 2\nu K & 0 \\ 2\nu K & 2(1-\nu)K & 0 \\ 0 & 0 & 1 \end{bmatrix} \begin{bmatrix} \frac{1}{2}\frac{\partial \omega_n}{\partial x} & -\frac{1}{2}\frac{\partial \omega_n}{\partial y} \\ -\frac{1}{2}\frac{\partial \omega_n}{\partial x} & \frac{1}{2}\frac{\partial \omega_n}{\partial y} \\ \frac{\partial \omega_n}{\partial y} & \frac{\partial \omega_n}{\partial x} \end{bmatrix}$$

$$= \mu \begin{bmatrix} \frac{1}{2}\frac{\partial \omega_n}{\partial x}\frac{\partial \omega_n}{\partial x} + \frac{\partial \omega_n}{\partial y}\cdot\frac{\partial \omega_n}{\partial y} & \frac{1}{2}\frac{\partial \omega_n}{\partial x}\frac{\partial \omega_n}{\partial y} \\ \frac{1}{2}\frac{\partial \omega_n}{\partial y}\frac{\partial \omega_n}{\partial x} & \frac{1}{2}\frac{\partial \omega_n}{\partial y}\frac{\partial \omega_n}{\partial y} + \frac{\partial \omega_n}{\partial x}\cdot\frac{\partial \omega_n}{\partial x} \end{bmatrix} \qquad (2.41)$$

All the above terms do not include the infinite term 'K'.

Cross Products

$$\underline{\alpha}^{t}_{DEV}\underline{X}\underline{\alpha}_{DIL}$$

$$= \underline{\alpha}^{t}_{DIL}\underline{X}\underline{\alpha}_{DEV} = \begin{bmatrix} \frac{1}{2}\frac{\partial w_n}{\partial x} & -\frac{1}{2}\frac{\partial w_n}{\partial x} & \frac{\partial w_n}{\partial y} \\ -\frac{1}{2}\frac{\partial w_n}{\partial y} & \frac{1}{2}\frac{\partial w_n}{\partial y} & \frac{\partial w_n}{\partial x} \end{bmatrix} \mu \begin{bmatrix} 2(1-\nu)K & 2\nu K & 0 \\ 2\nu K & 2(1-\nu)K & 0 \\ 0 & 0 & 1 \end{bmatrix} \begin{bmatrix} \frac{1}{2}\frac{\partial w_n}{\partial x} & -\frac{1}{2}\frac{\partial w_n}{\partial y} \\ -\frac{1}{2}\frac{\partial w_n}{\partial y} & \frac{1}{2}\frac{\partial w_n}{\partial y} \\ \frac{\partial w_n}{\partial y} & \frac{\partial w_n}{\partial x} \end{bmatrix}$$

$$= \begin{bmatrix} 0 & 0 \\ 0 & 0 \end{bmatrix}$$

The volumetric component is integrated using reduced integration thus alleviating "mesh locking". Full integration is employed on the remaining component of the matrix $\underline{C}$ to retain the rank of the matrix. It can be shown that, although the matrix $\underline{C}_{DIL}$ contains very large terms, it is singular and does not affect the overall solution of the equation (2.38) (51). The incompressibility constraint is imposed, since the product

$$\underline{C}_{DIL}\underline{u}_d = 0 \qquad (2.43)$$

where $\underline{u}_d$ is a deformation mode containing no-volume changes. To validate equation (2.43) consider a single four-noded element to keep the matrices simple (fig.2.3). Full

integration is carried out at 2X2 Guass Integration points and reduced integration at 1X1 Guass Integration points. Similar proof applies to the nine-noded element.

The velocity vector is interpolated as follows

$$\begin{bmatrix} (1-\xi_1)(1-\xi_2) & 0 & (1+\xi_1)(1-\xi_2) & 0 & (1-\xi_1)(1+\xi_2) & 0 & (1+\xi_1)(1+\xi_2) & 0 \\ 0 & (1-\xi_1)(1-\xi_2) & 0 & (1+\xi_1)(1-\xi_2) & 0 & (1-\xi_1)(1+\xi_2) & 0 & (1+\xi_1)(1+\xi_2) \end{bmatrix} \begin{bmatrix} u_1' \\ v_1' \\ u_2' \\ v_2' \\ u_3' \\ v_3' \\ u_4' \\ v_4' \end{bmatrix}$$

Using the above interpolation functions and using equations (2.34,2.39) the matrices are formed as

$$\underline{C}_{DEV} = t' \begin{bmatrix} \frac{1}{3} & 0 & -\frac{1}{2} & -\frac{1}{4} & -\frac{1}{12} & \frac{1}{4} & -\frac{1}{6} & 0 \\ & \frac{1}{3} & \frac{1}{4} & -\frac{1}{12} & -\frac{1}{4} & -\frac{1}{12} & 0 & -\frac{1}{6} \\ & & \frac{1}{3} & 0 & -\frac{1}{6} & 0 & -\frac{1}{12} & -\frac{1}{4} \\ & & & \frac{1}{3} & 0 & -\frac{1}{6} & \frac{1}{4} & -\frac{1}{12} \\ & & & & \frac{1}{3} & 0 & -\frac{1}{12} & \frac{1}{4} \\ \text{SYM.} & & & & & \frac{1}{3} & -\frac{1}{4} & -\frac{1}{12} \\ & & & & & & \frac{1}{3} & 0 \\ & & & & & & & \frac{1}{3} \end{bmatrix}$$

$$\underline{C}_{DIL} = \frac{\mu t}{4(1-2\nu)} \begin{bmatrix} 1 & 1 & -1 & 1 & 1 & -1 & -1 & -1 \\ & 1 & -1 & 1 & 1 & -1 & -1 & -1 \\ & & 1 & -1 & -1 & 1 & 1 & 1 \\ & & & 1 & 1 & -1 & -1 & -1 \\ & & & & 1 & -1 & -1 & -1 \\ & & & & & 1 & 1 & 1 \\ & & & & & & 1 & 1 \\ & & & & & & & 1 \end{bmatrix}$$

The matrix $\underline{C}_{DEV}$ does not contain any $(1/1-2\nu)$ terms and is thus finite. However, $\underline{C}_{DIL}$ contains the infinite terms as ν approaches 0.5.

The matrix $\underline{C}_{DIL}$ is made singular (because of reduced integration) and will not affect the overall solution of equation (2.38), but it will make any velocities involving volume change zero. To show the above to be true, consider fig.2.3, the nodal velocities $\underline{u}_d$

$$\underline{u}_d = \begin{bmatrix} 0 & v_1' & u_2' & v_2' & 0 & 0 & u_4' & 0 \end{bmatrix}$$

Considering a small velocity, with $v_1' = v_2'$ and $u_2' = u_4'$ the volume change is

$$dV = (1+u_2'\Delta t')\,(1-v_1'\Delta t) - 1^2$$
$$= 1^2 - 1v_1'\Delta t' + 1u_2'\Delta t - u_2'v_1'\Delta t'^2 - 1^2 \qquad (u_2'v_1'\Delta t'^2 = 0)$$
$$= 1\Delta t'\,(u_2' - v_1')$$

For no volume change

$$u_2' = v_1' = u'$$

and $\underline{u}_d = \left[0\ u'\ u'\ u'\ 0\ 0\ u'\ 0\right]$

Then $\underline{C}_{DIL}\underline{u}_d = 0$ for no volume change.

For any other $\underline{U}_d$, then $\underline{C}_{DIL}\,u_d \neq 0$

Hence $\underline{C}_{DIL}$ imposes the incompressibilty constraint without changing the character of the solution of equation (2.38).

For the nine-noded parabolic element used here the volumetric component of $\underline{C}$ is integrated using a set of 2X2 integration points, while the remaining terms of $\underline{C}$ are integrated fully using a set of 3X3 integration points.

2.6 Solution Method of the Matrix Equations

Equation (2.28) denotes an initial value problem for a system of non-linear ordinary differential equations. $\underline{C}$ is a linear, symmetric matrix whilst $\underline{N}(\underline{u})$ is a non-linear, non-symmetric matrix. $\underline{u}=\underline{u}(x,t)$ is a time-dependant function of x and t. To solve this problem, a time-stepping algorithm is used, based on the one-step "linearly implicit" predictor-corrector method as suggested by Hughes et al (40).The algorithm can be summarised as :

$$(\underline{M}+\gamma\Delta t\underline{C})\underline{u}^{i+1}_{n+1} = \underline{M}\tilde{\underline{u}}_{n+1} + \gamma\Delta t(\underline{F}_{n+1}-\underline{N}(\underline{u}^{i}_{n+1})\underline{u}^{i}_{n+1}) \quad \text{-Corrector-} \quad (2.44)$$

$$\tilde{\underline{u}}_{n+1}=\underline{u}_n +(1-\gamma)\Delta t\underline{a}_n \quad \text{-predictor-} \quad (2.45)$$

$$\underline{u}^{0}_{n+1}=\tilde{\underline{u}}_{n+1} \quad (2.46a)$$

$$\underline{a}_{n+1}=(\underline{u}_{n+1}-\tilde{\underline{u}}_{n+1})/\gamma\Delta t \quad (2.46b)$$

where Δt = Time step

$\underline{F}$ = Force vector at n'th timestep

$\underline{u}$ = velocity vector at n'th timestep

$\underline{a}$ = acceleration vector at n'th time step

γ = Positive parameter which governs stability and accuracy of the algorithm

i = number of iterations within each timestep.

The velocity vector at time t_{n+1} is defined as

$$u_{n+1} = u^{i+1}_{n+1}$$

In each timestep equations (2.44) and (2.45) are solved i+1 times. A local truncation-error analysis reveals that if i=0,

the algorithm is first-order accurate, whereas if i=1 and γ=0.5, then a second order accuracy is achieved (40). This requires twice as many solutions to equations (2.44) and (2.45) and is hence twice as expensive as the first order scheme. The solution procedure using an upwind scheme and i=0 was found to be stable by Hughes et al (40), if Δt satisfies a Courant Condition (52). Tests reveal that the solution procedure becomes unstable for i=0 for all $\Delta t > 0$, if standard Guass integration is used. However, for i=1, γ=1 and Δt chosen according to equation (2.49) the solution procedure is found to be stable.

The algorithm is initialised by specification of the initial velocity and acceleration $\underline{u}_o$ and $\underline{a}_o$. It is quite possible to start with a quiescent state ($\underline{u}_o = \underline{a}_o = 0$), but we find that in this case the convergence is very slow and many extra timesteps are required before steady state solution is obtained. Instead we initialise the algorithm by using Stokes Flow solution (Re=0) obtained by solving the linear equation (2.47). Hence the simplified algorithm used to solve the non-linear equation (2.28) becomes

$$\underline{C}\underline{u}_o = \underline{F} \quad \text{Initialisation} \tag{2.47}$$

$$(\underline{M} + \Delta t \underline{C})\underline{u}^{i+1}_{n+1} = \underline{M}\bar{\underline{u}}_{n+1} + \Delta t\,(\underline{F}_{n+1} - \underline{N}(\underline{u}^{i}_{n+1})\underline{u}^{i}_{n+1}) \tag{2.48a}$$

$$\bar{\underline{u}}_{n+1} = \underline{u}_n \tag{2.48b}$$

$$\underline{u}^{o}_{n+1} = \bar{\underline{u}}_{n+1} \tag{2.48c}$$

where $$\Delta t \leq \frac{1}{\left(\frac{|u_n|}{\Delta x} + \frac{|v_n|}{\Delta y}\right)} \qquad (2.49)$$

u_n and v_n are the nodal velocities for the element and Δx and Δy are the distance between the two adjacent nodes for that element in x and y direction respectively. Within each timestep equation (2.48) is solved twice. By carring out tests with i>1, it was found the convergence rate or accuracy for the solution does not increase significantly, however, there is considerable increase in cost of the analysis. The left hand side of equation (2.48) consists of matrices $\underline{C}$ and $\underline{M}$. Both are symmetric, positive definite and possess the band profile structure of $\underline{C}$. For a fixed timestep we need to form the left side of equation (2.48) once only. $\underline{M}\underline{u}_{n+1}$ and $\underline{N}(\underline{u}^i_{n+1})\underline{u}^i_{n+1}$ are formed as a product, element by element, and then assembled for the entire domain. $\underline{M}$ and $\underline{N}(\underline{u})$ are square matrices, while $\underline{u}$ is a column matrix. The product thus formed is a column matrix, which is relatively cheap and easy to store. $\underline{M}\underline{u}_{n+1}$ is formed at each timestep once only, while the non-linear matrix $\underline{N}(\underline{u}^i_{n+1})\underline{u}^i_{n+1}$ is formed at each iteration within the timestep but $\underline{N}(\underline{u}^i_{n+1})$ need not be formed explicitly. The right hand side of equation (2.48) is thus a column load vector which is updated at each iteration. The process is economical and does not require any additional storage. The major contributors to the computational cost of the algorithm are the forward-reduction/back-substitution of the factorised array in obtaining $\underline{u}^{i+1}_{n+1}$.

When it is required to solve for high Reynolds number flow, it is found that an incremental Reynolds number approach is cheaper. The Reynolds number is incremented in steps. To start off, a smaller Reynolds number is used and when the flow at this lower Reynolds number has reached steady-state, the Reynolds number is incremented to a higher value and the solution at the lower Reynolds number is used as the starting conditions. The number of increments depends on how high the flow Reynolds number is. Multiple factorisations are required if an incremental Reynolds number approach is used. The Reynolds number $(\rho ud/\mu)$ is incremented by increasing the value of density ρ . The new value is automatically incorporated when the non-linear convective matrix $\underline{N}(\underline{u})$is formed at each timestep. However, it is also required to update the mass matrix $\underline{M}$ with the new value of ρ. The assembly costs can be reduced by forming the matrices $\underline{M}$ and $\underline{C}$ once only, and just before factorisation of the term $(\underline{M}+\Delta t\underline{C})$, $\underline{M}$ is multiplied by the required increment in density. For example if the flow Reynolds number is 5000 and is analysed in the steps 100,500,1000,2000,5000, then the density increments are 5,2,2,2.5 based on the previous density value. This process can be easily carried out inside the solution module, by forming the new matrix $\underline{M}$, then $(\underline{M}+\Delta t\underline{C})$ and factoring and overwriting the old matrix for which a solution has already been obtained. This approach is used in section (7.3) to solve for flow inside a square cavity at high Reynolds number.

2.7 Convergence Criterion

At each timestep the non-dimensional Euclidean norm (Ec) of the difference of the solutions at any two successive iterations is compared against a sufficiently small value of the order $10^{-4} - 10^{-5}$.

$$Ec = \sum_{n=1}^{NE} \frac{|u_{n+1} - u_n|}{u_{max}} \times \frac{1}{NE} \qquad (2.50)$$

NE = number of equations

A gradual decrease in the value of Ec indicates convergence. However, if the value of Euclidean norm of the difference of the solution at any two successive iterations is larger than the value at a previous timestep and continues to increase in the following iterations, the execution is terminated and the timestep size and mesh density are further investigated. Usually a smaller timestep than the one selected is required or the mesh needs refining in the critical regions involving sharp corners and rapid flow changes. These points are further investigated in the following chapters.

To accelerate the convergence a weighted average of the velocities was also used in computing the velocity matrix for the next iteration. For example for the nth timestep

$$\underline{u} = e'(\underline{u}_n) + (1-e')u_{n-1} \qquad (2.51)$$

Where $0 < e < 1$. The above procedure is very useful if the problem to be solved exhibits an oscillatory convergence. When the value of Euclidean norm "Ec" is equal to or less than the value of Convergence Factor (typical value $10^{-4} - 10^{-5}$) we assume that the flow has reached a steady state. A steady state flow solution has been achieved for low to moderate Reynolds number flow inside a square cavity (section 7.3) and low Reynolds number flow over a backward facing step (section 7.2).

2.8 The Selection of the Timestep

The cost of the analysis (i.e. the number of operations required) is directly proportional to the number of timesteps required for the solution. It follows that the selection of an appropriate timestep is of much importance. The timestep must be small enough to obtain accuracy and stability in the solution, but not smaller than necessary, because this would mean that the solution is more costly than is actually required.

The timestep is selected according to equation (2.49) which is the Courant Stability condition (52) for two-dimensional flow. The inequality in equation (2.49) must be satisfied for each element in the mesh. The equation is solely a convection condition and is

independent of Reynolds number. In order to obtain a solution free from instabilities and one that converges towards the steady state solution, it is required to select a mesh which is fine enough to resolve the boundary layer. The boundary layer gets thinner as the Reynolds number is increased. As is shown in section 7.3 using too coarse a mesh in the boundary layer region leads to instabilities appearing as ripples in the velocity vector plots. These ripples slow down convergence and the solution fails to converge towards a steady state if the Reynolds number is high. The presence of instabilities indicates a need for mesh refinement in these regions. The element Reynolds number given as $Re_e = \frac{u_e \ell L_e}{\mu}$ (52) is required to be roughly equal to or less than 2, in these critical regions only. Everywhere else a much larger value of local Reynolds number can be used (section (7.3)). The new timestep is selected based upon this new mesh with smaller elements. Hence the timestep selection is also Reynolds number dependant. Investigations into mesh density and timestep selection for various example problems are further carried out in chapters 5 and 6.

2.9 The Fluid Element Selection and Formulation

One of the main problems associated with the selective reduced integration is that not all of the element families perform equally well. Studies have been undertaken to determine the most effective elements and quadrature scheme for use with the penalty methods. So far, these efforts have been largely empirical as no rigorous general theory yet exists. According to an heuristic theory (35), the most effective elements in applications of the type considered here are the "Lagrange" isoparametric elements with appropriate selective integration schemes. These elements, for the two-dimensional case, are schematically illustrated in fig.2.4. Triangular elements and "serendipity" quadrilateral elements are predicted to exhibit inferior behaviour, which has been confirmed numerically (53).

Previous studies undertaken by Prassas (51) using selective reduced integration show that the Lagrange family of elements exhibit better performance than the "serendipity" quadrilateral elements. A simple test of entry flow in a pipe was carried out using the eight-noded Serendipity and the nine-noded Lagrange elements, with different values of equivalent Poissons ratio ν tending towards 0.5. With eight-noded element ripples began to

appear in the flow field as the value of ν was increased beyond .4999999. However, with nine-noded element the solution was stable for all values of ν. It has been suggested (51) that for the element to show correct behaviour the number of parameters p' describing the variation of velocity $\underline{u}$ must be greater than the number of points of the reduced quadrature used α'. Otherwise the incompressibility constraints dominate the coefficient matrix and the elements "lock".

Based on the findings listed above, a two-dimensional nine-noded Lagrange Fluid Element is developed. The basic procedure in the isoparametric finite element formulation is to express the finite element coordinates and element displacements in the form of interpolations using the natural coordinate system of the element. For the 2-dimensional element the coordinate interpolations are

$$x = \sum_{i=1}^{9} w_i x_i \qquad (2.52)$$

$$y = \sum_{i=1}^{9} w_i y_i \qquad (2.53)$$

where x and y are the coordinates at any point of the element and x_i and y_i (i=1,9) are the coordinates of the element nodes. The interpolation functions w are defined in the natural coordinate system of the element, which has variables ξ_1 and ξ_2 that each vary from -1 to

+1. The fundamental property of the interpolation function w is that its value in the natural coordinate system is unity at node i and is zero at all other nodes. Using these conditions the functions w corresponding to a specific nodal point layout could be solved for in a symmetric manner. For a nine-noded parabolic element (fig. 2.5) these are given as below

$$w_1 = \frac{1}{4}\xi_1\xi_2(\xi_1-1)(\xi_2-1)$$

$$w_2 = \frac{1}{2}\xi_2(1-\xi_1^2)(\xi_2-1)$$

$$w_3 = \frac{1}{4}\xi_1\xi_2(\xi_1+1)(\xi_2-1)$$

$$w_4 = \frac{1}{2}\xi_1(\xi_1-1)(1-\xi_2^2)$$

$$w_5 = (1-\xi_1^2)(1-\xi_2^2)$$

$$w_6 = \frac{1}{2}\xi_1(\xi_1+1)(1-\xi_2^2)$$

$$w_7 = \frac{1}{4}\xi_1\xi_2(\xi_1-1)(\xi_2+1)$$

$$w_8 = \frac{1}{2}(1-\xi_1^2)(\xi_2+1)$$

$$w_9 = \frac{1}{4}\xi_1\xi_2(1+\xi_1)(1+\xi_2)$$

By means of the coordinate interpolation, the element can have curved boundries if required. The interpolation function matrix is thus

$$\underline{w} = \begin{bmatrix} w_1\,0 & w_2\,0 & w_3\,0 & w_4\,0 & w_5\,0 & w_6\,0 & w_7\,0 & w_8\,0 & w_9\,0 \\ 0\,w_1 & 0\,w_2 & 0\,w_3 & 0\,w_4 & 0\,w_5 & 0\,w_6 & 0\,w_7 & 0\,w_8 & 0\,w_9 \end{bmatrix} \qquad (2.54)$$

In the isoparametric formulation the element displacements are interpolated in the same way as the geometry.

$$u = \sum_{i=1}^{9} \omega_i u_i \qquad (2.55)$$

$$v = \sum_{i=1}^{9} \omega_i v_i \qquad (2.56)$$

where u and v are the local element displacements at any point of the element and u_i and v_i (i=1,9) are the corresponding element displacements at its nodes.

To be able to evaluate the element matrices, we need to evaluate the strain-displacement transformation matrix. The element strains are obtained in terms of derivatives of element displacements with respect to the local

coordinates. Because the element displacements are defined in the natural coordinate system (equation (2.55)), it is required to relate x and y derivatives to η_1 and η_2 derivatives, thus

$$x = f_1(\eta_1,\eta_2), \quad y = f_2(\eta_1,\eta_2) \tag{2.57}$$

The inverse relationship is

$$\eta_1 = f_3(x,y), \quad \eta_2 = f_4(x,y) \tag{2.58}$$

The derivatives $\partial/\partial x$ and $\partial/\partial y$ are also required and can be calculated using the chain rule

$$\frac{\partial}{\partial x} = \frac{\partial}{\partial \eta_1}\cdot\frac{\partial \eta_1}{\partial x} + \frac{\partial}{\partial \eta_2}\cdot\frac{\partial \eta_2}{\partial x}$$

and similiarly for $\partial/\partial y$. In the matrix form

$$\begin{bmatrix} \frac{\partial}{\partial \eta_1} \\ \frac{\partial}{\partial \eta_2} \end{bmatrix} = \begin{bmatrix} \frac{\partial x}{\partial \eta_1} & \frac{\partial y}{\partial \eta_1} \\ \frac{\partial x}{\partial \eta_2} & \frac{\partial y}{\partial \eta_2} \end{bmatrix} \begin{bmatrix} \frac{\partial}{\partial x} \\ \frac{\partial}{\partial y} \end{bmatrix}$$

or

$$\frac{\partial}{\partial \underline{\eta}} = \underline{J}\frac{\partial}{\partial \underline{x}} \qquad \frac{\partial}{\partial \underline{x}} = \underline{J}^{-1}\frac{\partial}{\partial \underline{\eta}} \tag{2.59}$$

$\underline{J}$ is the Jacobian operator relating the natural coordinate derivatives to the local coordinate derivatives. The inverse of the Jacobian is easily found, provided there is one-to-one correspondance between the natural and the local coordinates of the element. Thus the strains can be calculated as

$$\varepsilon = \begin{bmatrix} \varepsilon_{xx} \\ \varepsilon_{yy} \\ \varepsilon_{xy} \end{bmatrix} = \begin{bmatrix} \partial/\partial x & 0 \\ 0 & \partial/\partial y \\ \partial/\partial y & \partial/\partial x \end{bmatrix} \begin{bmatrix} u \\ v \end{bmatrix} = \underline{\partial}\underline{\omega}\underline{u} \qquad (2.60)$$

Hence $\underline{\varepsilon} = \underline{\alpha}\,\underline{u}$

where $\underline{\alpha} = \underline{\partial}\underline{\omega}$ (2.61)

and $\underline{\alpha}$ is the strain-displacement matrix. The matrix $\underline{\alpha}$ is split into two separate components, dilatational and deviatoric, and is numerically integrated using selective reduced integration as detailed in section (2.5).

The volume integration extends over the natural coordinate volume, and the volume differential, dV, can be written in terms of natural coordinates as

$$dV = d\xi_1\, d\xi_2\, t' \,|J| \qquad (2.62)$$

where t' is the uniform element thickness. Using all of the above parameters the matrices in section (2.6) are integrated numerically.

2.10 Pressure Recovery

The theory given in this section is developed directly from the use of finite elements in structural analysis. The extension to flow problems is obtained immediately by replacing displacements by velocities and strains by strain rates. The resulting equations are identical to those given in this section. The fluid pressure recovery is based upon the equivalent stress recovery procedure as used in plain strain stress analysis. For an isotropic material the stress-strain relationship is given as (50)

$$\underline{\sigma} = \underline{\underline{\chi}}\,\underline{\varepsilon} \tag{2.63}$$

where $\underline{\underline{\chi}}$ is the material property matrix. For the two-dimensional plain-strain case

$$\underline{\sigma} = \begin{bmatrix} \sigma_{xx} \\ \sigma_{yy} \\ \sigma_{xy} \end{bmatrix} = \mu \begin{bmatrix} 2(1-\nu)K & 2\nu K & 0 \\ 2\nu K & 2(1-\nu)K & 0 \\ 0 & 0 & 1 \end{bmatrix} \begin{bmatrix} \partial u/\partial x \\ \partial v/\partial y \\ \partial u/\partial y + \dfrac{\partial v}{\partial x} \end{bmatrix}$$

$$= \mu \begin{bmatrix} 2K\left[(1-\nu)\dfrac{\partial u}{\partial x} + \nu\dfrac{\partial v}{\partial y}\right] \\ 2K\left[\nu\dfrac{\partial u}{\partial x} + (1-\nu)\dfrac{\partial v}{\partial y}\right] \\ \dfrac{\partial u}{\partial y} + \dfrac{\partial v}{\partial x} \end{bmatrix}$$

thus

$$\sigma_{xx} = 2\mu K\left((1-\nu)\frac{\partial u}{\partial x} + \mu\frac{\partial v}{\partial y}\right)$$

$$\sigma_{yy} = 2\mu K\left(\nu\frac{\partial u}{\partial x} + (1-\nu)\frac{\partial v}{\partial y}\right)$$

$$\sigma_{xy} = \mu\left(\frac{\partial u}{\partial y} + \frac{\partial v}{\partial x}\right)$$

in the case of an incompressible material with ν=0.5 the pressure 'p' is given as (50)

$$P = -1/3(\sigma_{xx} + \sigma_{yy} + \sigma_{zz}) \qquad (2.66)$$

or for two-dimensional case

$$p = -1/2(\sigma_{xx} + \sigma_{yy}) \qquad (2.67)$$

Substituting for σ_{xx} and σ_{yy} from equation (2.65)

$$p = -\tfrac{1}{2}\cdot 2\mu K\left[\frac{\partial u}{\partial x}(1-\nu+\nu) + \frac{\partial v}{\partial y}(1+\nu-\nu)\right]$$

$$= -\mu K\left[\frac{\partial u}{\partial x} + \frac{\partial v}{\partial y}\right]$$

$$= -\frac{\mu}{(1-2\nu)}\left[\frac{\partial u}{\partial x} + \frac{\partial v}{\partial y}\right]$$

$$= -\lambda\left[\frac{\partial u}{\partial x} + \frac{\partial v}{\partial y}\right] \qquad (2.68)$$

where $\lambda = \frac{\mu}{(1-2\nu)}$ as $\nu \to 0.5$

The expression for p in equation (2.68) is the same as used previously in equation (2.7) to substitute for p.

The approach used to calculate pressure can be easily accommodated in a general purpose stress analysis package. With very few changes, the sum of direct stresses is the pressure for fluid analysis (33).

In order to calculate the fluid pressures acting on the structure, it is required to calculate the fluid pressure on the fluid-structure interface boundary. These elemental pressure forces are found by integrating the stress over the element. The following standard relationship as used in the stress analysis is used to derive the expression for the pressure forces (50)

$$\underline{K}\underline{r} = \underline{R} \tag{2.69}$$

The matrix $\underline{K}$ has the form

$$\underline{K} = \sum_{1}^{ne} \int_{V} \underline{\alpha}^{t} \underline{\chi} \underline{\alpha} \, dV$$

where $\underline{\alpha}$ is the strain-velocity matrix

$\underline{X}$ is the material property matrix

$\underline{R}$ is the force vector

$\underline{r}$ is the displacement matrix or the equivalent velocity matrix in the fluid analysis

The force vector can be evaluated as below if the element stresses or pressure are known. The force vector for the element is

$$\begin{aligned}\underline{R}_n &= \int_V \underline{\alpha}^t \underline{X} \underline{\alpha} \, dV . \underline{u}_n \\ &= \int_V \underline{\alpha}^t \underline{X} \underline{\varepsilon}_n \, dV \\ &= \int_V \underline{\alpha}^t \underline{\sigma}_n \, dV \end{aligned} \qquad (2.70)$$

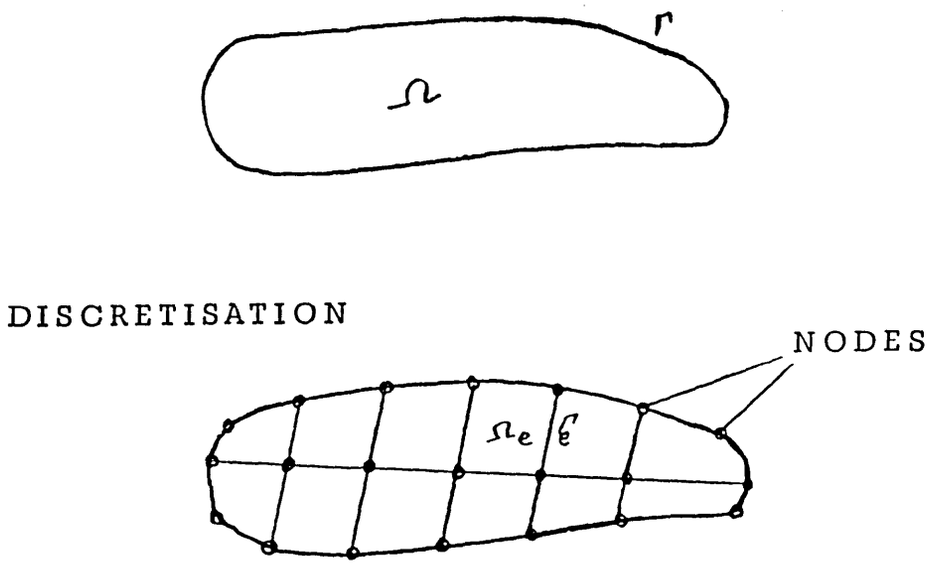

Fig.2.1 Finite Element Spatial Descretisation

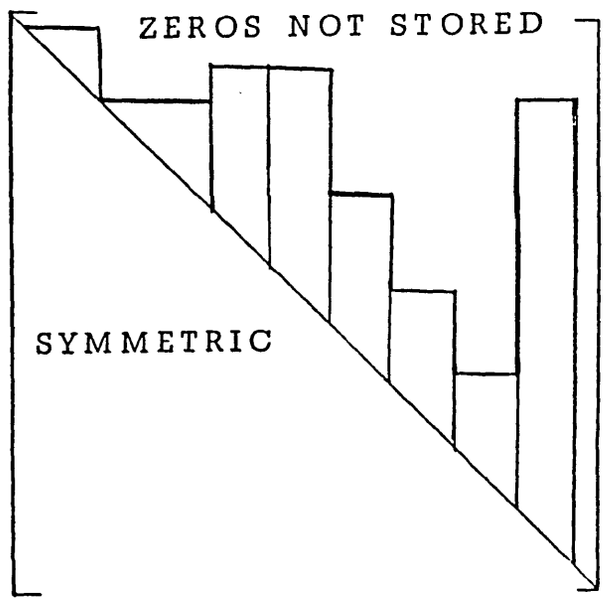

Fig.2.2 Symmetric Matrix with a Band-Profile Structure

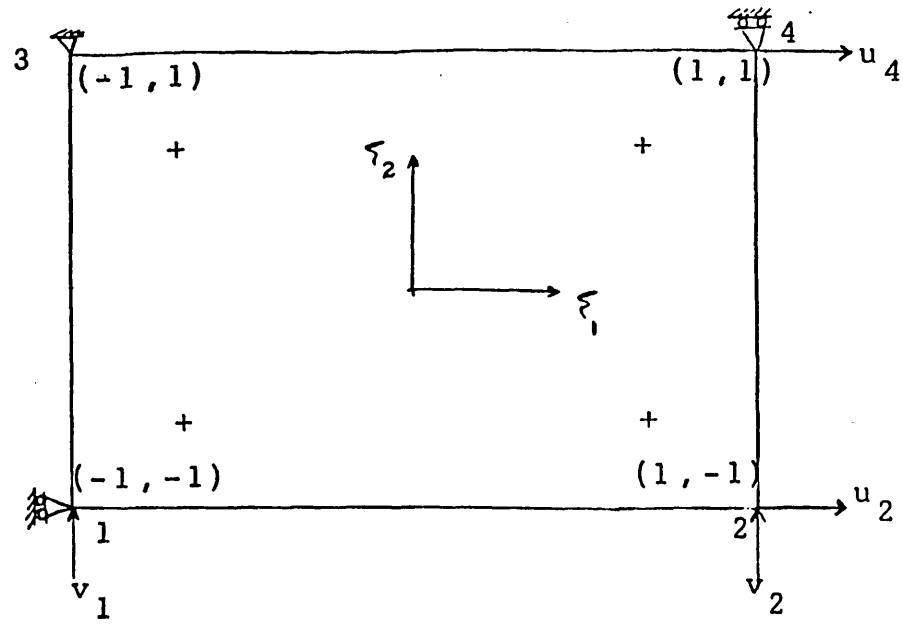

Fig.2.3 A Constraint and Deformed Flow Element

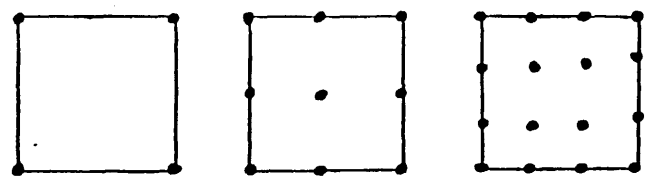

SHAPE FUNCTIONS	LINEAR	PARABOLIC	CUBIC
Integration used for -TERM	1X1	2X2	3X3
Integartion used for -TERM	2X2	3X3	4X4

Fig.2.4 Selective Guass-Integartion Rules for 2-D Isoparametric Lagrange Elements

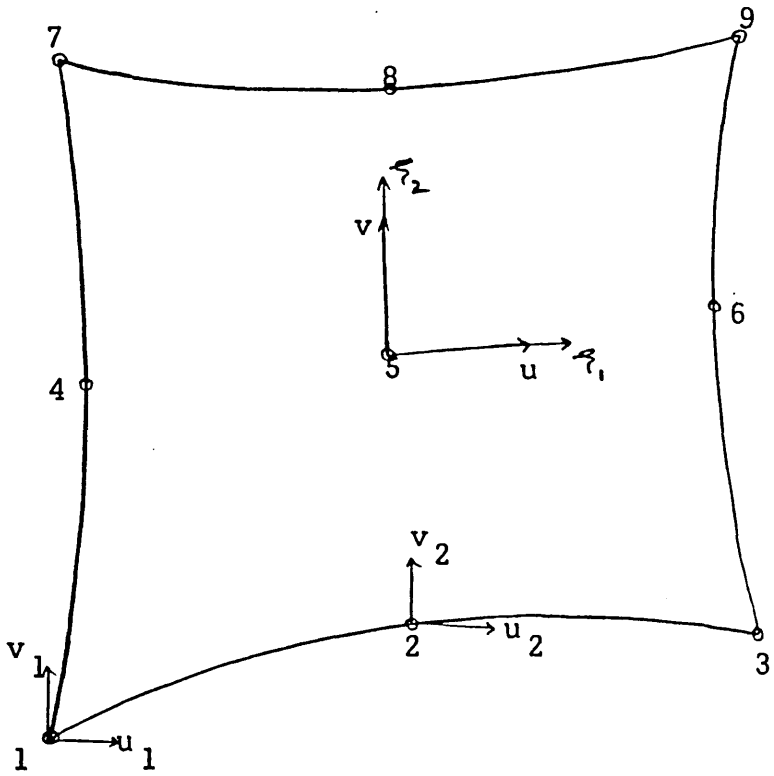

Fig.2.5 9-Noded Parabolic Element with Node Sequence to Evaluate Interpolation Functions

3. THE STRUCTURE IDEALISATION

The equation of motion of a structure is given by

$$\underline{M}_s \ddot{\underline{r}} + \underline{C}_s \dot{\underline{r}} + \underline{K}_s \underline{r} = \underline{R} \qquad (3.1)$$

where $\underline{M}_s$, $\underline{C}_s$, and $\underline{K}_s$ are the structural mass, damping and stiffness matrices. $\underline{R}$ is the external time varying load vector. For the examples given later a very simple structural idealisation has been used, where the cross-sectional shape has been assumed rigid, but rigid body translations and rotations are resisted by springs. For the case of a rigid circular cylinder, the structure is idealised as shown in fig. 3.1. The mass matrix and the stiffness matrix are both diagonal in this case.

$$\text{Mass matrix} \qquad \underline{M} = \begin{bmatrix} m & 0 & 0 \\ 0 & m & 0 \\ 0 & 0 & I \end{bmatrix}$$

$$\text{Stiffness matrix} \qquad \underline{K} = \begin{bmatrix} k_x & 0 & 0 \\ 0 & k_y & 0 \\ 0 & 0 & k_\theta \end{bmatrix}$$

$$\text{Load vector} \qquad \underline{R} = \begin{bmatrix} R_x \\ R_y \\ R_\theta \end{bmatrix}$$

where m = mass per unit length

I = Moment of inertia ($1/2md^2$ for a solid cylinder of radius 'd')

k_x = Stiffness in horizontal direction

k_y = Stiffness in vertical direction

k_θ = Rotational stiffness

R_x = Horizontal component of load vector (Lift)

R_y = Vertical component of load vector (Drag)

R_θ = Rotational component of load vector (moment)

The load vector $\underline{R}$, is formed by summing the nodal forces along the interface boundary about the centre of cylinder. The structural idealisation used in the fluid structure interaction examples to follow is indeed very simple, a more complicated general finite element model of the structure can, however, easily be incorporated into the method especially if the structural and fluid node points at the interface coincide. The associated finite element program FINEL has a wide range of structural elements and any of these can be used to represent a more complicated structure. The mass, stiffness and the damping matrices can be assembled using the standard routines inside the package. The force vector in this case will consist of the fluid forces corresponding to the nodes on the fluid structure boundary, found by solving the fluid equations. The process is relatively simple if the fluid and the

structure nodes coincide on the interface boundary. If the fluid and the structure nodes do not coincide on the interface boundary, some form of transformation matrix would be required to transform the fluid forces to equivalent values on the structure nodes and vice versa.

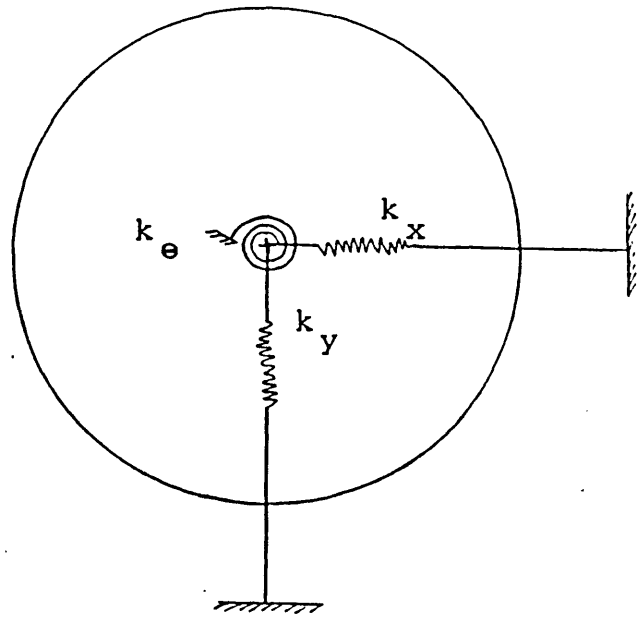

Fig.3.1 Simple Structure Idealisation

4. THE FLUID STRUCTURE INTERACTION

Both the structure and the control volume of the surrounding fluid are discretised by corresponding finite elements as shown in figure 4.1. The internal boundary conditions on the contact surface Γ_c are given by conditions for velocities and forces. The equation of motion for the fluid flow (eq.2.48) is solved first. The velocities obtained from this are used to calculate the fluid forces acting on the structure using the equation to calculate pressure forces (equation (2.70)) on the fluid-structure interface boundary

for the nth element $$\underline{R}_n = \int \underline{\alpha}^t \underline{\sigma}_n \, dV \qquad (4.1)$$

The nodal pressure force values for the element are calculated by integrating the element stresses for that element, following the procedure as outlined in section 2.10. The lift and drag forces are found by summing the inter-element forces for nodes along the interface boundary. For the simple case of a solid circular cylinder of unit length, the interface forces are transformed to the centre of the cylinder using a transformation matrix $\underline{T}$.

$$\underset{\sim}{R} = \begin{bmatrix} R_x \\ R_y \\ R_\theta \end{bmatrix} = \underset{\sim}{T}\,\underset{\sim}{R}_n \qquad (4.2)$$

$$\text{where } \underset{\sim}{T} = \begin{bmatrix} 1\ 0\ 1\ 0\ 1\ 0\ 1\ 0\ \text{-----} \\ 0\ 1\ 0\ 1\ 0\ 1\ 0\ 1\ \text{-----} \\ y_1\ x_1\ y_2\ x_2\ y_3\ x_3\ y_4\ x_4\ \text{-----} \end{bmatrix} \qquad (4.3)$$

$$\text{and} \quad \underset{\sim}{R}_n = \left\{ R_{x1}\, R_{y1}\, R_{x2} R_{y2} R_{x3} R_{y3} R_{x4} R_{y4} \text{-----} \right\} \qquad (4.4)$$

and x_1 and y_1 are the horizontal and vertical distance of interface node 1 from the centre c as shown in figure 4.2.

Thus

$$R_x = \sum_{i=1}^{ni} R_{xi} \quad , \quad R_y = \sum_{i=1}^{ni} R_{yi} \quad , \quad R_\theta = \sum_{i=1}^{ni} (y_i\, R_{xi} + x_i\, R_{yi}) \qquad (4.5)$$

ni= number of interface nodes

Similarly the structural matrices required to solve the equation of motion for the structure are reduced to a 3X3 form and the simple equation of motion of structure is solved

$$\begin{bmatrix} m & 0 & 0 \\ 0 & m & 0 \\ 0 & 0 & I \end{bmatrix} \begin{bmatrix} \ddot{r}_1 \\ \ddot{r}_2 \\ \ddot{\theta} \end{bmatrix} + \underline{C}_s \begin{bmatrix} \dot{r}_1 \\ \dot{r}_2 \\ \dot{\theta} \end{bmatrix} + \begin{bmatrix} k_x & 0 & 0 \\ 0 & k_y & 0 \\ 0 & 0 & k_\theta \end{bmatrix} \begin{bmatrix} r_1 \\ r_2 \\ \theta \end{bmatrix} = \begin{bmatrix} R_x \\ R_y \\ R_\theta \end{bmatrix} \qquad (4.6)$$

where m is the mass and I is the moment of inertia ($1/2\ md^2$ for a solid cylinder of radius 'd'.). k_x and k_y are the horizontal and vertical stiffness of the cylinder and k_θ is the rotational stiffness.

The simplified equation of motion of the structure under the action of fluid pressure forces is solved using the Newmark method. The solution at time $t+\Delta t$ is based upon using the equilibrium condition at $t+\Delta t$, and is thus an implicit method. The following assumptions are used (47)

$$\underline{\dot{r}}_{t+\Delta t} = \underline{\dot{r}}_t + ((1-\delta)\underline{\ddot{r}}_t + \delta \underline{\ddot{r}}_{t+\Delta t})\,\Delta t \qquad (4.7)$$

$$\underline{r}_{t+\Delta t} = \underline{r}_t + \underline{\dot{r}}_t \Delta t + ((1/2-\eta)\underline{\ddot{r}}_t + \eta \underline{\ddot{r}}_{t+\Delta t})\,\Delta t^2 \qquad (4.8)$$

where η and δ are parameters which govern the accuracy and stability of the solution. Unconditional stability is achieved if $\eta = 0.25$ and $\delta = 0.5$ are selected. This scheme is also known as the constant-average-acceleration method (fig.4.3). To obtain a solution for the displacements, velocities and accelerations at time $t+\Delta t$, the equilibrium equation at time $t+\Delta t$ is also considered along with equations (4.7) and (4.8).

$$\underline{M}_S \ddot{\underline{r}}_{t+\Delta t} + \underline{C}_S \dot{\underline{r}}_{t+\Delta t} + \underline{K}_S \underline{r}_{t+\Delta t} = \underline{R}_{t+\Delta t} \qquad (4.9)$$

Solving from equation (4.8) for $\ddot{\underline{r}}_{t+\Delta t}$ in terms of $\underline{r}_{t+\Delta t}$, and then substituting for $\ddot{\underline{r}}_{t+\Delta t}$ into equation (4.7), we obtain equations for $\ddot{\underline{r}}_{t+\Delta t}$ and $\dot{\underline{r}}_{t+\Delta t}$, each in terms of the unknown displacements $\underline{r}_{t+\Delta t}$ only. These two relations for $\dot{\underline{r}}_{t+\Delta t}$ and $\ddot{\underline{r}}_{t+\Delta t}$ are substituted into equation (4.9) to solve for $\underline{r}_{t+\Delta t}$ so that $\ddot{\underline{r}}_{t+\Delta t}$ and $\dot{\underline{r}}_{t+\Delta t}$ are then calculated using equation (4.7) and (4.8). The complete step by step algorithm is outlined as below

Initial Conditions and Calculations

1. Form the Stokes flow coefficient matrix $\underline{C}$, the mass matrix $\underline{M}$, and the force vector $\underline{F}$, for the fluid domain.

2. Solve the linear Stokes flow equation to obtain the initial value of velocity vector.

$$\underline{C}\underline{u}_o = \underline{F} \tag{4.10}$$

3. Form the structure mass matrix $\underline{M}_s$, the stiffness matrix $\underline{K}_s$, and the damping matrix $\underline{C}_s$.

4. Initialise $\ddot{\underline{r}}$, $\dot{\underline{r}}$ and $\underline{r}$ for the structure. The algorithm is started by selecting $\ddot{\underline{r}} = \dot{\underline{r}} = \underline{r} = 0$.

5. Select the structure timestep size Δt, and the parameter η and δ. In the present work η and δ are selected to obtain unconditional stability, $\eta = 0.25$ and $\delta = 0.5$. The timestep Δt is chosen to be the same as used for the fluid analysis. The reasons for this are discussed later in this section.

Based on the above values the integration constants are calculated

$$\begin{aligned} a_0 &= \frac{1}{(\eta \Delta t^2)} , & a_1 &= \frac{\delta}{(\eta \Delta t)} \\ a_2 &= \frac{1}{(\eta \Delta t)} , & a_3 &= \frac{1}{(2\eta - 1)} \\ a_4 &= \frac{\delta}{\eta} - 1 , & a_5 &= \frac{\Delta t}{2}\left(\frac{\delta}{\eta} - 2\right) \\ a_6 &= \Delta t(1-\delta) , & a_7 &= \delta \Delta t \end{aligned} \tag{4.11}$$

6. Form the effective stiffness matrix

$$\hat{\underline{K}} = \underline{K} + a_0 \underline{M}_s + a_1 \underline{C}_s \qquad (4.12)$$

7. Invert $\hat{\underline{K}}$. The process is simple for the examples considered, $\hat{\underline{K}}$ is diagonal and 3X3. For large and fully populated $\hat{\underline{K}}$ it is required to triangularise $\hat{\underline{K}} = \underline{L}\underline{D}\underline{L}^T$. Standard routines exist inside the finite element package FINEL to triangularise this kind of matrices.

Within each timestep

1. Solve the non-linear fluid equation (2.48), using the velocity vector $\underline{u}_o$ for the first timestep and then subsequently the velocity vector from the previous timestep.

2. Using the velocities found from the solution of equation (2.48), calculate the fluid pressures acting on the structure using equation (4.1), and transform to the required 3X1 form using the transformation matrix $\underline{T}$.

3. Calculate effective loads at time $t+\Delta t$.

$$\hat{\underline{R}}_{t+\Delta t} = \underline{R}_{t+\Delta t} + \underline{M}_s (a_0 \underline{r}_t + a_2 \dot{\underline{r}}_t + a_3 \ddot{\underline{r}}_t) + \underline{C}_s (a_1 \underline{r}_t + a_4 \dot{\underline{r}}_t + a_5 \ddot{\underline{r}}_t) \qquad (4.13)$$

4. Solve for displacements at time $t+\Delta t$.

$$\hat{\underline{K}}\ \underline{r}_{t+\Delta t} = \hat{\underline{R}}_{t+\Delta t} \tag{4.14}$$

5. Calculate accelerations and velocities at time $t+\Delta t$.

$$\ddot{\underline{r}}_{t+\Delta t} = a_0(\underline{r}_{t+\Delta t} - \underline{r}_t) - a_2\dot{\underline{r}}_t - a_3\ddot{\underline{r}}_t \tag{4.15}$$

$$\dot{\underline{r}}_{t+\Delta t} = \dot{\underline{r}}_t + a_6\ddot{\underline{r}}_t + a_7\ddot{\underline{r}}_{t+\Delta t} \tag{4.16}$$

6. The velocities $\dot{\underline{r}}_{t+\Delta t}$ are extrapolated back to the interface nodes using the transformation matrix $\underline{T}$.

$$\dot{\underline{r}}_n = \underline{T}^t\dot{\underline{r}} \tag{4.17}$$

These interface velocities are applied as a new set of boundary conditions for the fluid analysis. The equivalent force vector for the non-fixed freedoms is calculated using these new values of interface velocity boundary conditions and the fluid equation in step 1 is solved again.

The process is repeated until a solution for the desired time duration is obtained.

4.1 Timestep selection for the structural equation of motion

The major contributor to the cost of the fluid-structure interaction analysis is the solution of the fluid equation. The timestep is selected using equation (2.49) and is based upon the accuracy and stability considerations dependant on the fluid equation. In order to obtain a good approximation to the actual dynamic response of the system under consideration, it is required that the equilibrium equations are integrated to high precision. Δt should correspond to the smallest period "T" (Δt would have to be about T/10). In most of the examples studied in the next section, the fluid timestep is small enough to analyse the structural response. However, if the natural frequency of the structure is very high hence a small time period T is required, it is quite possible that $\Delta t_{STRUCTURE}$ (the time period required for structural analysis) to capture the high frequency behaviour is smaller than Δt_{FLUID}. In the present work same value of Δt for structure and fluid analysis is used. If a timestep Δt smaller than Δt_{FLUID} is selected, it would result in additional cost. The frequencies and mode shapes of the finite element mesh are often crude approximations to exact quantities and in many analyses there is little justification to include response predicted in the higher modes. The time integration scheme used for the structure equation is unconditionally stable and hence stable for any value of Δt used. On the other hand, the implicit algorithm used for the fluid equation

is conditionally stable and any increase in Δt would result in divergence. The problem of fluid-structure interaction is solved in chapter 8 using the above timestep selection approach and the dynamic response of the system is found to agree with the available experimental results.

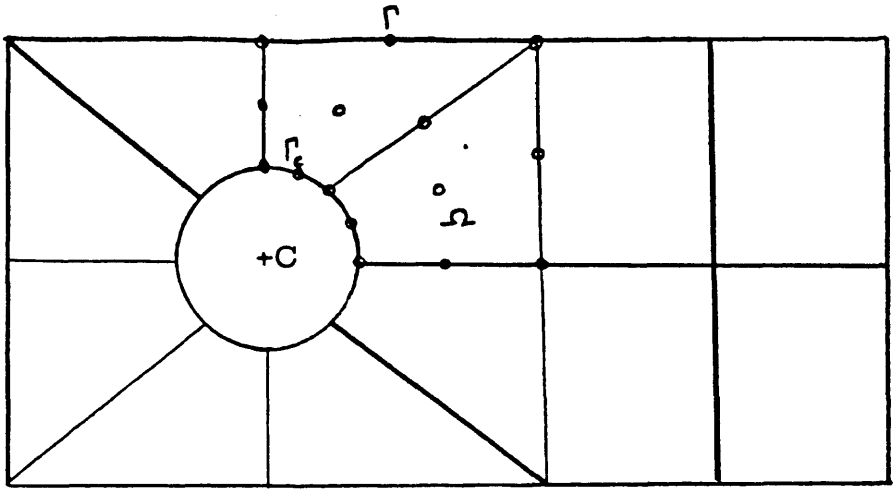

Fig.4.1 Structure and the Surrounding Fluid Domain

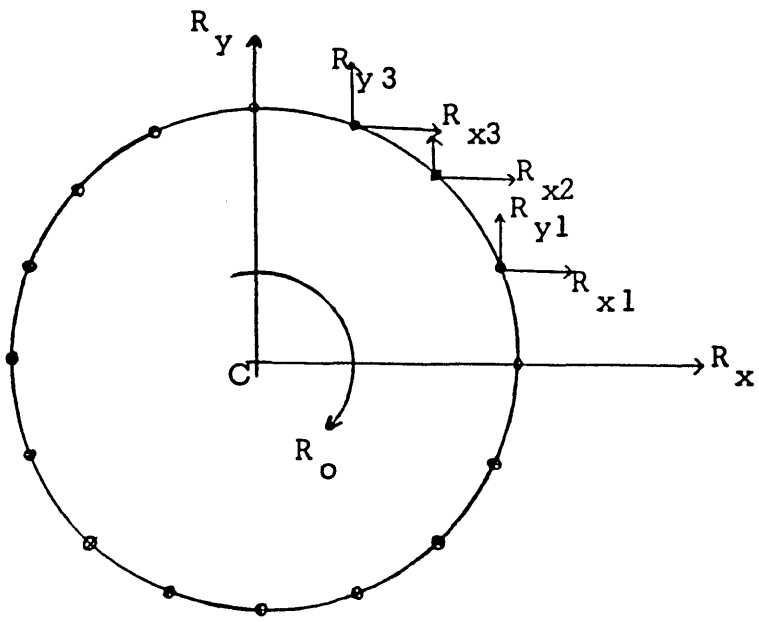

Fig.4.2 Idealisation of Structure and the Fluid-Structure Interface Boundary

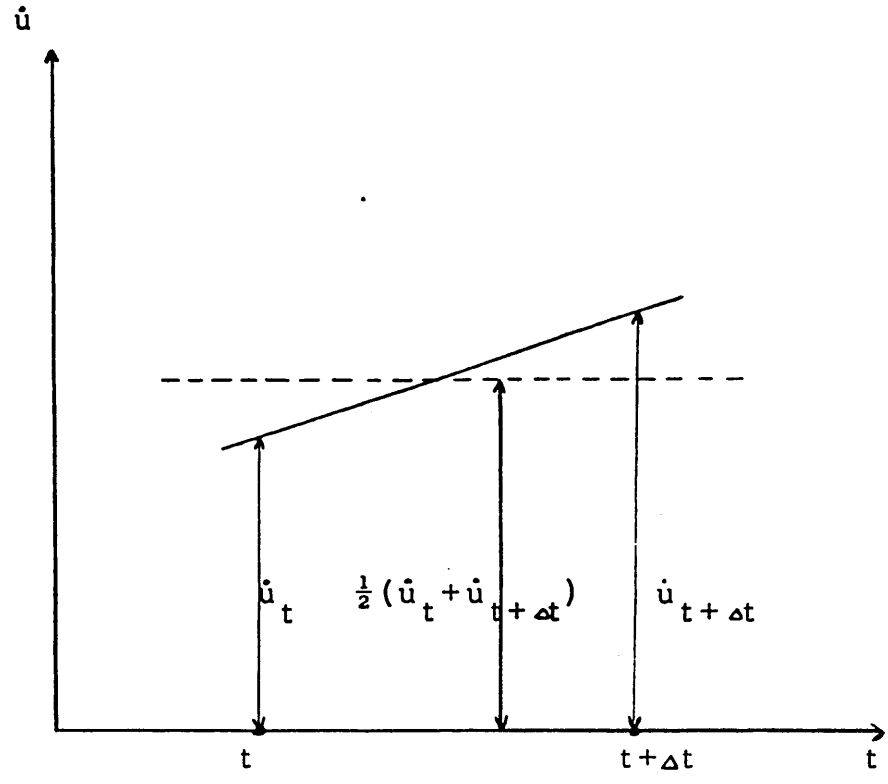

Fig.4.3 Newmark's Constant Average Acceleration Method

5. COMPUTER IMPLEMENTATION

The present development was carried out using the general purpose finite element package FINEL. FINEL is finite element analysis system used as a standard analysis tool, for teaching purposes and also as a research tool (33). The basis of FINEL follows directly the steps involved in the Finite Element Method. The computer implementation of the Finite Element Method is highly successful as it can be broken down into a set of discrete, almost unrelated, steps such as mesh definition, assembly of matrices, solution, stress recovery etc.. This feature is used within FINEL to define a modular structure for the program. The modules inside FINEL are independent and do not communicate directly with each other but indirectly through a common database (fig.5.1). The FINEL database is a random access mass storage file. The database along with the various common areas in the FINEL executive are the only means of inter-communication between the various modules. The executive passes control to any module. The module performs its task and then returns the control to the executive to be passed on to the next module. These modules are associated with a series of FINEL libraries in such a fashion that the programmer can modify or add routines into a library (fig.5.2).

In order to carry out the fluid and the fluid-structure interaction analysis, the modules were arranged in the following manner.

GRID

ASMB

OWN1

BNCN

CHOL

LOAD

OWN2

STRS

PLOT

GRID Sets up the finite element mesh for the fluid domain. The finite element mesh for the structure present inside the fluid domain can also be set up, if required for the fluid-structure interaction analysis. The nine-noded planar or axisymmetric fluid element is used to represent the fluid and a structure element to represent the structure (a choice of structure elements is available inside FINEL (33)). This is a standard FINEL module.

ASMB Standard matrix assembly module. The mass matrix and the Stokes flow matrix are assembled in this module.

Both of these matrices are symmetric matrices and possess a band-profile structure. The fluid element is used to form the relevant matrices using the selective reduced integration (section 2.5). This module will also set-up the structural matrices if a complicated structure is to be analysed for the fluid-structure interaction problem. This is a standard FINEL module but uses the special fluid element which is temporarily added to the FINEL Element Library for each run.

OWN1 Performs the summation ($\underline{M}+\gamma\Delta t\underline{C}$) (equation 2.44), and overwrites the original $\underline{C}$ matrix. This module was specially written for the fluid flow analysis.

BNCN This is the standard FINEL boundary condition module.

CHOL Standard FINEL Cholesky factorisation module. The matrix ($\underline{M}+\gamma\Delta t\underline{C}$) is factorised. CHOL is a standard FINEL module.

LOAD This is the standard FINEL load module.

OWN2 Solution Module. This is the module where the solution for the non-linear fluid equation (eq.2.44) is performed, based on the algorithm as detailed in section 2.6. If the fluid-strucure interaction analysis is to be

carried out then the relevant routines are called from the library to solve the equation of motion of the structure under the action of fluid forces (chapter 4). The module was specially written for the flow and fluid-structure interaction analysis.

STRS Modified FINEL stress recovery module to calculate pressure and shear stress if required. The module is almost identical to the standard FINEL stress module but the summation of the direct stresses has been included to calculate the fluid pressure.

PLOT Post-processing of results in the form of velocity vector plots and various other graphs takes place in this module. The data is read form the FINEL database where it was originally written in the OWN2 module and the STRS module.

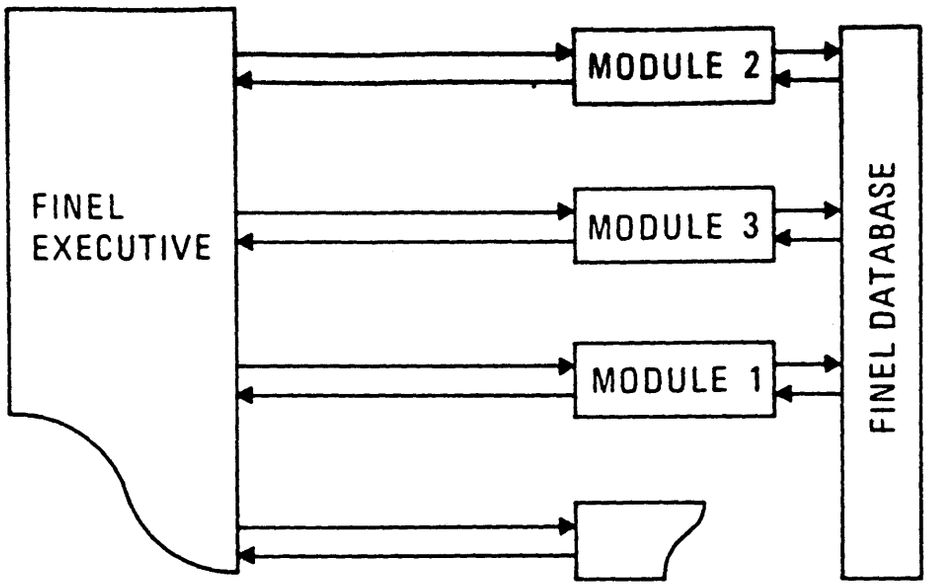

Figure 5.1 FINEL STRUCTURE

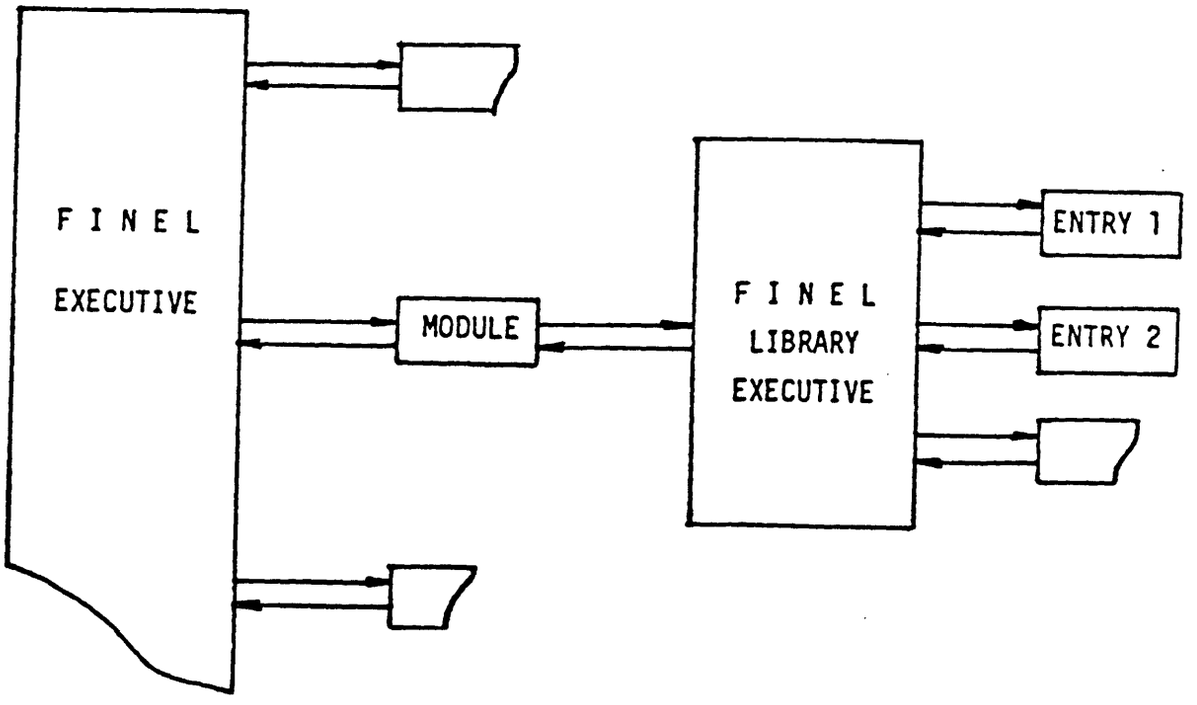

Figure 5.2 FINEL LIBRARIES CONCEPT

6. STOKES FLOW

The solution to the Stokes flow problem both in two dimension and axisymmetric cases is obtained by solving the linear Stokes flow equation (eq.2.47). The solution gives a good representation of low Reynolds number or creeping flow problems. Examples of two-dimensional entry flow in a duct and axisymmetric flow in a pipe are considered. The example of axisymmetric flow between two parallel plates is used to illustrate the use of incompressibility constraint and the importance of selecting the correct value of penalty parameter λ, as related to problems where compressibility effects are important.

The entrance region for laminar flow has received considerable attention in recent years. Not only is such a study of importance to industrial and viscometric applications, but also as a simple developing flow it provides a suitable example for evolution and evaluation of numerical solution procedures for linear and non-linear partial differential equations, for example, the Navier-Stokes equations. One of the first finite element solutions to such problems was achieved by Atkinson and co-workers (54,55) with a stream-function vorticity approach. Zienkiewicz and Godbole (56) have presented some finite element results for entry flow problems in two and three dimensions using parabolic elements and the penalty function approach. These results are compared with the results of Lew and Fung (57) using stream-function

approximation and a rectangular element. The associated experimental investigations done by many authors are discussed by Atkinson and co-workers (54). It has been suggested previously (56) that the only realistic experimental initial condition at low Reynolds numbers is the generation of a flat velocity profile at a known position within the conduit. Numerical examples covered in the literature also use a similar inlet boundary condition.

6.1 Two Dimensional flow

Two-dimensional flow in a duct is considered. Details of the numerical example are as shown in fig. 6.1.1. The top and bottom walls of the duct are no-slip walls. Because of the symmetric nature of the problem, only one half of the flow above the centre-line is analysed. A flat inlet flow profile is used with u=1.0. A range of uniform and non-uniform meshes are tried to solve the Stokes flow problem. The flow solution in the form of velocity vector plots is shown in fig. 6.1.2 for a 7X3 uniform mesh (fig.6.1.2a), 7X3 non-uniform mesh with a finer mesh in the corner near the entrance and the fixed wall (fig.6.1.2b), 7X5 uniform mesh (fig.6.1.2c) and a 7X5 non-uniform mesh (fig.6.1.2d and fig.6.1.2e). The solution is fairly smooth with the uniform meshes, however, some

flow is moving away from the fixed wall and towards the centreline when a finer mesh closer to the fixed wall is used (fig.6.1.2b and fig.6.1.2d). This is as a result of the flat inlet boundary condition. The element containing the wall boundary has u=0 at the wall and u=1.0 at all other nodes. The boundary condition is not smooth and this is made worse when a smaller element is taken near the fixed boundary. The distance between two adjacent nodes at the inlet and near the fixed boundary with u=0, is decreased, hence a large variation in velocity over a relatively short distance.

Effects of mesh sub-division on axial velocity development on the plane entry flow can be seen from the plot of centre-line velocity along the length of the duct (fig.6.1.3). The axial velocity increases sharply over the first half of the duct. Results are improved considerably when a finer mesh in this region is used. There is little difference between the results obtained using 7X3 non-uniform and 7X5 non-uniform meshes. The number of nodes in the horizontal direction (flow direction) is the same for the two meshes. The results are in good agreement with theory and also with the results of Atkinson et al (54) obtained using a stream-function vorticity approach. From the obtained results it shows that mesh refinement in the axial direction is sufficient to obtain a good solution to the flow problem. Fig.6.1.2e having mesh

refinement in the axial direction only gives a smooth as well as accurate solution.

6.2 Axisymmetric flow

Bodies of revolution under axisymmetric loads are two dimensional in so far as analysis for stresses and deformation is concerned. For the case of fluids, the velocities are confined to the radial (r) and axial (z) directions. Accordingly, little change is needed to adopt the two-dimensional elements of the previous section to the axisymmetric elements.

Developing flow in a pipe is considered. Details of mesh and boundary conditions are as shown in fig.6.2.1. The initial condition is a flat velocity profile. In fig.6.2.2 a simple solution of an axisymmetric entry flow region is shown for two different meshes. The flow behaves very much like the two-dimensional flow and moves towards the centreline when a finer mesh in the radial direction and near to the fixed wall is used. Axial velocity is plotted along the centreline of the pipe in fig.6.2.3 for the 7X5 uniform and 7X5 non-uniform mesh. There is an improvement in the results when a finer mesh is used near to the inlet and in the axial direction.

The velocity field obtained from the Navier-Stokes equation applied to the pipe entry flow problem may be expressed as (54)

$$u = f (r,z,Re) \qquad (6.2.1)$$

where r is the distance in the radial direction

z is the distance in the axial direction

(fig.6.2.1)

and Re is the flow Reynolds number

For the centre-line velocity

$$u_{CL} = f (z,Re) \qquad (6.2.2)$$

From theoretical results, the final dimensionless centreline velocity is 2. From the results in fig.6.2.3, this velocity is attained at z/r = 1.5 and for z/r $>$ 1.5, the flow remains fully developed with dimensionless u = 2.0. These results are in good agreement with the results obtained by Atkinson et al (54).

Axisymmetric flow between two parallel plates is considered to illustrate the importance of the value of penalty parameter λ. Fig.6.2.4 shows the mass flow rate between the inlet and outlet of two parallel plates for various values of Poissons ratio. A fully developed flow with a maximum velocity of 1m/sec is applied on the inner radius. The gap between the two plates is taken as 0.1. We see that there is a considerable loss in mass flow rate between the two stations for small values of penalty parameter λ i.e. values of Poissons ratio not very close to 0.5. However as ν approaches 0.5 the value of penalty

parameter increases and the mass flow rate improves at the outlet. When a value of ν=.49999995 is used the mass flow rate at the inlet and outlet is exactly the same. The incompressibility constraint is fully satisfied and there is no loss in the mass flow rate. The compressibility effects get more important as the gap between the two plates is further decreased. With a narrower gap a higher value of λ was required in order to satisfy continuity in mass flow rate. Hence the constraint of incompressibility is very much dependant upon the value of penalty parameter λ, specially in the regions where compressibility effects are important, as is indicated by the problem of flow between two parallel plates with a narrow gap.

6.3 Aspect ratio

The example of fig.6.2.4 was used to investigate the maximum possible value of aspect ratio to which the fluid finite elements could be stretched. A uniform mesh of 40 elements is used and the radial dimension is increased or decreased to attain the desired aspect ratio. For this particular example of fully developed flow we stretched the elements to an aspect ratio of 2000 in the regions of fully developed flow with little changes in flow characteristics. For such high values of aspect ratio it is very important to use ν as near as possible to 0.5, in order to satisy continuity. A value of ν=.4999999995 was

sufficient to give results for aspect ratios of up to 800. Using the same value of ν but aspect ratio increased to 1200, resulted in some loss in mass flow which was recovered by using ν=.499999999995. The above mentioned values of aspect ratio apply to the regions where changes in flow velocities and/or geometry are negligible. Much smaller values of aspect ratio are required in the regions where flow is undergoing rapid changes, in order to capture all details of the steep velocity gradients.

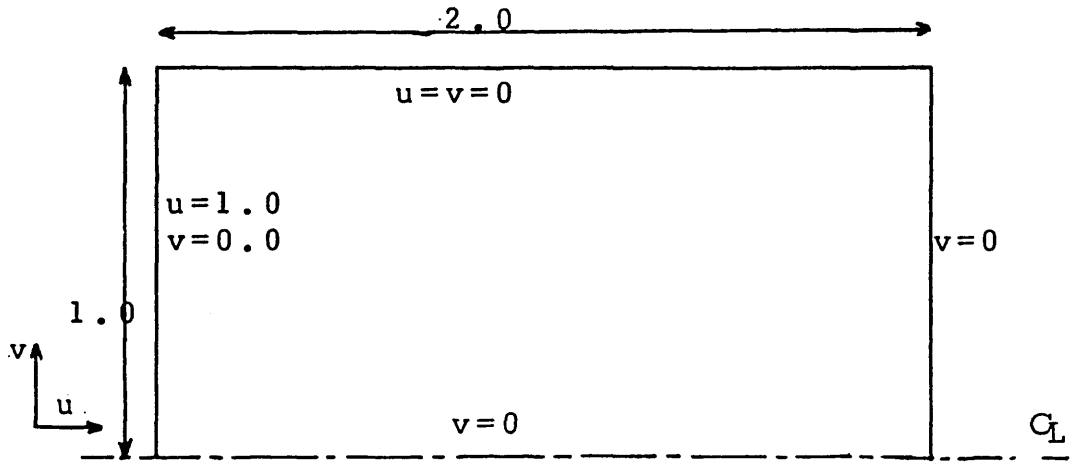

Fig.6.1.1 Two-Dimensional Flow
Problem Description and Boundary Conditions

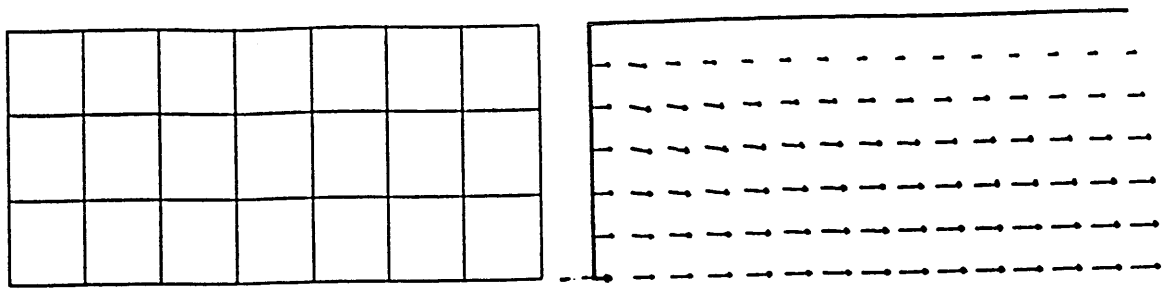

(a) 3X7 uniform mesh

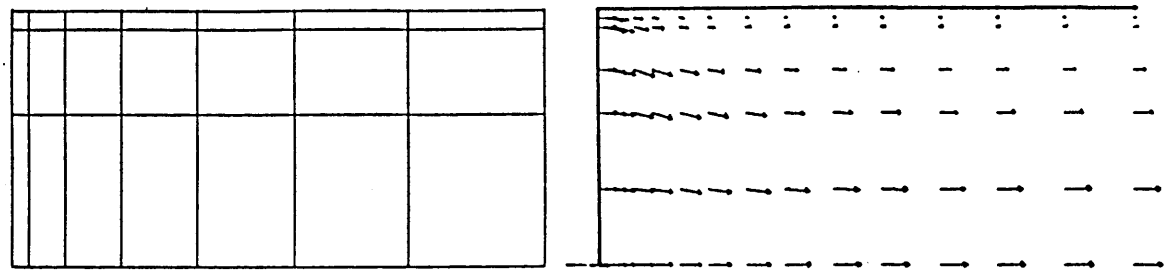

(b) 3X7 non-uniform mesh

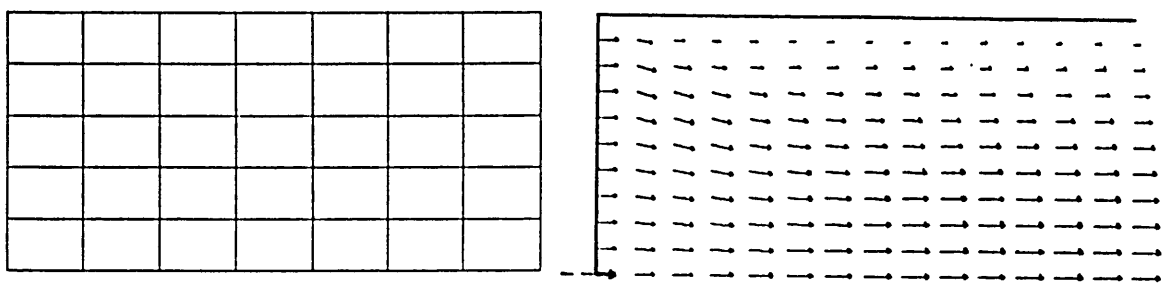

(c) 5X7 uniform mesh

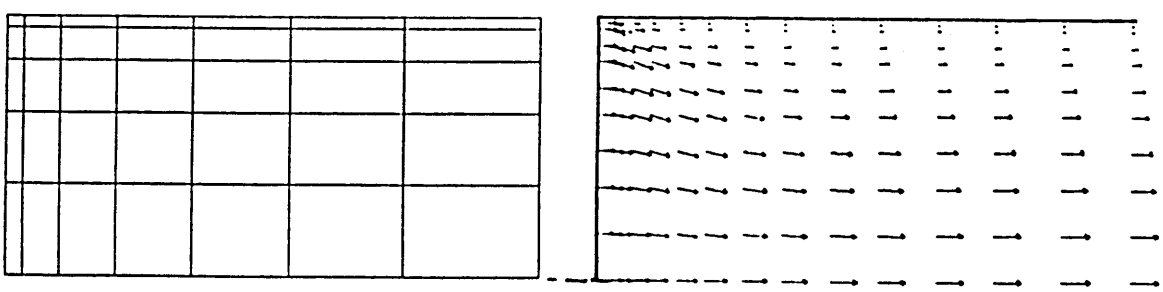

(d) 5X7 non-uniform mesh

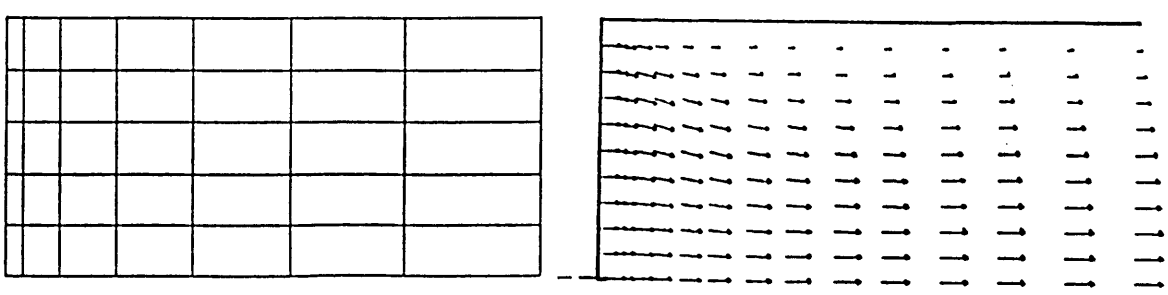

(e) 5X7 non-uniform mesh

Fig.6.1.2 Two-Dimensional flow
Finite Element Mesh and Velocity Vector Plots

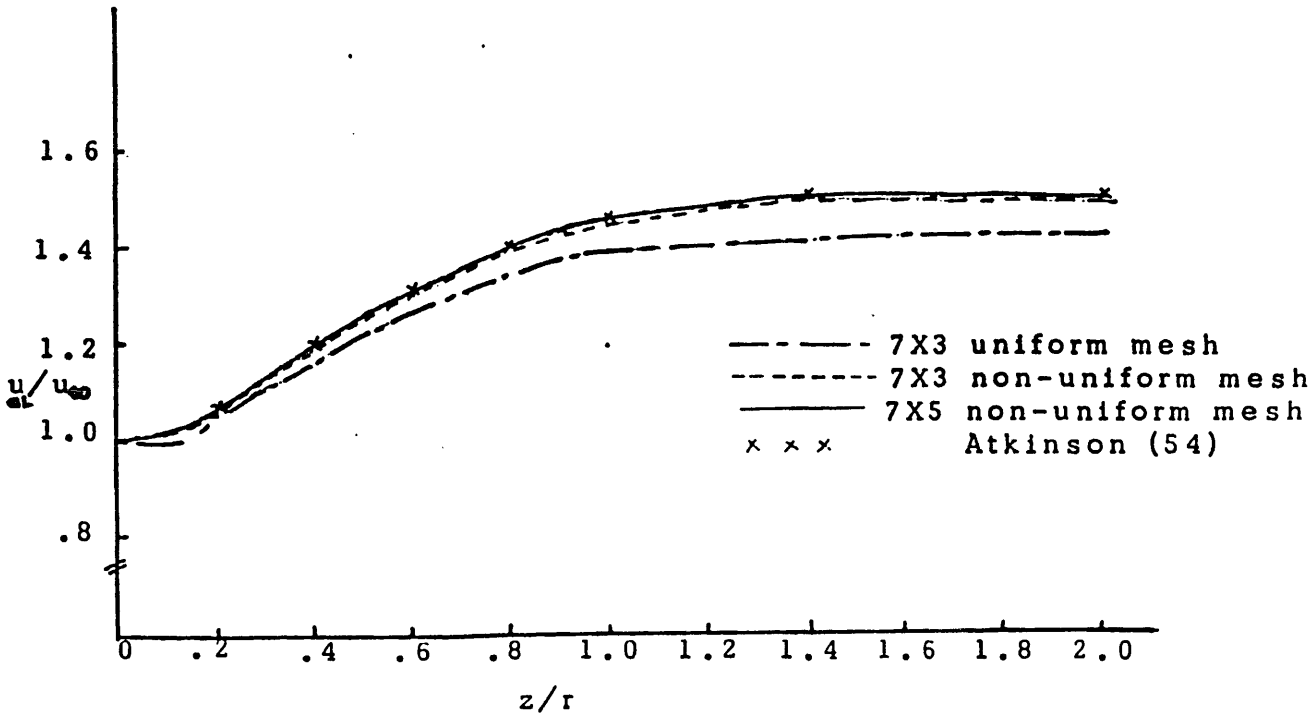

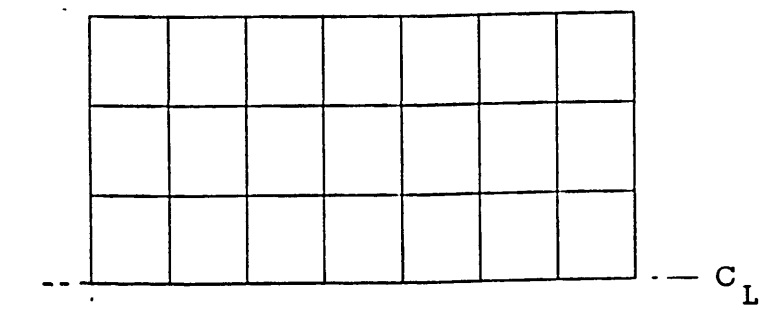

3X7 uniform mesh

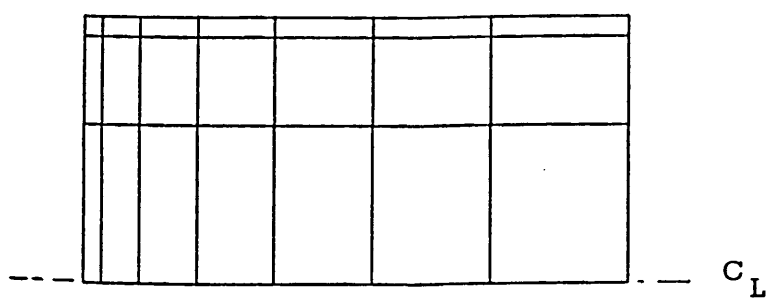

3X7 non-uniform mesh

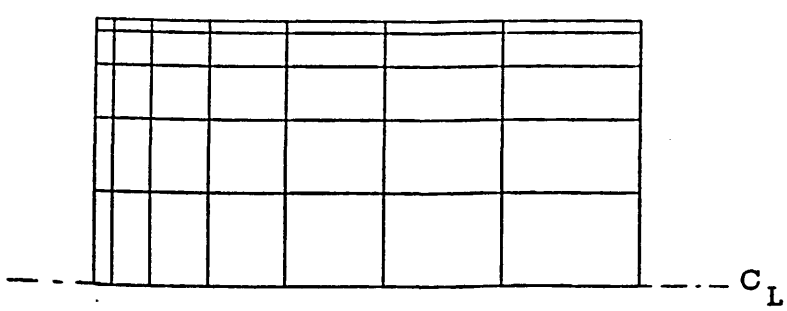

5X7 non-uniform mesh

Fig.6.1.3 Effects of Mesh Subdivision on the Axial Flow Development - Two-Dimensional Flow

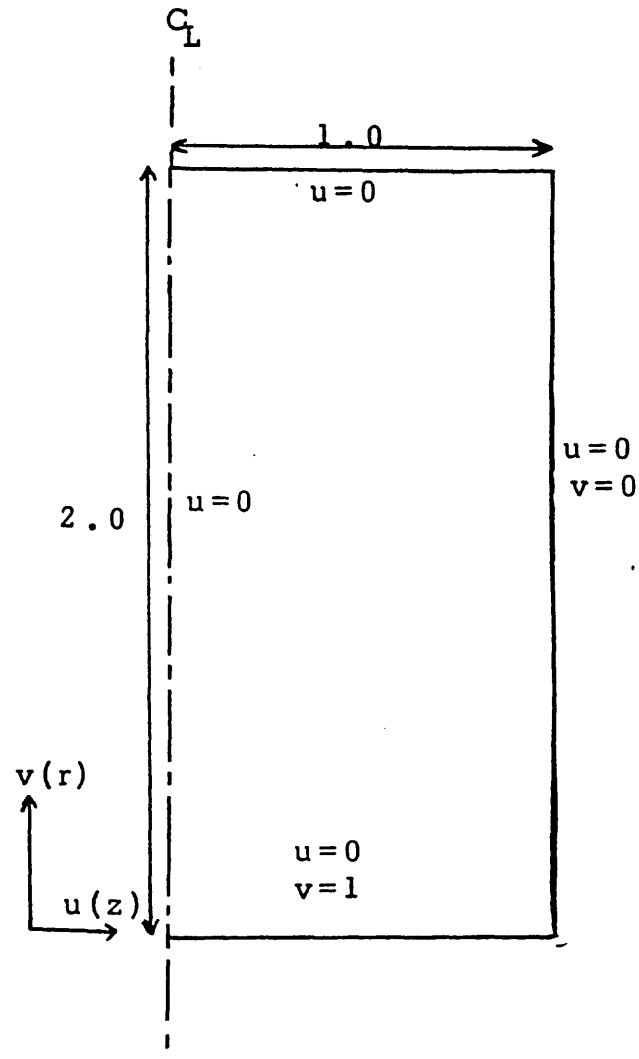

Fig.6.2.1 Axisymmetric Flow
Problem Description and Boundary Conditions

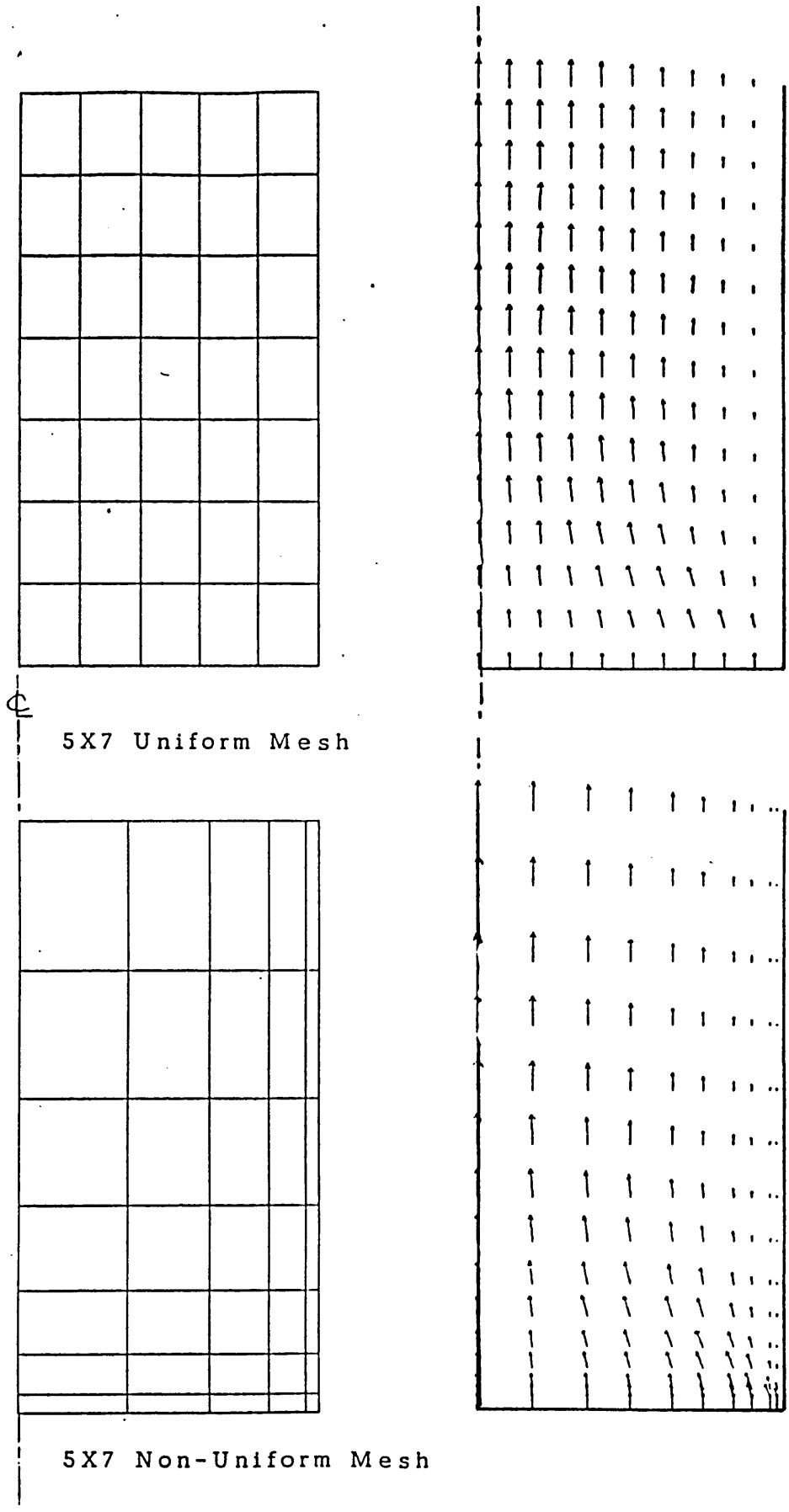

Fig.6.2.2 Axisymmetric Flow - Finite Element Mesh and Velocity Vector Plots

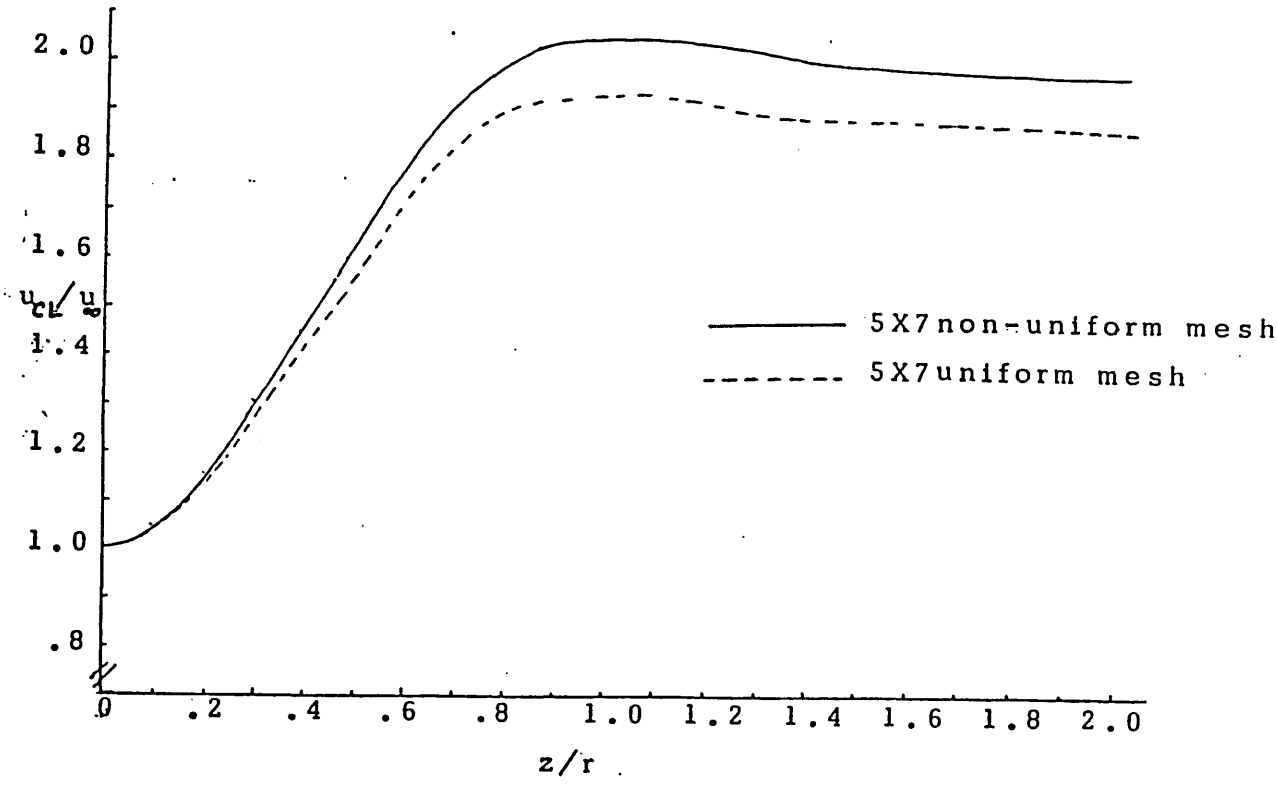

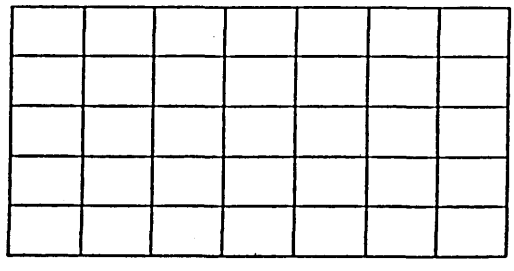

5X7 uniform mesh

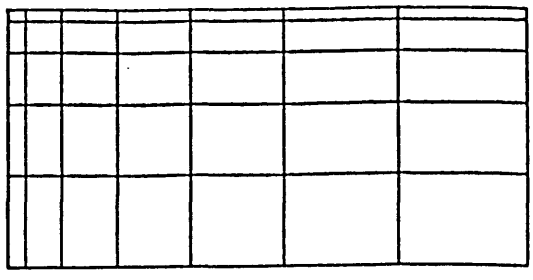

5X7 non-uniform mesh

Fig.6.2.3 Effects of Mesh Subdivision on the Axial Flow Development - Axisymmetric Flow

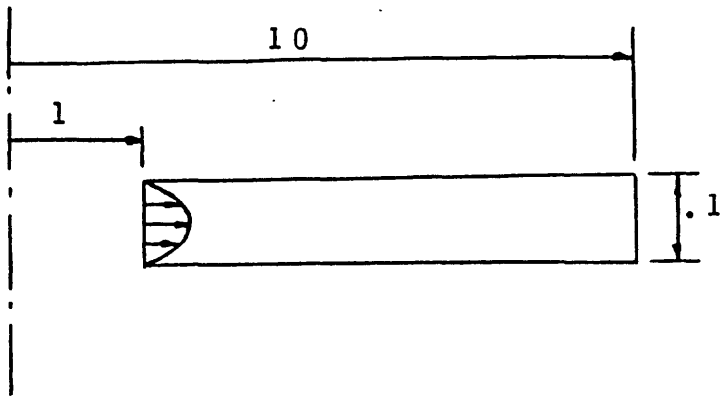

Poissons Ratio	Inlet/Outlet Mass Flow Ratio
.49995	.155
.499995	.7675
.4999995	.9723
.49999995	.9972
.499999995	1.0

Fig.6.2.4 Incompressibility Test

7. UNSTEADY INCOMPRESSIBLE VISCOUS FLOW

The solution for unsteady incompressible viscous flow is obtained by solving the complete set of non-linear equations (eq. 2.47 and 2.48). The initial solution is obtained by solving the linear Stokes flow equation (eq.2.47). The timestep is selected using equation 2.49. Examples of flow over a step, flow over a backward facing step, flow in a cavity and vortex shedding behind a circular cylinder at low and moderate Reynolds number are considered. The results are compared with the available numerical and experimental results.

7.1 Flow over a Step

The problem is that of laminar flow in a channel over a square step. The square step forms a portion of the lower boundary domain. The top boundary is located near the top of the step and is a no-slip wall. In order to compare our results and make the problem identical to those of ref. 40,59 , the step is located fairly close to the inlet region.

There are relatively few studies of flow over a step. Two related situations have been studied in more detail. These are of flow through a pipe orifice and flow through a channel with sudden expansion (the backward facing step). Earlier work on flow over a step employing FDM and using the stream-function/vorticity approach with upwind

treatment of advection for Reynolds number up to 1000, has been reported by Greenspan (60) and Freeman (61). Hughes et al (40) presented some results using the finite element method on a very coarse uniform mesh. For Re=200 the conventional Galerkin method produced spurious wiggles in the velocity vectors upstream of the step. A reasonable recirculation eddy downstream of the step was obtained. Upwind methods were used to eliminate these wiggles and obtain a smooth solution. A solution for $Re=10^7$ was also presented using the same coarse mesh and upwinding. Leone and Gresho (59) and Gresho and Lee (62) present some more results using finite element method and no upwinding, for flow over a step for Re=200 for a range of non-uniform meshes. It is shown that smooth solutions can be obtained without using upwinding. Bercovier and Engelman (63) present some results for time-dependant flow past a square step without any comment or detailed explanation. The example of flow over a step characterises flow over sharp corners. Problems involving sharp corners are also encountered in the analysis of clusters of fast reactor fuel subassemblies. Fluid-structure interaction problems involving sharp corners are discussed by Donea and Giuliani (28).

In this section, results are presented for flow over a square step for a range of Reynolds numbers and using uniform and non-uniform meshes. The nine-noded fluid

element using the conventional Galerkin method is used throughout. The problem definition is depicted in figure 7.1.1. A coarse uniform mesh of 48 elements (fig.7.1.2) similiar to the one used by Hughes et al (40) is used. The inlet boundary condition is a flat velocity profile, u=1. Thus the problem is more of a developing flow over a step in a channel. No-slip boundary conditions are used on the top and bottom wall. The density ρ is incremented in order to obtain the desired Reynolds number, other parameters in the Reynolds number equation ($Re = \rho u l/\mu$) are taken as unity. The channel height is taken as 1 and the length of the channel is 4. The Reynolds number is based on the channel height and not on the step height. These parameters are chosen to make the example identical to those of other authors. The timestep, $\Delta t = .04$ is chosen using equation (2.49). The flow Reynolds number is taken as 200. The initial flow solution is obtained from the solution of the Stokes flow equation. Velocity vector plots at 20 timestep intervals are presented in figure 7.1.3.

As is clearly visible from the velocity vector plots (fig.7.1.3) instabilities in the form of "ripples" appear upstream of the step. These ripples are virtually absent from the initial solution to the Stokes flow problem (fig.7.1.3a), but as the non-linear convective terms are introduced, the ripples appear upstream of the step and

these are present throughout the solution. They occur in the region between the inlet and the front face of the step and do not appear anywhere else in the flow, even after many timesteps. A recirculation eddy appears downstream of the step which elongates with time. In addition to the dowstream eddy there is another recirculation region at the top of the channel near the outlet where the flow is trying to re-enter the channel. This small region gets pushed outside the channel after about 80 timesteps. The main eddy downstream of the step continues to grow with time (fig.7.1.3e), which indicates that the flow has not quite reached a steady-state as yet.

Investigation into the cause of ripples

An attempt is made to find the cause and cure of these ripples, before going any further. Hughes et al (40) believe that the presence of ripples demonstrates the inappropriateness of the Gauss-Legendre integration of the convection term and suggests the use of optimal upwinding to eliminate these ripples. Solutions for flow over a square step are presented in reference 40, using a coarse uniform mesh of 48 nine-noded elements similar to the one in figure 7.1.2. Results are presented for flow at Re=200 and $Re=10^7$ in the form of velocity vector plots. These solutions free from any upstream ripples are very

identical to each other, which indicates that upwind schemes are insensitive to the input value of Reynolds number. Also at large Reynolds number, most of the viscosity is artificial (i.e. numerical) and the resulting effective Reynolds number can be many orders of magnitude less than the input value. At high Reynolds number the flow becomes more complex and a coarse mesh simulation will often not recognise these complexities. Results obtained by the use of upwind methods are often independent of the flow Reynolds number.

From observation, the possible cause of ripples could be a combination of the following factors

(i) The rapid change in flow velocity between inlet and the step as a result of fixed boundary condition at the step.

(ii) The sharp edge singularity at the leading corner of the step.

(iii) The inlet boundary condition is not smooth.

(iv) The mesh too coarse to resolve the steep gradients upstream of the step and in the direction of the flow.

Investigation into the cause of ripples has been carried out by Gresho et al (59). It was found that if a parabolic inlet flow profile is used, the ripples are reduced by about 10%. Smoothing the inlet boundary condition by using $u=0.75$ at the midside nodes of the corner elements reduces the ripples by a small amount only. Moving the step further downstream in the channel does not make much difference to the ripples.

To shed further light on this, the problem was reanalysed but rounding off the front edge of the step (fig.7.1.4). The number of elements and nodes was exactly the same as used in the previous example as was the flat velocity profile at the inlet. The velocity vector plots of fig.7.1.5 show that the ripples upstream of the step have disappeared. The eddy downstream is correctly modelled and is identical to that of the previous test with the square step. Overlaying the vector plots of the two geometries at the same time show that the only difference is upstream. This proves that a cause of the upstream ripples is the sharp corner on the front face of the step and the mesh immediate to the front corner of the step. This indicates that a slight rounding of the geometry can lead to a significant improvement in the numerical stability of the results. Further work is required to investigate the sensitivity of the results to the radius of the corner.

Using a uniform mesh of 128 elements does not eliminate ripples to any extent and the results are not reported here. However using a non-uniform mesh of 128 elements with finer mesh upstream of and around the step and (fig.7.1.6) eliminates these ripples and the solution obtained is smooth. The solution in the form of velocity vector plots is presented in figure 7.1.7. The timestep was recalculated for this fine mesh and was found to be 0.015 for stability and convergence. This is about three times smaller than the previous timestep used with the uniform coarse mesh. The cost of analysis increases as a result of the smaller timestep and the increased number of equations that have to be solved at each timestep. The non-uniform mesh of 128 elements was found to be suitable to solve for flow at Re=200. Using the same mesh of fig.7.1.6 but incrementing the flow Reynolds number to 500, the flow solution in the form of velocity vector plots is presented in figure 7.1.8. For this run the inlet flow was modified by using u=0.75 at the midside nodes of the top and bottom element adjacent to the walls (59). Velocity vector plots are presented at 30 timestep intervals upto T=1.35 and then at T=3.6,4.05 and 4.50. The initial solution at T=0 is free from any ripples, but at T=0.45 ripples appear upstream of the step and also near the top and bottom wall close to the inlet. The ripples closer to the wall could be as a result of the slightly

modified inlet boundary condition with u=0.75 near the walls. This is to make the inlet condition smoother and is known to reduce the ripples (56). The ripples upstream of the step are similar to those obtained with the coarse uniform mesh and Re=200. This indicates that the mesh used, although fine enough to deliver a solution free from any ripples for Re=200, is not sufficiently fine for Re=500. In order to obtain a smooth solution at higher Reynolds number further refinement closer and upstream of the front edge of the step is required. The increased mesh density and the consequential need for a shorter timestep makes the solution at higher Reynolds numbers progressively more expensive.

The flow solution at Re=500, however, presents some interesting features. A small recirculation bubble has appeared at the top of the step, which is small to start with but elongates and moves further downstream into the flow. At T=3.6, while the main eddy is growing larger and moving downstream into the flow, another eddy is appearing near the bottom of the step and growing in size. At T=4.05 and T=4.5 the small eddy present above the step has moved downstream of the step and is located near the top downstream corner. A small recirculation region is also present upstream of the step near the bottom wall. At the top wall near the outlet some flow is recirculating back in the channel and this region gets pushed out of the

channel with time. In the above example at Re=500 steady state flow was not reached at 300 timesteps. Numerical results of flow over a step at high Reynolds number are difficult to find. The flow behaviour also depends on the outlet boundary condition. If the outlet is left open (fig.7.1.4 and 7.1.8), some of the flow recirculates back in the channel and most of the flow is heading downwards. Using v=0 at the outlet leads to a very much compressed downstream eddy and forces the flow to come out as fully developed. Furthermore, a region of instabilities appears upstream of the step and near the bottom wall. Details of out flow boundary condition are discussed in ref.59.

The ripples in the flow arising from the numerical solution are also present in the analysis of Stokes flow, particularly when there are sharp changes in geometry and/or if a coarse mesh is used in the regions of rapidly changing flows. Axisymmetric flow between two parallel plates is examined, with flow coming from end A and B, and exhausting from C (fig.7.1.9). As the gap between the two plates (h) was decreased, ripples appeared in the regions indicated by dotted lines in fig.7.1.10. These disappeared to a large extent after the corners were rounded off.

From the numerical test cases carried out so far, it can be seen clearly that any instabilities present in the flow solution appear as ripples in the velocity vector plots. These are a strong and useful signal that some important portion of the solution is being inadequately modelled. These also indicate the region of the flow where the solution is particularly defficient. An approximate solution can be obtained to the flow problem in hand, using a coarse mesh and with instabilities present in the solution, but if an accurate solution is to be obtained, these must be eliminated from the important regions of the flow. Refining the mesh by using more elements in these regions, eliminates these ripples and a smooth and accurate solution can be obtained. This, however, results in more nodes and a smaller timestep for stability and convergence of the solution. The cost of solution thus increases. Slight changes in geometry i.e. rounding off the front sharp corner of the step also eliminates ripples and delivers a smooth solution even on a coarse mesh. Slight changes in geometry,(provided that these do not alter the original problem definition), are thus a cheaper option. How to obtain a ripple free solution, depends very much upon the type of problem and on the accuracy of solution required. If the ripples are present in the regions of lesser importance, or if these are small throughout the entire grid and the numerical solution

looks physically reasonable, then the solution of the original equation is probably adequately approximated everywhere. It is however clear that these ripples are caused by the poor resolution of a rapidly changing flow field.

Upwind methods for such problems are dangerous and often lead to false sense of security as any coarse mesh can be used for any Reynolds number. Upwind methods are less accurate methods compared to the conventional Galerkin methods and should only be employed on meshes with more nodes. The flow invariably becomes more complex and difficult at higher Reynolds numbers, yet coarse meshes are used with upwind methods to obtain solutions which are stable but do not represent the true solution for that Reynolds number. In fact, upwinding introduces artificial viscosity and so the numerical Reynolds number can be much lower than the one that is actually required.

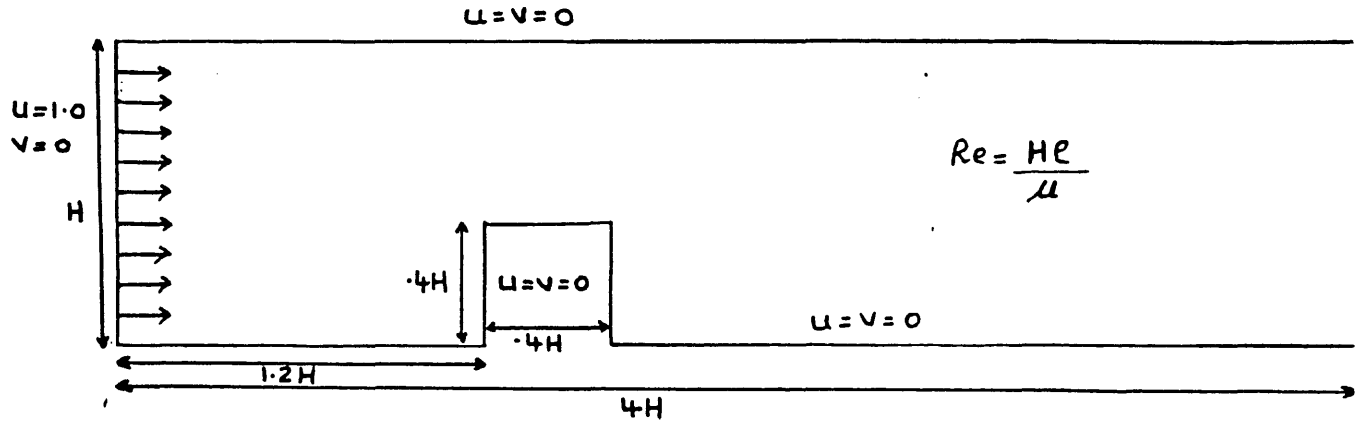

Fig.7.1.1 Flow over a Step - Problem Definition and Boundary Conditions

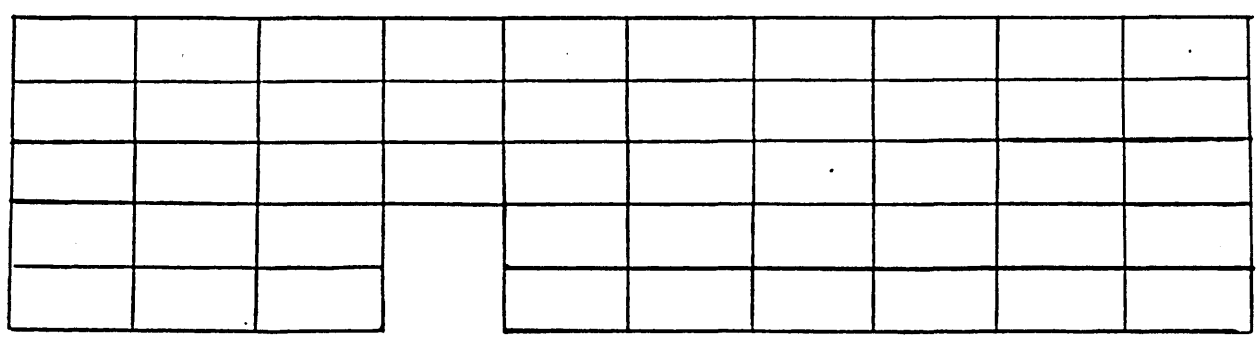

Fig.7.1.2 Uniform Finite Element Mesh of 48 Elements

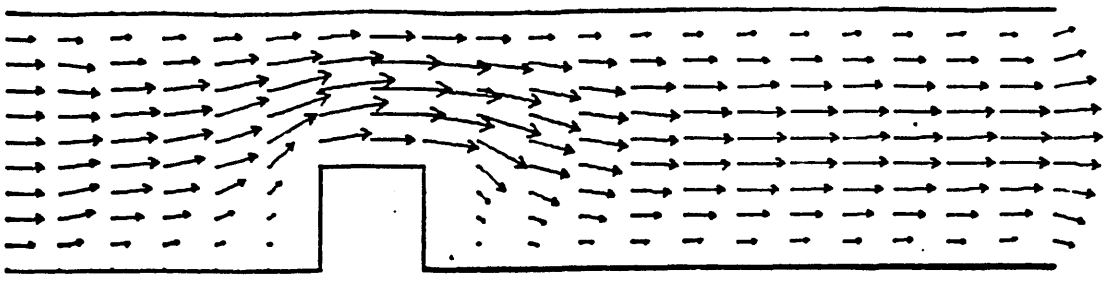

(a) n=0, Time=0.0 Initial Flow Solution

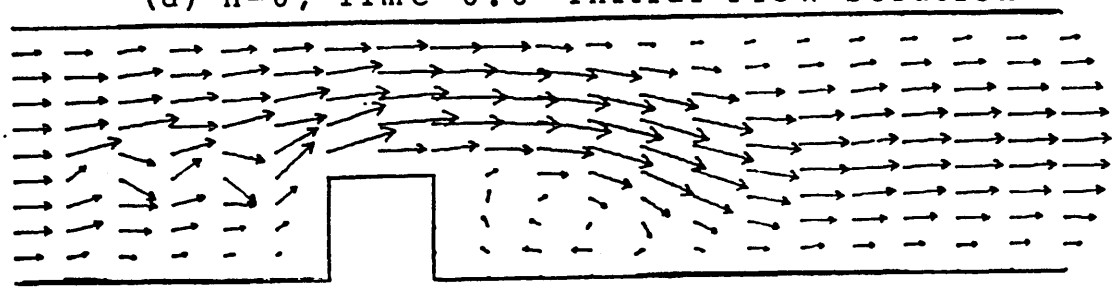

(b) n=20, Time=0.8

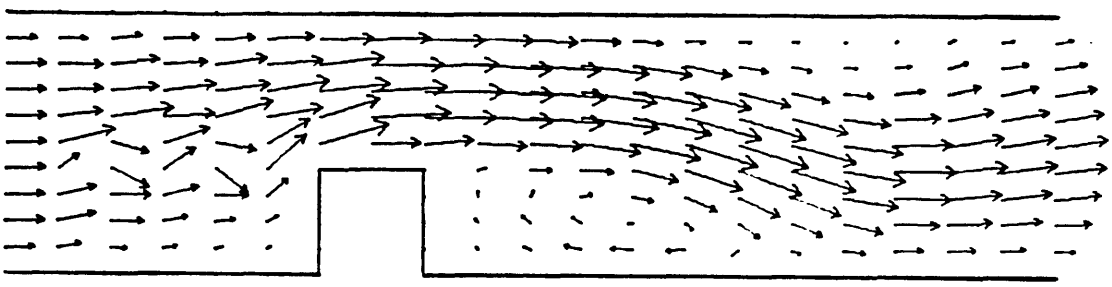

(c) n=40, Time=1.6

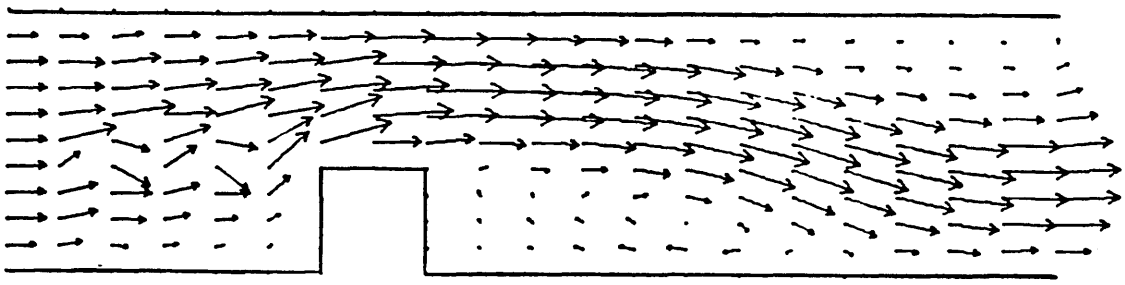

(d) n=60, Time=2.4

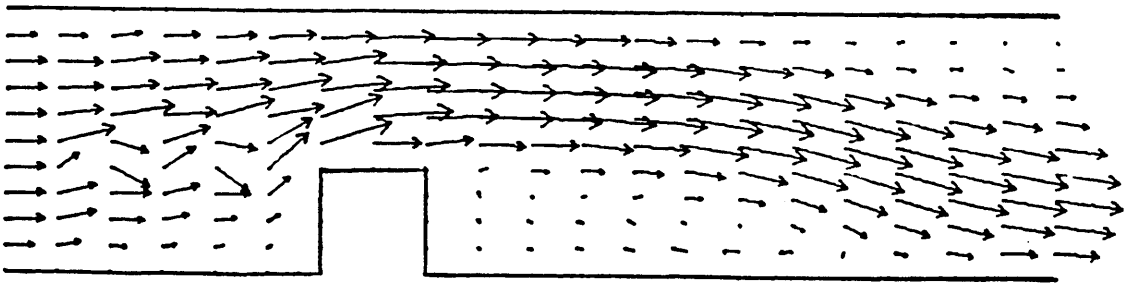

(e) n=80, Time=3.2

Fig.7.1.3 Velocity Vector Plots, Flow over a Step
Uniform mesh of 48 Elements Re=200

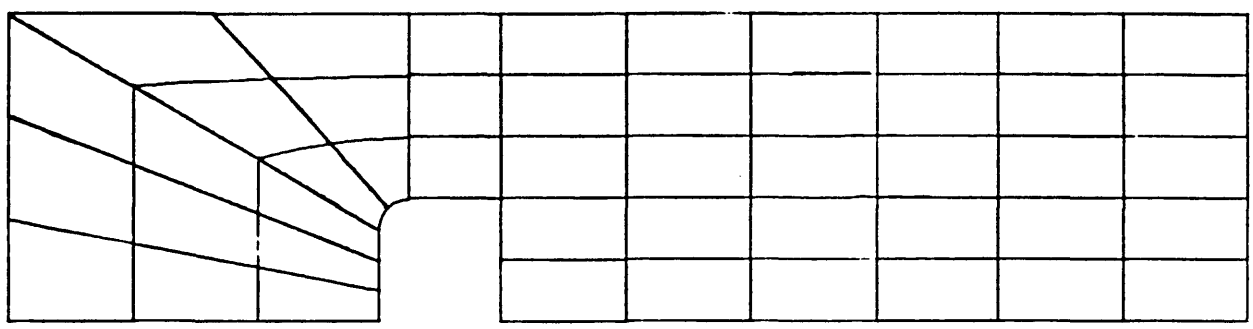

Fig.7.1.4 Step with Rounded Front Edge - Finite Element Mesh of 48 Elements

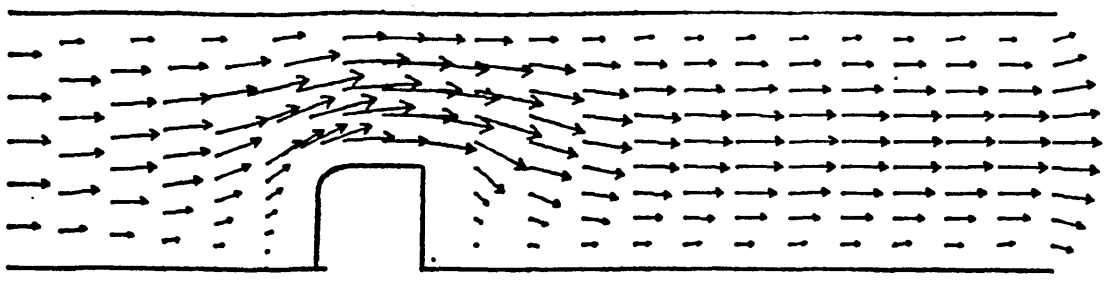

(a) n=0, Time=0.0 Initial Flow Solution

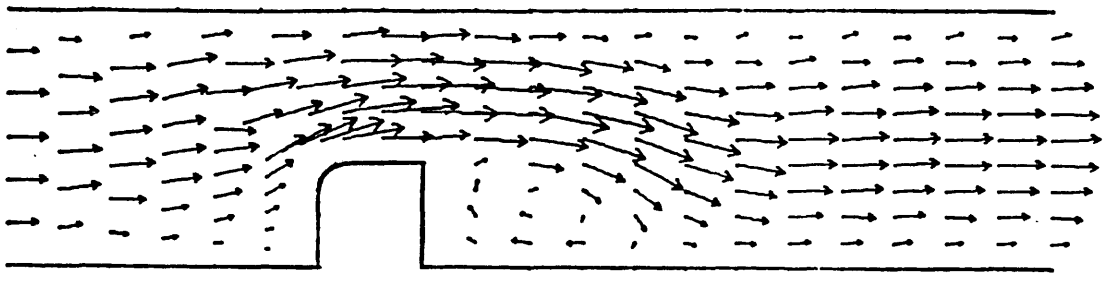

(b) n=20, Time=0.8

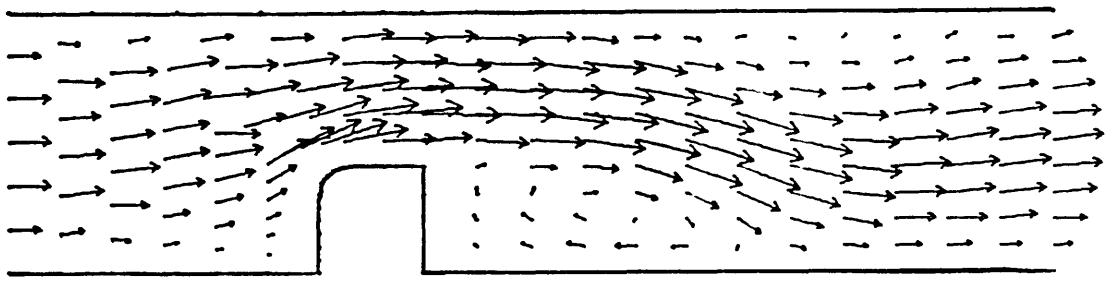

(c) n=40, Time=1.6

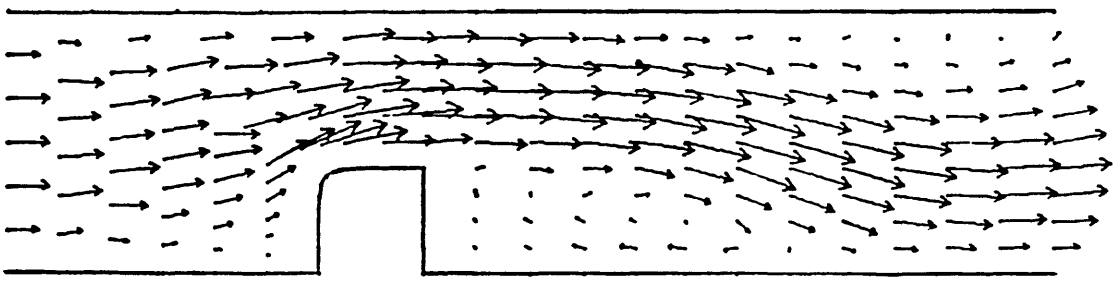

(d) n=60, Time=2.4

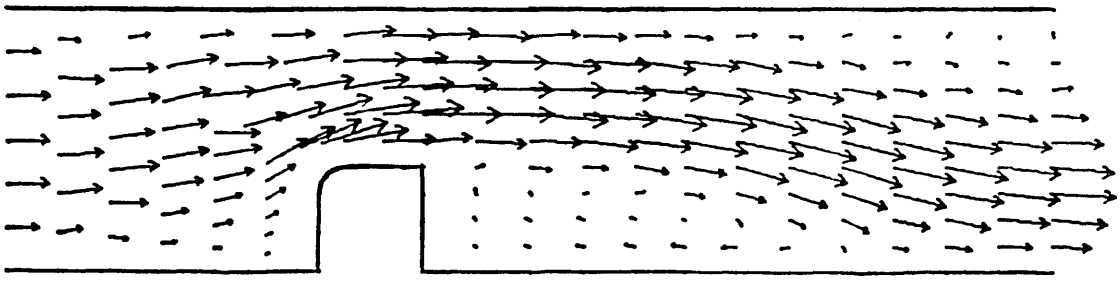

(e) n=80, Time=3.2

Fig.7.1.5 Velocity Vector Plots, Flow over a Step with Rounded Front Edge - 48 Elements, Re=200

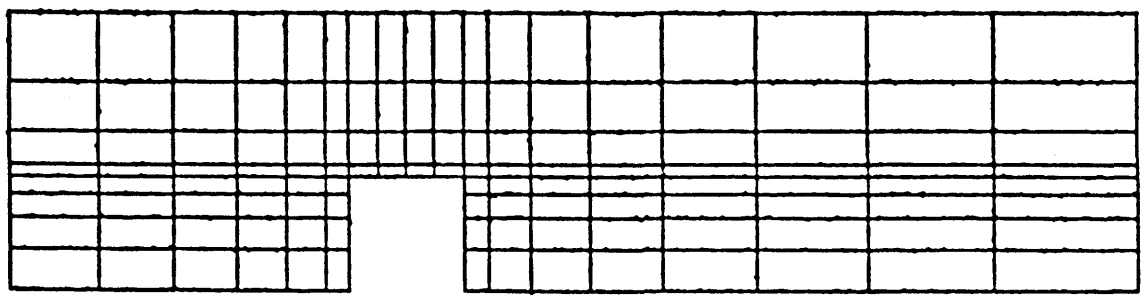

Fig.7.1.6 Non-Uniform Finite Element Mesh of 128 Elements

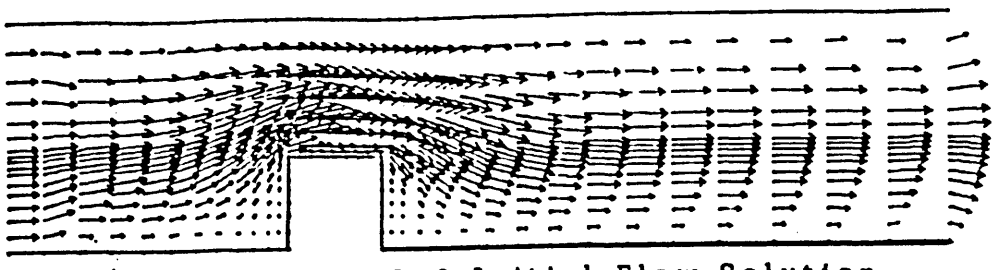

(a) n=0, Time=0.0 Initial Flow Solution

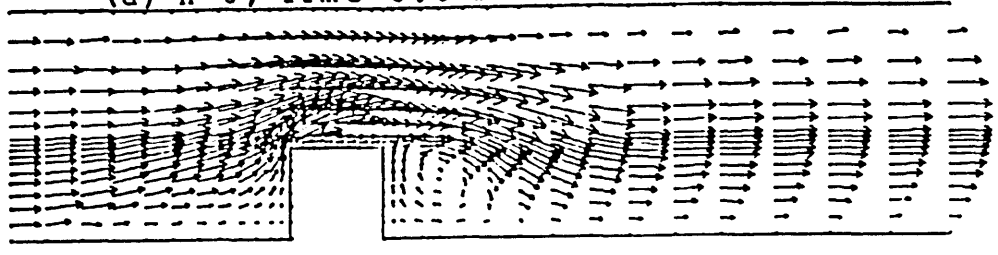

(b) n=20, Time=0.3

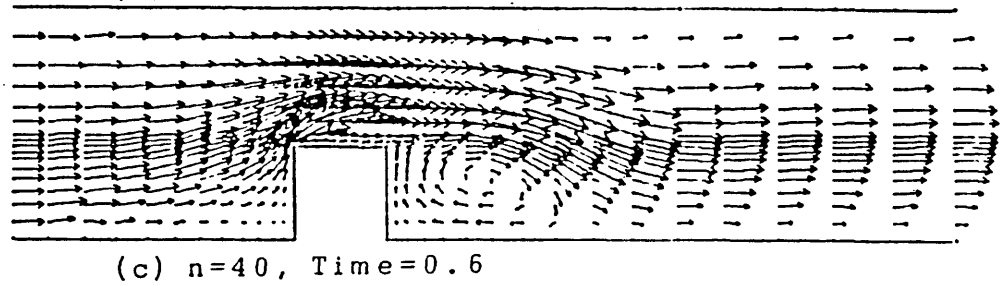

(c) n=40, Time=0.6

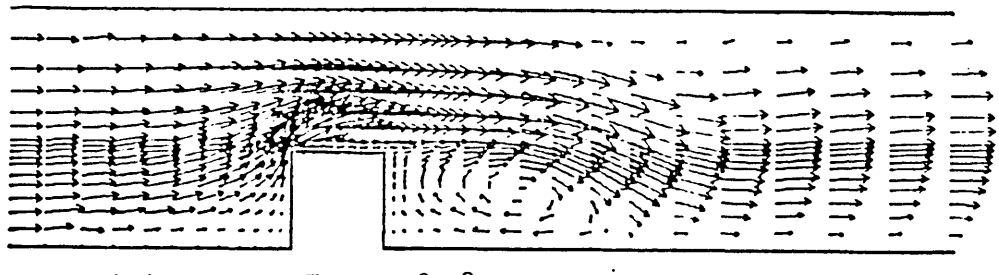

(d) n=60, Time=0.9

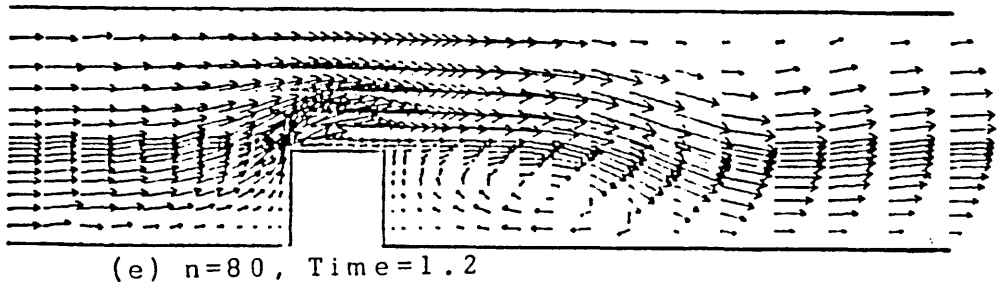

(e) n=80, Time=1.2

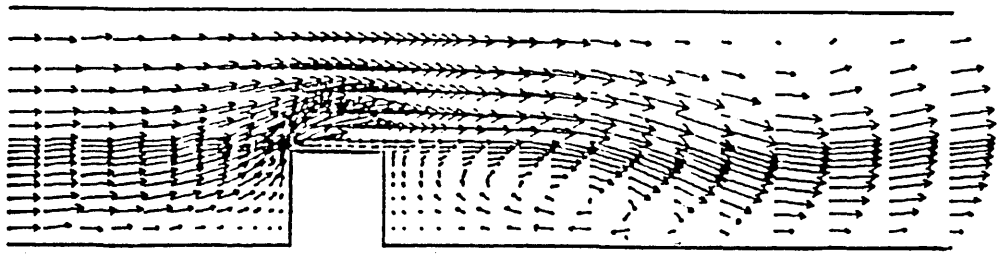

(f) n=100, Time=1.5

Fig. 7.1.7 Velocity Vector Plots, Flow over a Step
Non-Uniform Finite Element Mesh of
128 Elements, Re=200

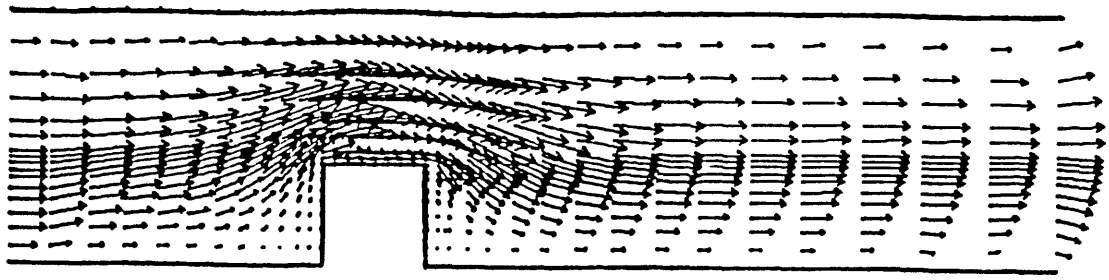

(a) n=0, Time=0.0 Initial Flow Solution

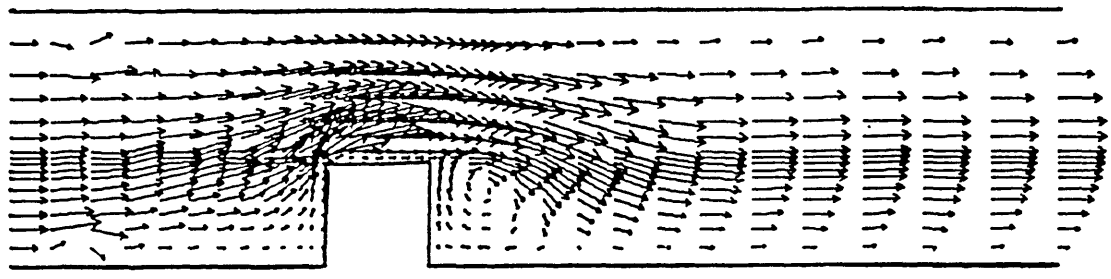

(b) n=30, Time=0.45

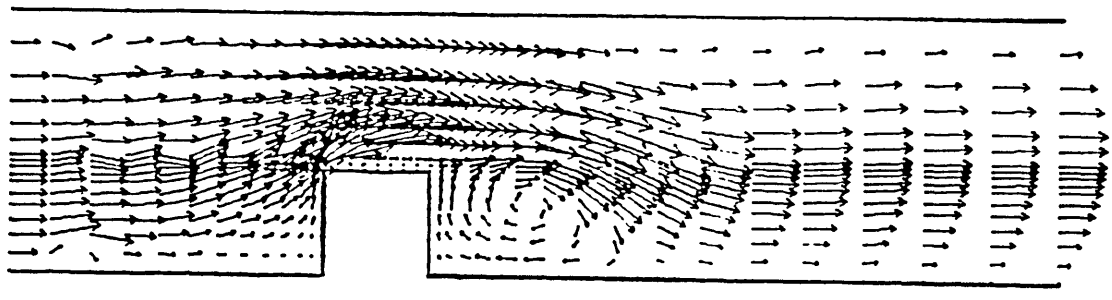

(c) n=60, Time=0.9

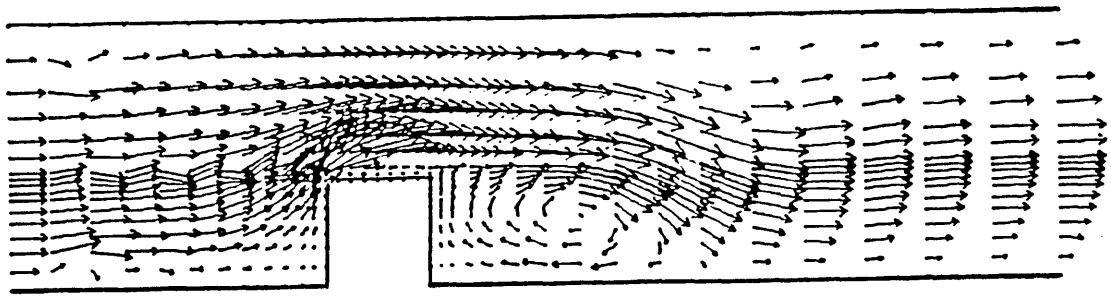

(d) n=90, Time=1.35

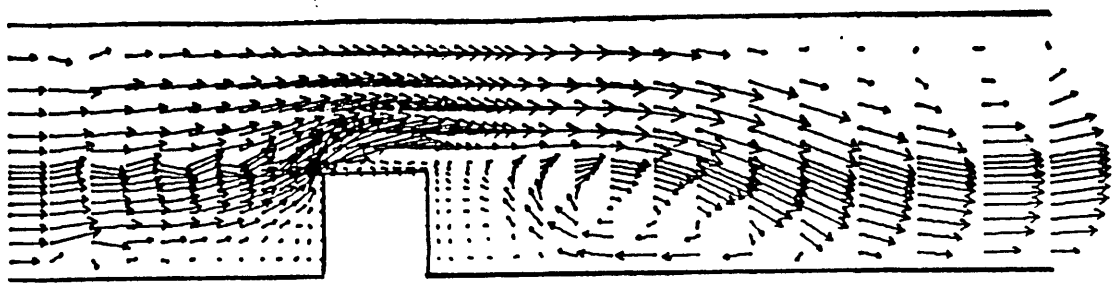

(e) n=240, Time=3.6

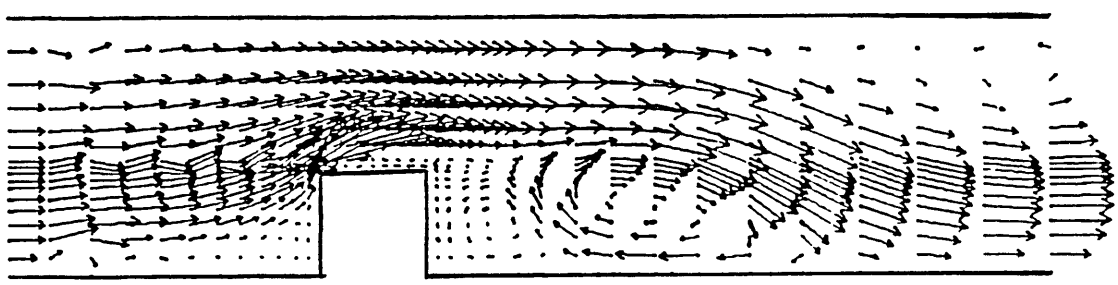

(f) n=270, Time=4.05

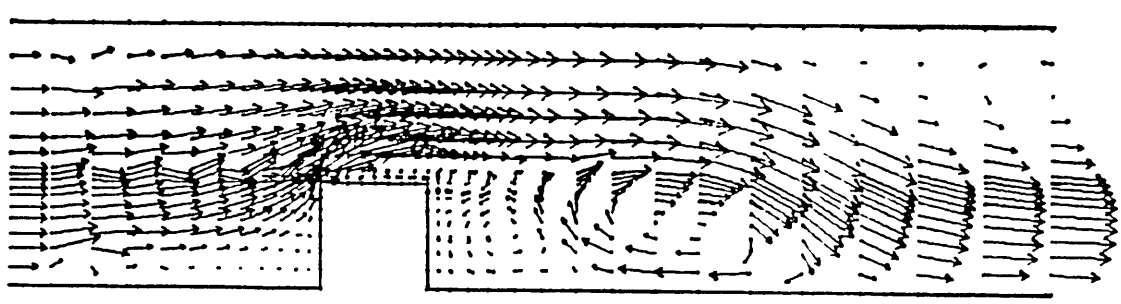

(g) n=300, Time=4.50

Fig. 7.1.8 Velocity Vector Plots, Flow over a Step
Non-Uniform Mesh of 128 Elements, Re=500

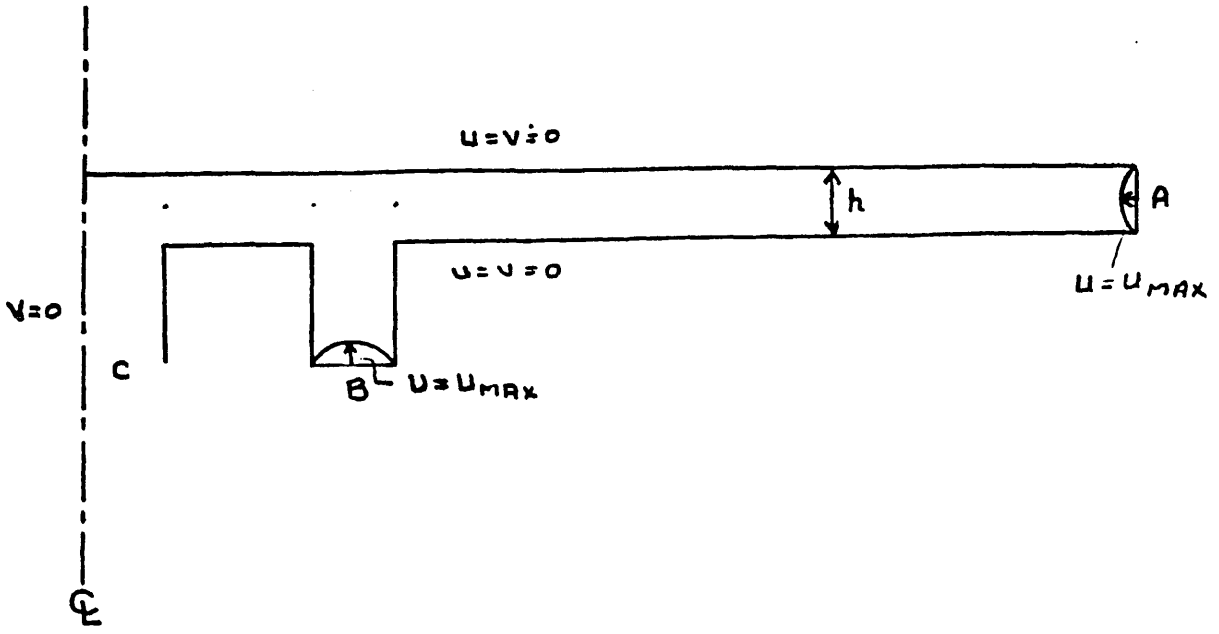

Fig.7.1.9 Axisymmetric Flow between two Parallel Plates Involving Sharp Corners - Problem Definition and Boundary Conditions

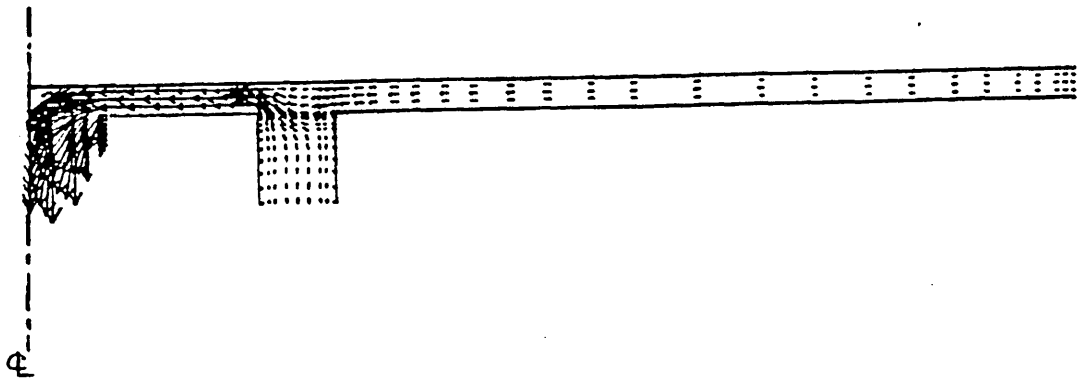

Fig.7.1.10 Axisymmetric Flow between two Parallel Plates - Velocity Vector Plot Stokes Flow

7.2 Flow over a Backward Facing Step

The flow over a backward facing step has been used as a test case for numerical model of fluid flow for many years. Several features contribute to its interest namely, separation and reattachment, a recirculation bubble and a fairly simple and well defined geometry. Over a dozen experimental investigations of such flows have been reported in the literature (64). All of these, except one, deal with the turbulent regime and are, therefore, ill-suited for testing numerical methods since their prediction also depends on the turbulent model adopted. Low Reynolds number measurements for flows over a backward facing step have been carried out in ref.65 with the specific intention of providing experimental results to compare with the numerical ones.

The numerical simulation of the back step problem has been treated extensively by Roache and Mueller (66) and analytically by Moffatt (67) and Weinbaum (68). Roache and Mueller used the FDM and upwind differencing; detailed results are presented for Reynolds number in the range 0.1- 100. One of the key results is the numerical demonstration of the fact that the flow separates even for Stokes flow, a small corner eddy appears and the separation point moves up the face of the step, approaching the corner as the Reynolds number is increased. These facts were previously predicted by Kawaguti (69) and verified experimentally by Matsui et al (70) for Reynolds number range 5-50. Weinbaum (68) also

predicted that separation could occur below the sharp corner. He predicted an approximate form of the corner singularity via an analysis of the biharmonic equation for the stream function and the argument that Stokes flow will prevail sufficiently close to the corner.

Some results of laminar and turbulent flow over a backward step are presented by Taylor et al (71) using FEM. Turbulent models are constructed using one equation modelling. Results for Re=50,150 are presented by Ecer, Rout and Ward (72) using a variational formulation. Comparision of finite difference and finite element predictions with experiment for turbulent flow for this example are presented in ref.73. Some further results using FEM and laminar flow are presented in ref.74,40. Hutton and Smith (76) have reported successful simulation of this flow employing FEM and no upwinding.

The problem of laminar flow over a backward facing step is analysed using the fluid finite element. The problem is defined in figure 7.2.1. The channel width upstream of the step is 0.5 (h) and downstream is 1.0 (H). The step height is therefore 0.5 (H-h). The computational domain extends 3X(H-h) upstream and 11X(H-h) downstream of the step. The top and bottom walls of the channel and the step itself are no-slip walls. A fully developed flow at the inlet is used with Umax=1.0. The outlet is left open. The flow Reynolds number is based on the step height ($Re=Umax(H-h)\rho/\mu$). A non-uniform finite element mesh of

54 elements and 251 nodes (fig.7.2.2) is used to analyse the flow problem. Based on the findings of the flow over a step problem (section 7:1), a finer mesh is used near the step corner. Because of the sharp change in geometry, the flow undergoes a rapid change in this region. An incremental Reynolds number approach was used for the solution (section 2.6). The flow Reynolds number is incremented using the density parameter ρ in the Reynolds number equation. Calculations are performed using a fixed timestep $\Delta t=0.09$. We are interestedin obtaining a steady-state solution at low Reynolds number, in order to compare with the available numerical and experimental results. The difference in solution at two consecutive timesteps is compared with a tolerance factor. When the difference in solution at two consecutive timesteps is less than the tolerance factor (10^{-5}), the flow is assumed to have reached a steady-state. The Reynolds number is incremented to the next value at this stage.

The calculations were performed in three sequences. In the first sequence, the initial conditions were as obtained from the Stokes flow solution and Re=50. The sequence consisted of 71 timesteps and steady flow was achieved. This flow was used as the initial condition for the second sequence in which Re=100. After a further 108 timesteps

steady flow was achieved and using this solution as the initial solution, finally, solution was obtained for Re=150. The final stage took a further 134 timesteps before a steady-state solution was achieved. Velocity vector plots for the steady-state solution at the three Reynolds numbers is presented in figure 7.2.3. The length of the recirculation bubble downstream of the step can be seen to elongate as the flow Reynolds number is increased. The variation of the recirculation zone length with the Reynolds number is plotted in figure 7.2.4. This is compared with some of the available experimental and numerical results. For Reynolds number up to 100, the numerical and experimental results seem to agree quite well, but at higher Reynolds numbers the discrepancy between the various results obtained using different techniques increases (fig. 7.2.5).

The shear stress along the top and bottom wall of the channel is calculated using equation 2.65. The non-dimensional shear stress is given as

$$\tau = (H-h) \,/\, Re\ U_{max} \cdot \partial u/\partial y \qquad (7.2.1)$$

The value of shear stress is plotted in figure 7.2.6 for Re=50 and in figure 7.2.7 for Re=150. Experimental (65) and numerical (72) results are available for the case of flow over a backward step at Re=150. From the graph in

figure 7.2.8, it can be seen that the results obtained using the fluid finite element are in reasonable agreement with the experimental results and the numerical results obtained using a variational formulation. The value of shear stress upstream of the step τ_{UP} and downstream of the recirculation eddy after it attains a constant value τ_{DOWN} is compared with the available results in Table 7.2.9. The values of τ_{UP} and τ_{DOWN} obtained using the fluid finite element are in good agreement with the equivalent theoretical and experimental values.

All of the numerical test cases reported here were run on a CDC 855 mainframe. The computer time used for the above example is listed in Table 7.2.10. Similar test case but using a variational formulation was run on a VAX-780 by Ecer, Rout and Ward (72). The computer time and the number of timesteps taken in the above reference are also tabulated in Table 7.2.10 along with the current results. The two computers used above are different from each other and hence the computer time used on the two machines is not comparable. The two computer times, however give an idea of the time the two different numerical schemes will take. The number of timesteps taken before a steady-state solution was achieved, indicate the effectiveness of the Penalty-Function formulation for such problems.

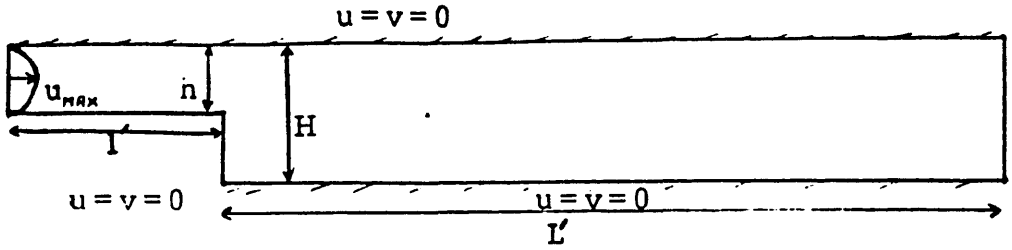

H=1.0
h=0.5
L'=5.5
l'=1.5

Fig.7.2.1 Flow over a Backward Facing Step
Problem Definition and Boundary Conditions

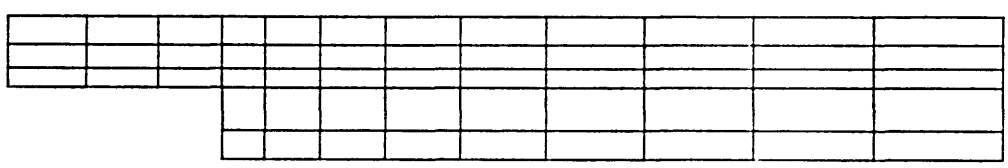

Fig.7.2.2 Flow over a Backward Facing Step
Non-uniform Finite Element Mesh

(a) Re=50, n=71, Time=6.39

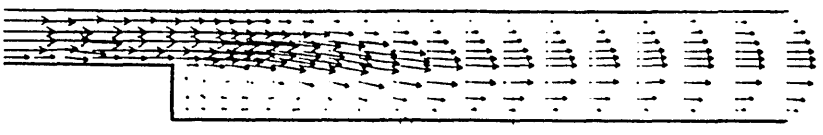

(b) Re=100, n=179, Time=16.11

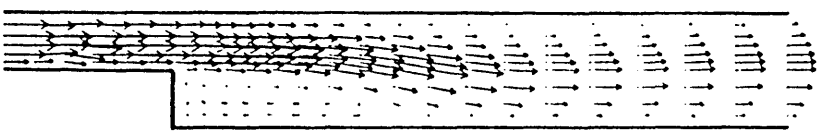

(c) Re=150, n=313, Time=28.17

Fig. 7.2.3 Flow over a Backward Facing Step, Velocity Vector Plots Representing the Steady-State Flow Solution

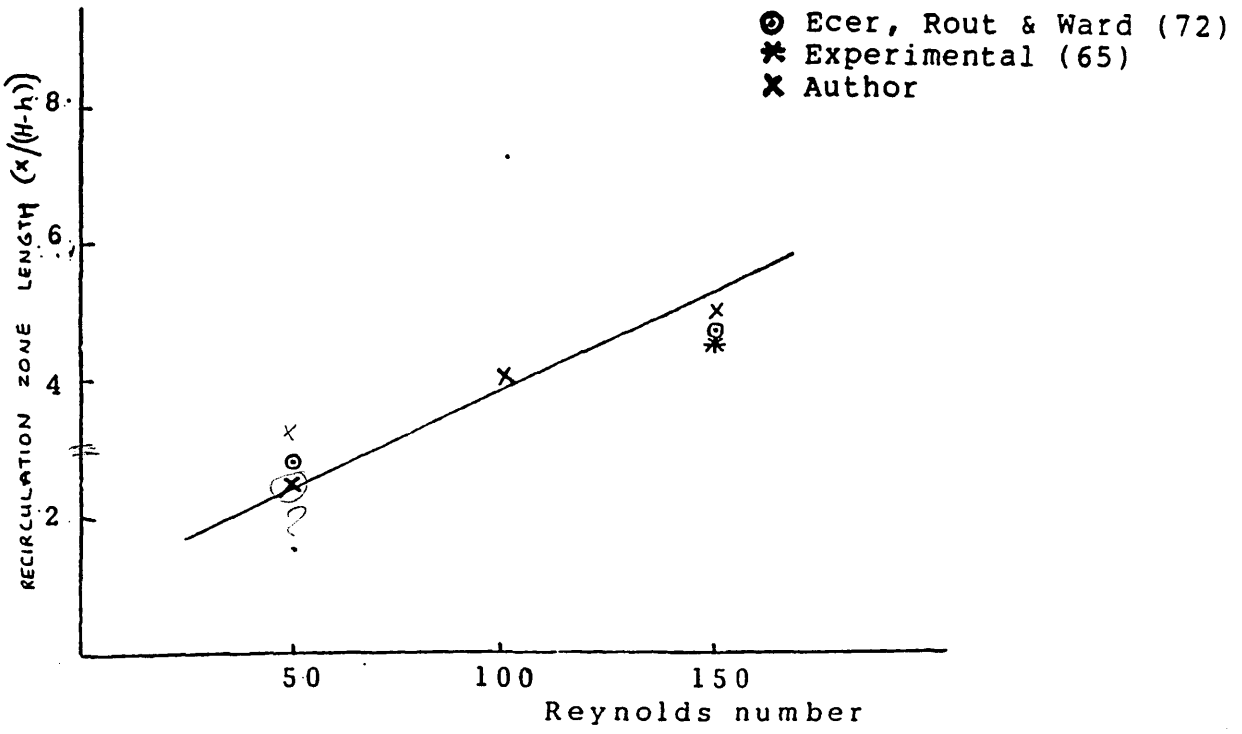

Fig.7.2.4 Variation of Recirculation Zone Length with Flow Reynolds Number

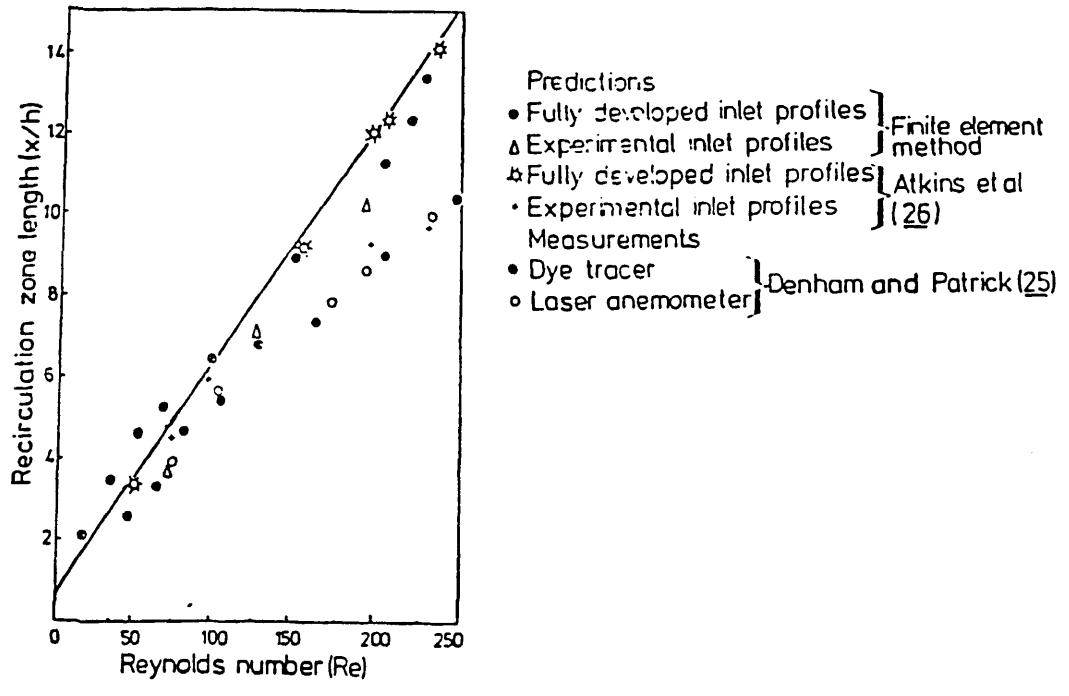

Fig.7.2.5 Variation in Recirculation Zone Length With Flow Reynolds number- Experimental and Numerical Predictions

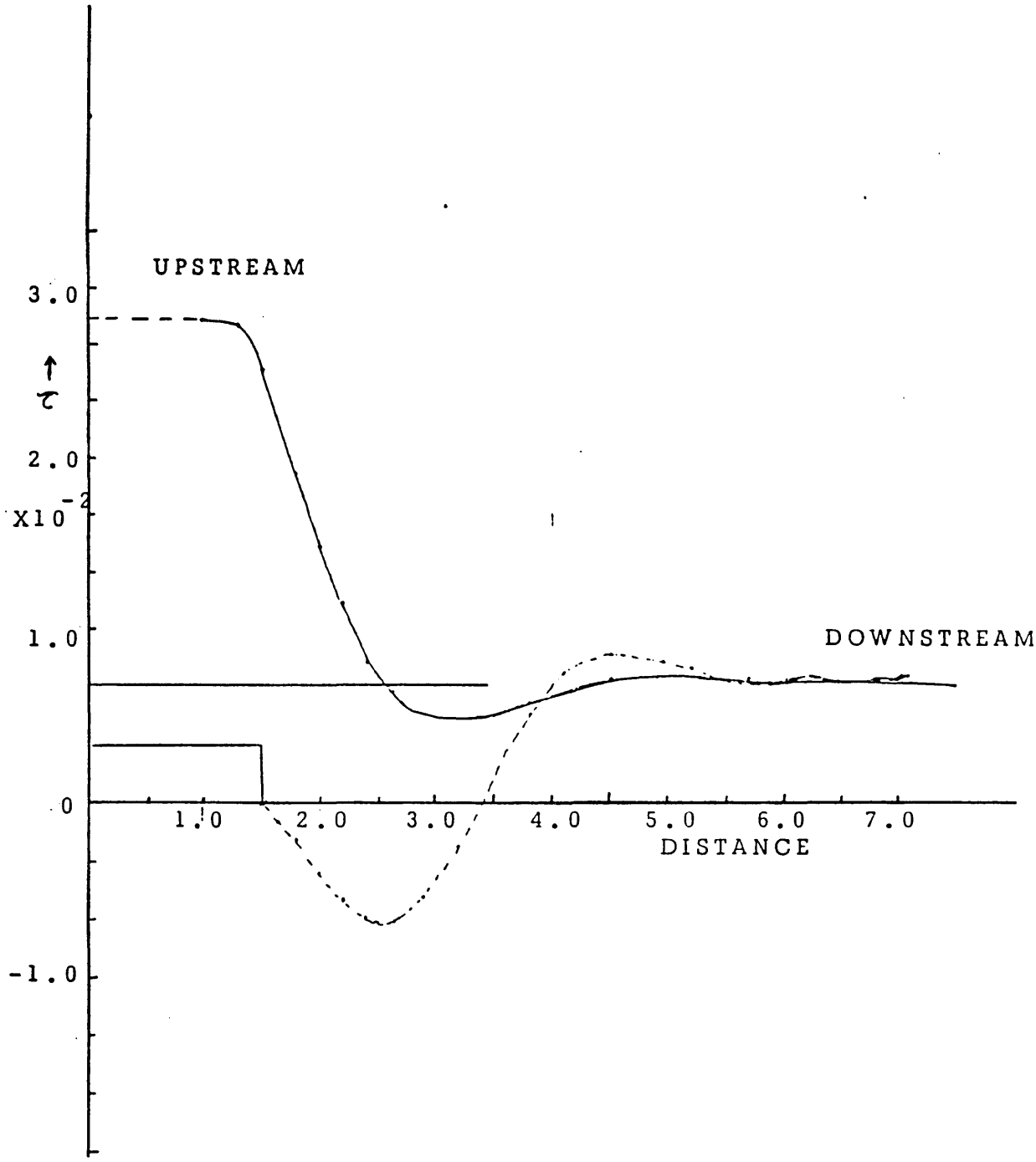

Fig. 7.2.6 Shear Stress (τ) Distribution along the Top and Bottom Walls - Flow past a Backward Step Re=50

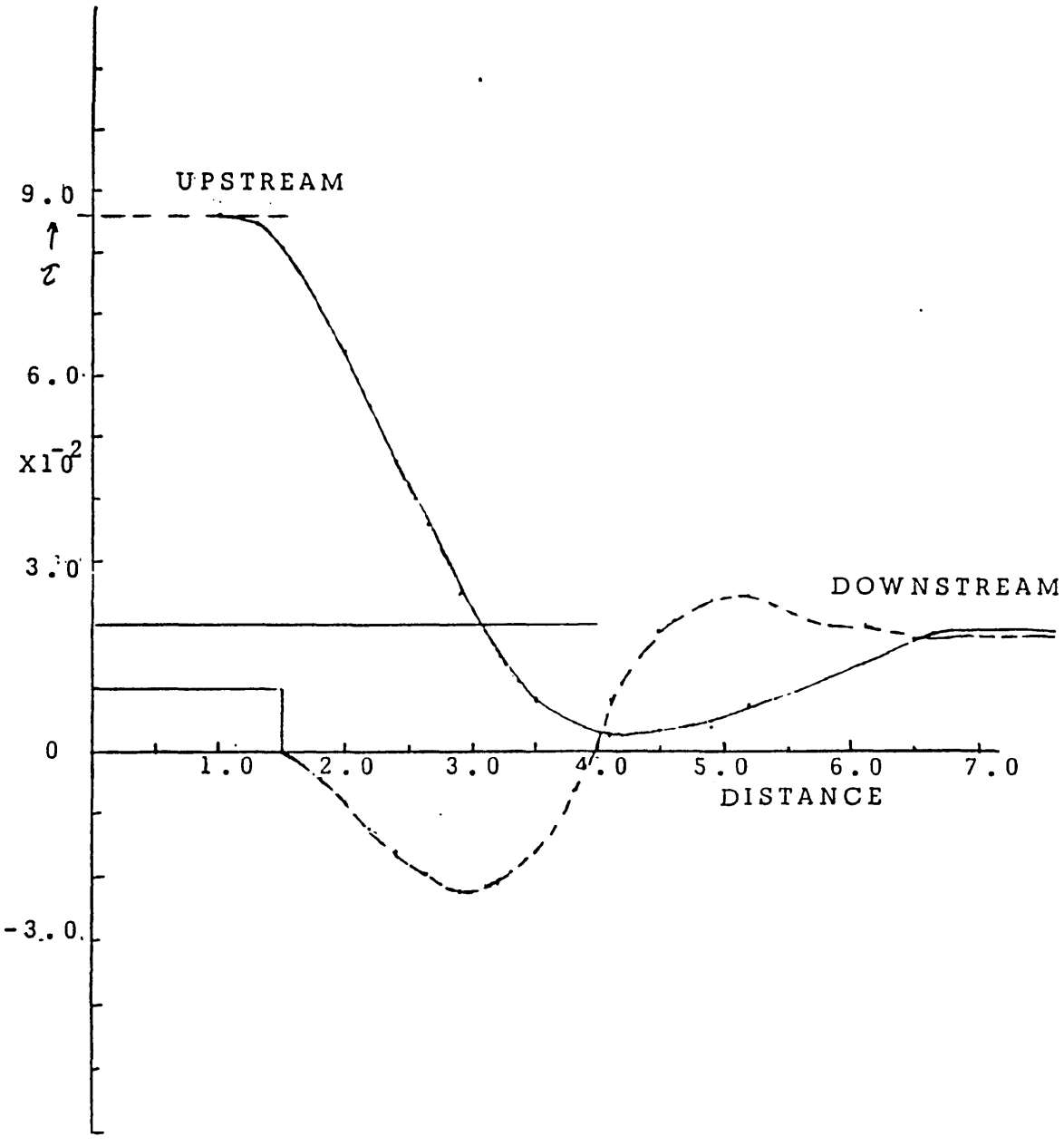

Fig. 7.2.7 Shear Stress (τ) Distribution along the Top and Bottom Walls - Flow past a Backward Step Re=150

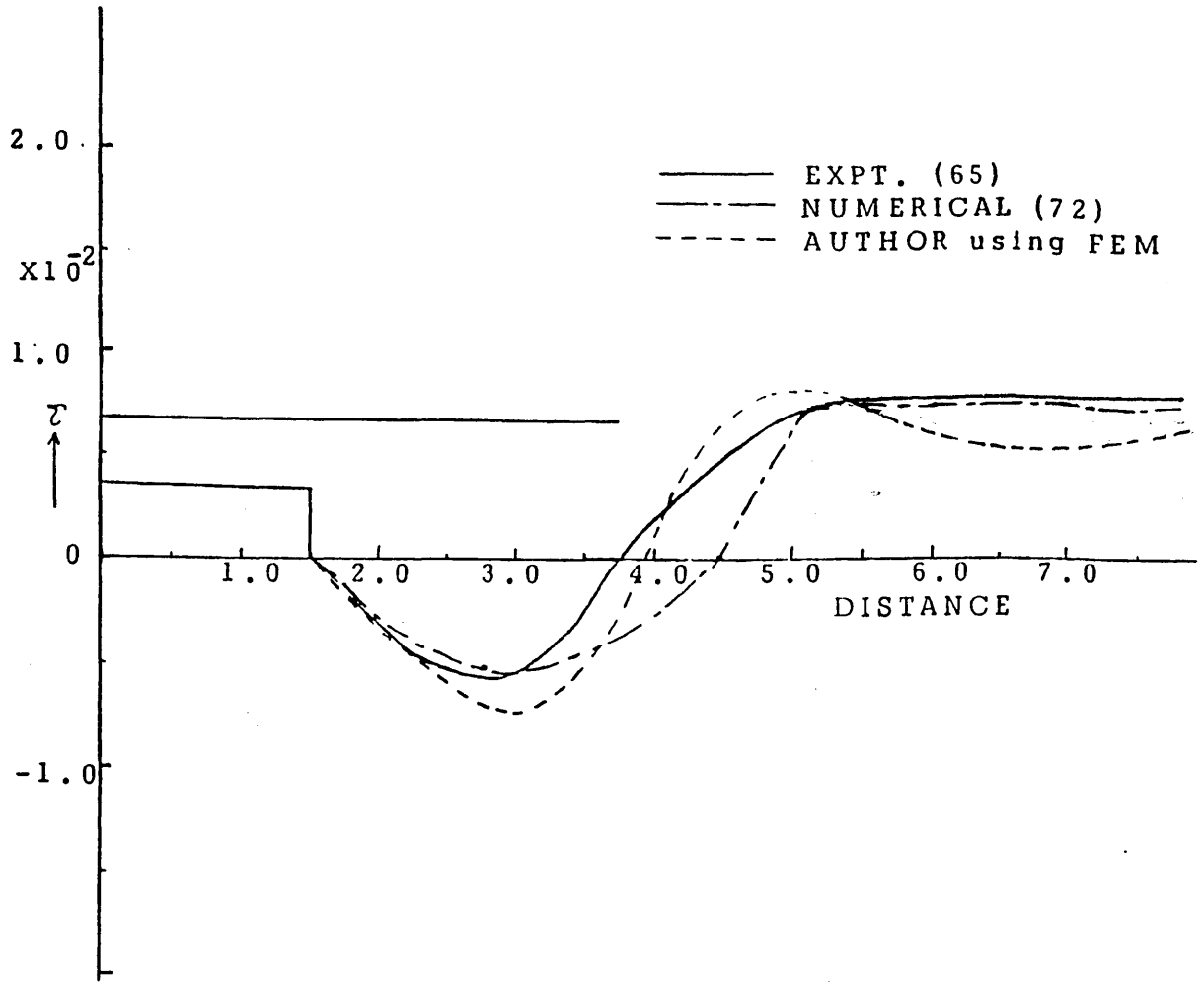

Fig. 7.2.8 Shear Stress Distribution along the Bottom Wall Flow Past a Backward Step, Comparison of Results Re=150

	THEORY (65)	EXPT. (65)	NUMERICAL (72)	AUTHOR FEM
Re=50 UP				$8.5X10^{-2}$
Re=50 DOWN			$2.61X10^{-2}$	$1.9X10^{-2}$
Re=150 UP	$2.67X10^{-2}$	$2.67X10^{-2}$		$2.8X10^{-2}$
Re=150 DOWN	$.67X10^{-2}$	$.67X10^{-2}$	$.68X10^{-2}$	$.67X10^{-2}$

Fig. 7.2.9 Shear Stress (τ) Upstream and Downstream of the Backward Step, Comparison of Results

		ELEMENTS	NODES	TIMESTEPS	COMPUTER TIME
Re=.50	Ref.72	418	462	305	12 cpu Hours on Vax 780
	Author	54	251	71	110 170-855 cpu secs on Cyber 855
Re=150	Ref.72	418	462	875	22.5 cpu Hours on Vax 780
	Author	54	251	313	490 170-855 cpu secs on Cyber 855

Fig. 7.2.10 A Comparison of Computer Time used to Analyse the Flow Past a Backward Step

7.3 Flow in a Cavity

The classical problem of a wall-driven cavity on a unit square, with u=1 along the entire upper boundary including the corner nodes can be considered as an ideal physical problem from the viewpoint of obtaining numerical solution to the Navier-Stokes equations to describe fluid motion. Because of its geometric simplicity and comparatively minor singularities, it provides a model problem for testing new numerical schemes and as a benchmark solution. It allows comparisons to be made among various schemes using different methods of problem formulation, discretisation, iteration and approximation. One of the main problems in doing numerical fluid mechanics is that the grid size must decrease as the Reynolds number increases so that numerical stability is obtained. A majority of the analysis methods have been tried on this problem and a limited number of results are available.

Burgraaf (76) was the first to do an extensive numerical study on the cavity flow problem using a modified relaxation method. His calculations were for a square cavity in the Reynolds number range from 0 to 400 with mesh spacing from 1/10 to 1/40. The motion of the vortex centre towards the centre of the cavity is demonstrated as the Reynolds number is increased. The behaviour of the secondary vortices in the lower corners is also examined. He noted that the secondary vortex pattern was viscosity-dominated in contrast with the relatively

non-viscous primary eddy.

Using the same relaxation scheme as Burgraaf, Pan and Acrivos (77) obtained detailed numerical solution to the problem of creeping flow in a cavity. They also conducted a flow-visualisation study of the cavity flow problem over a wide range of Reynolds number from 80 to 4000. The visualisation studies produced flow fields consistent with the Batchelor model (78). The value of 4000 was the Reynolds number at which flow instabilities began to appear. Greenspan (79,80) considered the cavity flow problem numerically by means of the generalised Newton's method with overrelaxation. Solutions for Reynolds number up to 10^5 are presented. Another set of studies carried out at Imperial College by Runchal, Spalding and Wolfshtein (81), Runchal and Wolfshtein (82) and Gosman et al (83), presented two new features; use of non-uniform mesh system to improve the accuracy of the solution, and evaluation of wall vorticity which was an improvement over that used by previous investigators. Results for Reynolds number up to 10^4 were presented using non-uniform meshes. Mills (84) examined the cavity flow problem at Re=100 for different aspect ratios using central differencing. Nallasamy and Krishnaprasad (85) have presented detailed results for Reynolds number in the range of 0-50,000 using finite difference techniques. A further review of computing methods for recirculating flows (cavity flow)

was carried out by Tuann and Olson (86) and Bozeman (87). A survey of earlier work (until 1973) was carried out by O'Brian (88).

All the earlier work uses techniques other than the Finite Element Method which is comparatively new in this field. However, there are some results for this example obtained by solving the steady Navier-Stokes equation using FEM. A survey of earlier work (up to 1977) was carried out by Tuann and Olson (86). Hughes et al (40) present results for Reynolds number up to 400. In another paper (46) results for higher Reynolds number (up to 10^4) are presented using an incremental Newton-Raphson scheme. A coarse non-uniform mesh of 165 nodes was used. Results for Reynolds number up to 1000 are presented by Bercovier and Engelman (63). A penalty function type of isoparametric finite element and uniform mesh is used.

The most recent work using FEM is by Huffenus and Khaletzky (89 (1984)) and Gresho et al (90). The method of characteristics is used in ref.89, while Gresho et al use a modified FEM as detailed in ref. 91. A comparative study of the central and upwind difference schemes using the primitive variables is demonstrated using this example by Timin and Esmail (92). Results are presented for Reynolds number upto 1000 using a central difference scheme and upto 5000 using upwind differencing.

In this work results are presented for flow in a cavity for a range of Reynolds numbers. An attempt was made to achieve a solution for the highest possible Reynolds number, prior to convergence problems. Particular attention was paid to mesh density and timestep size as the Reynolds number was increased. An incremental approach was used to obtain the solution at the higher Reynolds numbers. The parameter chosen to increment the Reynolds number was the density ρ. The solution at each timestep was checked for convergence and the Euclidean norm (Ec) of the difference of the solution at any two successive timesteps was compared with a convergence factor 'e'. The value of the convergence factor e was taken as 10^{-5}. When Ec=e the solution can be assumed to have reached steady state. At this stage the Reynolds number was incremented to the next higher value.

Problem Definition and Characteristics of Flow

For the case of a square cavity the problem description is as shown in fig.7.3.1 . u=1 along the entire upper boundary including the corner nodes. The nature of the vortex formed in the cavity depends on the Reynolds number defined as $Re = ud\rho/\mu$, where u is the velocity along the upper boundary, d is the width of the cavity, ρ is the

density and μ is the viscosity. Aspect ratio (cavity width to height ratio) also plays an important role. For an aspect ratio of unity and relatively low Reynolds number, the centre of the primary vortex is located about three-quarters of the cavity height from the bottom and at midwidth, with most of the strength concentrated in the upper portion of the cavity. A pair of small counter-rotating secondary vortices of much smaller strength are located in the lower corners of the cavity. The size of corner vortices changes as the Reynolds number is increased. For an aspect ratio greater than unity, the number of vortices in the cavity depend on the value of aspect ratio (84).

For relatively low Reynolds number (order of zero) the flow is well represented by a 5X5 uniform mesh (fig.7.3.2a). This gives a good solution for Re=0 (fig.7.3.2b), but for Re=100 (fig.7.3.2b), instabilities start to appear near the upper boundary. In fact it can be seen in fig.7.3.2b that the velocities at the second row of the nodes away from the driven surface and parallel to it are accelerating in the wrong direction. With the use of 10X10 uniform mesh (fig.7.3.3a) the flow solution is well represented for Re=0 (fig.7.3.3b), reasonably well for Re=100 (fig.7.3.3c) except for the top left hand corner, and the solution obtained at Re=400 (fig.7.3.3d) is similar to the Re=100 solution with the 5X5 uniform

mesh. Although the movement of the centre of rotation of the primary vortex is well represented in the velocity vector plots (fig.7.3.3b to 7.3.3d) of 10X10 uniform mesh, the presence of ripples near the top moving boundary and a region of reversed flow near the top wall is not correct. The presence of these ripples indicate that the flow near the top boundary is undergoing rapid changes and is inadequately modelled. The 7X8 non-uniform mesh with finer mesh near the top (fig.7.3.4a) gives a smooth solution for Re=100 (fig.7.3.4c) and also for Re=400 (fig.7.3.4d). The flow solution at Re=400 still has a few ripples near the top. However, the reversed flow region is absent. This indicates that the mesh is adequately refined in the vertical direction, but further refinement is required in the horizontal direction. At least ten elements are required along the horizontal direction to resolve the flow properly at Re=400. The 10X10 non-uniform mesh (fig.7.3.5) gives a smooth solution for Re=400 (fig.7.3.6b), but ripples start to appear as the flow Reynolds number is increased, indicating that further mesh refinement is required in horizontal direction (fig.7.3.6c), and in both horizontal and vertical direction (fig.7.3.6d, Re=2000 and fig.7.3.6e, Re=3000). A 14X11 non-uniform mesh (fig.7.3.7) gives a smooth solution for Reynolds upto 1000 in figure 7.3.8. A solution for Reynolds number upto 5000 was obtained using this mesh . The solution failed to converge when the Reynolds number

was incremented beyond 5000.

The behaviour of the primary eddy is best studied by following its centre as a function of the Reynolds number. Midplane horizontal velocity is plotted for a range of Reynolds numbers in fig.7.3.9. From the velocity vector plots we see that the centre of circulation of primary eddy moves upstream at Re=100 with respect to its location at Re=0. As the Reynolds number is further incremented it moves towards the centre of the cavity. Similiar behaviour has been observed by other authors mentioned previously (46,85).

In the present study, secondary eddies appeared at Re=100. As these are much weaker in strength compared to primary eddy, these can not be seen in the velocity vector plots. In order to see their exact location and direction of rotation, it is required to magnify the velocity vectors in the two corners. Their position, however was found by looking at the velocity values for the nodes in the two bottom corners. The upstream secondary eddy was found to be larger compared to the downstream eddy and it further grows with increasing Reynolds number. In the finite difference literature (85) similiar behaviour of the secondary eddies was observed. It was found that the upstream secondary eddy grew to a maximum at about Re=500, and then started to decrease in size when the Reynolds

number was further increased (85). The downstream eddy more or less stayed the same size upto Re=500, then continued to grow as the Reynolds number was increased. The available finite element results for cavity flow do not go into the details of the secondary eddies.

The physical mechanism behind the growth and decay of the secondary eddies can be explained by the fact that there is a strong deceleration of the flow from (**1**,1) to (**0**,0) (fig.7.3.1). At (1,0) the flow hits the wall which results in further increase in pressure. The kinetic energy of the fluid stream in the vicinity of the wall at low Reynolds number is low and the stream is unable to negotiate this pressure hill, with the result that it separates, forming an eddy at the corner. As the Reynolds number increases the stream kinetic energy also increases and hence the eddy shrinks in size. A similiar situation prevails on the bottom wall of the cavity. However, the stream along this wall possesses a much smaller kinetic energy as a result of frictional loss along the bottom wall. Therefore, it needs a much larger Reynolds number to overcome the adverse pressure gradient, hence the observed behaviour of the downstream eddy. Similiar phenomenon has been observed by Leal [18] who studied decelerating flow over a flat plate. The behaviour of these recirculation eddies and the complex variation of pressure along the side walls is covered in ref.85.

In fig.7.3.10 the results are presented for flow in a cavity of aspect ratio 3, and at Re=100. The velocity vectors in the right hand side of the cavity are magnified to see the exact location and direction of rotation of any secondary eddies that might be present. The magnification factor is X9 in figure 7.3.10a and applies to the velocity vectors away from the line and in the direction of the arrow. In the successive plots, the velocity vectors further away from the driven wall are magnified. In figure 7.3.10b, the secondary eddy can be clearly seen. In order to see if another recirculation region is present near the right hand wall of the cavity, the velocity vectors in this region were magnified to a maximum of X2494. Only two counter-rotating recirculation eddies are seen in the velocity vector plots. The one away from the moving wall is much smaller in strength compared to the one near the moving wall. The strength of the secondary eddy as compared to the main eddy can be estimated from the magnification values as used in figure 7.3.10. Compared to the example of square cavity, there is only one secondary eddy in the case of the rectangular cavity.

From the above test cases, the following observations are made.

(i) It is clear that nodes are required inside the

boundary layer region to obtain a smooth solution. The boundary layer is the thin layer close to the solid boundary within which vorticity varies rapidly as a result of the combined effects of viscous diffusion and convection, and outside which vorticity is zero or non-zero and varies slowly. Hence effects of viscosity are important in this region. The boundary layer gets thinner as the Reynolds number is increased. The thickness of the boundary can be estimated to be of the order $Re^{-\frac{1}{2}}$ (94). As long as there are node points inside the boundary layer, steep gradients are captured with very few or no oscillations.

(ii) For stability the cell Reynolds number, $Re_c = \rho u \Delta x/\mu$ should not exceed 2 (52), where Δx is the distance between two adjacent nodes for the element and u is the nodal velocity for that element. In fig.7.3.6 and Re=400, the flow is stable. The cell Reynolds number, although not less than 2 is sufficiently small near the top moving boundary. Away from the top boundary as the cell size increases the effective cell Reynolds number also increases and is much greater than 2 for cells with high velocities. As the Reynolds number is incremented by incrementing the parameter ρ, Re_c also increases and ripples begin to appear near the top boundary for Re=1000 (fig.7.3.6c) and a region of reversed flow developes as ρ is incremented further. In figure 7.3.8 and Re=1000

smaller elements are used near the top boundary, hence a smaller Re_c. The solution obtained is stable and free from any ripples. This indicates that as long as the Reynolds number is sufficiently small in critical regions where flow details are changing rapidly, smooth solutions with reasonable accuracy can be obtained.

(iii) To fulfil the stability conditions outlined above, it is necessary to use a non-uniform mesh. This has the benefit that a finer mesh can be used in the regions where the flow is undergoing rapid changes and sufficient nodes are present inside the boundary layer region. Everywhere else in the flow where flow velocities are relatively small and not changing rapidly a coarse mesh is used. The total number of nodes and hence the number of equations required to solve the problem reasonably accurately are greatly reduced compared to a uniform fine mesh with smaller elements everywhere. The timestep for stability of solution is selected according to equation 2.49, and the equation needs to be satisfied for every element in the mesh. Based on the smaller elements near the top boundary with large velocities the timestep is small. Although a small timestep is used and many steps are required before a steady-state solution is achieved, the overall cost of the analysis is less as the effective number of equations required to solve at each timestep is reduced by the use of non-uniform mesh.

(iv) The presence of ripples slows down convergence. Using a 10X10 uniform mesh 160 timesteps were taken before a steady state solution was obtained for Re=400. With 10X10 non-uniform mesh the solution obtained was smoother and it took only 128 timesteps to achieve a steady state solution. Although a lesser number of timesteps are required to achieve the steady state solution, the total cost of analysis is slightly more with the use of non-uniform mesh as a smaller timestep results from the presence of smaller elements in the finer mesh region. The solution obtained, however, is a great deal smoother and more accurate.

(v) Near Re=4000 convergence problems arose. Around this Reynolds number the flow is changing to a turbulent one and the equations of constant viscosity no longer hold. The choice of higher Reynolds number is also limited by the rapidly increasing cost of analysis, which results when a finer mesh along with a smaller timestep is used.

(vi) This particular problem of cavity flow involves sharp corners. In the previous example of flow over a step, it was observed that most of the ripples can be eliminated by rounding off these corners. The two top corners seem to be the region where flow velocities are going through a rapid change. Based on the previous

findings, it can be expected that rounding of the corners near the top boundary will reduce or even eiminate these ripples.

The numerical study of a complex flow is possible with the use of the fluid element. One such example is presented with the flow over a square obstacle inside a square cavity (fig.7.3.11). The flow enters from the bottom left side of the cavity and leaves the cavity from the top right side. The flow was analysed at Re=1000. Steady-state flow was not achieved after 146 timesteps in this case.

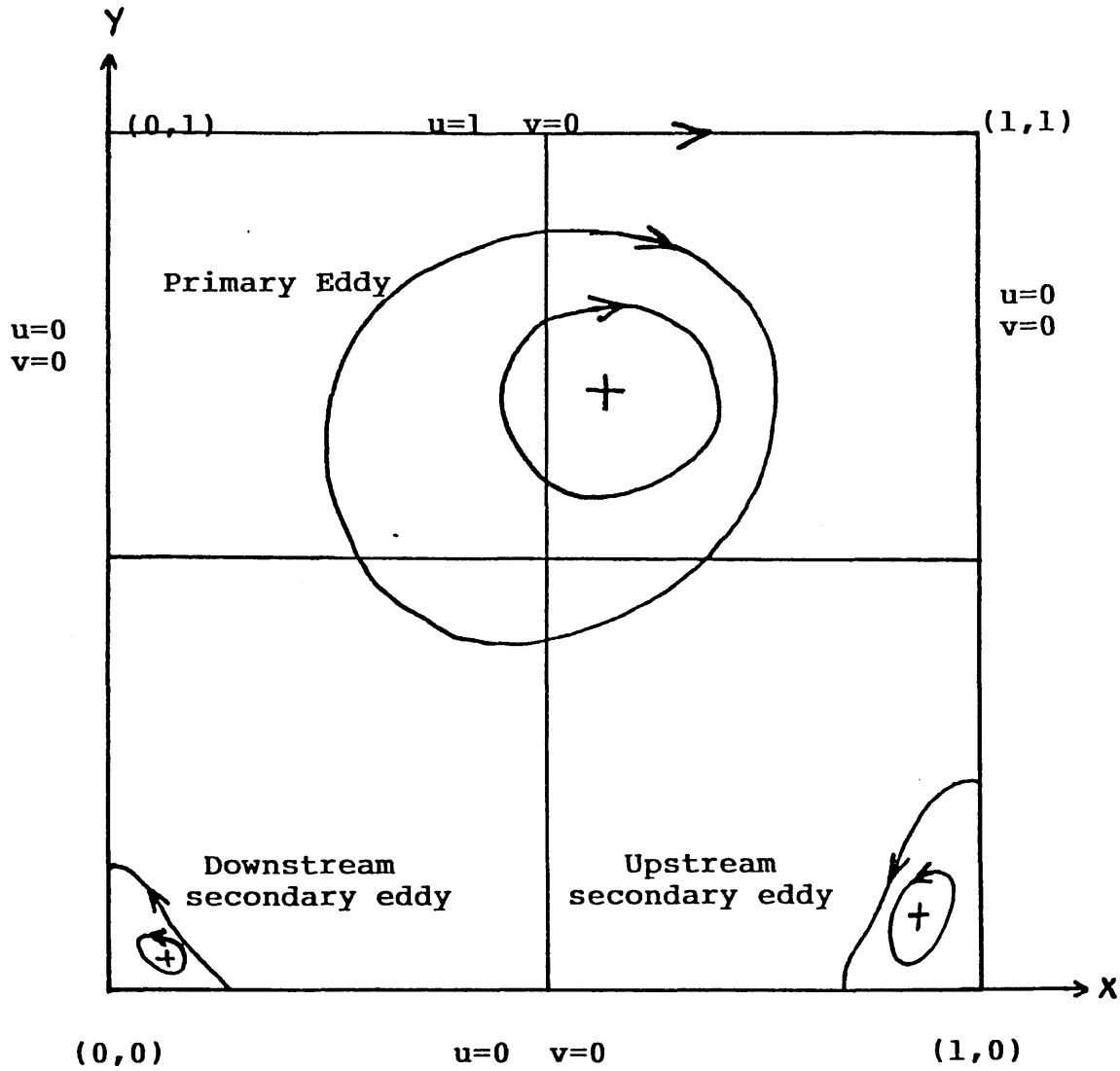

Fig. 7.3.1 Problem Definition and Characteristics of Flow in a Cavity

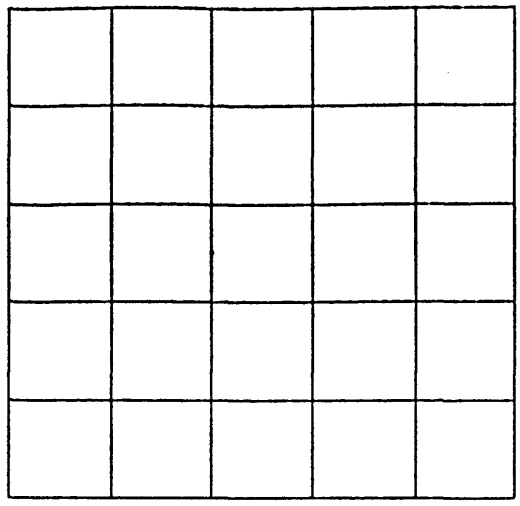

Fig.7.3.2a 5X5 Uniform Finite Element Mesh

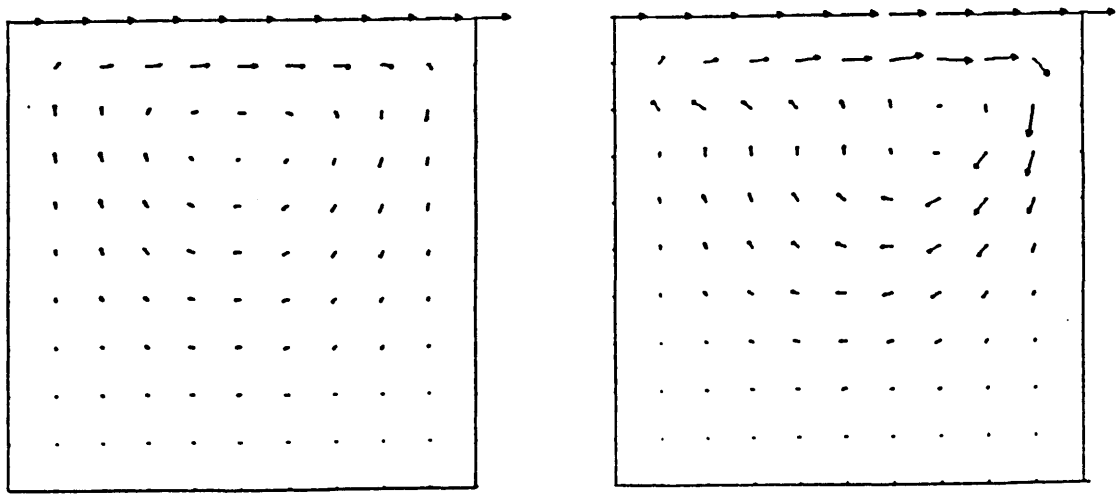

Re=0 Initial Flow Solution

Re=100

Fig.7.3.2b Velocity Vector Plots- Flow in a Cavity
5X5 uniform mesh

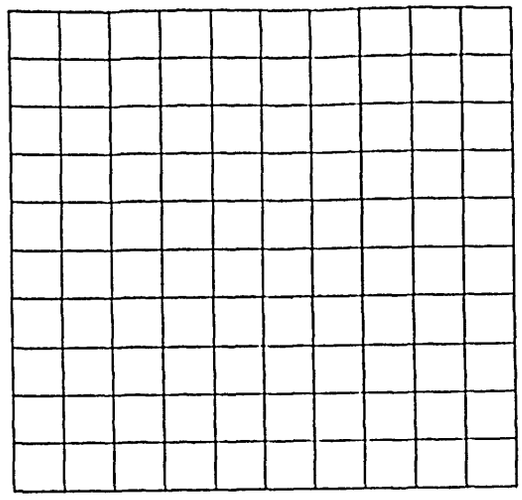

Fig.7.3.3a 10X10 Uniform Mesh

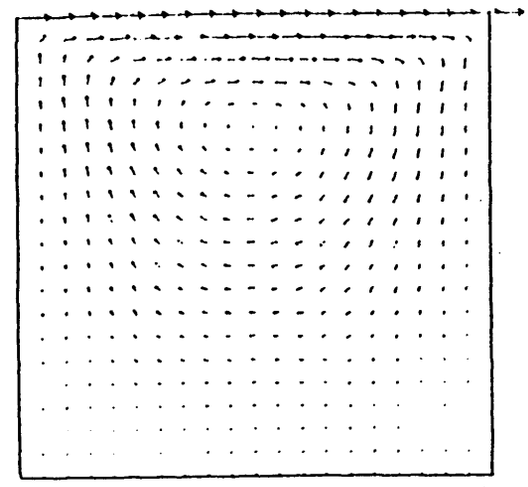

(b) Re=0, Initial Flow Solution

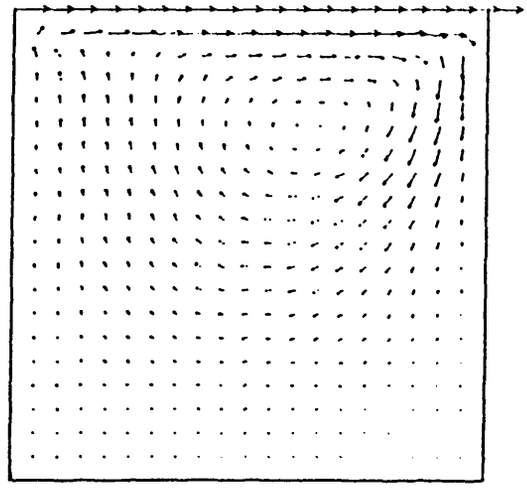

(c) Re=100, n=39

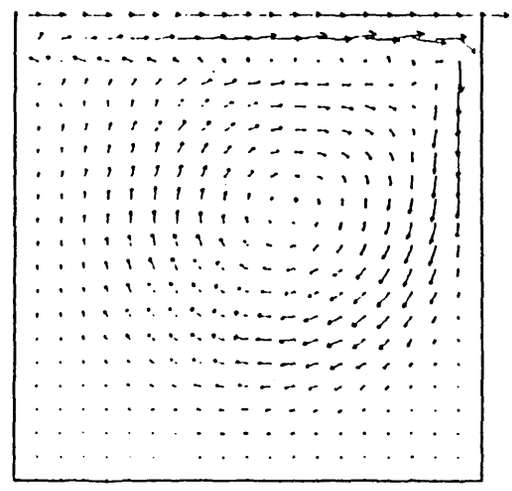

(d) Re=400, n=160

Fig.7.3.3 Flow in a Cavity 10X10 uniform Finite Element Mesh and Velocity Vector Plots

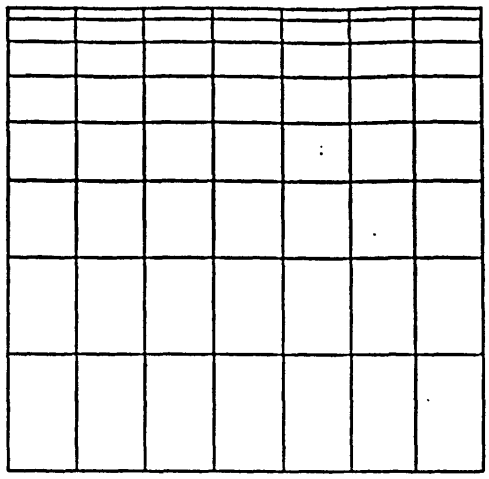

(a) 7X8 Non-Uniform Mesh

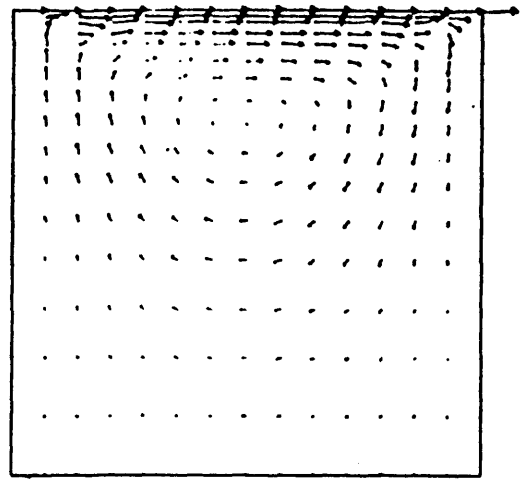

(b) Re=0 Initial Flow Solution

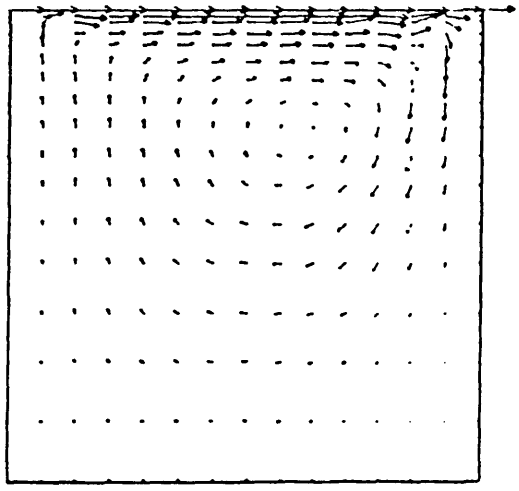

(c) Re=100, n=36

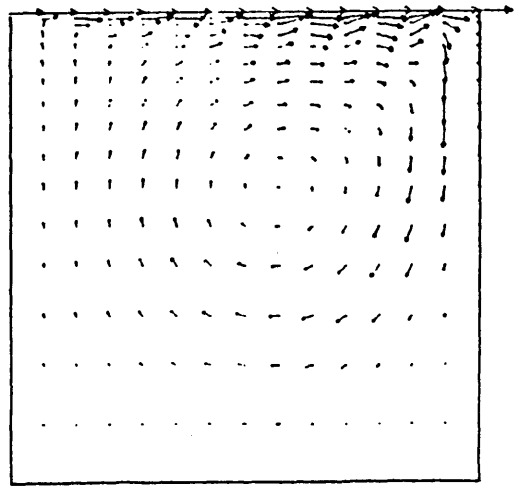

(d) Re=400, n=138

Fig.7.3.4 7X8 Non-Uniform Finite Element Mesh and Velocity Vector Plots - Flow in a Cavity

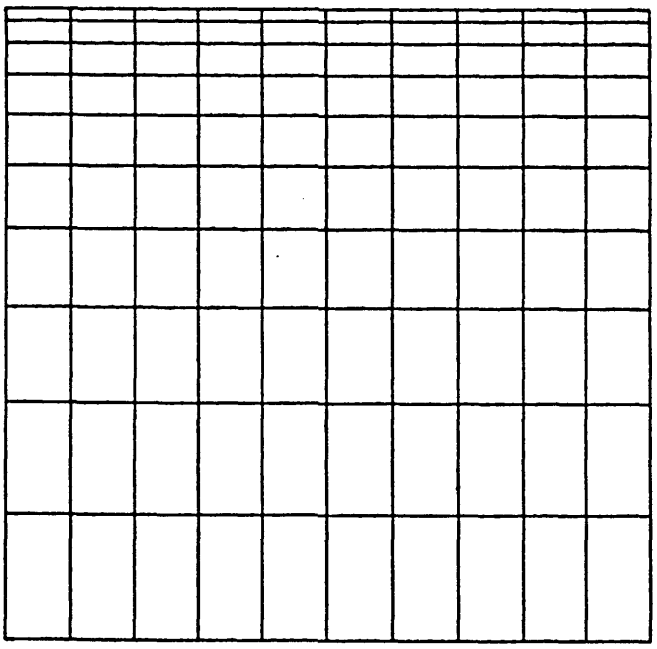

Fig.7.3.5 10X10 Non-Uniform Mesh

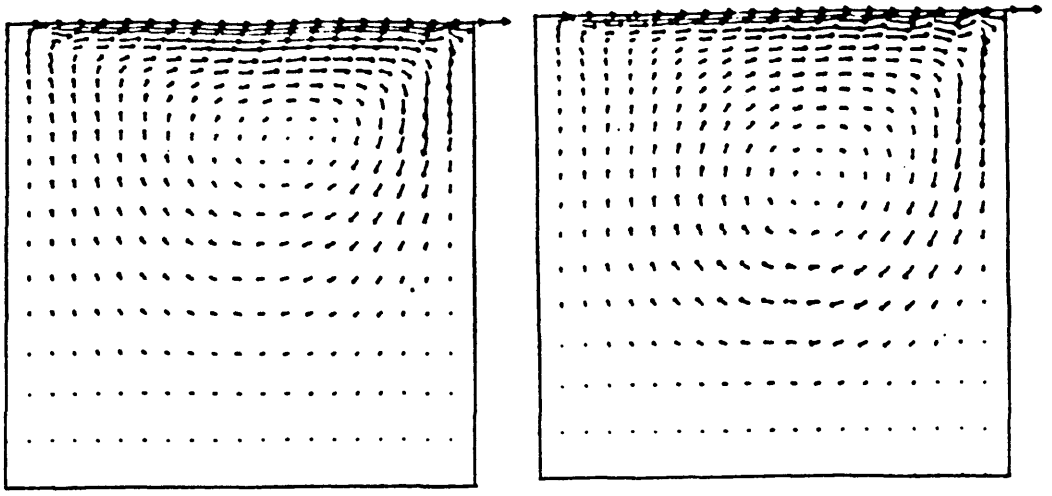

(a) Re=100, n=38 (b) Re=400, n=128

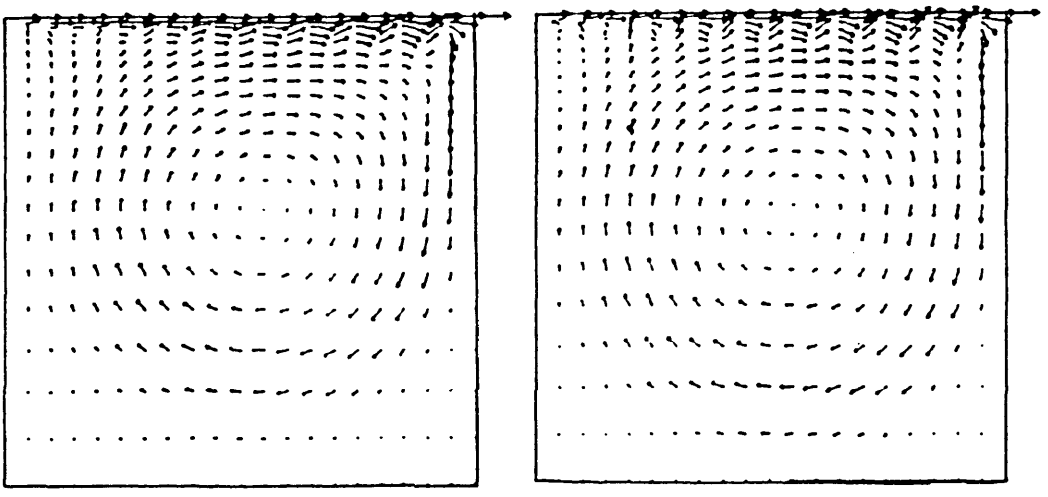

(c) Re=1000, n=240 (d) Re=2000, n=363

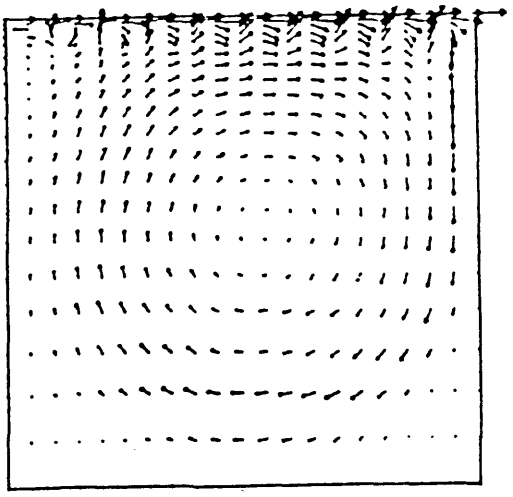

(e) Re=3000, n=411

Fig.7.3.6 Steady-State Flow Solution for Flow in a Cavity
10X10 Non-Uniform Mesh

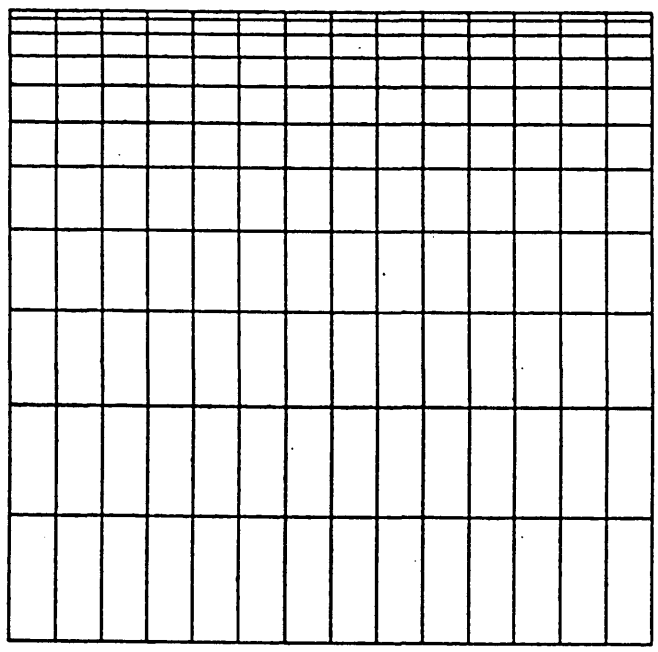

Fig.7.3.7 14X11 Non-Uniform Mesh

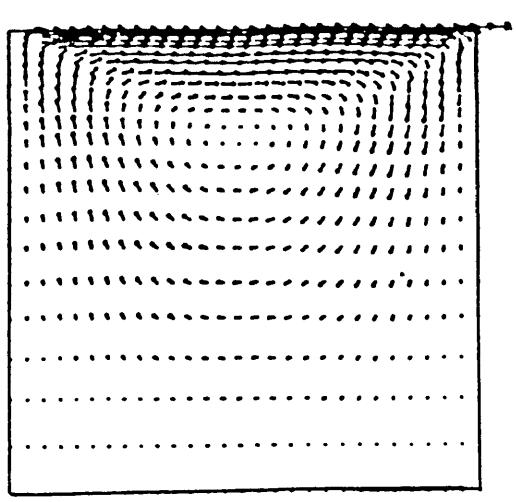

(a) Re=0, Initial Flow Solution

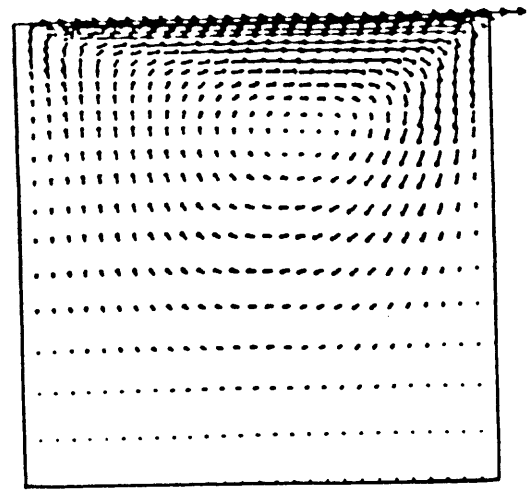

(b) Re=100, n=36

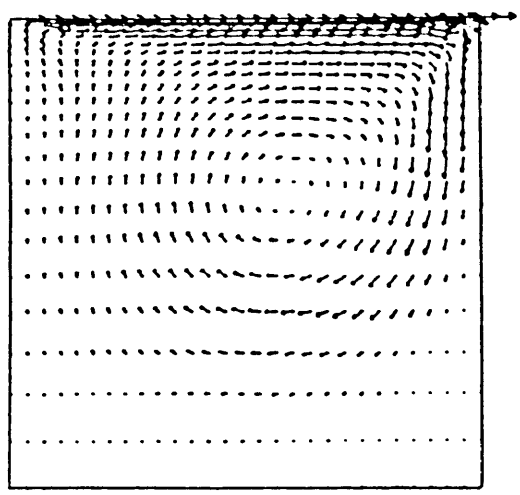

(c) Re=400, n=120

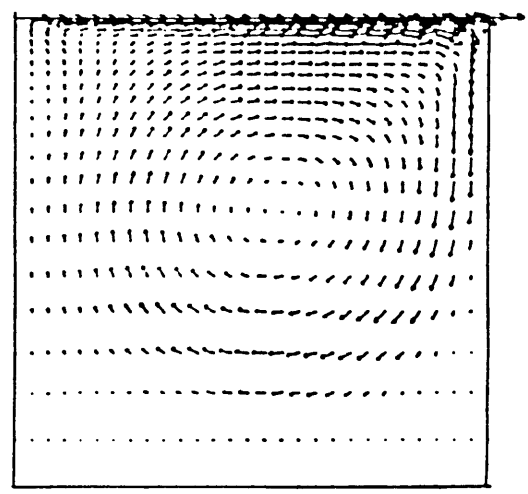

(d) Re=1000, n=220

Fig.7.3.8 Steady-State Flow Solution - Flow in a Cavity, 14X11 Non-uniform Mesh

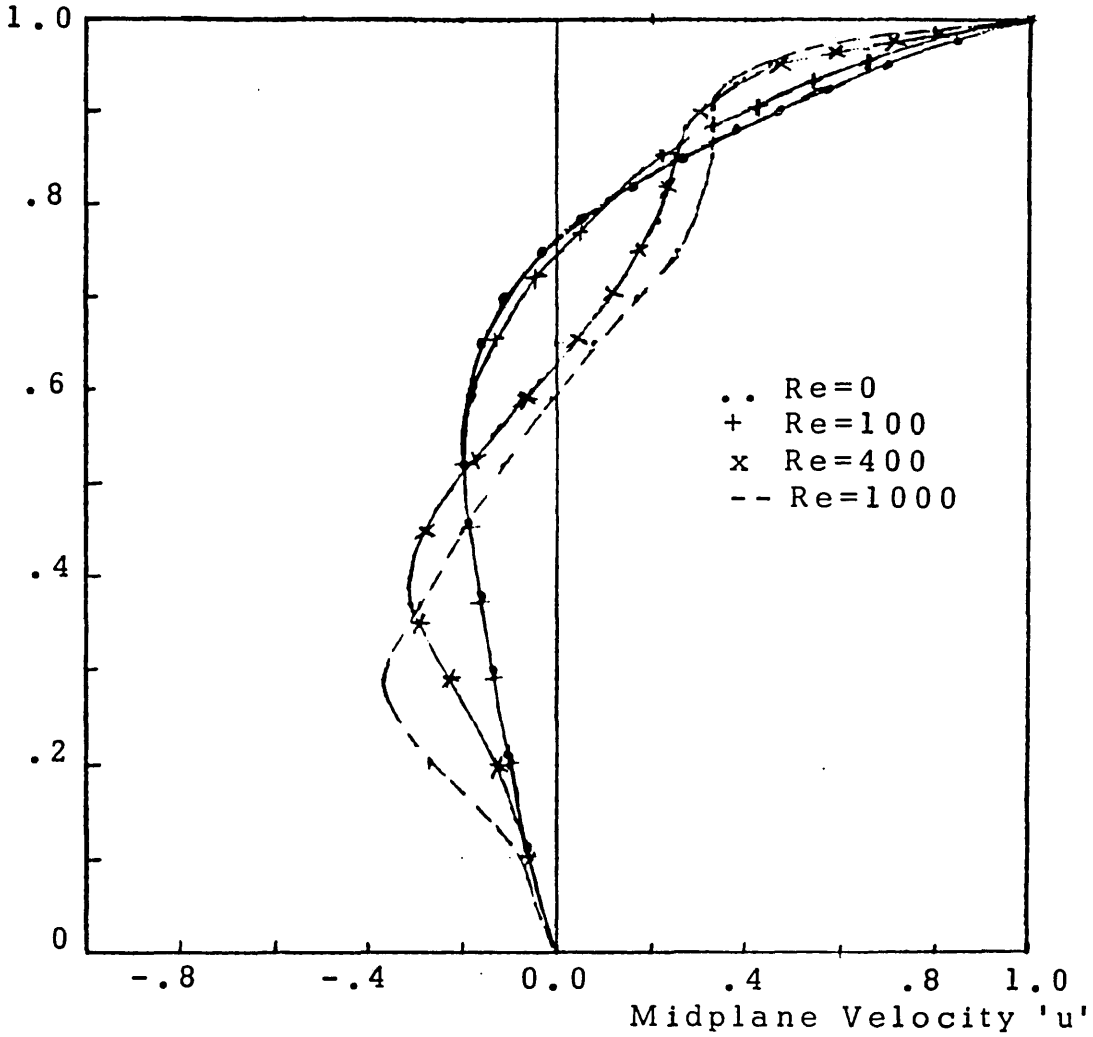

Fig.7.3.9 Midplane Velocity Profiles for Driven Cavity Flows at various Reynolds Number

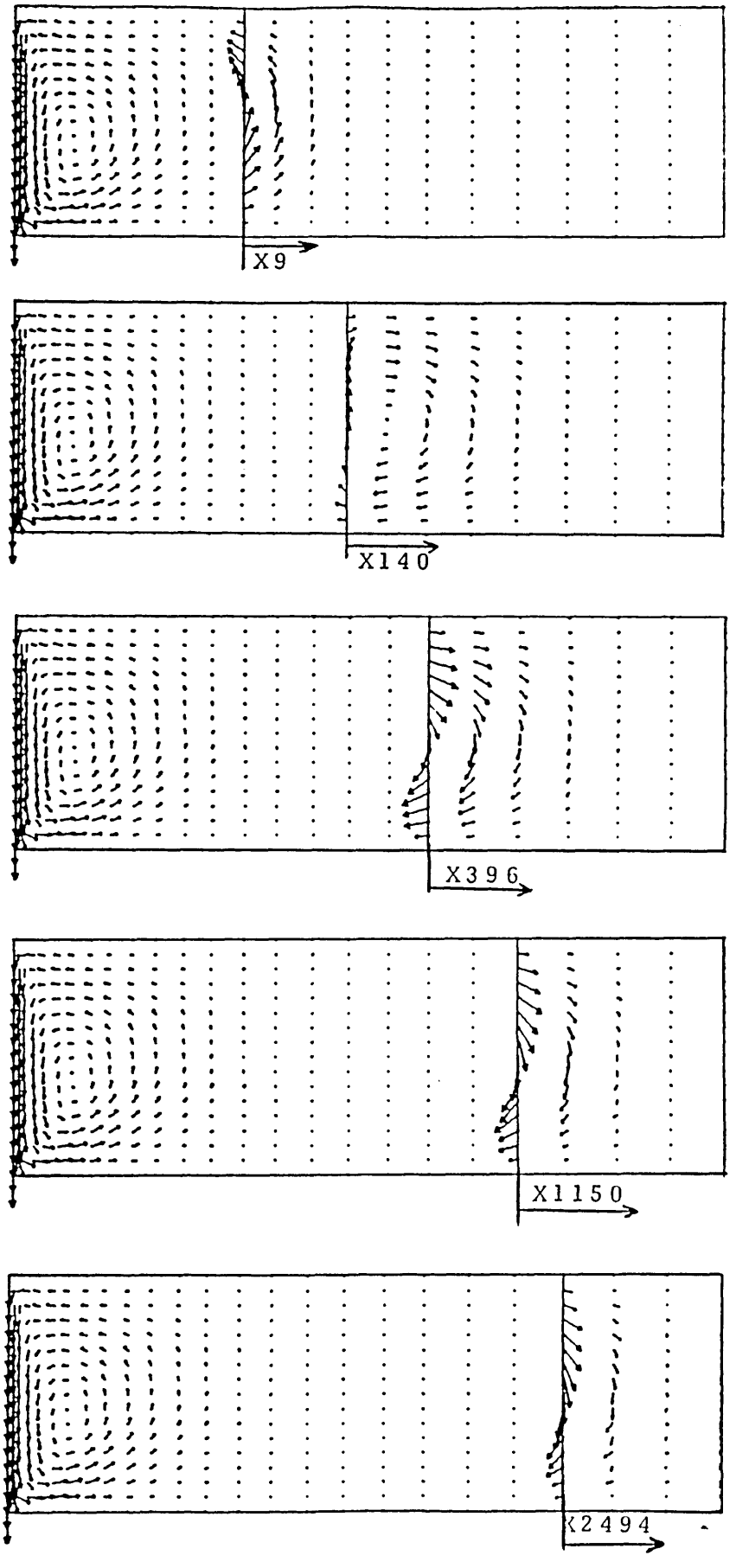

Fig.7.3.10 Flow in a Cavity of Aspect Ratio 3
Velocity Vectors Magnified to see the direction of rotation of secondary eddy

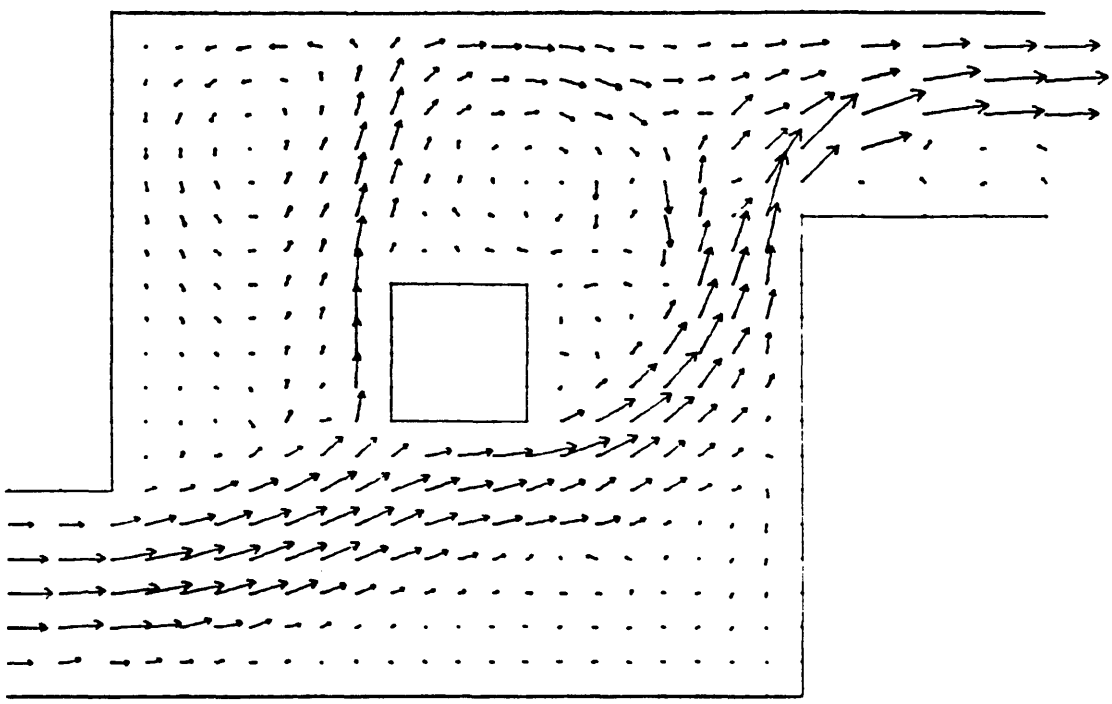

Fig.7.3.11 Flow over a Square Obstacle inside a Square Cavity, Re=1000

7.4 Vortex Shedding Behind a Circular Cylinder

As a fluid particle flows towards the leading edge of a bluff cylinder, the pressure in the fluid particle rises from the free-stream pressure to the stagnation pressure. The high fluid pressure near the leading edge impels the developing boundary layers about both sides of the cylinder. However, at high Reynolds number the pressure forces are not sufficient to force the boundary layers around the backside of a bluff cylinder. Near the widest section of the cylinder, the boundary layers separate from each side of the cylinder surface and form two shear layers that trail aft in the flow. These two shear layers bound the wake. Since the innermost portion of the shear layers moves much more slowly than the outermost portion of the layers which are in contact with the freestream, the free shear layers tend to roll up into discrete, swirling vortices.

Any structure with a sufficiently bluff trailing edge sheds vortices in a subsonic flow. At very low Reynolds number based on the cylinder diameter the flow does not separate. As the Reynolds number is increased, a pair of fixed vortices is formed immediately behind the cylinder. As the Reynolds number is further increased, the vortices elongate until one of the vortices breaks away and a periodic wake and a staggered vortex street is formed. Up to Reynolds number of approximately 150, the vortex street is laminar. At about Re=300, the street is turbulent and

it degenerates into fully turbulent flow beyond approximately 50 diameters downstream of the cylinder. The Reynolds number range of 300 to approximately $3x10^5$ has been called the subcritical range, because it occurs prior to the onset of turbulent boundary layer which occurs at a Reynolds number of approximately $3x10^5$ (fig.7.4.15), depending upon the freestream turbulence and surface roughness. In the subcritical Reynolds number range, the shedding occurs at a well defined frequency. The Strouhal number (S) is the constant of proportionality between the predominant frequency of vortex shedding (f_s) and the freestream velocity (u) and cylinder width (D)

$$S = f_s D/u \qquad (7.4.1)$$

The general relationship between S and Re is well documented (fig.7.4.16), but absolute values of S also depend upon cylinder surface roughness, length/diameter ratio, turbulence levels, proximity effects and velocity profiles (103).

The earlier work on vortex shedding behind a circular cylinder includes that of Jordan and Fromm (95), Tritton (96), Swanson and Spaulding (97) using the Finite Difference Method. Tritton showed that the vortex shedding occurs at a Reynolds number of around 100. Glowniski et al

(98) and Bristeau et al (99) have briefly presented some vortex shedding results using primitive variables and a least squares finite element method. In the field of finite element method Smith and Brebbia (100) computed vortex shedding using the stream-function vorticity approach. Vortex shedding behind a circular cylinder using the finite element method and primitive variables is presented by Gresho et al (101). The recent work by the same author (90) uses a modified finite element method as detailed in ref. 91. Detailed results are presented for Reynolds number up to 400. A detailed study for this problem is carried out by Kawahara and Hirano (102) using a finite element method and a two step explicit scheme. Results are presented for $Re=50, 1.5x10^{2}, 1.5x10^{4}, 1.5x10^{5}$ on a mesh of 4718 triangular elements and 2428 nodes. The most accurate and detailed results for this problem would seem to be that of ref.95 where more than 12000 nodes are used.

To analyse the flow around a circular cylinder a finite element mesh of 114 nine-noded elements giving a total of 508 nodes (Fig.7.4.2) was used. Although accurate solutions without any ripples have been obtained for low Reynolds number laminar flows using coarse meshes (around 400 nodes), a finer mesh gives a better representation of the flow when presented in the form of velocity vector plots. The computational domain extends 3.5 cylinder

diameters above, below and upstream of the cylinder and about 12 diameters downstream. The boundary conditions are symmetric as shown in fig.7.4.1. Asymmetry is introduced by using a slightly different mesh density in one half along the line of symmetry. In figure 7.4.2, the row of elements along the top of the cylinder are different in size compared to the elements in the adjacent rows below the cylinder. Also downstream of the cylinder and along the centreline, the elements below the centreline are slightly smaller in size than the elements in the row above the centreline. These differences are all small and are not obvious in the mesh plot. This helps to cut down on the "gestation time", since for a completely symmetric mesh, the non-symmetric vortex shedding is initiated by rounding errors in the solution. Using a symmetric coarse mesh also leads to shedding, but the process takes longer. A coarse mesh is used downstream of the cylinder which also introduces asymmetry and acts as a triggering mechanism for vortex shedding. Asymmetry can also be introduced by changing the loading to be non-symmetric for a few timesteps and then returning to the actual load. This is demonstrated later using the example of flow over a diamond shaped object (fig.7.4.14). The input flow velocity below the centreline was increased for a single timestep and then returned to normal. This was found to be sufficient to initiate vortex shedding, and can be clearly seen in the velocity vector plots at 270 and 300 timesteps

(fig.7.4.14). As we are mainly interested in the vortex shedding phenomenon, every effort is made to cut down on the "gestation time" and hence save some computer time.

A non-uniform mesh was used in this example. The critical region is that which is next to cylinder surface i.e. the boundary layer region and upstream of cylinder where the flow velocities and pressures are rapidly changing. A coarse mesh upstream of the cylinder resulted in the appearance of upstream ripples. The diameter of the cylinder, the inlet velocity and the dynamic viscosity are taken as unity while the value of density is chosen to obtain the desired Reynolds number (that is this example has arbitrary units). The timestep is based upon the stability limit and chosen using equation (2.49). For this particular example $\Delta t=0.1$.

Five cases of flow for the Reynolds numbers of 100,400,1000,5000, and 10000 were computed. For each case the linear Stokes flow solution for Reynolds number of the order of zero is taken as the initial solution. Velocity vector plots for a few shedding cycles and starting from the initial conditions are shown in figure 7.4.3 for laminar flow at 40 timestep intervals. The flow Reynolds number in this case is taken as 100. A non-symmetric mesh is used in this case and the higher Reynolds number cases to initiate vortex shedding. From fig.7.4.3 it can be

seen that the flow pattern is identical above and below the centreline that is, it is symmetric until 40 timesteps. However, from the velocity vector plot for n=80, the flow is no longer symmetric along the centreline. (In an equivalent run using fully symmetric mesh and Re=100, the flow was found to be symmetric until about 120 timesteps, and only after this time did the shedding phenomenon start.) The recirculation region above the centreline is longer than the one below the centreline and has started to move further downstream of the cylinder. After about 200 timesteps the formation of vortices and their alternate shedding from the top and bottom of the cylinder can be clearly seen. As a result of this shedding the flow downstream of the cylinder oscillates, and these oscillations can be seen in the velocity vector plots. The horizontal and vertical velocity, eight diameters downstream of the cylinder (u_8 and v_8) is plotted against time in figure 7.4.4. As vortices are shed in the flow, the flow oscillates downstream of the cylinder. The vertical velocity component oscillates at the same frequency as the vortex shedding, however, the horizontal component oscillates at twice the shedding frequency. The amplitude of oscillation is increasing in figure 7.4.4, which indicates that the flow has not quite reached a steady-state. The time period for one complete shedding cycle can be estimated from figure 7.4.4b. This is the time taken to shed one vortex

from the top and one from the bottom of the cylinder. From the time period τ, the Strouhal number is calculated and compared with other numerical and experimental values for this Reynolds number in figure 7.4.16. The lift and drag forces are also calculated by summing the interelement forces for nodes along the surface of the cylinder. From the values of lift 'L' and drag 'D' forces the lift coefficient and the drag coefficient are evaluated using the following equations.

$$\text{Drag coefficient } C_D = \frac{D}{\frac{1}{2}\rho u^2 A} \qquad (7.4.2)$$

$$\text{Lift coefficient } C_L = \frac{L}{\frac{1}{2}\rho u^2 A} \qquad (7.4.3)$$

where ρ is the density

u is the inlet velocity

A is the cross-sectional area of the cylinder

These values of lift and drag coefficients are plotted against the timesteps in fig.7.4.5 , for a complete shedding cycle. The lift coefficient C_L, oscillates at the shedding frequency and exhibits an essentially steady oscillation. The drag coefficient at this Reynolds number is increasing with time and does not show any oscillatory behaviour until 300 timesteps. The value of u_g ,v_g and C_D

C_L for Re=400 are plotted in figure 7.4.7, 7.4.8 and for Re=1000 in figure 7.4.10, 7.4.11. The amplitude of oscillation has increased as the Reynolds number is increased form 100 to 400. Also the drag coefficient at Re=400 and 1000 can be seen to oscillate at twice the frequency of oscillation of the lift coefficient. The lift coefficient oscillates at the shedding frequency. The oscillation is not steady which is perhaps because of the turbulent nature of the flow at this Reynolds number. Also there is a continous rise in the drag coefficient which probably indicates that the flow has not yet reached a steady-state.

As the flow Reynolds number is increased, but still using the same mesh as before, some ripples start to appear upstream of the cylinder. The vortex pattern downstream of the cylinder is not as clear for the higher Reynolds number runs, when compared to the Reynolds number of up to 400. A complete cycle of shedding is shown in figure 7.4.6 for Re=400, and also for Re=1000 (fig.7.4.9) and Re=5000 in figure 7.4.12 . At Re=400 the recirculation region downstream is clearly visible, although it is much more compressed and near to the cylinder. The flow downstream of the cylinder is oscillating as the vortices are shed in the flow, and these oscillations are much larger in amplitude than the one at Re=100 flow. The recirculation region downstream gets more and more complex as the flow

Reynolds number is increased and this can be seen in the velocity vector plots (fig.7.4.9 and fig.7.4.12). This is to be expected as the vórtex street is fully turbulent at this Reynolds number. The oscillations in the flow downstream are still seen at high Reynolds number, and from these oscillations the Strouhal number, the lift coefficient and the drag coefficient are calculated and compared with the results of other authors (103) in figure 7.4.16 (shown as crosses), and figure 7.4.17.

From the results in figure 7.4.16 and figure 7.4.17 we observe that:

(i) The computed Strouhal numbers for the four Reynolds numbers (shown as crosses in fig.7.4.16) are in good agreement with the experimental results of ref.103.

(ii) Drag coefficient values for Re=100 and 400 are in reasonable agreement with the results of Jordan and Fromm (95) given as 1.5 for Re=100 and 1.2 for Re=400. The values of C_L calculated in this work are lower than the ones in ref.90 . (Experimental values for C_L for the above Reynolds number are difficult to find.)

(iii) Values of u_s v_s and u_{max} for Re=100 and 400 are presented in ref.90. These values are somewhat higher than the ones obtained in this work. A modified FEM with mass

lumping and 1-point quadrature to generate all matrices is used in ref.90.

The values of u_g, v_g, u_{max}, C_D and C_L are expected to be higher, once the flow has reached a steady-state. A constant increase in the amplitude of oscillation is noticed in figure 7.4.4 to figure 7.4.11, indicating that the oscillation and hence the flow is still to reach a steady-state.

Figure 7.4.14 shows the vortex shedding behind a diamond at Re=150. The problem definition and boundary conditions are shown in figure 7.4.13a. Because of the sharp corners involved in this case, a finer mesh is required near the diamond and upstream of it to resolve the sudden changes in geometry and hence the flow characteristics. The mesh used consisted of 134 elements and 581 nodes (fig.7.4.13b). Vortex shedding was initiated by a sudden change in loading for one timestep in one half of the mesh and then returning to normal loading. The vortex shedding started soon after this load change.

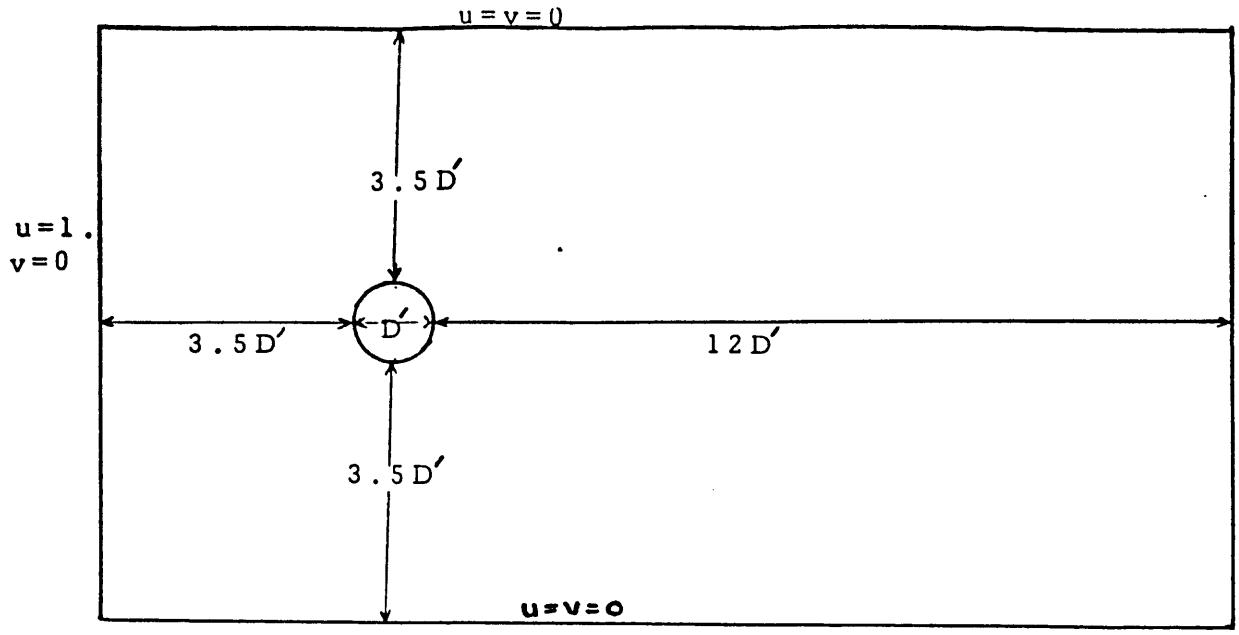

Fig.7.4.1 Problem definition and Boundary conditions
Flow around a circular cylinder

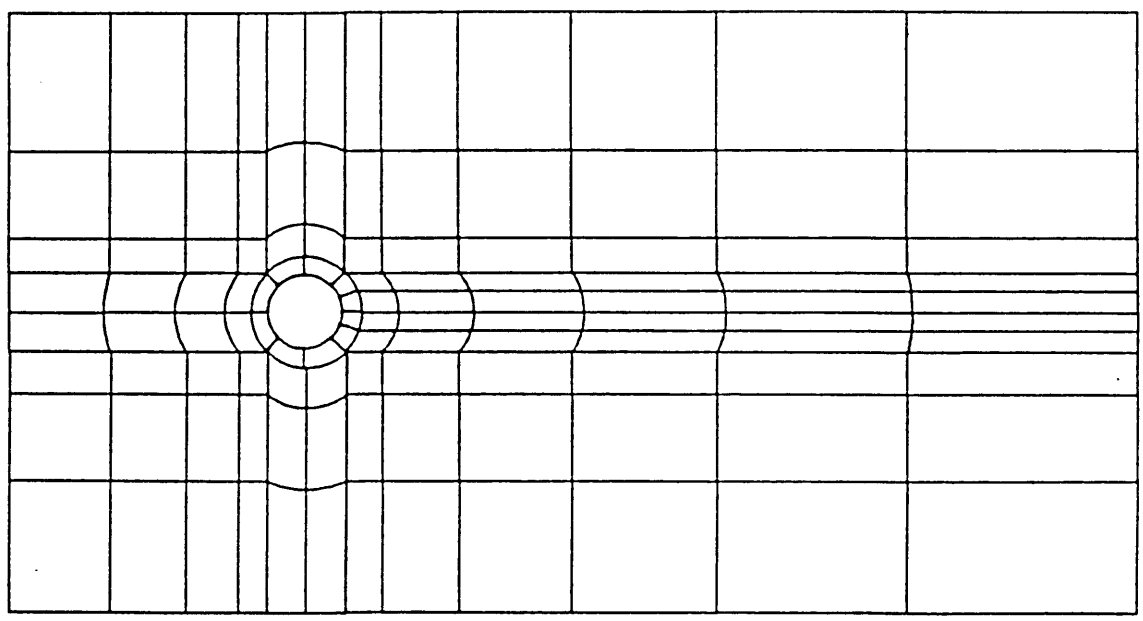

Fig.7.4.2 Finite Element mesh - Flow around a
circular cylinder 114 Elements, 508 Nodes

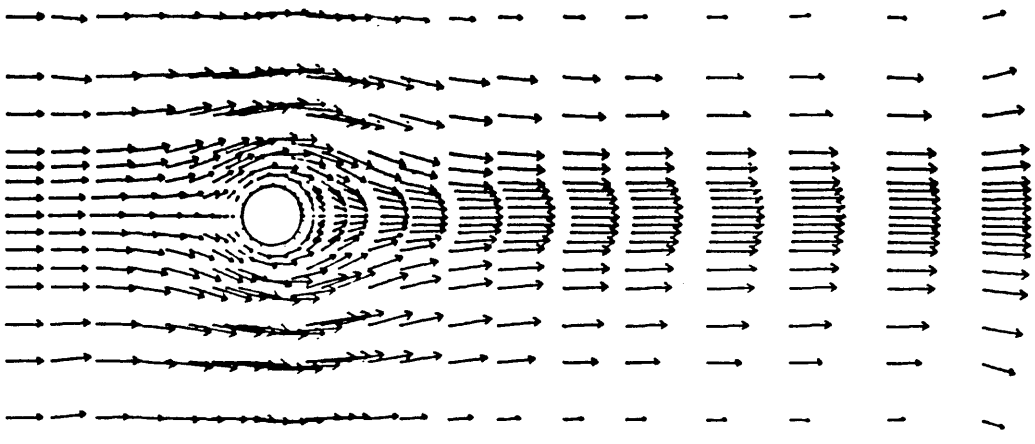

n=0 Initial Flow Solution

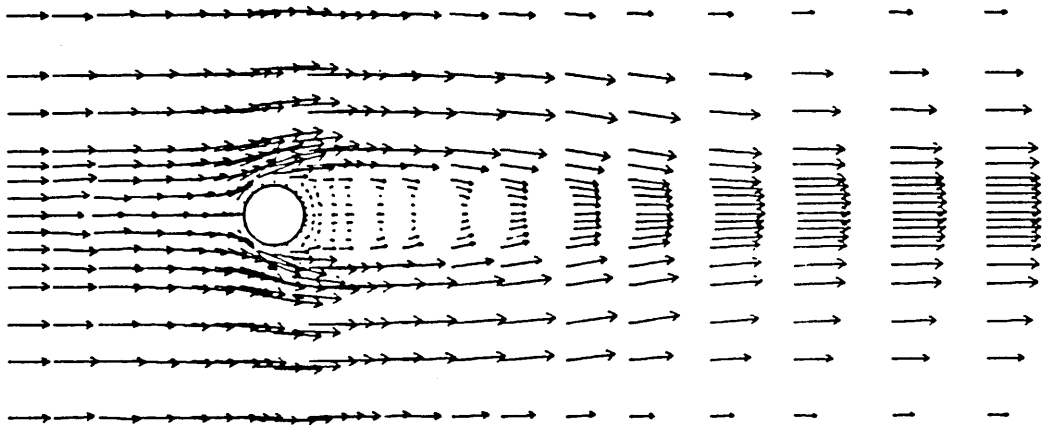

n=40

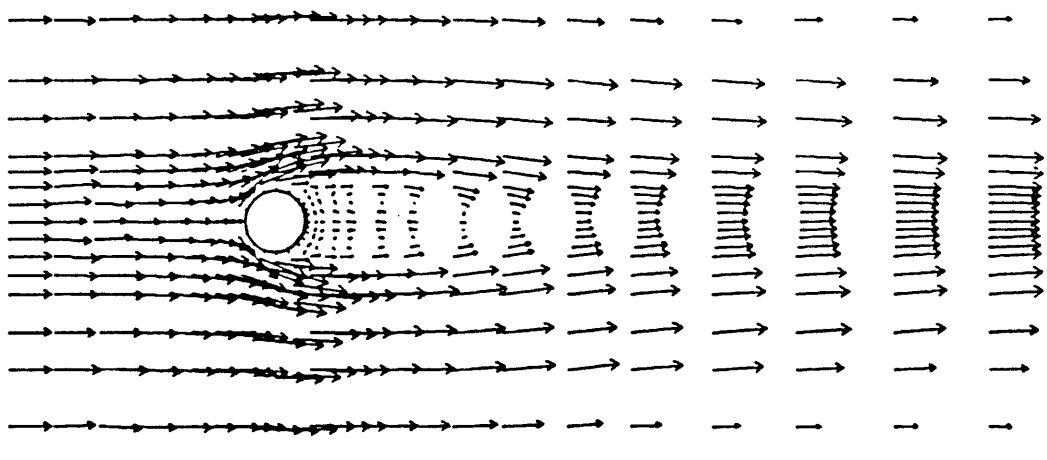

n=80

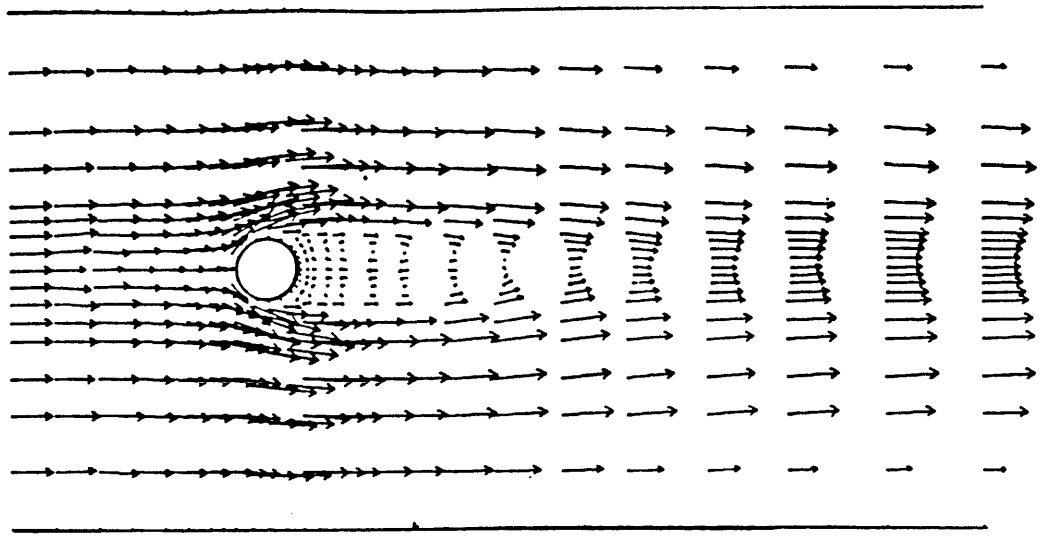

n=120

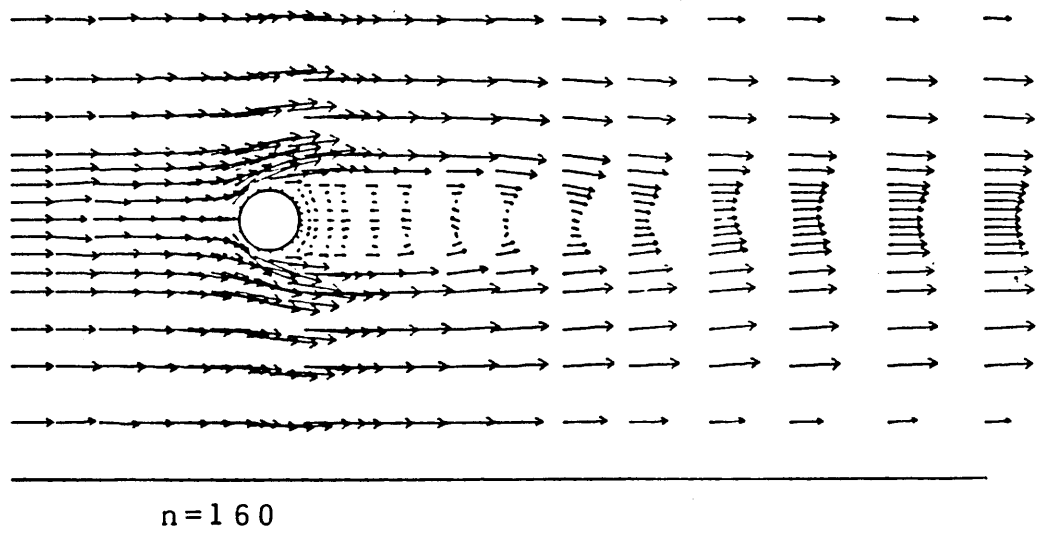

n=160

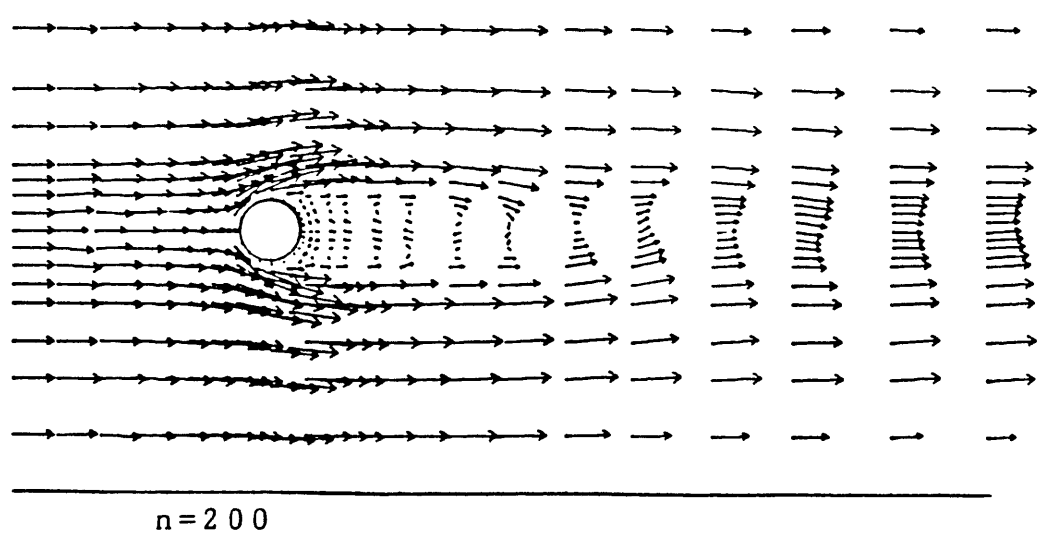

n=200

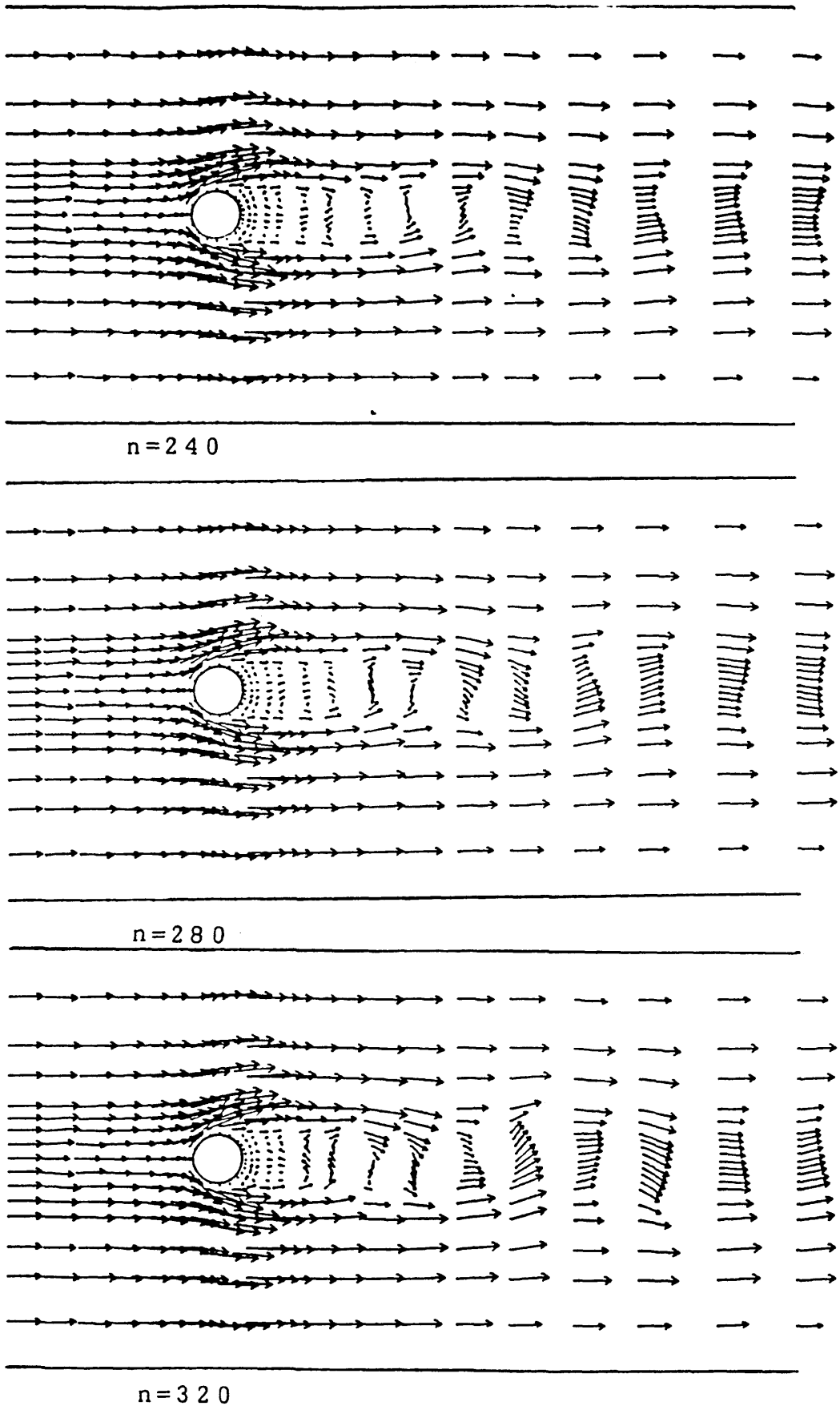

Fig.7.4.3 Velocity vector plots - Vortex Shedding behind a circular cylinder Re=100

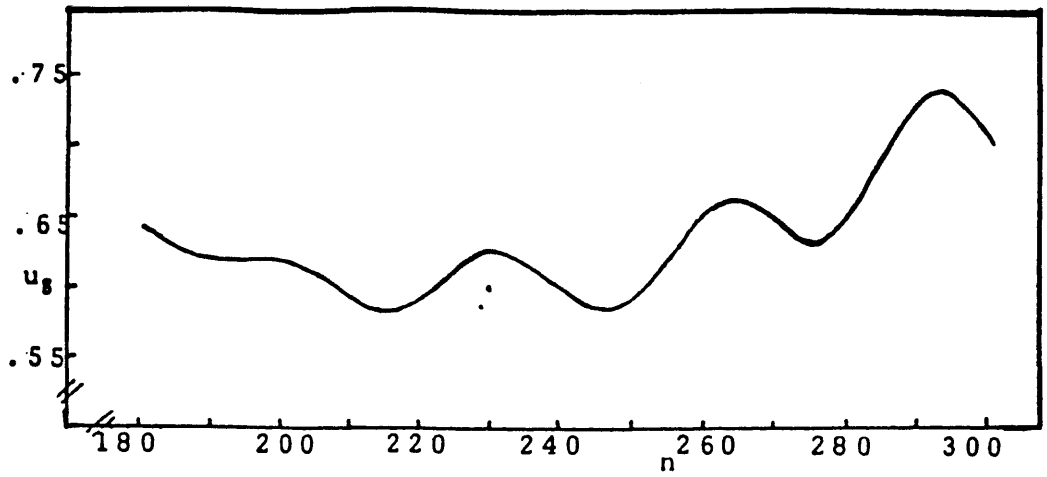

Fig.7.4.4a Time variation of Horizontal Velocity 'u_g Re=100

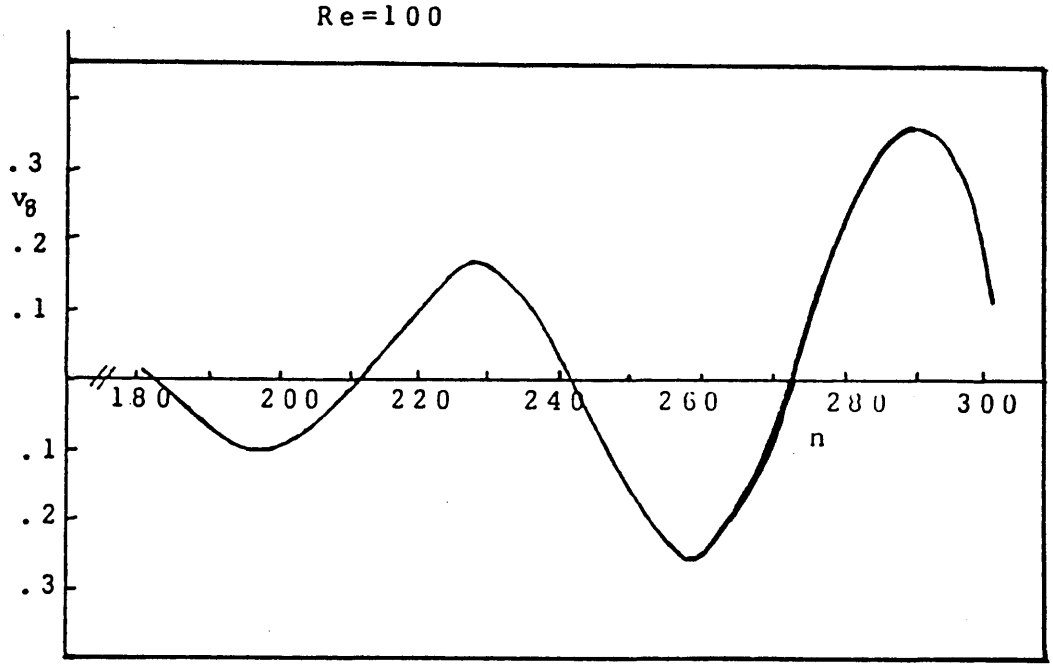

Fig.7.4.4b Time variation of Vertical Velocity 'v_g' Re=100

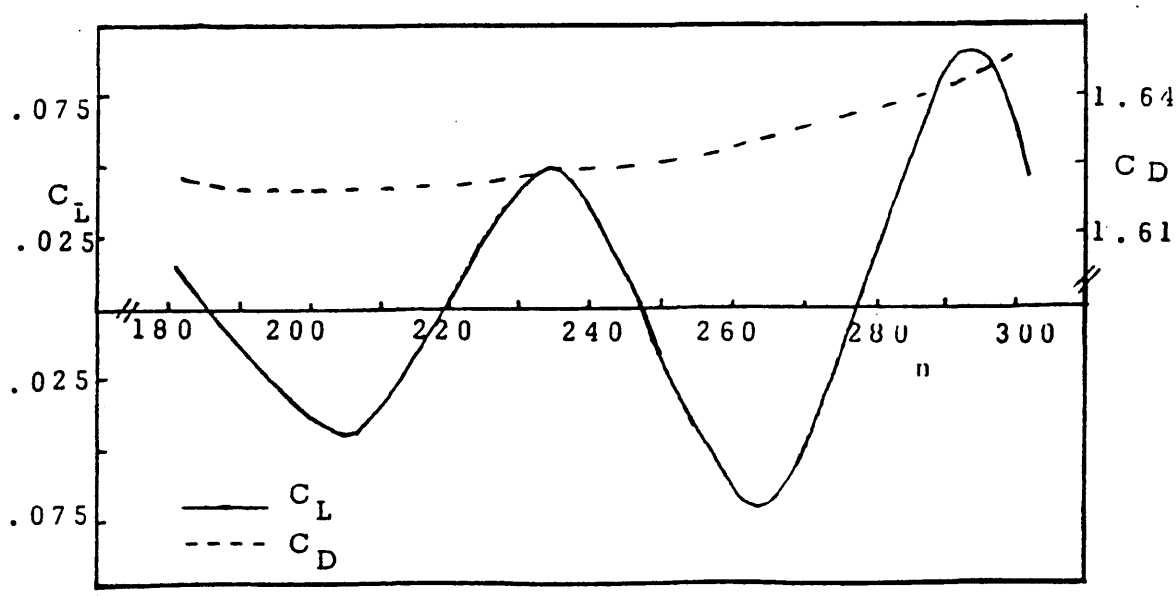

Fig.7.4.5 Time variation of C_L and C_D Re=100

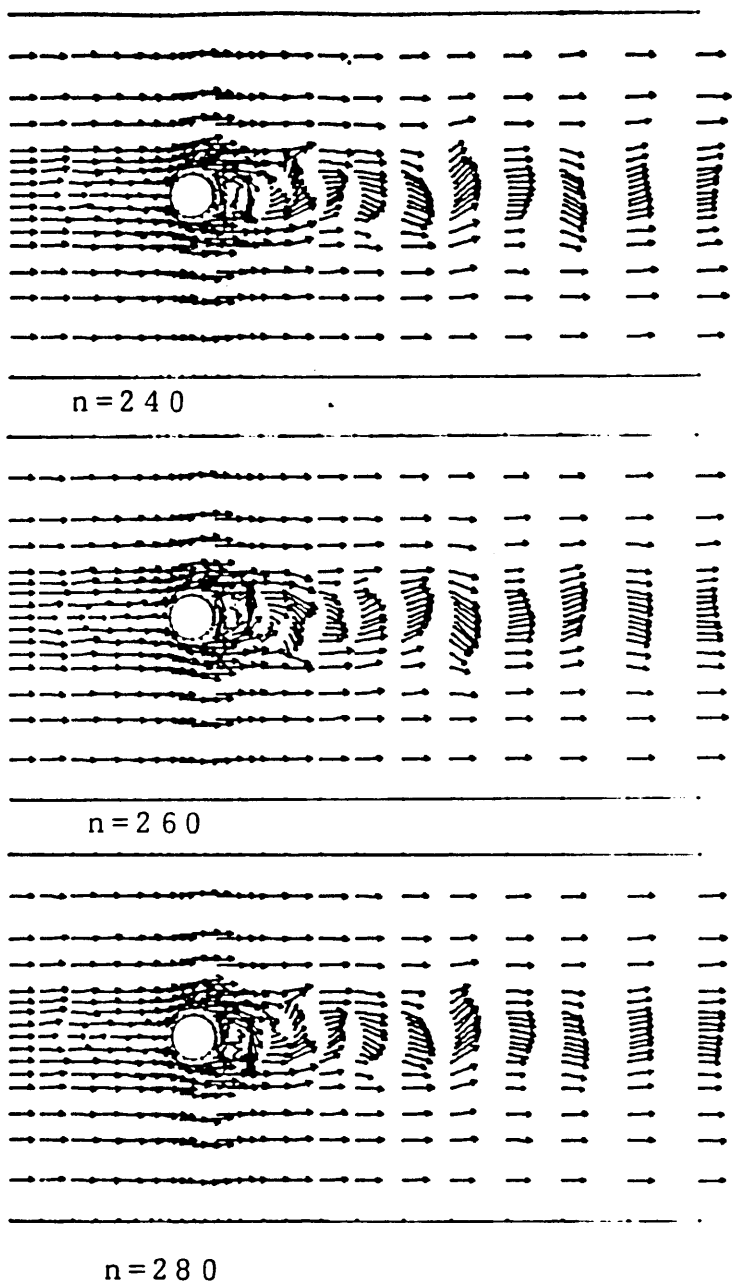

Fig.7.4.6 A complete cycle of Vortex Shedding behind a circular cylinder Re=400

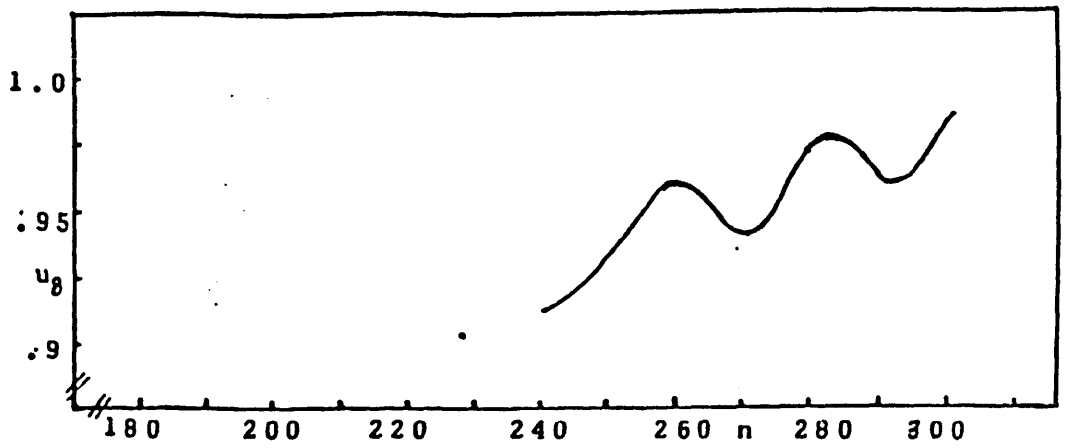

Fig.7.4.7a Time variation of 'u_δ' Re=400

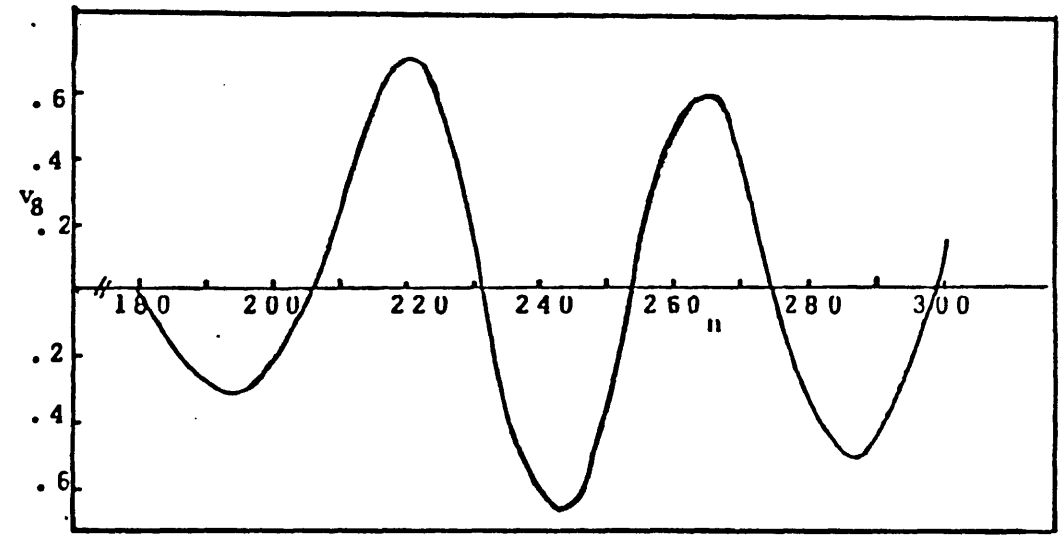

fig.7.4.7b Time variation of 'v_δ'
Re=400

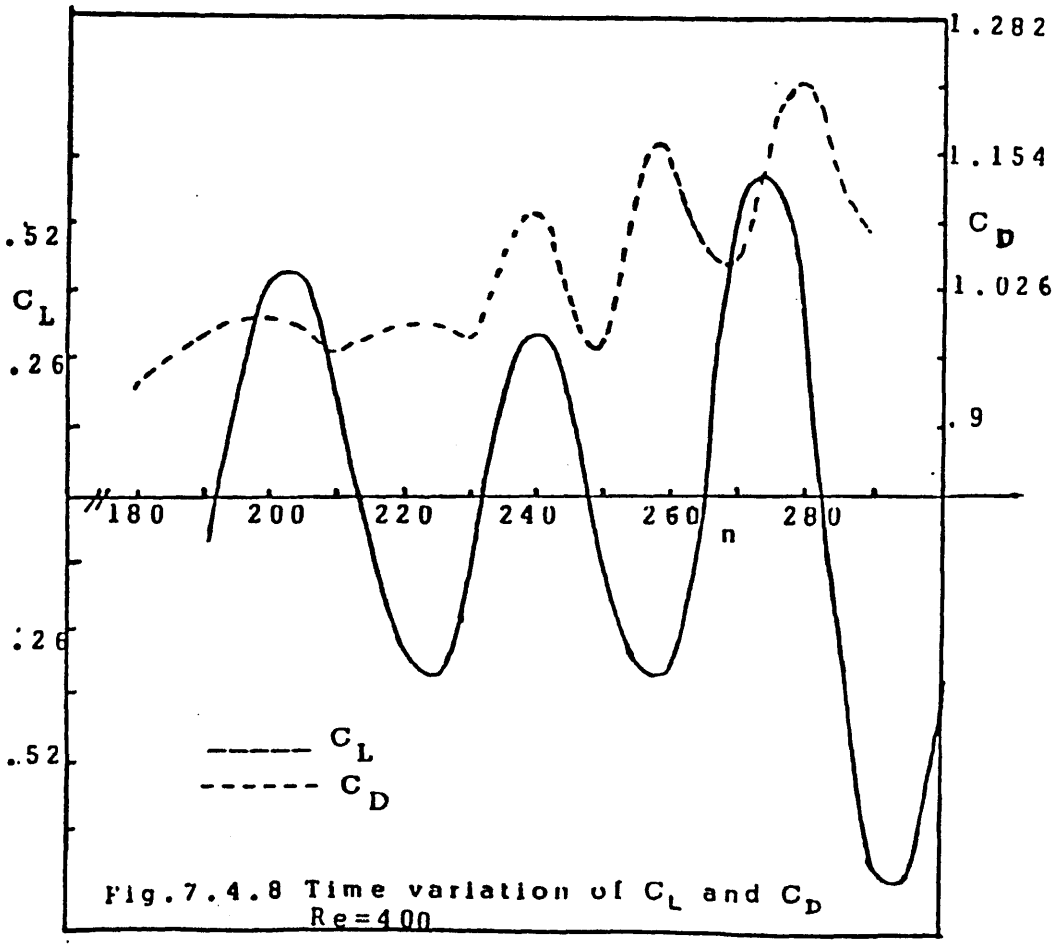

Fig.7.4.8 Time variation of C_L and C_D
Re=400

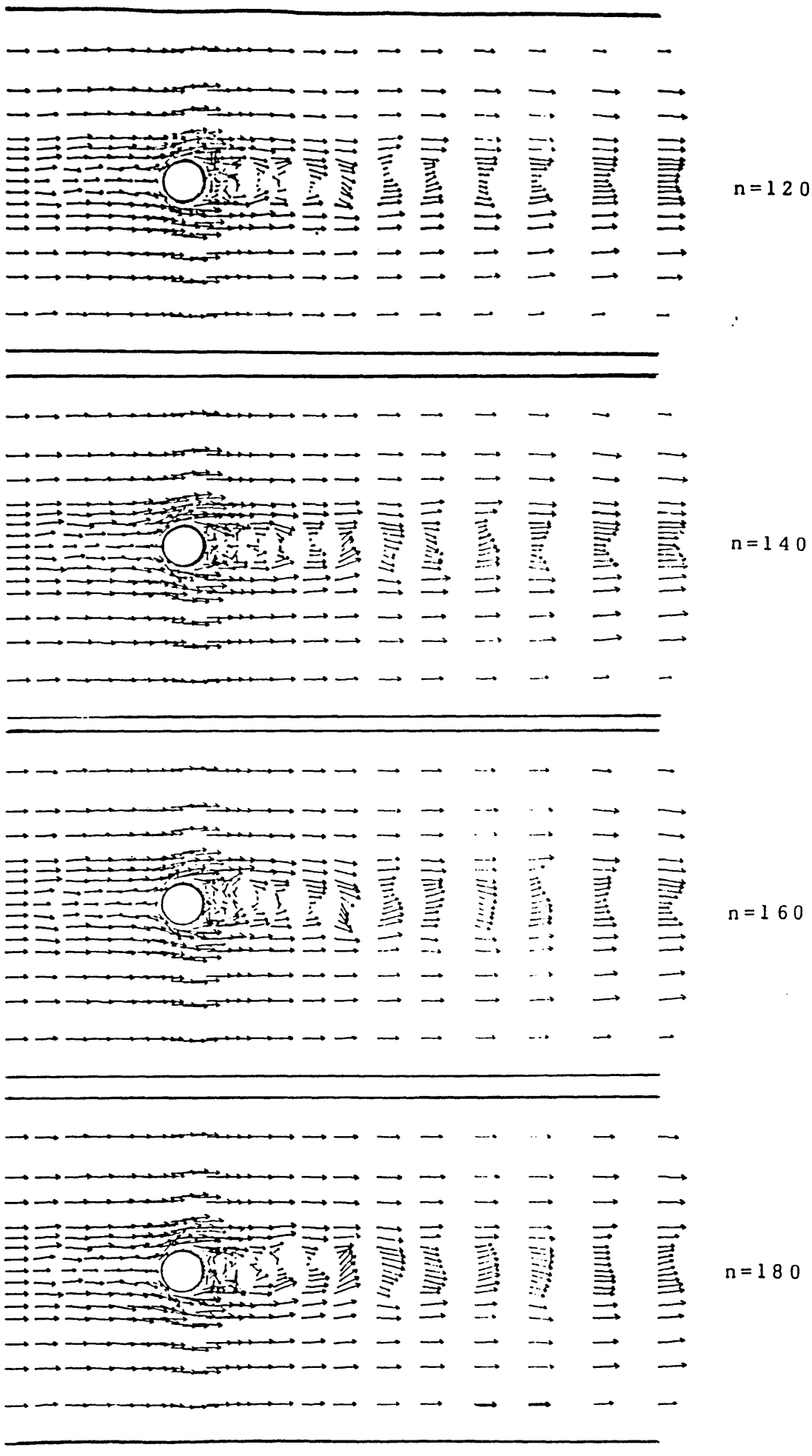

Fig. 7.4.9 Vortex Shedding behind a circuler cylinder
Re = 1000

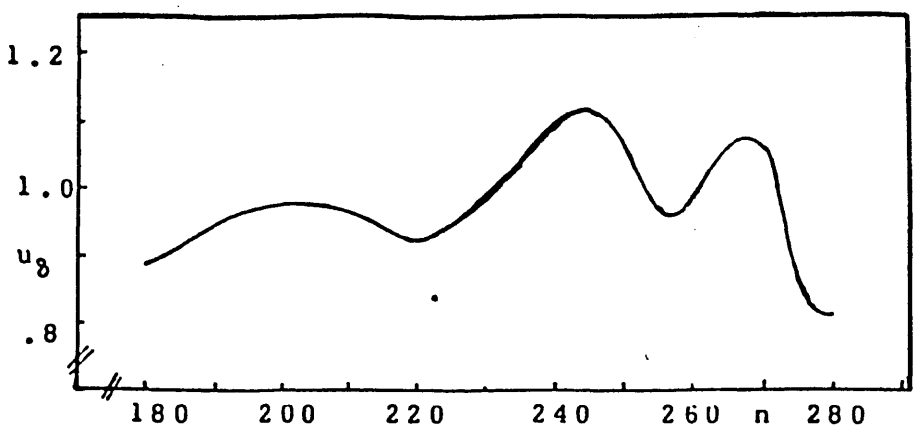

Fig.7.4.10a Time variation of 'u_8' Re=1000

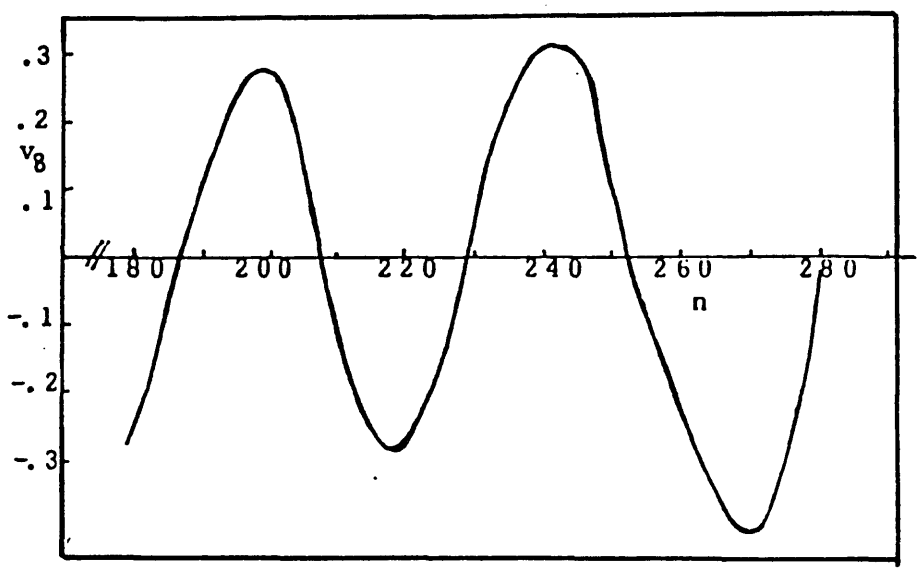

Fig.7.4.10b Time variation of 'v_8' Re=1000

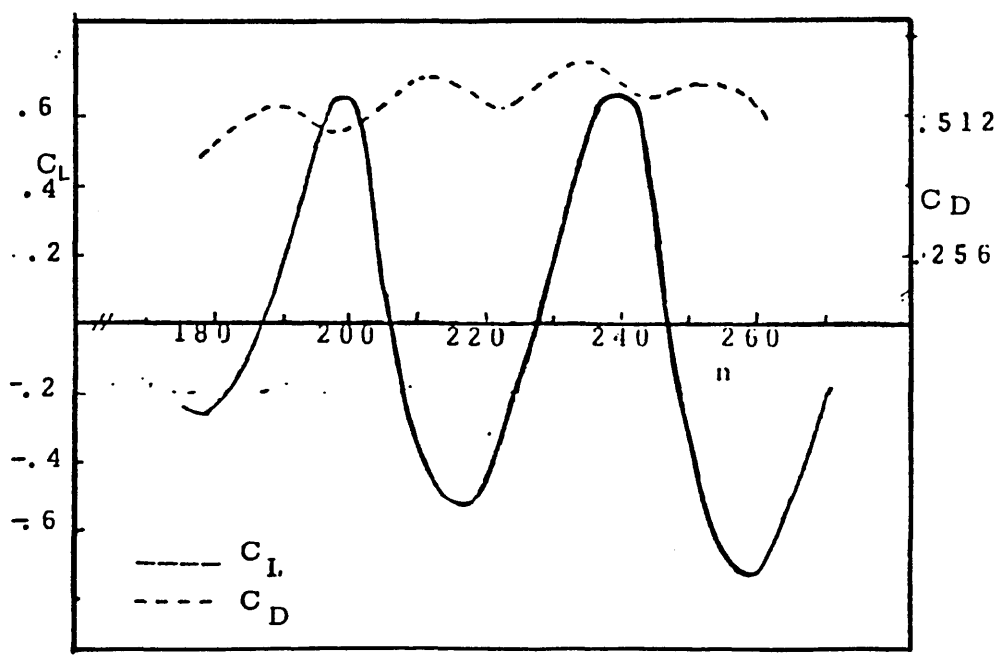

Fig.7.4.11 Time variation of C_L and C_D
Re=1000

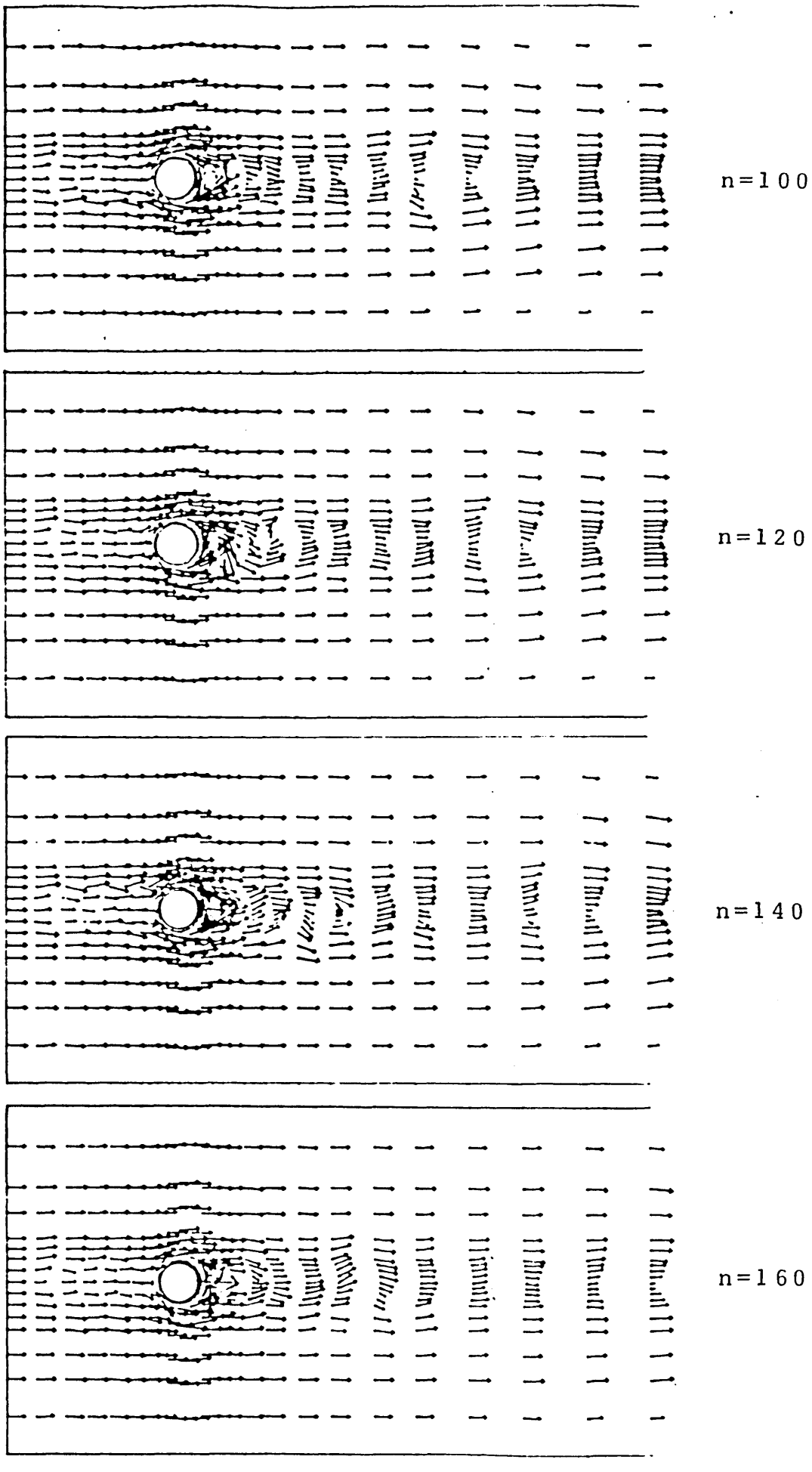

Fig.7.4.12 Velocity Vector Plots, Flow around a Circular Cylinder, Re=5000

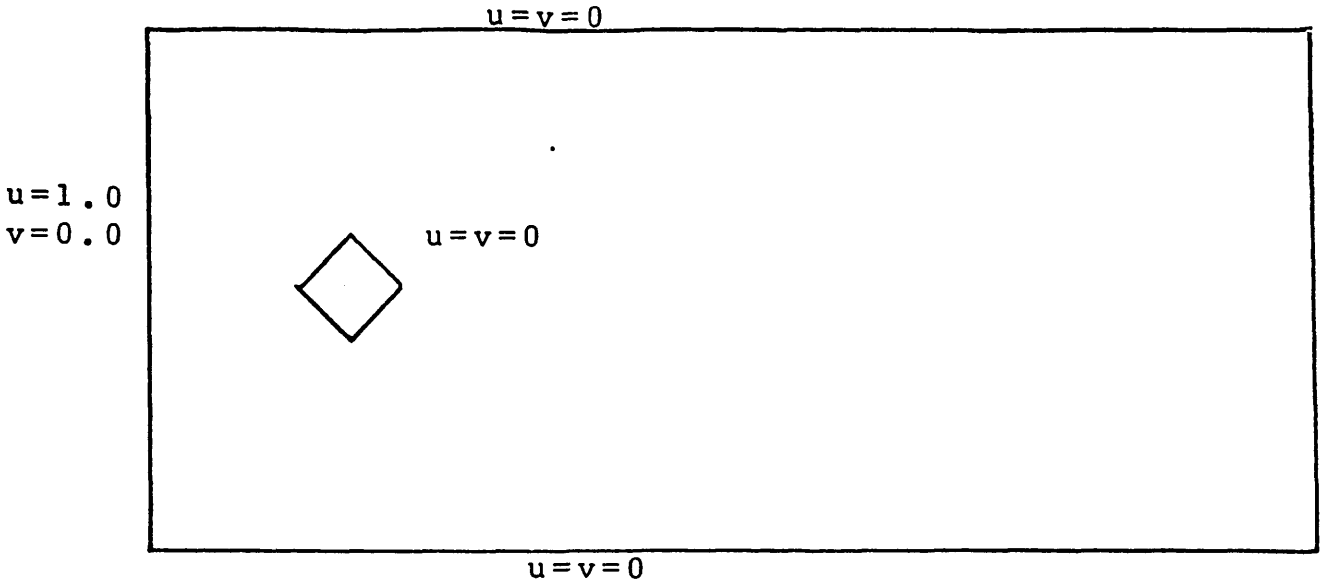

Fig.7.4.13a Flow around a Diamond - Problem Definition and Boundary Conditions

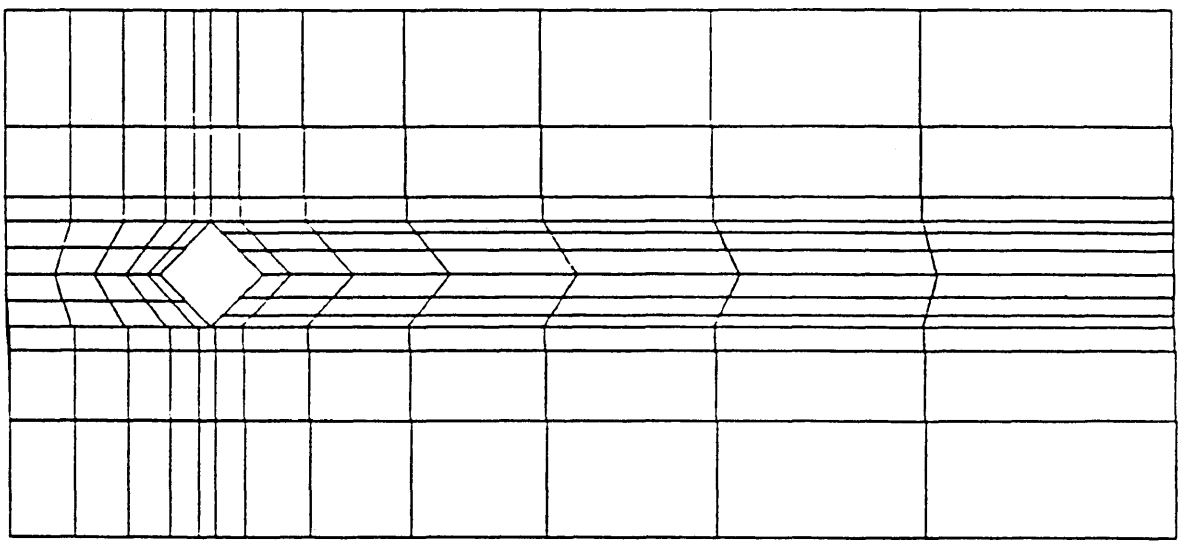

Fig.7.4.13b Finite Element mesh used to analyse the Flow around a Diamond

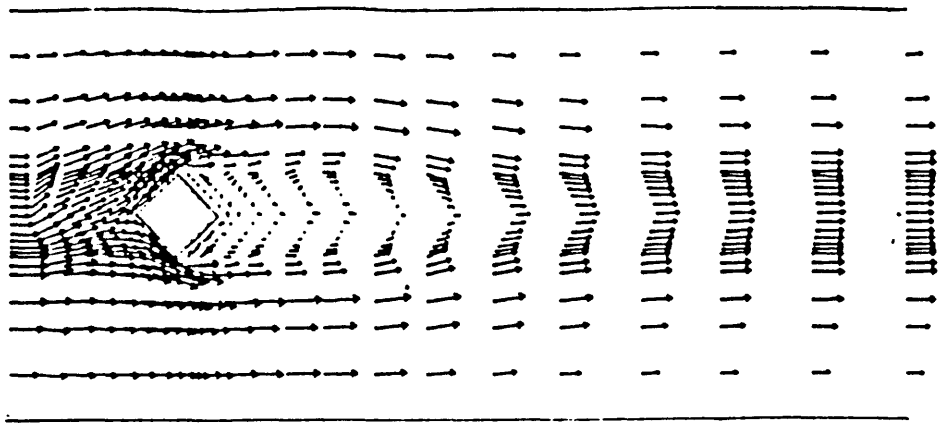

n=210

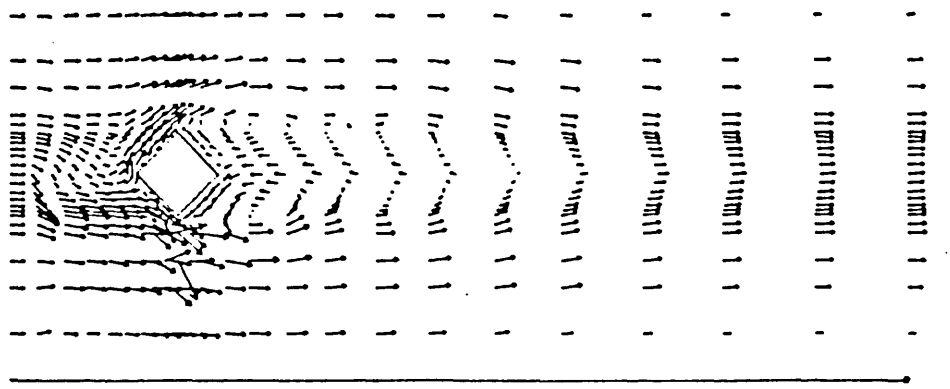

n=240

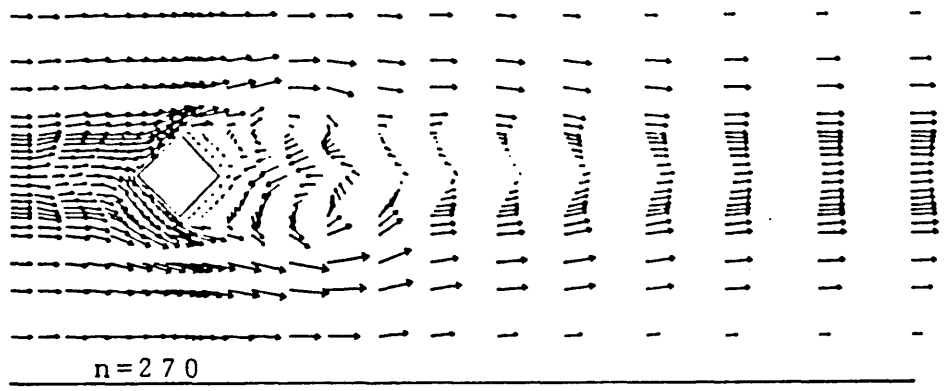

n=270

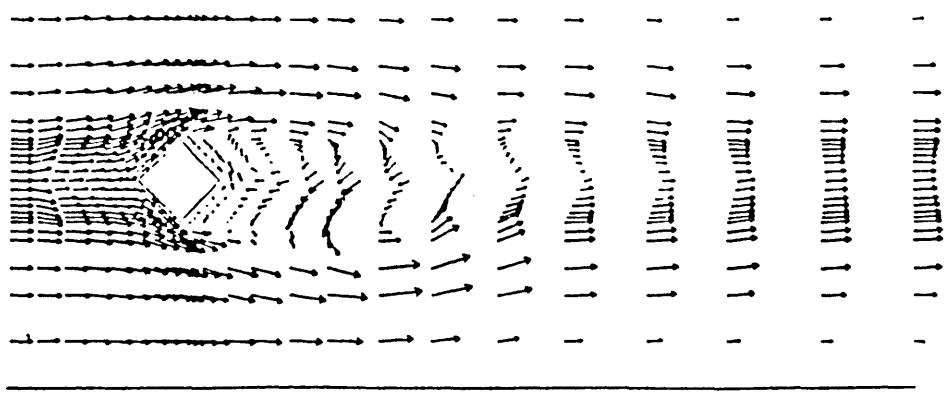

n=300

Fig.7.4.14 Velocity Vector Plots - Flow around a Diamond

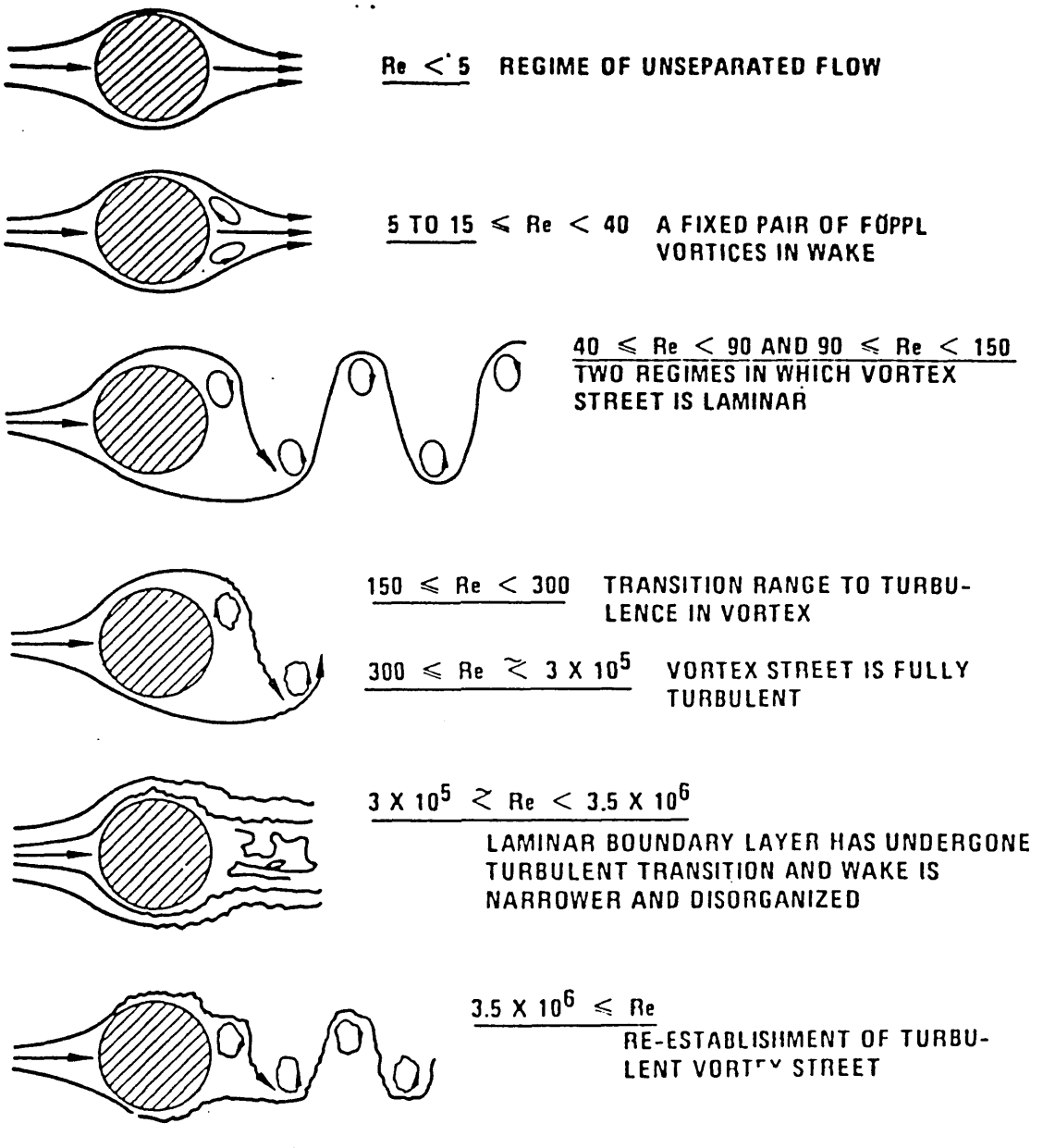

Fig.7.4.15 Regimes of Fluid Flow across Circular Cylinders (132)

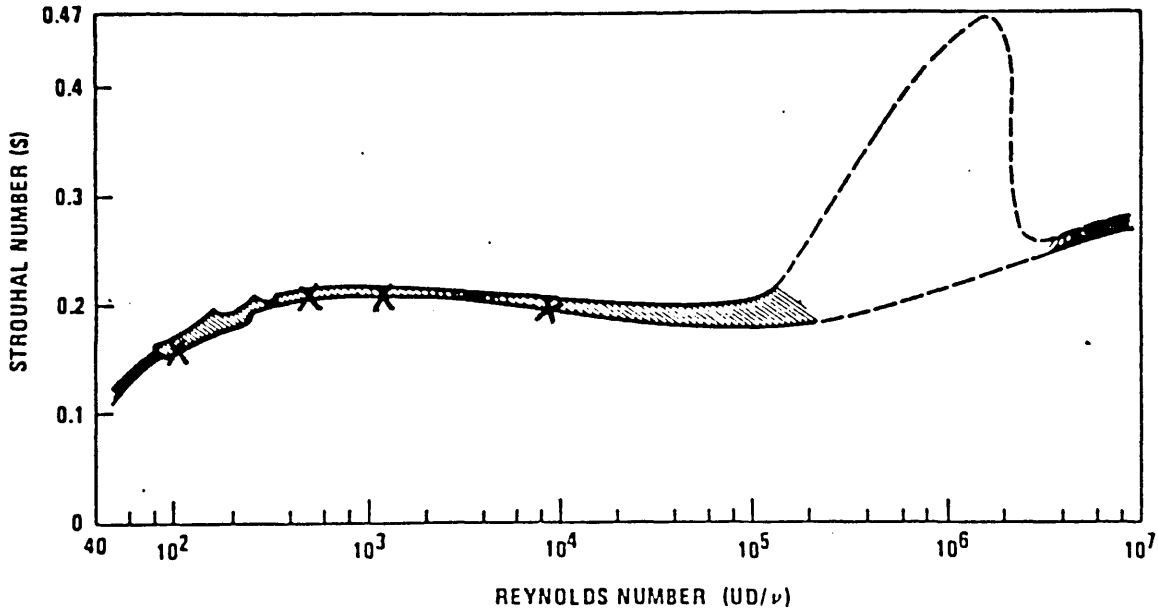

Fig.7.4.16 The Strouhal-Reynolds Number Relationship for Circular Cylinders (103)

Reynolds Number	Period	Strouhal Number	C_D Average	C_D Peak to Peak	C_L Peak to	Range of u_8	Range of v_8	Range of u_{max}
100	6.0	.166	1.6	.023	.16	.6-.7	+.35	1.34-1.37
400	4.7	.21	1.14	.16	1.3	.94-.97	+.7	1.52-1.64
1000	4.5	.22	.56	.076	1.25	.64-1.1	+.35	1.6 -1.80
10000	5.0	.20	.30	.38	1.60	.8-1.16	+.24	1.78-2.02

Fig.7.4.17 Summary of Results - Vortex Shedding behind A circular Cylinder

8. FLOW INDUCED VIBRATION

Flow-induced excitation is a consequence of energy transfer from a fluid to a structure around which the fluid is flowing. The three feedback mechanisms by which the transfer of energy from a fluid to a structure may be amplified and controlled are ; fluid-dynamic, fluid-resonant and fluid-elastic (129). The occurance of flow induced vibration fretting wear in process equipment such as heat exchangers and steam generators account for the majority of the failures due to vibration. There are numerous possible vibration and instability problems caused by flow induced vibrations in nuclear plant and internal components. When a plant is operating at the top end of its capacity, the flow sets up vibrations in the tubes and as the tubes rub against the baffle plates, they rapidly wear away. Dozens of the steam generator tubes at Ringhals 3 reactor in Sweden were found to have worn down to only 10% of their original thickness. Sometimes leakage is caused by the "shake and break" phenomenon, which occurs as a result of the sudden vibration in the tube bundles.

These problems have been discussed extensively in various forums, such as the SMiRT conferences (131), Keswick conferences (133), Karlsruhe conferences (133) and at different ASME meetings (113,130). Failures in the past caused by flow induced vibration have been documented in some detail in ref. 104-107. The progress upto 1979 in the field of instabilities of tube arrays subject to

cross-flow is covered in ref. 108. Since then the analytical developments in this subject are covered in a series of papers (109-113). Experimental studies were also conducted by various investigators to determine the stability constants (114-117), verifying the mathematical models (118), and investigating the detailed flow field around tube arrays (119). The three major flow excitation sources are turbulent buffeting, vortex shedding and acoustoelastic vibration. The random pressure fluctuations exist practically for all flow velocity ranges. Numerous studies have been made on turbulence induced vibration (120). If the turbulence spectrum and spatial correlations in a cylinder array are known, and if the cylinder oscillations do not affect the flow field, it is possible to calculate the cylinder response from the basic equation of motion. However, the information on the level of turbulence, its spectral distribution and scale is not known in general.

The characterisation of vortex shedding across a single cylinder and synchronisation of a single cylinder with vortex shedding are fairly well understood (120,121), although analytical solution of the detailed interaction process remains difficult (122). The problem of two cylinders in crossflow also has been discussed in some detail (123). However, for the case of cylinder arrays, the basic question of the existance of vortex shedding has

not yet been answered satisfactorily. Strouhal numbers associated with vortex shedding for in-line and staggered tube arrays have been collected from different sources (124). Parameters such as cylinder arrangement, cylinder pitch, upstream turbulence and vibration amplitude are known to affect the periodicity of vortex shedding. One of the difficulties is to separate the vortex excitation from other flow excitations. Previous studies on flow-induced vibration using the finite element method are covered in section 1.1.

The present study, is restricted to vortex induced vibration only. As a regular pattern of vortices is formed in the wake, it interacts with the cylinder motion and this is the source of the effect called vortex induced vibration. Each time a vortex is shed from the cylinder, it alters the local pressure distribution and the cylinder experiences a time-varying force at the frequency of vortex shedding. If the natural frequency of the cylinder is sufficiently close to the dominant frequency of vortex shedding, and if the cylinder damping is sufficiently low, sustained vibrations of the cylinder can be excited. During vibration amplitude build up, the correlation length of vortex shedding increases appreciably, and the vortex shedding is controlled by the cylinder motion. The excitation mechanism outlined above is restricted to flow separation and vortex shedding.

In air-flow, chimneys, telegraph wires, transmission lines (and suspended pipe lines in water) oscillate almost invariably in a direction normal to the flow. These are cross-flow oscillations. There has been rare exceptions when cylinder in air-flow have oscillated in the direction of flow (i.e. in-line motion) but these have been due to peculiarities of their installation. In water, marine piles, submarine periscopes and braced members of offshore structures can be excited to oscillate in both in-line and cross-flow direction. The in-line oscillations can be excited at flow velocities much lower than the critical velocities for cross-flow motion (125).

8.1 Flow Induced Vibration of a Single Cylinder

It has been shown in the previous section that a stationary cylinder is subjected to a fluctuating lift force which varies at the vortex shedding frequency (Strouhal frequency), f_s, when it is placed in fluid flow. This force acts in a direction perpendicular to that of flow. A fluctuating drag force is also exerted on the cylinder, acting in the direction of the flow with a frequency $2f_s$. In addition to these forces there are inertia and other effects which have the impressed frequency f. These forces act simultaneously on the

oscillating cylinder and produce records with complex waveforms.

When the forcing frequency, f , of the cylinder approaches the vortex shedding frequency, f_s, the two sets of forces become synchronized. The system of cylinder and wake, oscillates at the imposed frequency f of the cylinder only and the vortex shedding frequency f_s is lost. This is also known as the lock-in effect. This lock-in or synchronization effect was first documented by Bishop and Hassan (126). This sychronization persists over a range of frequency which may be termed as the lock-in band. The lock-in band at low Reynolds numbers was measured by Koopman (127). In this range the recorded waveform have a fairly constant amplitude when the frequency is fixed. Within the lock-in range, the lift and drag forces suffer changes in phase and amplitude as the imposed frequency is varied. The phase angle between the force exerted by the fluid and the impressed motion changes in a manner corresponding to the response of a simple oscillator under the influence of an applied harmonic force (126). Lift and drag forces are also synchronized, when the forcing frequency is near an integral multiple of the Strouhal frequency (126).

To analyse flow induced vibrations of a solid cylinder we use the mesh of fig.7.4.1. Flow at Re=300 and Re=1000 are

considered. The forcing frequency (natural frequency) of the cylinder is calculated from the relationship

$$f = 2\pi\sqrt{\frac{k}{m}} \qquad (8.1.1)$$

where k is the stiffness and m the mass/unit length of the cylinder.

Vortex shedding frequencies for these Reynolds numbers were computed and verified in section 7.4.The natural frequency of the cylinder was chosen so that it is close to f_s. At Re=300 (fig.8.1.1) we see that, to start with the two motions are out of phase, but later in time a change in phase occurs and the two frequencies lock-in. As a consequence there is an increase in amplitude of cylinder oscillation. The forcing frequency in this case is 4% lower than the vortex shedding frequency. As f is increased to .32 Hz (fig.8.1.2) no lock-in effect is observed up to n=340. However, the vortex shedding frequency continously increases from .2 Hz at n=250 to .26 Hz at n=320. The cylinder continues to oscillate at its natural frequency of .32 Hz. In this case the forcing frequency is 30% higher than shedding frequency. The lock-in band for low Reynolds number flows is found to be ±25% (127). Thus we see that outside this range the

shedding frequency is affected somewhat by the forcing frequency.

For the same value of f and f_s but with the Reynolds number increased to 1000 (fig.8.1.3) the shedding frequency increases from .23 Hz to .32 Hz and finally locks-in with the cylinder motion. There is a rapid increase in the amplitude of cylinder oscillation. Also the cylinder displacement in the upward direction is considerably greater than the downward (-ve) displacement, which indicates that some lift is generated. The amplitude of the shedding frequency is decreasing since the structure is constantly gaining energy, and is introducing damping into the fluid.

Increasing f further to .65 Hz, we observe that the cylinder motion no longer affects the shedding frequency. Vibration of the cylinder normal to flow is not excited for either of the Reynolds numbers (fig.8.1.4). For Re=300 the vertical displacement of the cylinder was found to be very small (.001D, D is the cylinder diameter). Although f is very close to $3*f_s$ (an integer multiple of shedding frequency), no lock-in effect is observed. However, for Re=1000 (fig.8.1.4), the cylinder is oscillating at approximately f/3, although the amplitude of oscillation is very small and constant.

To see if synchronization occurs, if the forcing frequency is near an integral multiple or division of f , we compute the response for f_s=.22 Hz, f=.11 Hz and Re=1000 (fig.8.1.5). Initially the fluid and the structure motions are completely out of phase, but a change in the fluid motion occurs at n=100 and the two frequencies lock-in. The system oscillates at 2f in this case. The very sudden increase in the amplitude of cylinder oscillation resulted in very large interface velocities, and we were unable to analyse the response any further since the effects of changes in geometry are not included in the analysis. When the two frequencies lock-in there is a sudden increase in lift and drag forces and the vertical displacement of the cylinder increases from .05D to over .2D.

The cylinder continues to oscillate in the horizontal direction at or near twice the frequency of cylinder oscillation in the vertical direction. Throughout the computations a rapid increase in horizontal displacement of the cylinder was not observed.

From the tests carried out so far we observe various features in the numerical solution, that correspond to experimentally observed effects (120,126,127,128).

(i) The cylinder vibrates at or near the shedding frequency and the motion normal to the free-stream

velocity builds up to higher values than the transverse vibration.

(ii) In the lock-in range the frequency of vortex shedding changes from the fixed cylinder shedding frequency to the cylinder natural frequency. As a result large amplitude oscillations are produced.

(iii) The lock-in range is also Reynolds number dependant. We find that it expands with increasing Reynolds number.

(iv) There is a small increase in the drag force over that for the fixed cylinder.

(v) There is an increase in the vortex strength indicated by a increase in lift and drag forces compared to the fixed cylinder.

We have also observed that synchronization can occur when the forcing frequency is an "integer division" of the shedding frequency (fig.8.1.5) and this results in very large amplitude of oscillation. In this case the system oscillated near the shedding frequency. This phenomenon of frequency multiplication and frequency division is also reported in ref.126. In the previous examples the locking in of the two systems occured by the shedding frequency changing to the structural frequency. In this case, where

the two frequencies are related by an integer multiple, the opposite occured and the response was much stronger. This strong lock-in only occured when the shedding frequency was higher than the structure frequency. Only a few cases have been examined so far and more calculations have to be carried out to confirm these conclusions.

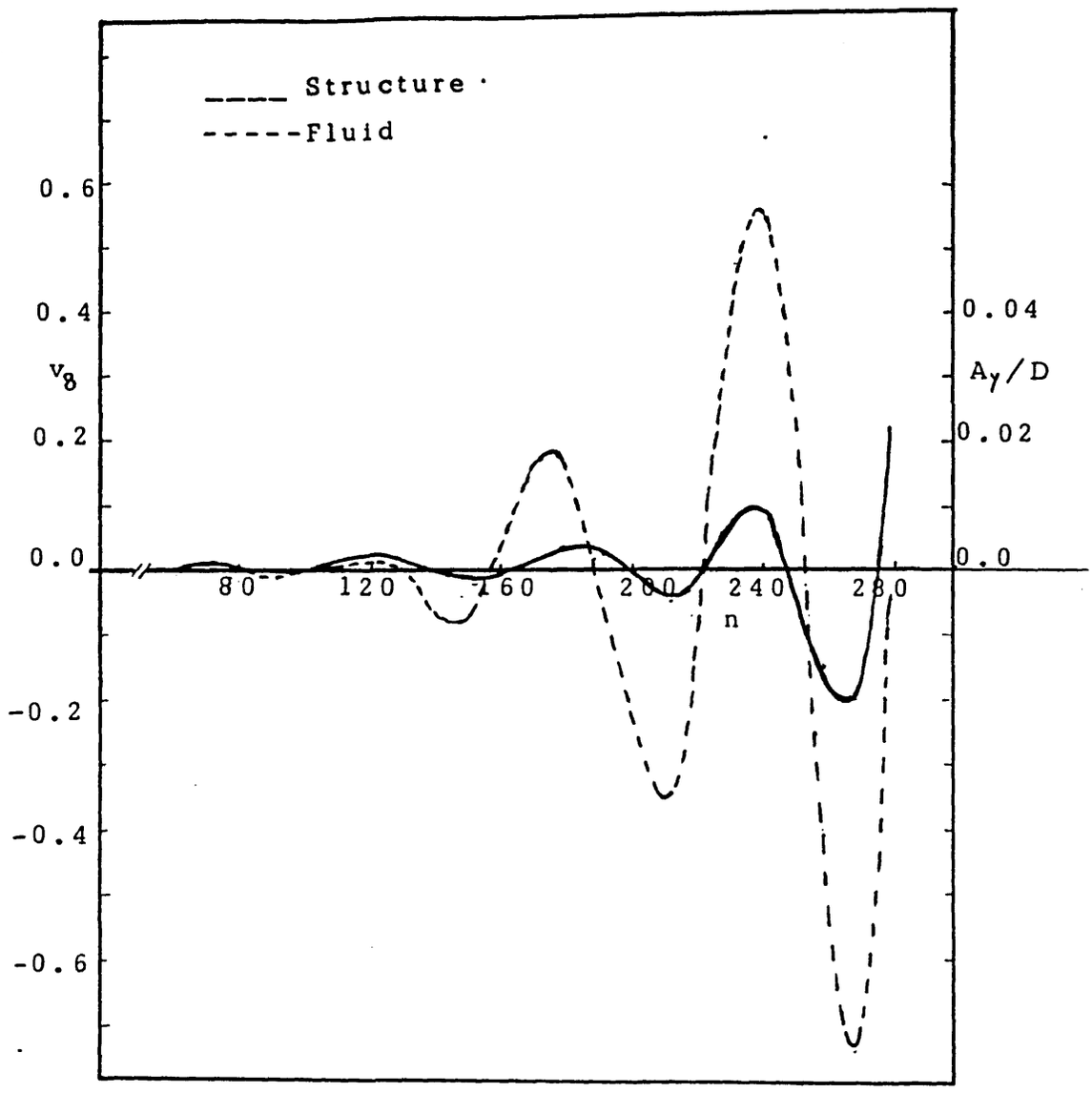

Fig.8.1.1 Fluid and Structure Response
Re=300, f_S =.213 f =.205

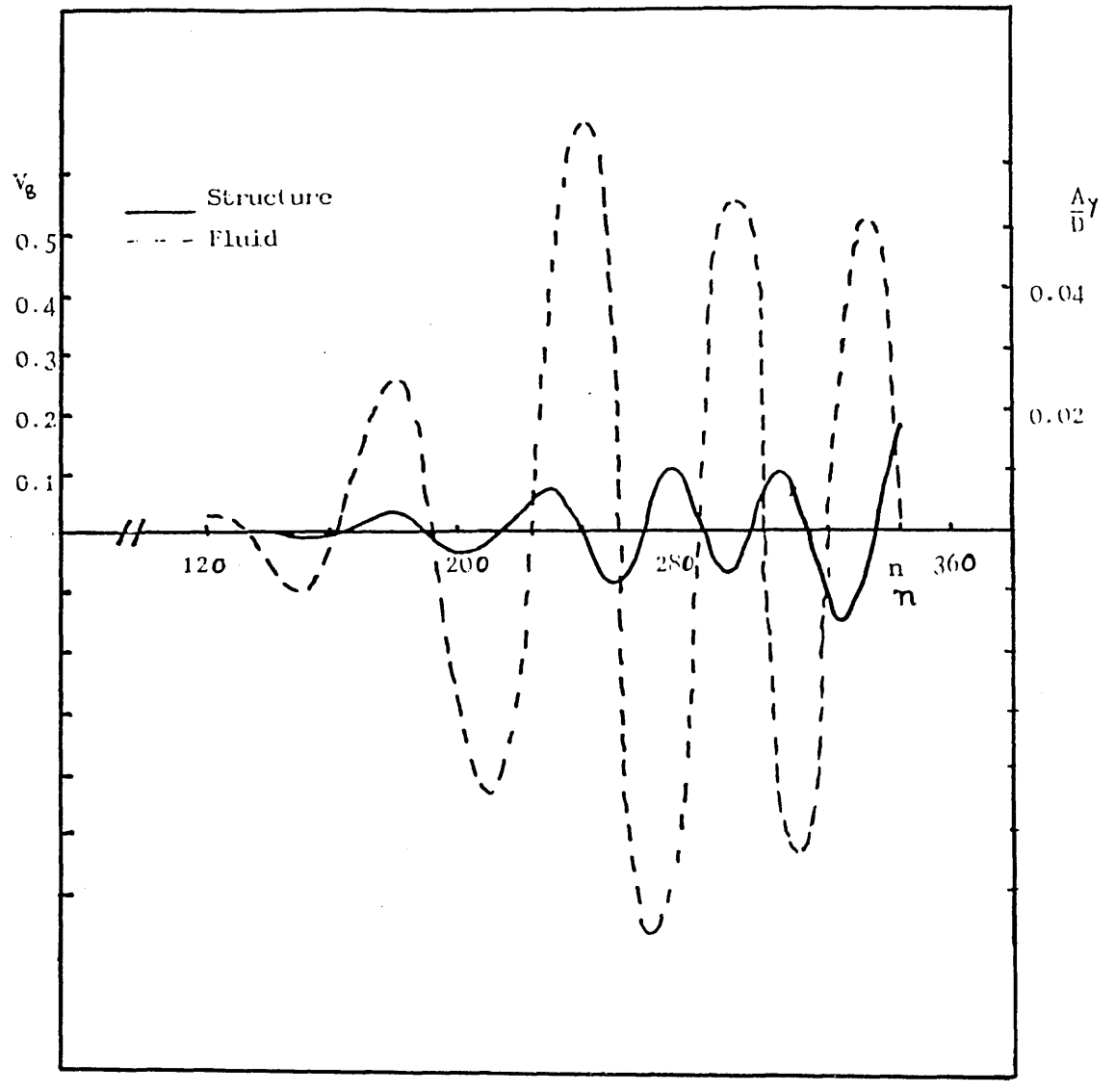

Fig.8.1.2 Fluid and Structure Response
Re=300 f_s=.213 f=.32

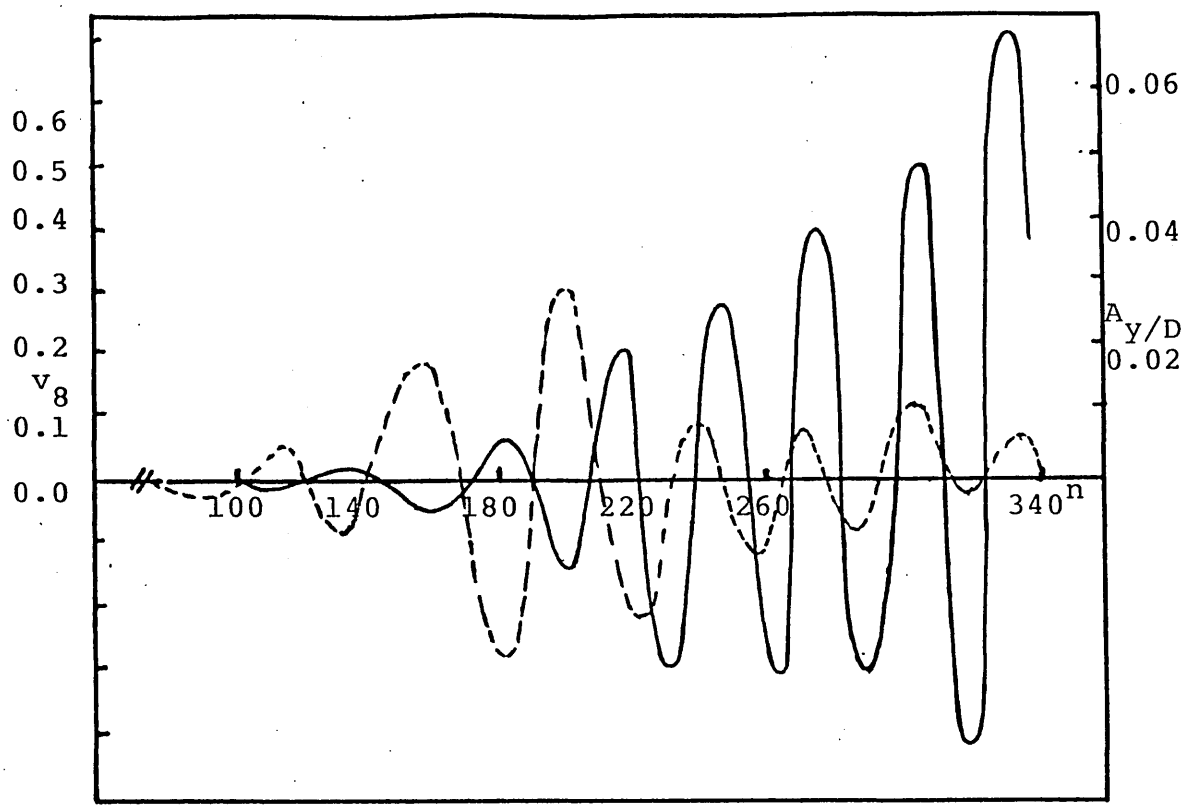

Fig. 8.1.3 Fluid and Structure Response
Re=1000, f_s=.22, f=.32

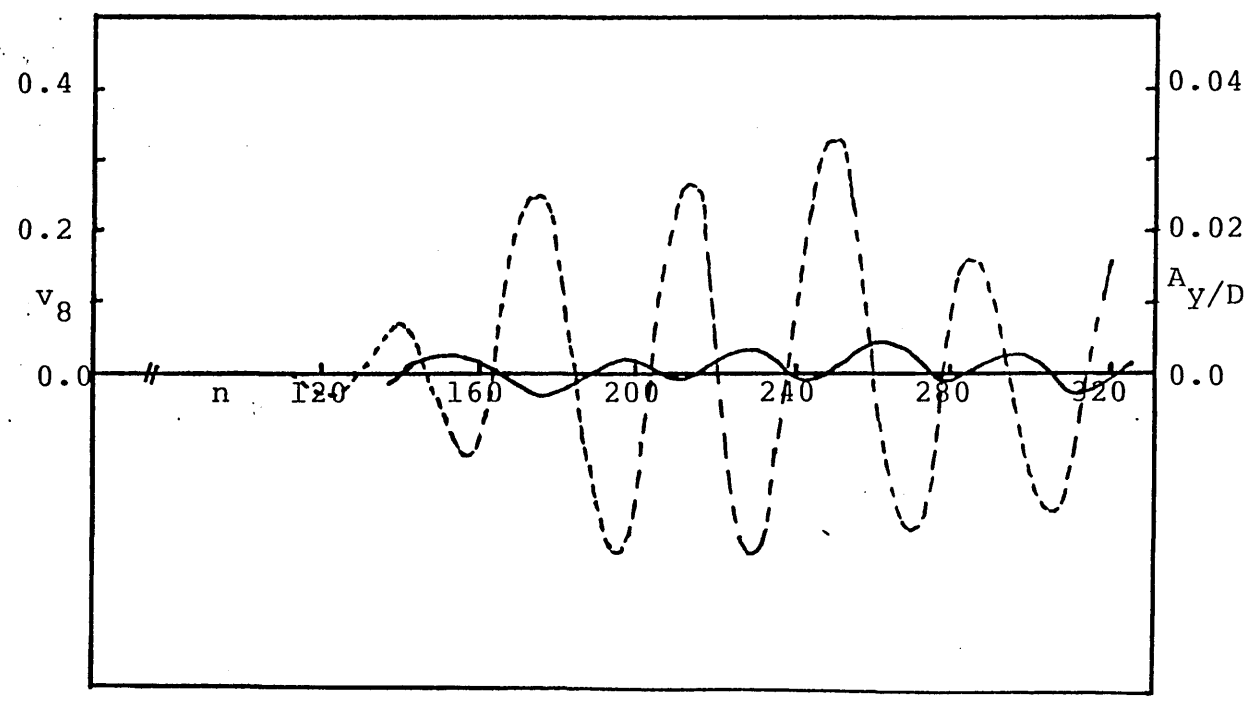

Fig. 8.1.4 Fluid and Structure Response
Re=1000, f_s=.22, f=.65

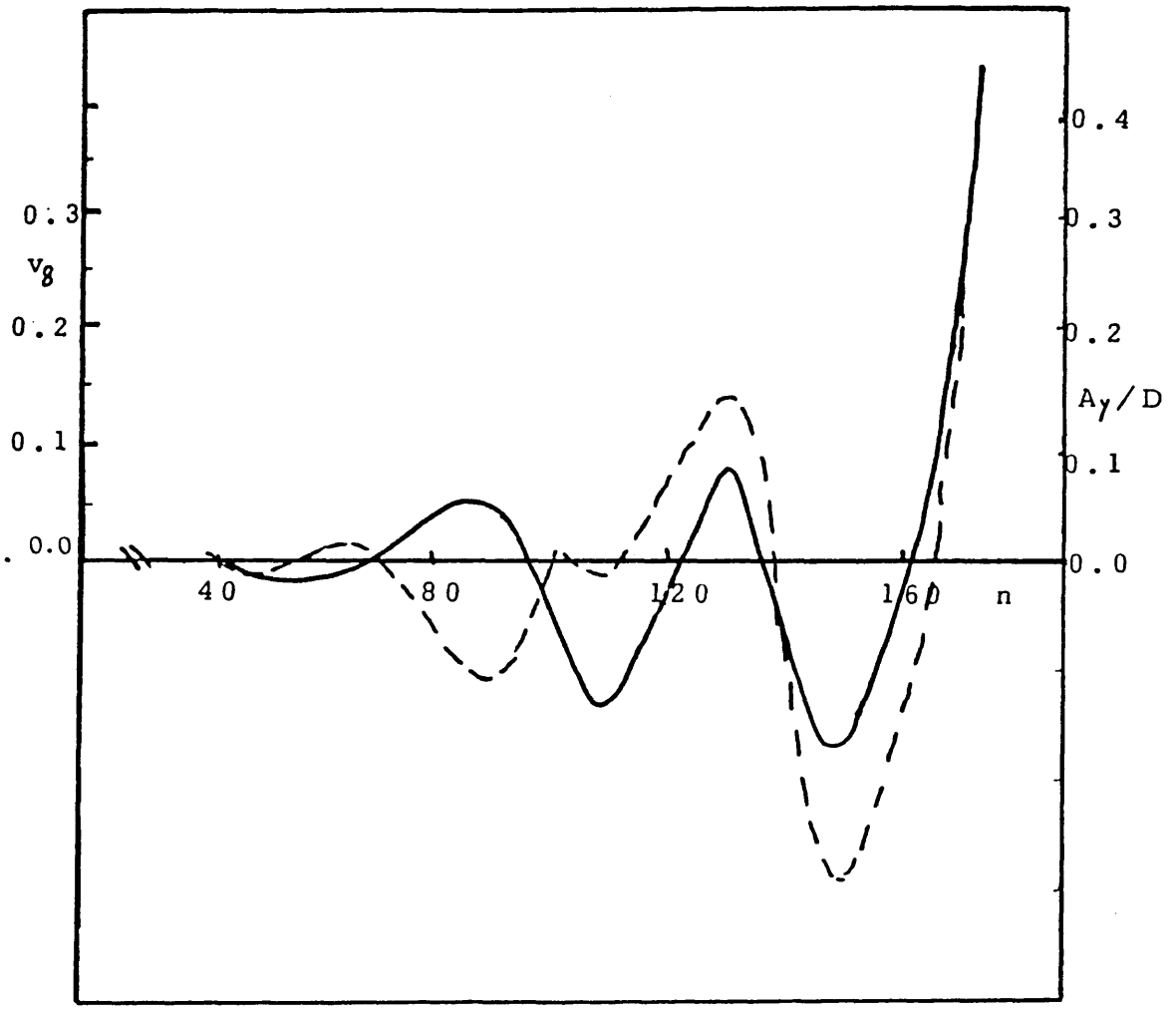

Fig. 8.1.5 Fluid and Structure Response
Re=1000 f_s=.22 f=.11

8.2 Flow Induced Vibration of a Column of Cylinders

The phenomenon for the flow-induced vibration of cylinder rows and cylinder arrays is far more complicated than the flow-induced vibration of a single cylinder. In the previous section (8.1) vortex-induced vibration of a single cylinder in cross-flow was considered. The vortex shedding as an excitation source applies only to tube bundles with wide tube spacings. If the tube spacings are narrow, other sources, such as wake swing, jet switch, jet instability and vortex pairing may be the main excitation mechanisms (130). The forces on tubes in a tube bank are generated by the interaction of flow fields about adjacent tubes. For circular cylinders three types of dynamic instability across a flowing medium have been discussed in the literature (108).

(a) Wake Induced Flutter - This occurs when more than one cylinder is present. The wake behind the upstream cylinder contains periodicities and general turbulence. When this wake strikes the downstream cylinder, large oscillations can be excited in the cylinder. This is called wake-induced flutter, wake galloping or wake-induced oscillation and has been observed with two, three, four or more conductor arrangements.

(b) Jet-switching Instability - When a stream flows across a closely spaced cylinder row, a series of similarly sized and spaced jets appear in the wake. These jets pass downstream of the cylinders and coalesce in

pairs. If the cylinders oscillate, the oscillation can cause the jets to switch back and forth forming different pairs. Cylinder motion and jet switching are thus coupled and large oscillations of the cylinder can occur.

(c) Fluid-Elastic Instability - If a cylinder in an array in a cross-flow is displaced from its equilibrium position, fluid forces exerted on the cylinder change. If the variation in these fluid forces is sufficiently large, then large oscillations of the cylinder can occur. This type of motion is also described as fluid-elastic orbital vibration, fluid-elastic whirling, whirling instability, aeroelastic coupling and hydroelastic instability.

A vast amount of literature is available on the experimental and analytical work carried out in this field (120), however, very little work is available on the numerical work using finite element method for this particular problem. Yu and Vanburen (131) have presented the dynamic analysis of a submerged four-tube array using the added mass approach. The hydrodynamic mass matrix for the tube array is generated using the substructure technique. By combining the substructure hydrodynamic mass with the structure, dynamic events such as normal modes, shock spectrum and the history analysis for a single numerical problem are carried out.

Flow around three cylinders in a column is analysed in this section. The two-dimensional, structural model for the cylinder column is shown in fig. 8.2.1. k_x and k_y are the stiffnesses of the cylinders parallel and normal to the free stream flow, k_θ is the rotational stiffness. The finite element mesh used to analyse the flow around this column consisted of 204 elements and 898 nodes (fig. 8.2.3). The distance between the cylinders is one cylinder diameter. The top and bottom of the flow domain are no slip walls (fig. 8.2.2). Thus the example considered is that of flow around a column of three cylinders in a duct. Based on our experience with the flow around a single cylinder, a slightly different mesh density is taken above and below the centre line in order to introduce asymmetry into the flow. Velocity vector plots at twenty timestep intervals are presented in fig. 8.2.4. The flow Reynolds number was 150. The initial flow solution (8.2.4a) is obtained by solving the Stokes flow equation. In the velocity vector plots to follow, the flow can be seen to oscillate downstream of the cylinders. The flow escapes through the gap between the cylinders and moves away from the central cylinder in the form of jets at high velocity. The flow changes direction further downstream and is moving towards the centre again. The flow behind the central cylinder is beginning to roll up into vortices and these are being shed alternately from the top and the bottom of the cylinder. The velocity vectors are seen to

oscillate downstream of the other two cylinders also. There is a clear recirculation region behind the top and bottom cylinders which moves downstream into the flow with time. The vortex shedding behind the central cylinder resembles the vortex shedding phenomenon for a single cylinder (section 8.1). In the velocity vector plots at a later time (fig.8.2.4g onwards), the three cylinders seem to be shedding vortices more or less individually, and most of the flow through the gaps between the cylinders is moving in a straight line with very little oscillation. This probably indicates that the gap between the cylinders is large and is not affecting the flow pattern too much. The horizontal and vertical components of the velocity, eight diameters downstream of the cylinders, are plotted against time in fig. 8.2.5 and 8.2.6. Lift and drag forces acting on the individual cylinders is calculated by summing up the relevant nodal forces about the centre point. Drag coefficient C_D and Lift Coefficient C_L are also calculated using equation 7.1.1. These are plotted in fig. 8.2.7 and 8.2.8. The vertical component of the velocity downstream of the cylinder oscillates as vortices are shed in the flow. The oscillation in fig. 8.2.6 is by no means steady. The amplitudes for the top and bottom cylinders are decreasing with time, while it is increasing for the central cylinder. This is because most of the flow moves through the gaps between the cylinders towards the fixed wall in the early stages of the process (fig.8.2.4c

and 8.2.4d) but slowly settles down and moves in a straight line at later times (fig.8.2.4e onwards). An incremental Reynolds number approach is used in this case (section 2.6) and the flow Reynolds number is incremented suddenly from 0 to 150. In the test cases with a single cylinder (section 7.4), flow solutions were obtained by incrementing the Reynolds number in large steps. The flow is more complex around a bank of cylinders and smaller increments are probably required to obtain a smooth solution. Further tests with smaller increments in Reynolds number are required to check this behaviour. The time period 'τ' taken to shed a pair of vortices can be calculated from fig. 8.2.6. The Strouhal Number 'S' can be calculated using

$$S = f_s D/u \qquad (8.2.1)$$

where f_s is the predominate frequency of vortex shedding

u is the freestream velocity

and D is the diameter of the cylinder.

The Strouhal number for the top and bottom cylinder is found to be 0.19 and 0.25 for the central cylinder (fig.8.2.6). The Strouhal number for a single cylinder at Re=150 is around .17 (fig.7.4.16). A cylinder in an array of cylinders sheds vortices at a different frequency compared to a single cylinder. The frequency of shedding and hence the Strouhal number also depends upon the arrangement of cylinders in the array. The oscillations in the flow behind the central cylinder seem to be more in-phase with the upper cylinder than the lower cylinder (fig.8.2.6). The oscillations in figures 8.2.5 to 8.2.8 are not steady and indicate that the flow has not reached a steady-state as yet. From figures 8.2.7 and

8.2.8, it is possible to obtain approximate values of C_D average, C_L peak-to-peak and C_L average. All three cylinders have a similar value of C_D average (fig.8.2.7). C_L peak-to-peak for the top and bottom cylinders is the same (fig.8.2.8). This is because of the symmetric nature of the flow. There is a discrepancy in C_L average values for the two cylinders. The top cylinder has a higher C_L average value, probably because the central cylinder is oscillating in phase with this cylinder (fig.8.2.6). The value of C_D and C_L peak to peak is much smaller for the central cylinder. The oscillations in the flow behind the central cylinder are restricted because of the presence of high-speed flow near and downstream of the central cylinder. The distance between the no-slip wall and the end cylinder is large and the flow is unrestricted in this region. Hence the flow behind the top and bottom cylinders oscillates with larger amplitude. Some experimental and theoretical results for instabilities in tube rows and tube arrays are presented in ref.120 for certain configurations. Numerical results for flow around a column of tubes are hard to find.

Only a single example of flow around a bank of three cylinders is considered. The flow around a group of cylinders is much more complex than that around a single cylinder. A finer mesh is required to solve the flow problem reasonably accurately. The mesh used to analyse the flow around a column of three cylinders consisted of nearly 900 nodes and the timestep for

stability and accuracy of the solution was found to be 0.065. All the calculations were carried out on a Cyber 855 mainframe. The computer times used for the flow analysis and the fluid-structure interaction analysis for a single cylinder and a column of three cylinders is presented below.

Single Cylinder

Flow analysis

4.0 170-855 cp secs/timestep

Fluid-Structure Interaction analysis

9.02 170-855 cp secs/timestep

Column of Three Cylinders

Flow Analysis

7.5 170-855 cp secs/timestep

Fluid-Structure Interaction Analysis

16.08 170-855 cp secs/timestep

The present test problem was run for 200 timesteps and steady-state flow was not achieved at the end of this time. The total time used for the analysis is thus considerable (3200 cpu secs +). The computer time to analyse the flow around a group of three cylinders is significantly more than that for a single cylinder. Although a simple example of the flow around a bank of three cylinders was examined, it is quite possible to model a bank of cylinders with more than three cylinders. This would require more storage and considerably more computer time.

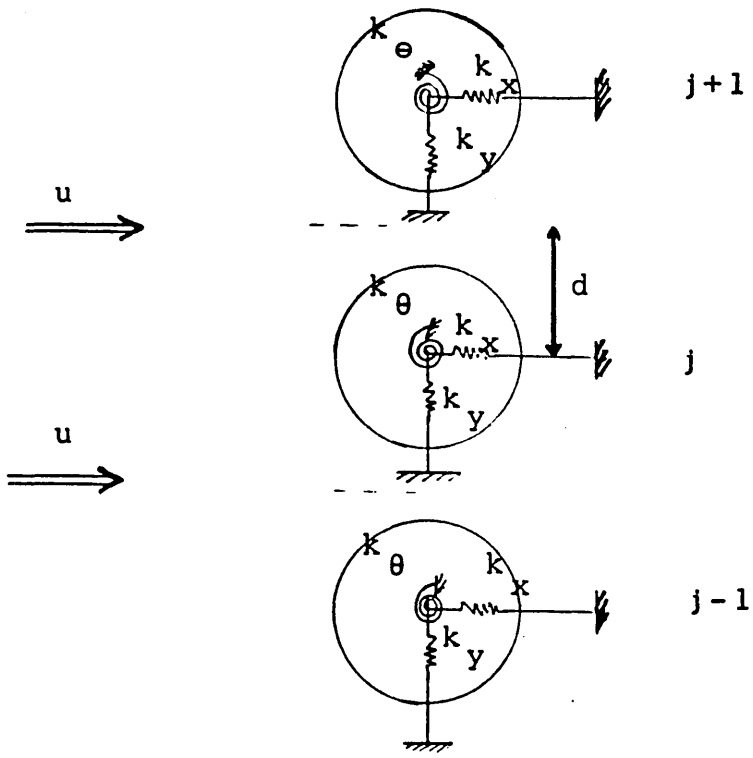

Fig.8.2.1 Two-Dimensional Structural Model for the Cylinder Column

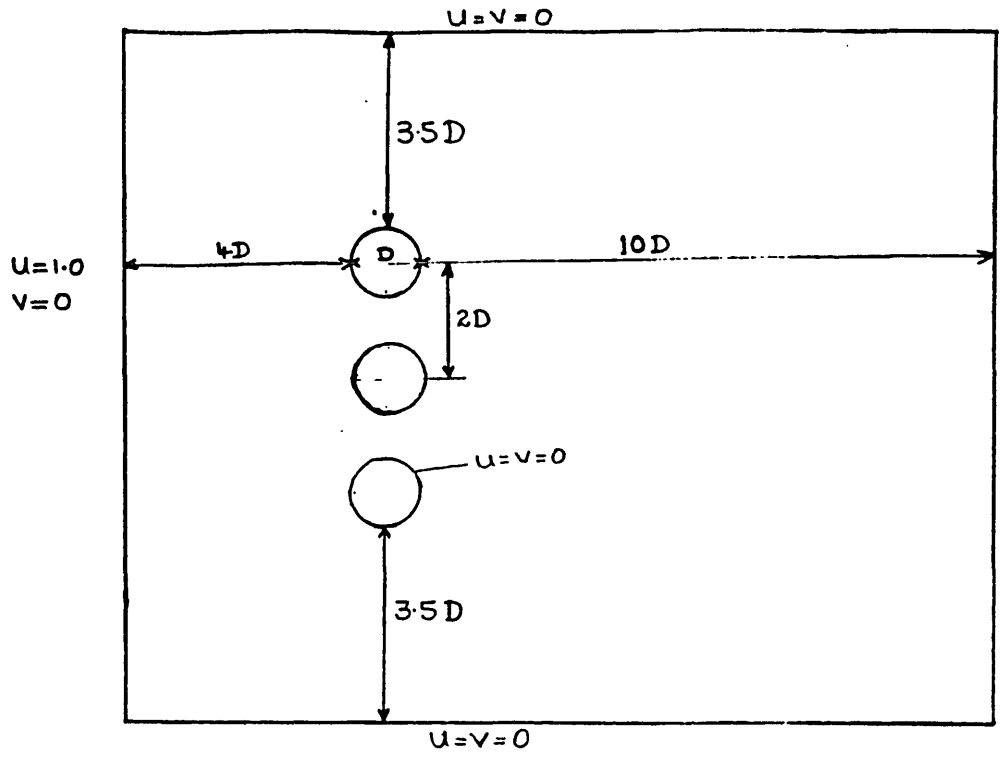

Fig.8.2.2 Flow around a Column of Three Cylinders
Problem Definition and Boundary Conditions

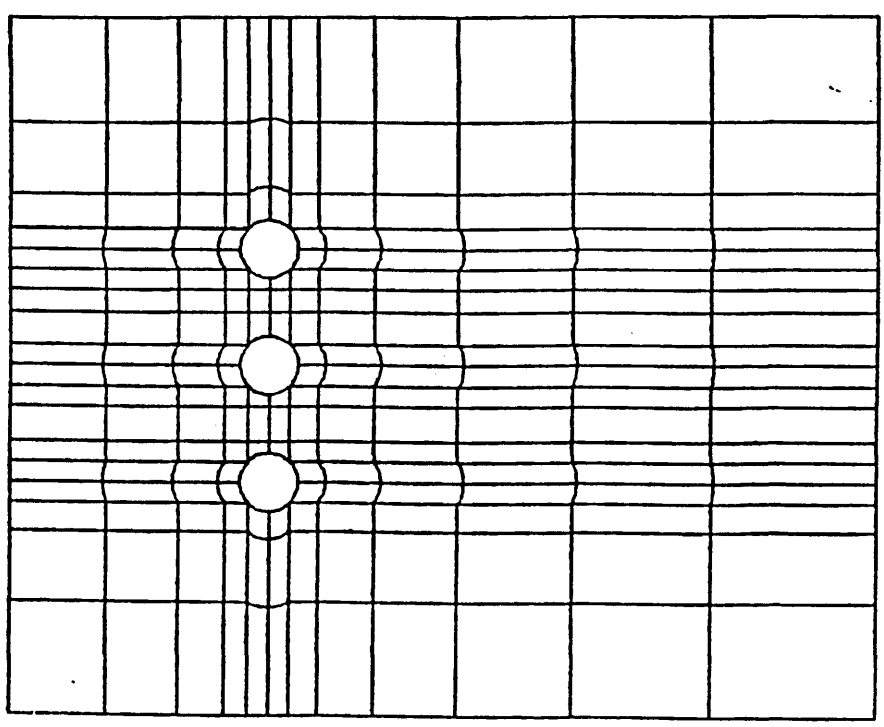

Fig.8.2.3 Flow around a Column of Three Cylinders
Finite Element Mesh, 204 Elements, 898 Nodes

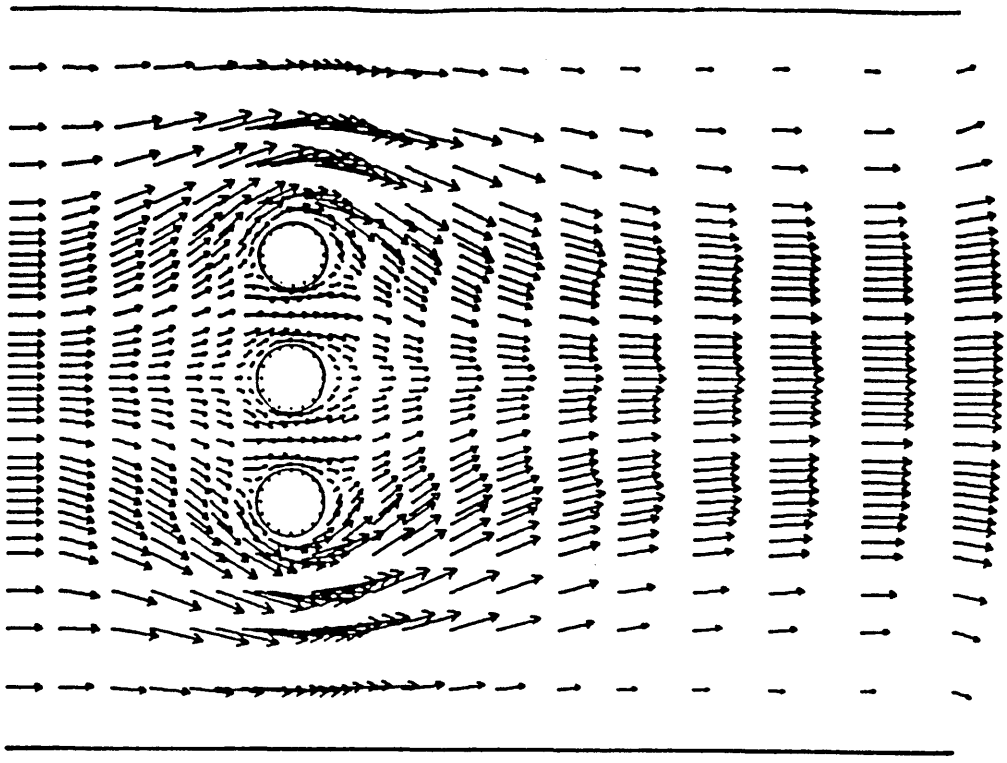

Fig.8.2.4a Initial Flow Solution 'n' = 0

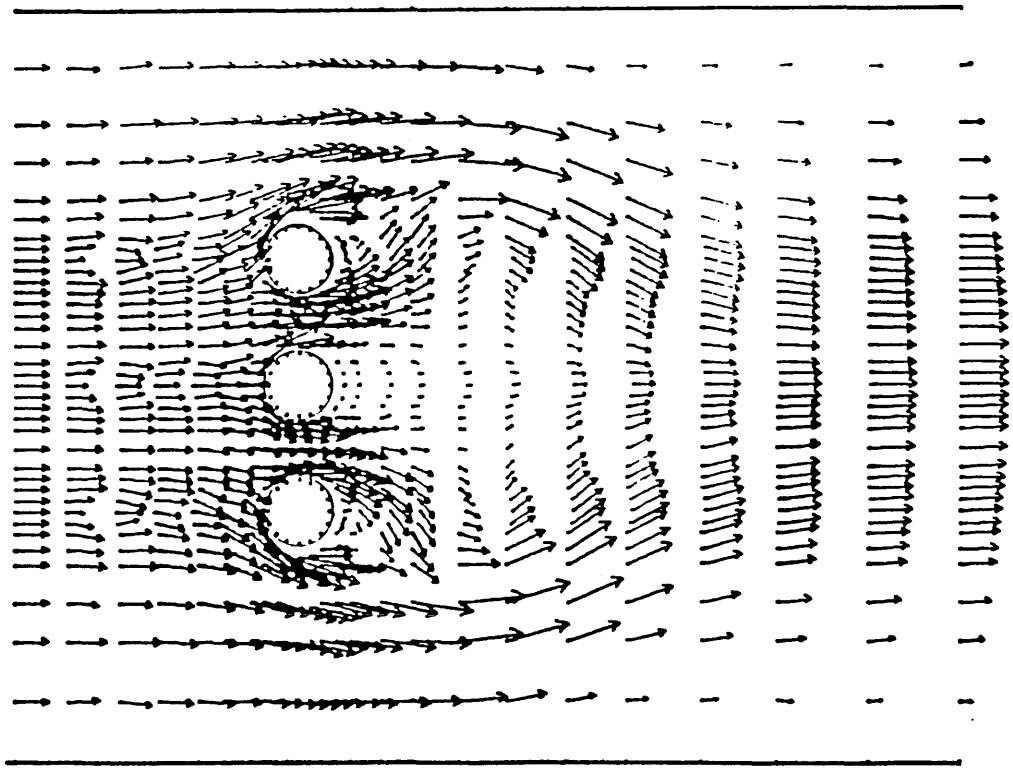

Fig.8.2.4b n = 40

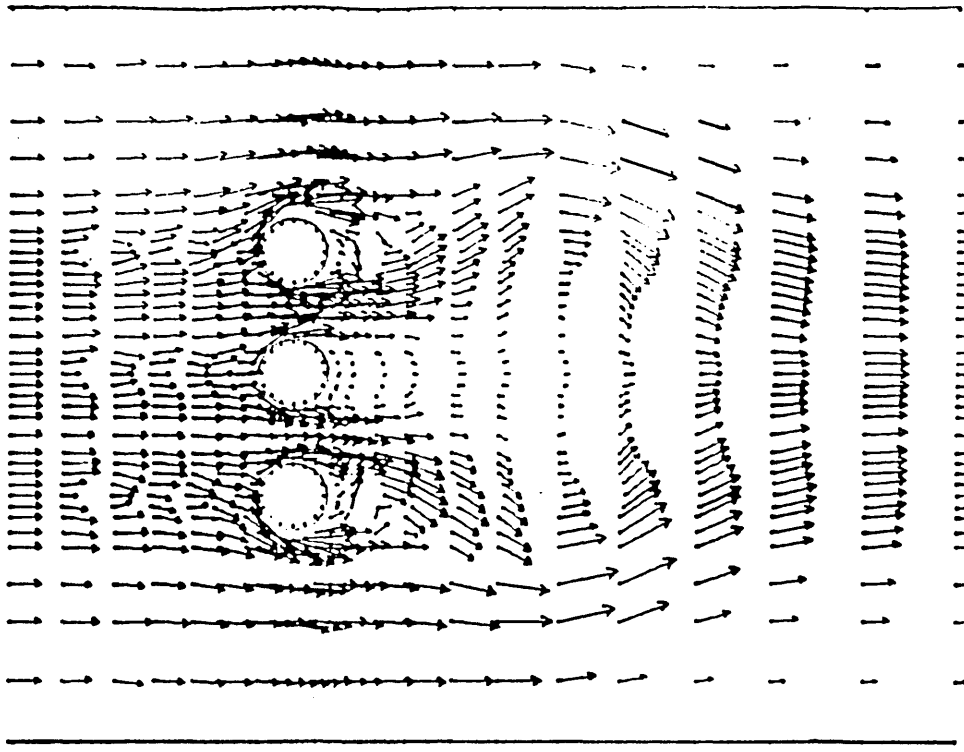

Fig.8.2.4c n = 60

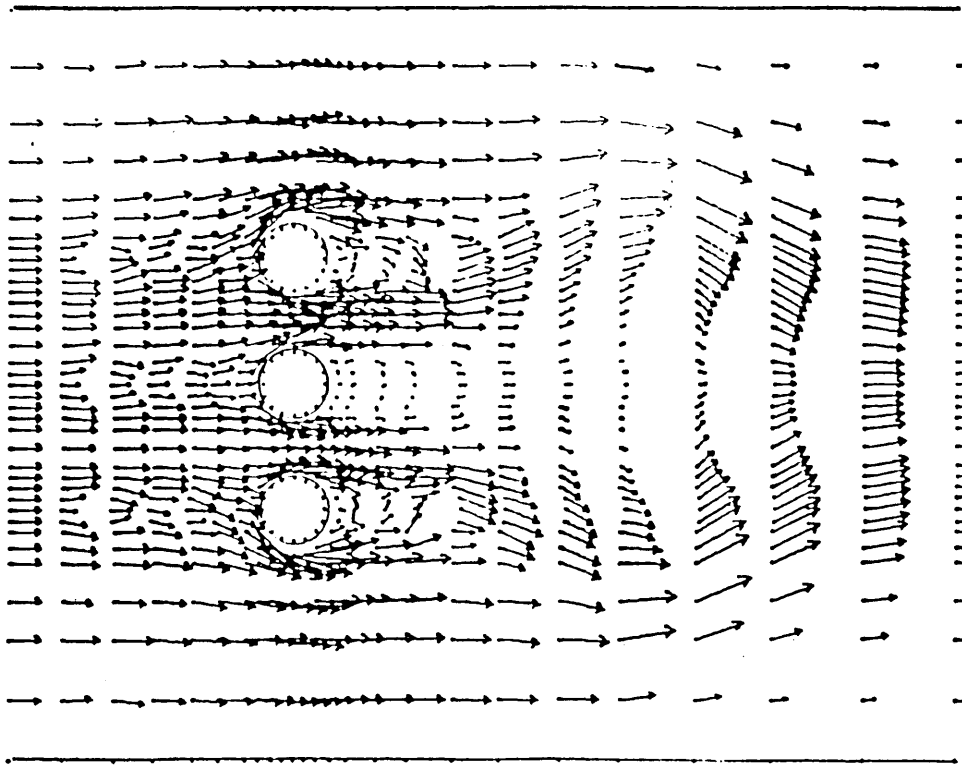

Fig.8.2.4d n = 80

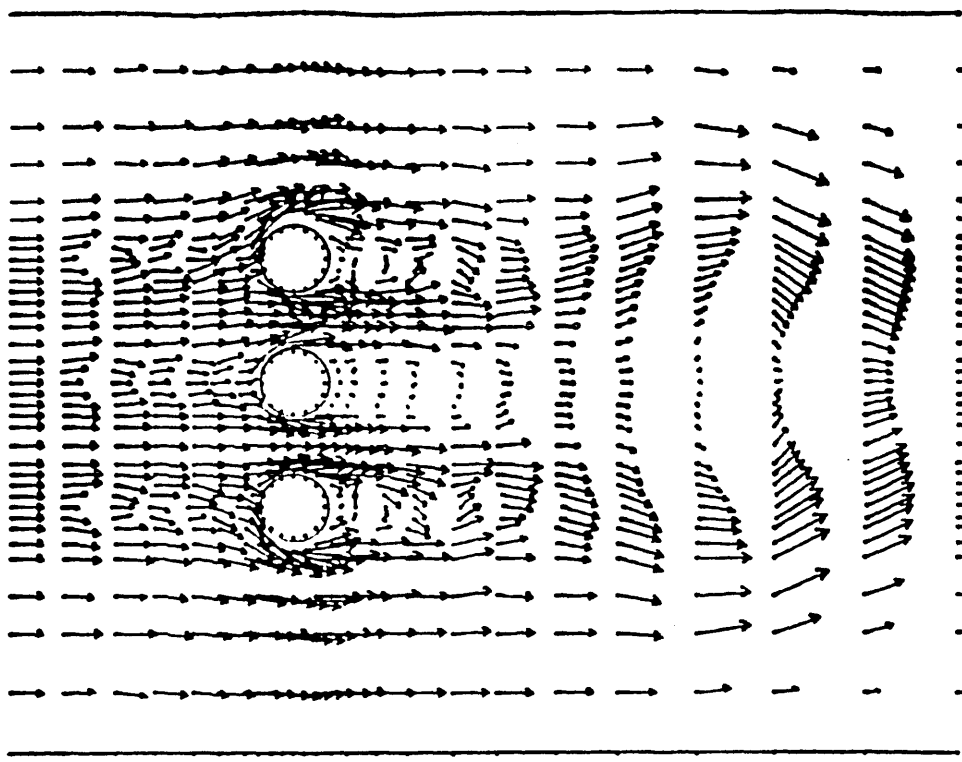

Fig.8.2.4e n = 100

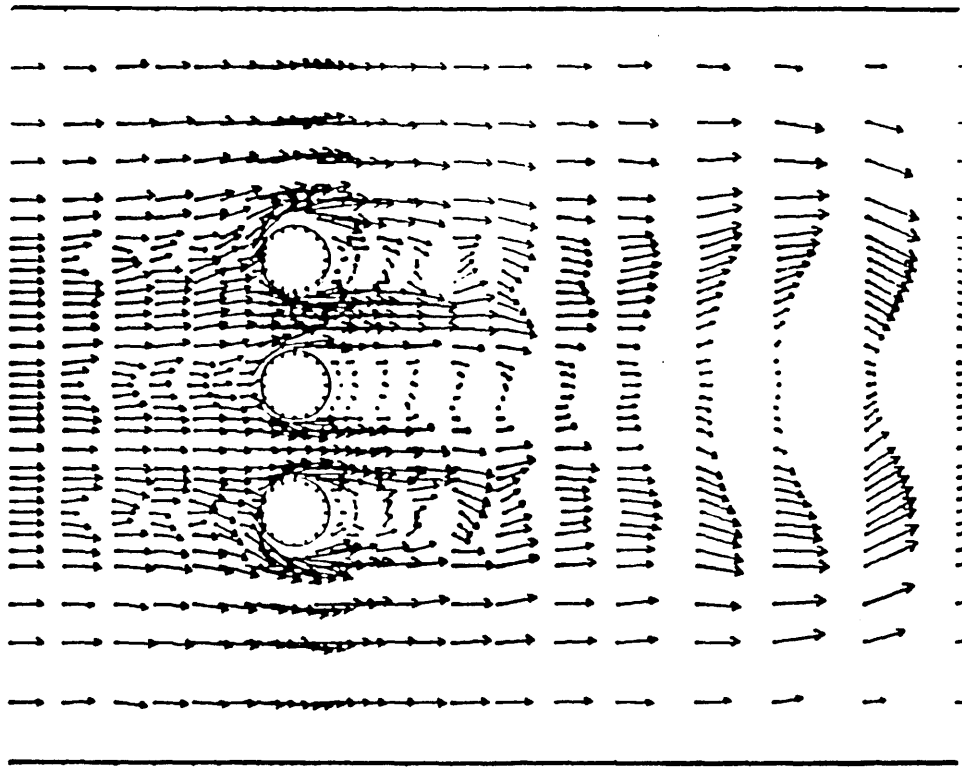

Fig.8.2.4f n = 120

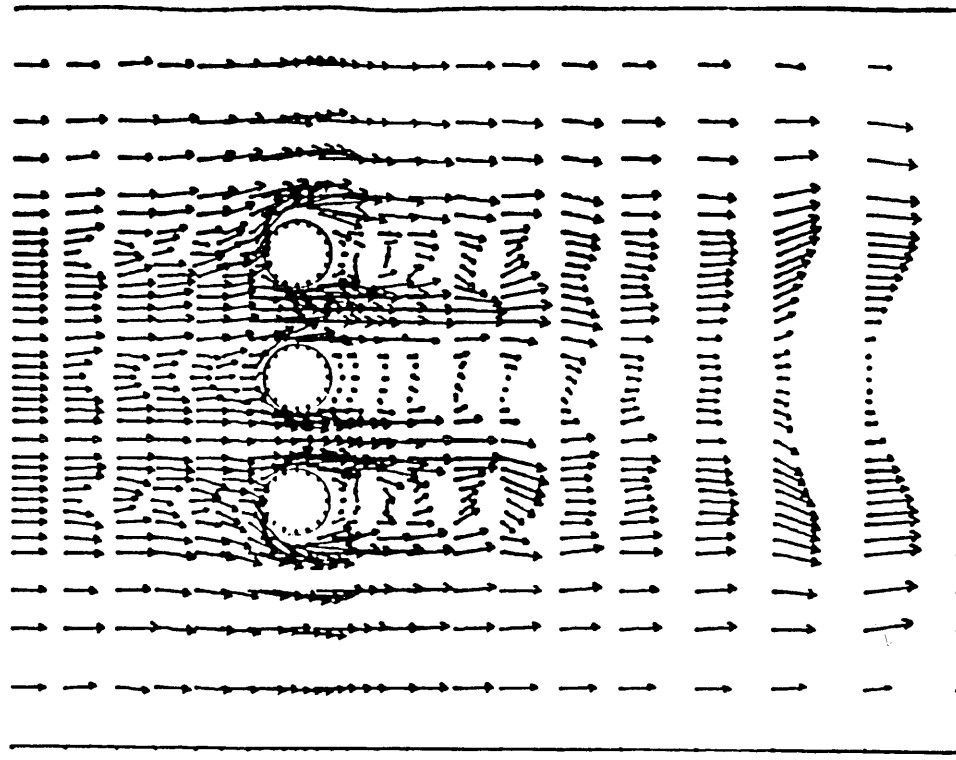

Fig.8.2.4g n = 140

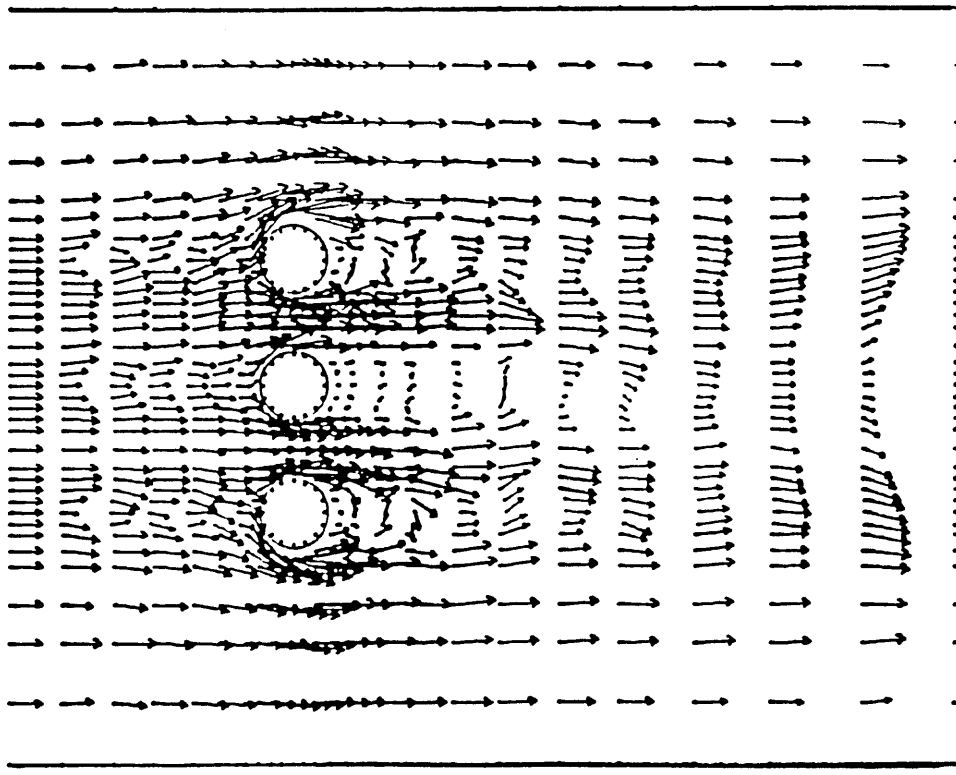

Fig.8.2.4h n = 160

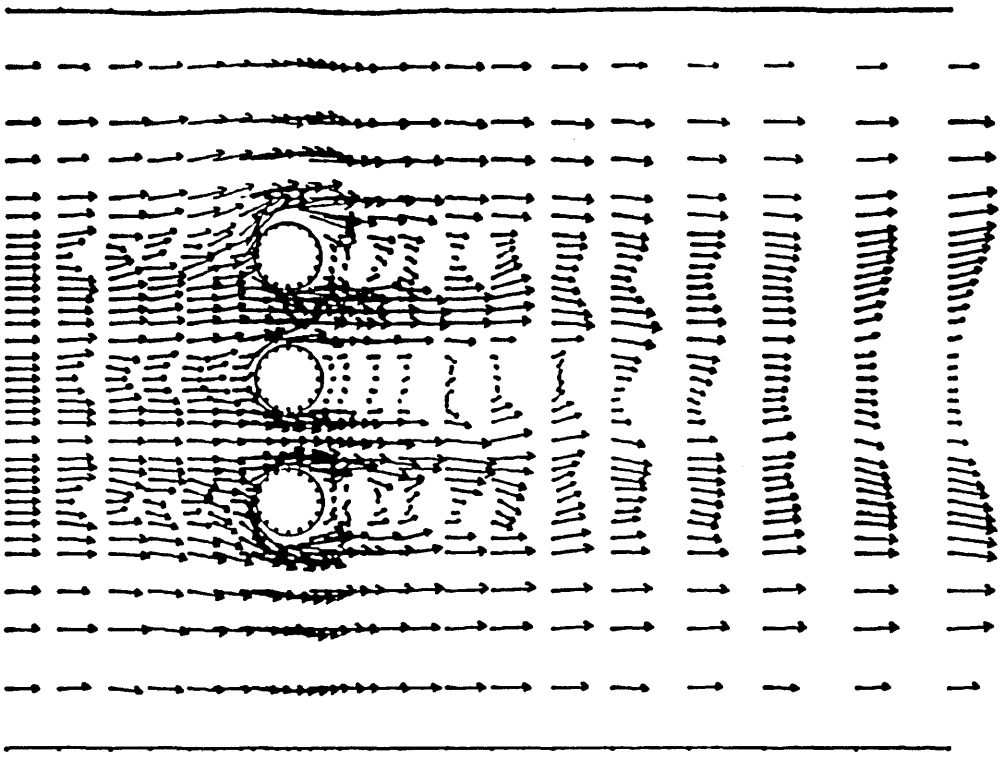

Fig.8.2.4i n = 180

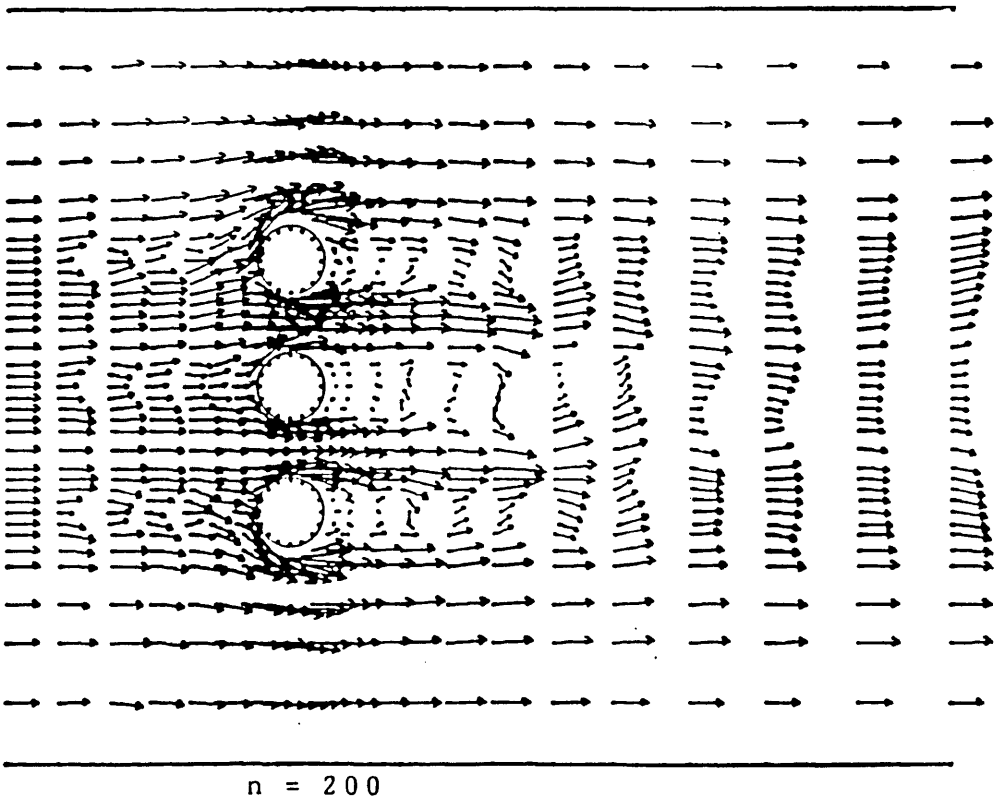

n = 200

Fig.8.2.4 Flow around a column of three cylinders
Velocity Vector Plots Re=150

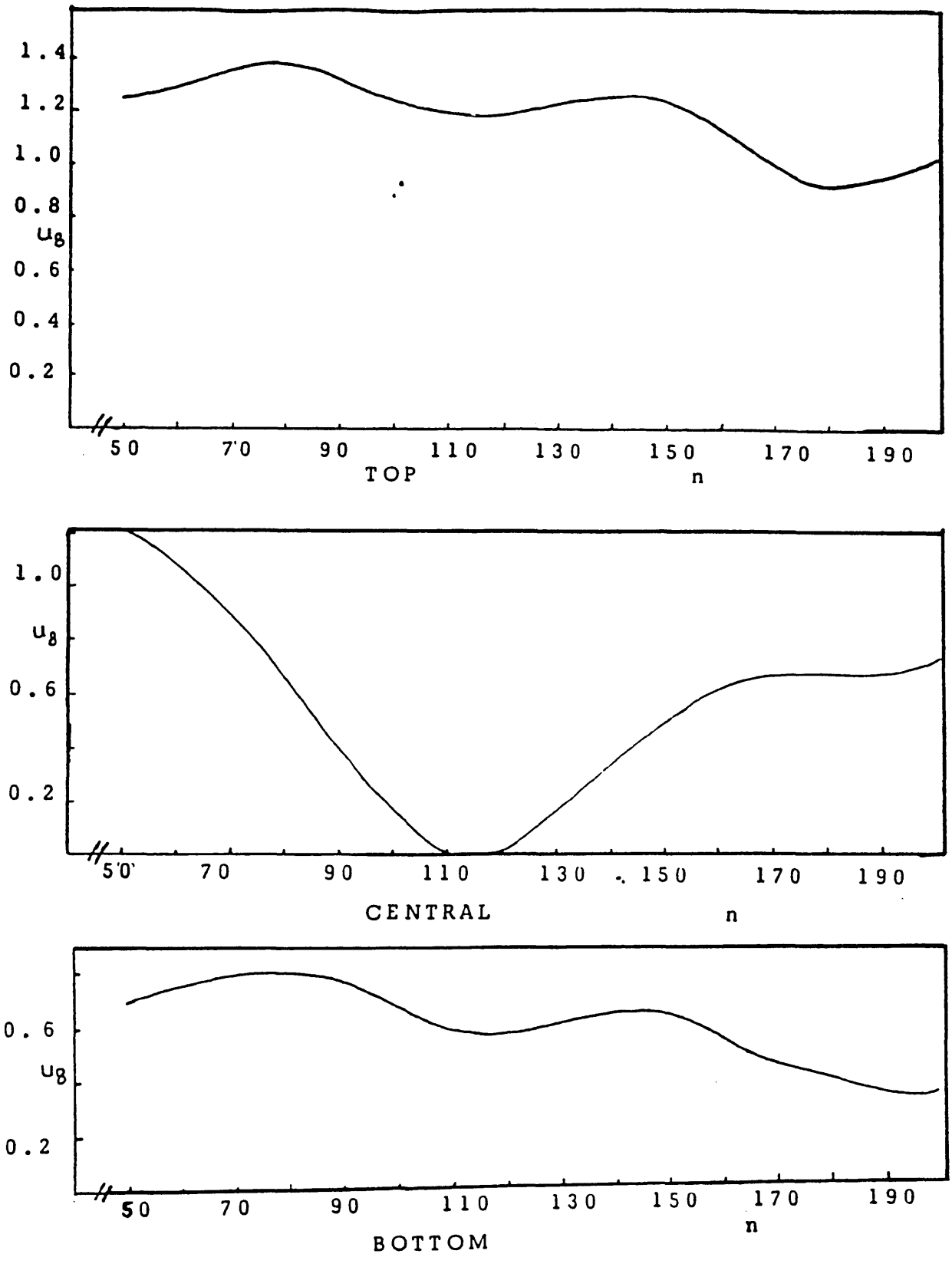

Fig.8.2.5 Horizontal Velocity 'u_8' - Flow around a Column of three Cylinders Re=150

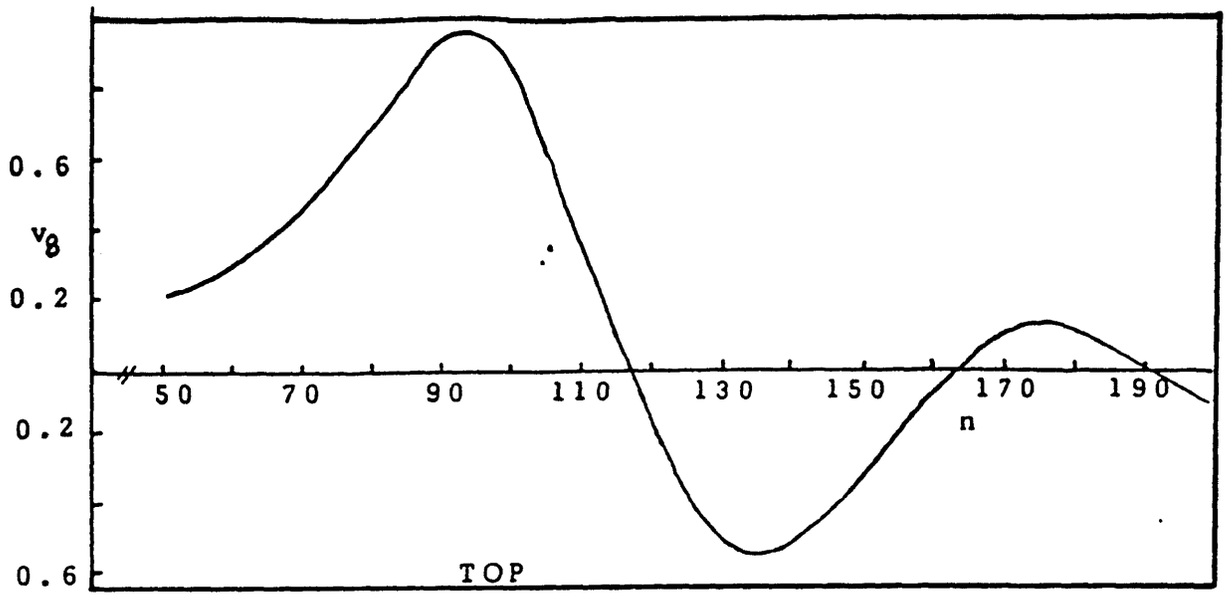

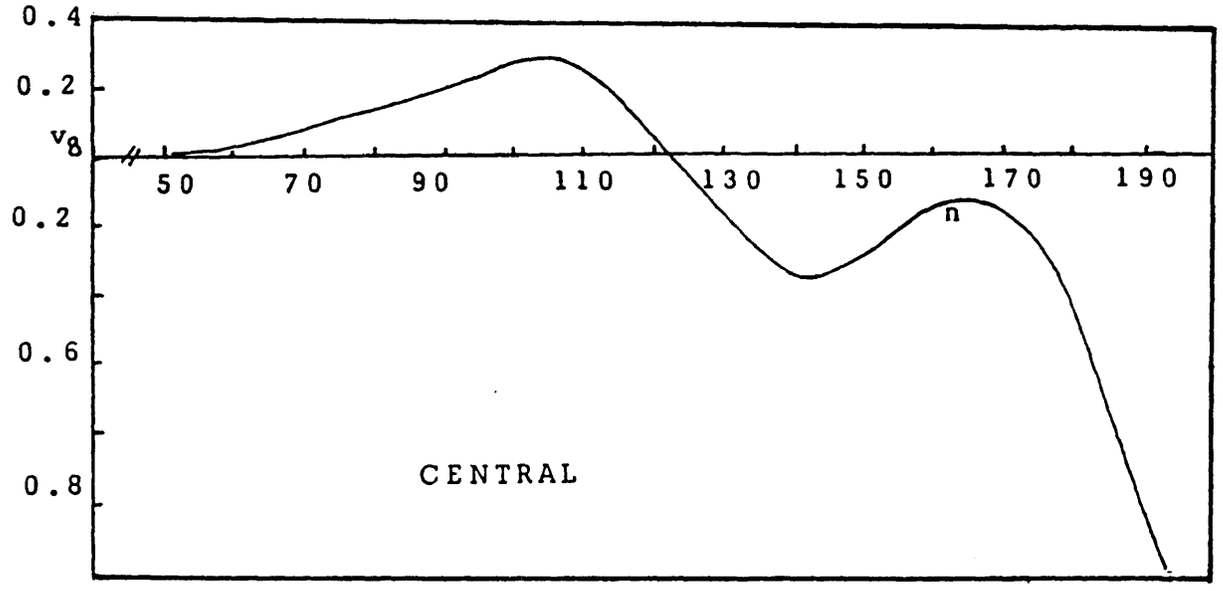

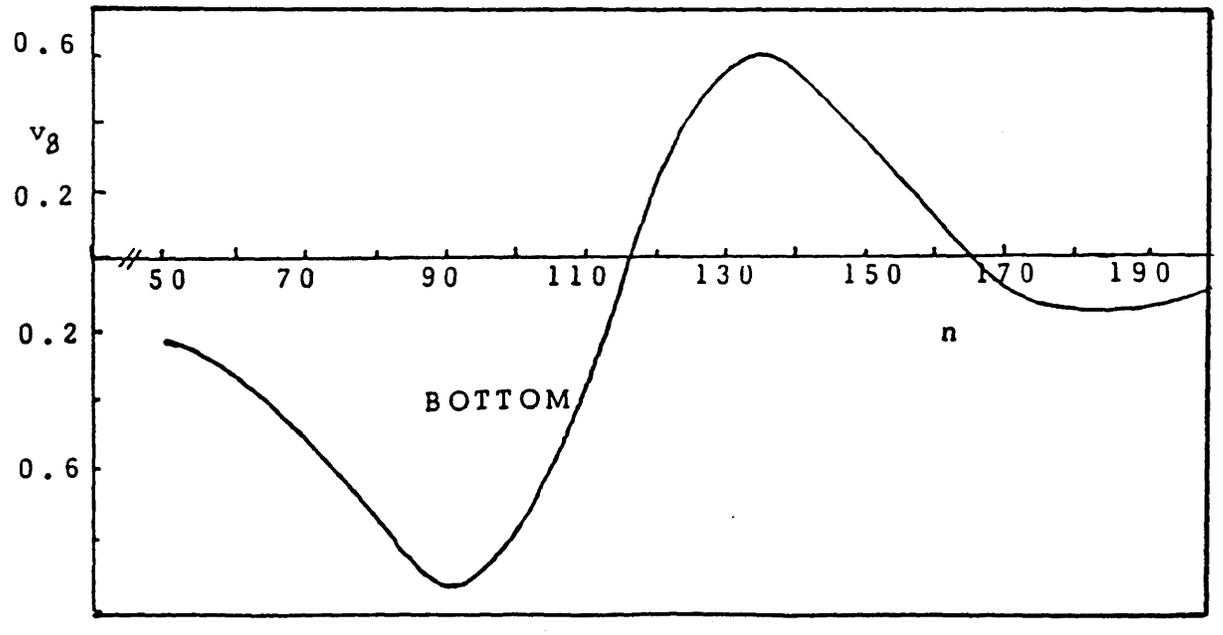

Fig.8.2.6 Vertical Velocity 'v_θ' Re=150

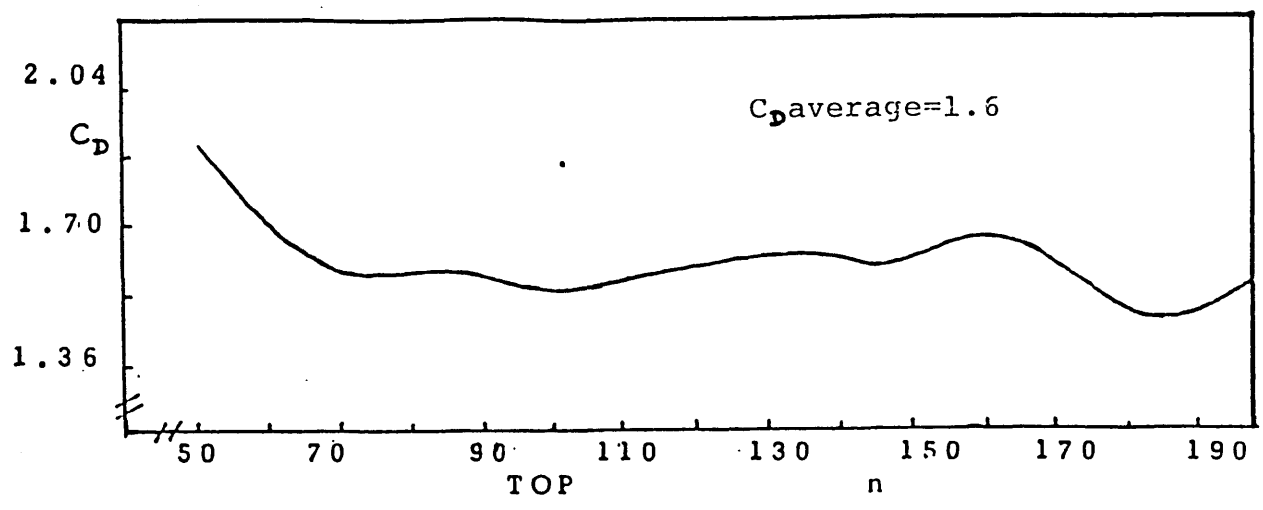

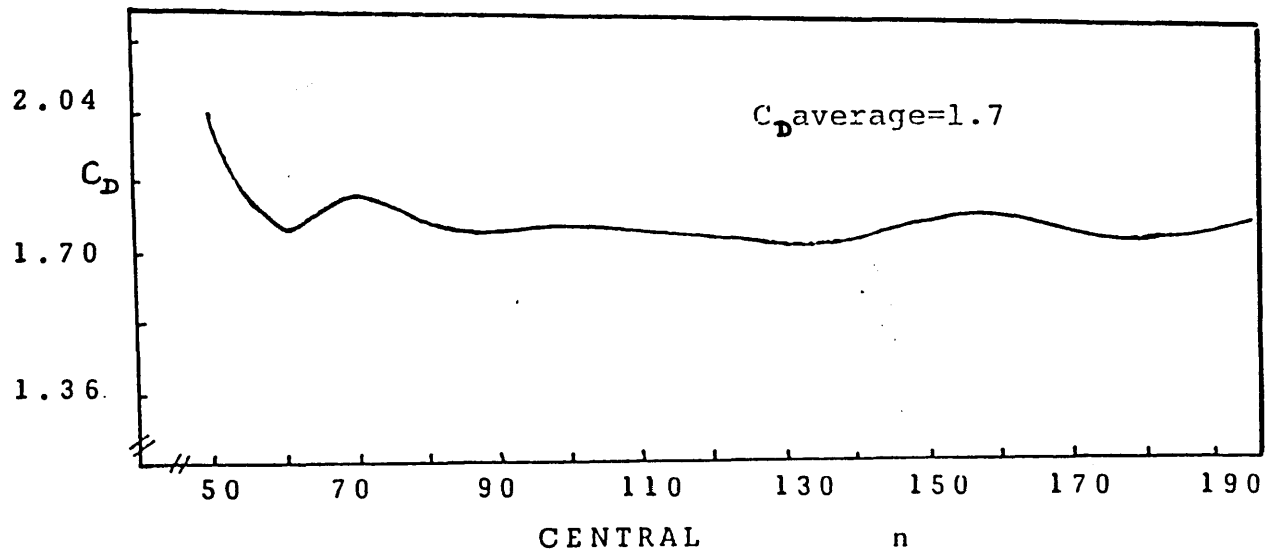

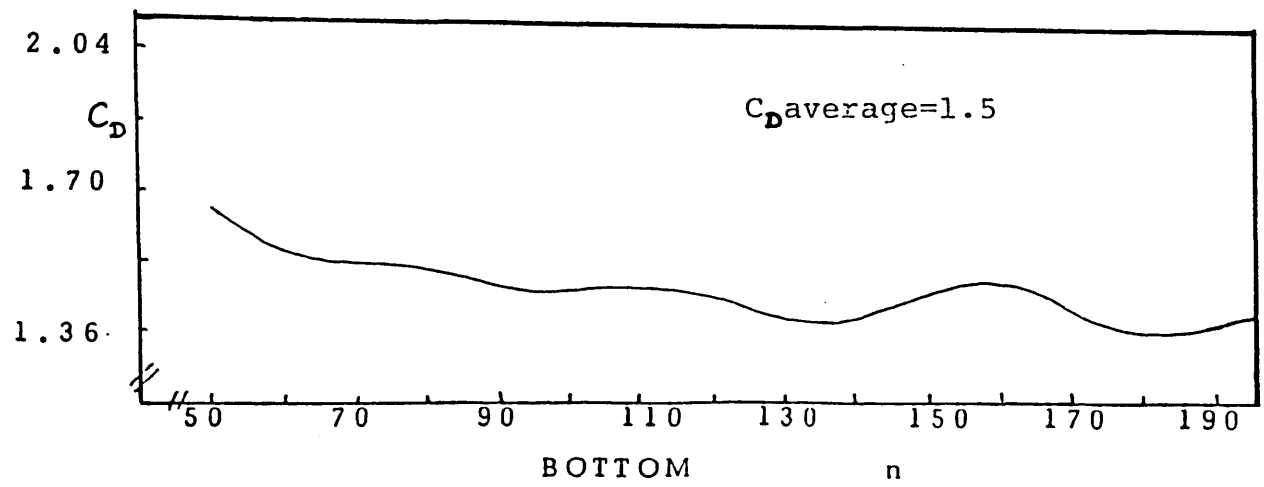

Fig.8.2.7 Drag Coefficient 'C_D' - Flow around a Column of three Cylinders Re=150

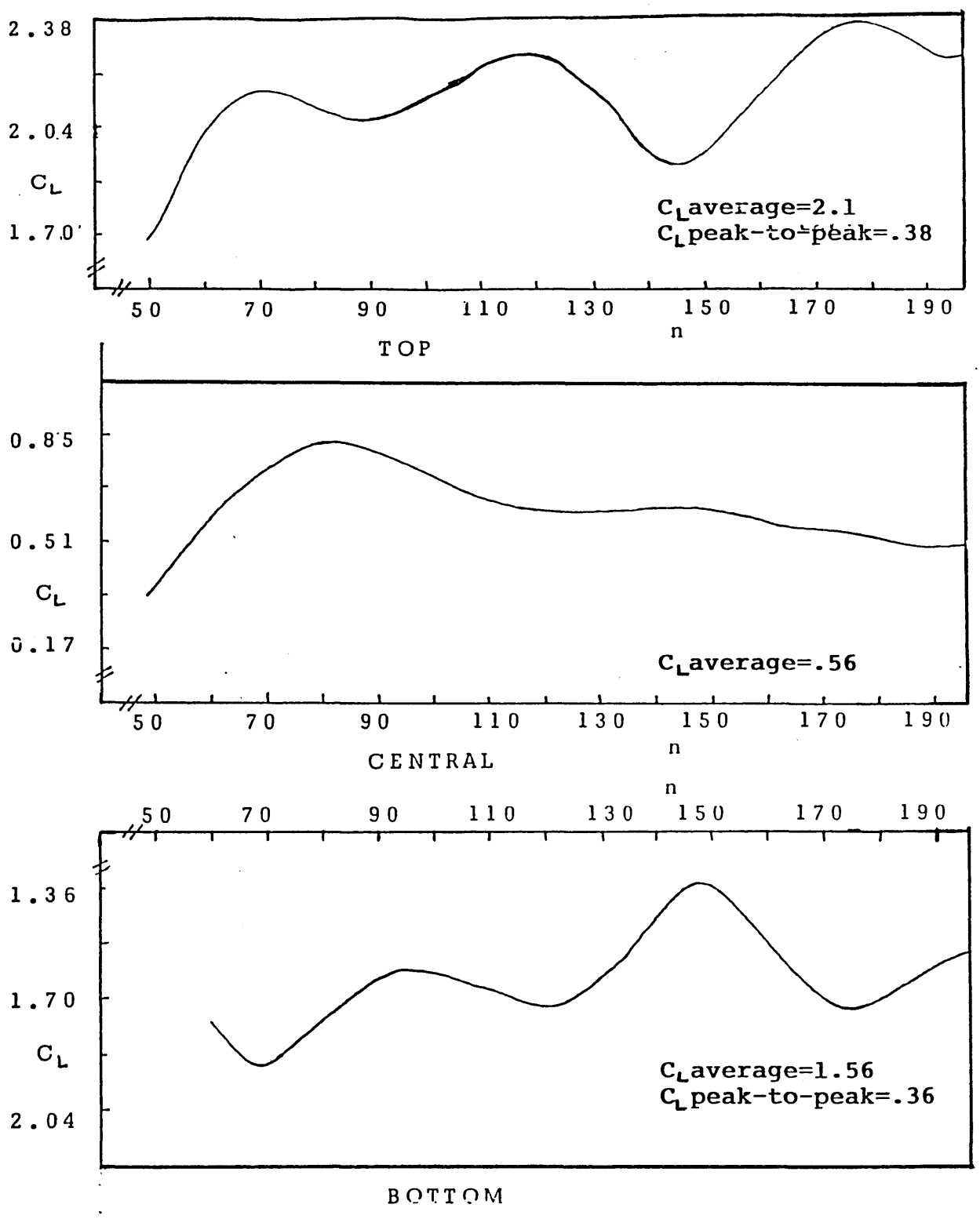

Fig.8.2.8 Lift Coefficient 'C_L' - Flow around a column of three Cylinders Re=150

9. SUMMARY AND SUGGESTIONS FOR FURTHER WORK

A finite element procedure for fluid flow and for the fluid-structure interaction problems has been developed. As the two systems are solved independently and coupled by use of velocity and force boundary conditions, the procedure is also suitable for fluid dynamic and structural dynamic problems. The Penalty function formulation of the Navier-Stokes equations is studied in detail. A variety of flow problems are solved for a range of Reynolds numbers. The results obtained are in good agreement with the available experimental and numerical results. It can be said that the solution procedure used to solve the Navier-Stokes equations gives a true representation of the flow at low and moderate Reynolds numbers, provided that the correct mesh is used. The appearance of instabilities in the form of ripples indicate that a mesh refinement is required in the areas where these occur. Use of upwind methods have been suggested to obtain smooth solutions on coarse meshes but they have not been used in this work. These are relatively insensitive to the input value of Reynolds numbers. The method used in this thesis does not use any upwinding. Updating of mesh is required as the Reynolds number is increased. It is essential to have nodes inside the boundary layer. As long as the boundary layer is resolved and a finer mesh is used in the critical regions, the solution obtained gives a good representation of the flow. Use of non-uniform meshes serves this purpose by utilising enough nodes in critical areas only, thus reducing the

overall cost of the analysis. Slight changes in geometry are also considered. When the leading edge of a step is slightly rounded off, the ripples are eliminated and the solution is identical to that obtained by using a much finer mesh on a square step. Small changes in geometry, as shown in the flow over a step example, do not alter the flow characteristics. The flow downstream of the step with the rounded front edge is identical to the flow downstream of the standard square step. Slight changes in geometry in the critical areas thus offers the cheaper option of obtaining a relatively smooth, ripple free solution on a coarse mesh. Whether to change the geometry of the problem slightly or use a finer mesh in the critical areas, depends very much on the problem in hand and on the accuracy of the solution required. A similar procedure can be adopted in the cavity flow problem i.e. rounding off the top two corners. Thus it is possible to obtain solution at high Reynolds number using coarse mesh when compared to the one originally used in the cavity flow problem. Hence mesh and geometry considerations are very important in the finite element analysis of flow problems (48).

The equation used to select the timestep, although independent of the flow Reynolds number, does take its effect into account indirectly. It is required to reduce the element size in the boundary layer regions as the flow

is analysed at high Reynolds numbers in order to obtain a smooth solution and hence a smaller timestep for stability and convergence. All the above requirements agree well with the physics of the flow (62), and are ignored when upwind methods are used.

The effect of the value of parameter $\underline{\lambda}$ is also clearly shown to affect the solution (section 6.2). It is important that the incompressibility constraint is fully satisfied otherwise a loss in mass flow rate occurs. This leads to a net pressure loss. Pressure and shear stress are compared with the experimental values for the case of flow over a backward step. These are in reasonable agreement. For all of the examples, results are displayed as velocity vector plots. Postprocessing in this form is cheap and gives a good physical representation of the flow.

A well banded matrix with a small bandwidth is important, in order to have an economical analysis. A standard algorithm is used to renumber the mesh and obtain a matrix with the minimum possible bandwidth. The savings could be in the order of 20-30% compared to an ordinary mesh.

The method that has been adopted for fluid-structure interaction analysis is very simple and easy to code. It can be comfortably included into any general purpose FE

program. Good agreement has been found for the interaction results when compared with other numerical and experimental results. Although only a relatively simple geometry has been considered here, the program can analyse arbitrary geometries of any complexity. In all of the fluid-structure interaction examples presented in this thesis we have dealt with small structural displacements (5-10% of cylinder diameter). The resultant changes in geometry for this kind of movement can be classed as negligible. Sustained vibration of a cylinder is known to occur at amplitude of 0.5D or more. For this kind of movement, updating of the mesh is required. This can be included in the program by updating that part of the mesh which is adjacent to the cylinder. The example of flow around a cylinder column indicates that it is quite possible to analyse the flow around tube banks and to study the fluid-structure interaction behaviour of the complicated tube banks. The effort required to model such an example is significantly more than a single tube. The flow is much more complex in this case and a finer mesh is required to capture all of the flow details. The approach can be easily extended for axisymmetric and 3-D analysis. Although the cost for 3-D analysis would be high.

A working finite element method computer code has been developed and included in the general purpose finite element package FINEL. This is a significant step towards

the development of a general purpose, modularised, fluid-structure interaction, finite element program suitable as a general engineering tool. However, there are certain limitations, especially for high Reynolds number flows mainly related to the choice of a sufficiently fine mesh and the fact that no turbulence model is included.

10. REFERENCES

1. Westergaard, H.M., Water Pressures on Dams During Earthquake, Trans. ASCE, 98 (1933) 418-433.

2. Abramson, H.N. (ed.), The Dynamic Behaviour of Liquids in Moving Storage Containers, Report No. SP-106, National Aeronautics and Space Adminstration (1966).

3. Zienkiewicz, O.C., Finite Element Method in Continuum Mechanics, McGraw-Hill 1967.

4. Kotsubo, S., Dynamic Water Pressure on Dam due to Irregular Earthquakes, Memoirs Faculty of Engineering, Kyushu University, Fukuoka, Japan, Vol. 18, No. 4,1959.

5. Chen, C.C., The Effect of Dynamic Fluid Pressure on a Dam During Earthquakes, Journal of Applied Mathematics and Mechanics, Vol. 25, No. 1, 1961.

6. Sayhi, M.N. and Ousset, Y., A Direct Determination of the Added Mass Matrix in Fluid-Structure Interaction Problems, Structural Engineering Journal, ASCE ST12, Dec. 1979.

7. Orsero, P. and Armand, J.L., A Numerical Determination of the Entrained Water in Ship Vibrations, Int. Journal for Num. Meths. in Eng., Vol.13, 1978, pp 35-48.

8. Zienkiewicz, O.C. and Bettess, P., Infinite Elements in the Study of Fluid-Structure Interaction Problems, Second Int.

Symp. on Comp. Meths. in App. Science and Engg., Versailles, France (1975).

9. Zienkiewicz, O.C., Dynamic Fluid-Structure Interaction-Numerical Modelling of Coupled Problems, Int. Symp. Num. Meths. in Offshore Engg., Swansea, Wales (1977).

10. Clough, R.W., Niwa, A. and Clough, D.P., Experimental Seismic Studies of Cylindrical Tanks, Structural Engg. Journal, ASCE ST12, Dec. 1979.

11. Hall, J.F. and Chopra, A.K., Two-dimensional Dynamic Behaviour of Concrete and Embankment Dams including Hydrodynamic Effects, Earthquake Engg. Struc. Dynamics, 10, pp 305-332, 1982.

12. Chopra, A.K. and Chakrabarti, P., Earthquake Analysis of Concrete Gravity Dams including Dam-Water Foundation Rock Interaction, Earthquake Engg. Struc. Dynamics, 9, pp 363-383, 1981.

13. McNeal, R.H., Citerly, R. and Chargin, M., A New Method for Analysing Fluid-Structure Interaction using MSC/NASTRAN, Fifth Int. Conf. on Struc. Mech. in Reactor Tech., Paper B4/9, Aug. 13-17, 1979.

14. Combescure, A., Gilbert, R.J., Jeanipierre, F., Hoffman,

A. and Livolant, M., Fluid-Structure Interaction, A General Method in Ceasant Programs, Int. Conf. On Engg. Applications of the Finite Element Method, Hovik, Norway, May 1979.

15. Buragohain, D.N. and Agarwal, B.L., Hydrodynamic Forces on Large Offshore Structures under Ground Excitation, Numerical Methods for Coupled Problems, Proc. of the Int. Conf. held at the University College, Swansea. 7-11 Sept. 1981. Eds. Hinton, E., Bettess, P. and Lewis, R.W. pp. 209-221.

16. Paul, D.K., Ziekiewicz, O.C. and Hinton E., Transient Dynamic Analysis of Reservoir-Dam Interaction using Staggered Solution Schemes, same as ref. 15, pp. 255-268.

17. Park, K.C., Fellipa, C.A. and Deruntz, J.A., Stabilisation of Staggered Solution Procedures for Fluid-structure Interaction Problems, Computational Methods for Fluid-Structure Interaction Analysis, Eds. Belytscko, T. and Geers, T.L., AMD Vol. 26, ASME, N.Y. 1977, pp. 95-124.

18. Shantaram, D., Owen, D.R.J. and Zienkiewicz, O.C., Dynamic Transient behaviour of 2-Dimensional and 3-Dimensional Structures, including Plasticity, Large Deformation and Fluid Interaction, Eathquake Engng. and Struc. Dynamics 4, pp. 561-578.

19. Wilson, E.L., Finite Elements for Foundations, Joints and Fluids, Chapter 10, Finite Elements in Geomechanics, Ed. by Gudehus, G.Wiley, Chichester. pp 319-350.

20. Wilson, E.L. and Chopra, A.K., Earthquake Analysis of Reservoir Dam Systems. Fourth World Conference on Earthquake Engng., Santiago, Chile. Jan.1969.

21. Zienkiewicz, O.C. and Bettes, P., Fluid-Structure Dynamic Interaction and Wave Forces, an Introduction to Numerical Treatment, Int. J. of Num. Meths. in Engng. 13, pp 1-16 (1978).

22. Belytschko, T., Methods and Programs for analysis of Fluid-Structure Systems, Nuclear Engng. Design, 42. pp 41-52 (1977).

23. Bathe, K.J. and Sonnad, V., On Effective Implicit Time Integration in Analysis of Fluid-Structure problems, Int. J. of Num. Meths. in Engng. 15, pp 943-948 (1980).

24. Wilson, E.L. and Khalvati, M., Finite Elements for the Dynamic Analysis of Fluid-Solid Systems, Int. J. of Num. Meths. in Engng. 19, pp 1657-1668 (1983).

25. Hamdi, M.A. and Ousset, T., A Displacement Method for Analysis of Vibrations of Coupled Fluid-Structure Systems,

Int. J. of Num. Meths. in Engng., 13, pp 139-150 (1978).

26. Deshpande, S.S., Belkune, R.M. and Ramesh, C.K., Dynamic Analysis of Coupled Fluid-Structure Interaction Problems, as in 15, pp 367-378.

27. Hughes, T.J.R., Liu, W.K. and Zimmermann, T.K., Lagrangian-Eulerian Finite Element Formulation for Incompressible Viscous Flows, U.S.-Japan Seminar on Interdisciplinary Finite Element Analysis, Cornell University, Ithaca, New York, August 7-11, 1978.

28. Donea, J. and Giuliani, S., Fluid-Structure Interaction in Problems with Interfaces Involving Sharp Corners, Trans. of the Sixth Int. Conf. on Structural Mechanics in Reactor Tech., 13, Aug. 1981.

29. Liu, W.K. and Belytchko, T., Fluid-Structure Interaction with Sloshing, Trans. of the 7th Int. Conf. on Structural Mechanics in Reactor Tech. (SMiRT), Vol. B, Aug. 1983.

30. Belytschko, T. and Kennedy, J.M., Computer Models for Sub-assembly Simulation, Preprint.

31. Donea, J., Fasoli-Stella and Giuliani, S., Lagrangian and Eulerian Finite Element Techniques for Transient Fluid-Structure Interaction Problems, Trans. of the Fourth

Int. Conf. on Structural Mechs. in Reactor Tech., San-Francisco, August 1977.

32. Daniel, W.J.T., Modal Methods in Finite Element Fluid-Structure Eigenvalue Problems, Int. J. of Num. Meths. in Engng., 15, 1980, pp 1161-1175.

33. FINEL, Hitchings, D., General Purpose Finite Element Package, Department of Aeronautics, Imperial College, London SW7.

34. Hughes, T.J.R., Generalisation of Selective Integration Procedures in Anisotropic and Non-Linear Media, Int. J. of Num. Meths. in Engng., 15, 1980, pp 1413-1418.

35. Malkus, D.S. and Hughes, T.J.R., Mixed Finite Element Method - Reduced and Selective Integration Techniques: A Unification of Concepts, Computer Meths. in Applied Mechanics and Engng., 15, 1978, pp 63-81.

36. Baker, A.J., A Highly Stable Explicit Integration Technique for Computational Continuum Mechanics, Num. Meths. In Fluid Dynamics, Ed. Connor, J.J. and Brebbia, C.A., Pentech Press, London, 1974, pp 99-121.

37. Gresho, P.M., Lee, Stullich, T.W. and Sani, R.L., Solution of the Time-Dependant Navier-Stokes Equations via

Finite Element Method, Second Int. Conf. on Finite Elements in Water Resources, London, July 10-14 1978.

38. Smith, S.L. and Brebbia, C.A., Applied Math. Mod., 1, 1977, pp 234-266.

39. Temam, R., Navier-Stokes Equations, North Holland, Amsterdam 1977.

40. Hughes, T.J.R., Liu, W.K. and Brooks, A., Finite Element Analysis of Incompressible Viscous Flows by the Penalty Function Formulation, J. of Computational Physics, 30, 1979 pp 1-60.

41. Heinrich, J.C. and Marshall, R.S., Viscous Incompressible Flow by a Penalty Function Finite Element Method, Pergamon Press Ltd., U.K. 1981.

42. Oden, J.T., Finite Element Analogue for Navier-Stokes Equation, Trans. ASCE J. Engng. Mech. Div. 96, EM4, 1970, pp 529-534.

43. Temam, R. and Thomasset, F., Solution of the Navier-Stokes Equations by Finite Element Methods, Proc. Fourth Int. Conf. Num. Meths. Fluid. Mechs., Edited by R.D. Richtmyer, 1974, pp 392-395.

44. Herrmann, L.R., Elasticity Equations for Incompressible or nearly Incompressible Materials by a Variational Theoram, AIAA J., 3, 1965, pp 1896-1900.

45. Nickel, R.E., Tanner, R.I. and Caswell, B., The Solution of Viscous, Incompressible Jet and Free-Surface Flows using Finite Element Methods, J. Fluid Mechs., 65, 1974, pp 189-206.

46. Hughes, T.J.R., Taylor, R.L. and Levy, J.F., High Reynolds Number, Steady, Incompressible Flows by a Finite Element Method, Finite Elements in Fluids, Edited by Gallagher, Zienkiewicz, Oden, Morandi-Cecchi and Taylor, 3, Wiley, New York 1978.

47. Bathe, K.J., Finite Element Procedures in Engineering Analysis, Prentice-Hall, Inc., Englewood Cliffs, New Jersey 07632, 1982.

48. Hitchings, D., Prassas, A.G. and Gossain, S.R., Mesh and Geometry Considerations in Finite Element Solution of Fluid Flow Problems, Proc. Third Int. Conf. on Finite Elements in Non-Linear Mechanics, Universitat der Stuttgart, Sept. 10-14, 1984.

49. Oden, J.T., Finite Elements in Non-Linear Continua, McGraw-Hill, New York 1972.

50. Zienkiewicz, O.C., The Finite Element Method, McGraw-Hill, New York 1977 (3rd Edition).

51. Prassas, A.G., Finite Element Analysis of Heat Transfer in Fluid and Solid Media, Ph.D. Thesis, Dept. of Aeronautics, Imperial College, London, 1985.

52. Roache, P.J., Computational Fluid Dynamics, Hermosa Publishers 1972.

53. Malkus, D.S., Int. J. Solids Struct., 12, 1976 731-738.

54. Atkinson, B., Brocklebank, M.P. ,Card ,C.C.M. and Smith, J.M., Low Reynolds Number Developing Flows , A.I.Ch.E.J., 15, 1969, pp. 548-563.

55. Atkinson, B., Card, C.C.M. and Irons, B.M., Application of the Finite Element Method to Creeping Flow Problems, Trans. Inst. Ch. Eng., 48, 1970, pp. 276-284.

56. Zienkiewicz, O.C., and Godbole, P.N., Viscous Incompressible Flow with Special Reference to Non-Newtonion (Plastic) Fluids, Finite Elements in Fluids , Vol.1, Ed. Gallagher, Zienkiewicz, Oden, Morandi, Cecchi, and Taylor. pp. 25-55.

57. Lew, H.S. and Fung, Y.C., On Low Reynolds Number Entry Flow into a Circular Tube, J. of Bio-Mechanics, 2, 1969, pp. 105-119.

58. Bosnor, F.K., Fox, R.L. and Schmidt, L.A., The Generation of Interelement Compatible Stiffness and Mass Matrices by the use of Interpolation Formulae, Proc. Conf. Matrix Meths. Structural Mech., Wright - Patterson AFB, Ohio (1968).

59. Leone, J.M., Gresho, P.M., Finite Element Simulations of Steady, Two-Dimensional, Viscous, Incompressible Flow over a Step. Journal of Computational Physics. 41, (1981) pp. 167-191.

60. Greenspan, D., J. Engrg. Math. 3 (1969), 21.

61. Friedman, M., J. Engrg. Math. 6 (1977), 285.

62. Gresho, P.M., and Lee, R.L., Don't Suppress the Wiggles - They're Telling You Something, Computers and Fluids, 9, pp. 223-253.

63. Bercovier, M., and Engelman, M., A Finite Element for the Numerical Solution of Viscous Incompressible Flows, J. of Comp. Physics, 30, 1979, pp. 181-201.

64. Durst, F., and Tropea, C., Turbulent, Backward Facing

Step Flows in Two - Dimensional Ducts and Channels. Third Symp. Turbulent Shear Flows - Sept. 9-11, 1981, Davis, California, U.S.A.

65. Kueny, J.L., Binder,G., and Barbet, J., GAMM Workshop on Viscous Flow over a Backward Facing Step, An Experimental Investigation. Bievres, France. Jan. 1983.

66. Roache, P., and Mueller, T., AIAA J. 8. No.3 (1970), 530.

67. Moffatt,H., J. of Fluid Mechanics. 18, (1964), 1.

68. Weinbaum, S., J of Fluid Mechanics. 33, Part 1, (1968), 38-63.

69. Kawaguti, M., Numerical Solutions of the Navier-Stokes Equations for Flow in a Channel with a Step, Tech. Summary Rept. 574, Mathematics Research Centre, University of Wisconsin, Madison, 1965.

70. Matsui, T., Hiramatsu, M. and Hanaki, M., Fourth Biennial Symp. on Turbulences in Liquids, University of Missouri, Rolla, 1975, pp. 291-296.

71. Taylor, C., Thomas, C.E., and Morgan, K., Modelling Flow over a Backward Facing Step using the F.E.M. and the two equation model of Turbulence, Int. J. for Num. Meths. in

Fluids, Vol.1, 295-304 (1981).

72. Ecer, A., Rout, R.K., and Ward, P., Laminar Flow Past a Backward Step. SDRC (Structural Dynamics Research Corporation), Report 1983.

73. Cliffe, K.A., and Wilkes, N.S., Comparison of Finite Difference and Finite Element Predictions with a Experiment for Turbulent Flow Over a Backward Facing Step. Report HTFS RS437, AERE R10586.

74. Gresho, P.M., Lee, R.L., and Stullich, T.W., Solution of the Time-Dependent Navier-Stokes Equations via F.E.M., Finite Elements in Water Resources, Vol. 19.

75. Hutton, A., and Smith, R., The Predictions of Laminar Flow Over A Downstream-Facing Step by the Finite Element Method, RD/B/N3660, Central Electricity Generating Board, London, England, April 1979.

76. Burggraf, O., Analytical and Numerical Study of Separated Flows. J. Fluid Mech., 24 (1966), pp. 113-151.

77. Pan, F., and Acrivos, A., Steady Flows in Rectangular Cavities, J. Fluid Mech., 28 (1967), pp. 643-655.

78. Batchelor, G.K., On Steady Laminar Flow with Closed

Streamlines at Large Reynolds Numbers, J. Fluid Mech., 1 (1956), 177-190.

79. Greenspan, D., Numerical Studies of Prototype Cavity Flow Problems, Comput. J. 12, (1969), pp. 89-94.

80. Greenspan, D., Lectures on the Numerical Solution of Linear, Singular, and Non-linear Differential Equations, Prentice Hall, N.Y., 1968.

81. Runchal, A.K., Spalding, D.B., and Wolfshtein, M., Numerical Solution of the Elliptic Equations for Transport of Vorticity, Heat and Matter in 2-D Flow, Phys. Fluid, 12, (1969),.

82. Runchal, A.K., and Wolfshtein, M., Numerical Integration Procedures for the Steady State N-S Equations, J.M.E. Sci. II (1969), pp. 445-453.

83. Gosman, A.D., Pan, W.M., Runchal, A.K., Spalding, D.B., and Wolfshtein, M., Heat and Mass Transfer in Recirculating Flows, Academic Press, N.Y., 1969.

84. Mills, R.D., Numerical Solutions of the Viscous Flow Equations for a Class of Closed Flows, J. Roy. Aero. Soc., 69, 1965, pp. 714-718.

85. Nalasamy, M., and Krishna Prasad, K., On Cavity Flow at High Reynolds Number, J. Fluid Mech., (1977), Vol. 79, Part 2, pp. 391-414.

86. Tuann Shih-Yu, and Olson, M.D., Review of Computing Methods for Recirculating Flows, J. of Comp. Phys. 29, 1978, pp. 1-19.

87. Bozeman, J.D., and Dalton, C., Numerical Studies of Viscous Flow in a Cavity, J. of Comp. Phys. 12, p. 348.

88. O'Brian, V., Closed Streamlines Associated with Channel Flow over a Cavity, Phys. Fluids, 15, 2089.

89. Huffenus, J.P., and Khaletzky, D., A FEM to solve the Navier-Stokes Equations using the Method of Characteristics, Int. J. for Num. Meths. in Fluids, Vol 4, (1984), pp. 247-269.

90. Gresho, C.M., Chan, S.T., Lee, R.L., and Upson, C.D., A Modified Finite Element Method for Solving Time-Dependant, Incompressible Navier-Stokes Equations, Part 2: Applications, International J. for Num. Meths. in Fluids, Vol 4, (1984), pp. 619-640.

91. Gresho, C.M., Chan, S.T., Lee, R.L., and Upson, C.D., A Modified Finite Element Method for Solving the Time-Dependant, Incompressible Navier-Stokes Equations, Part 1: Theory,

International J. for Num. Meths. in Fluids, Vol 4, (1984), pp. 557-598.

92. Timin, T. and Esmail, N., A Comparitive Study of Central and Upwind Difference Schemes Using the Primitive Variable, Int. J. for Num. Meths. in Fluids, Vol 3, (1983), pp. 295-305.

93. Leal, L.G., Steady Separated Flow in a Linearly Decelerated Free Stream, J. Fluid Mech., 59, (1973), p. 513.

94. Griffiths, D.F., On the Approximation of Convection Problems in Fluid Dynamics, Dept. of Mathematics and Statistics, University of Calgary, Alberta, Canada, Research Paper No. 317 (Sept 1976).

95. Jordan, S.K., and Fromm, J.E., Oscillatory Drag, Lift, and Torque on a Circular Cylinder in Uniform Flow, The Physics Of Fluids, 15, (1972), pp. 371-376.

96. Tritton, D., Physical Fluid Dynamics, Van Nostrand Reinhold Co., N.Y., 1977.

97. Swanson, J.C., and Spaulding, M.L., Three Dimensional Numerical Model of Vortex Shedding from a Circular Cylinder, Nonsteady Fluid Dynamics, ASME, N.Y., 1978.

98. Glowinski, R., Mantel, B., Periaux, J., and Pironneau,

O., A Least Squares Method for the Navier-Stokes Equations in Numerical Methods in Laminar and Turbulent Flow, Proceeding of the First International Conference held at University College, Swansea, U.K., July 1978, pp. 17-21, Pentech Press, London.

99. Bristeau, M., Glowinski, R., Periaux, J., Perrier, P., Pironneau, O., and Poirier, G., Application of Optimal Central and Finite Element Methods to the Calculation of Transonic Flows and Viscous Incompressible Flows, Research Report No. 294, Institut de Recherche d'Informatique et d'Automatique, Le-Chesnay, France, (1978).

100. Smith, S.L., and Brebbia, C.A., Improved Stability Techniques for the Solution of Navier-Stokes Equations, Aplied Mathematics Modeling, Vol. 1, (1977), pp. 227-234.

101. Gresho, P.M., and Lee, R.L., On the Time-Dependant Solution of the Incompressible Navier-Stokes Equations in Two and Three Dimensions, Recent Advances in Numerical Methods in Fluids, Vol.1, Ed. Taylor and Morgan, University College of Swansea, Swansea, U.K., 1980, Pineridge Press Ltd.

102. Kawahara, M., Hirano, H., A Finite Element Method for High Reynolds Number Viscous Fluid Flow Using Two Step Explicit Scheme, Int. J. for Num. Meths. in Fluids, Vol.3, pp. 137-163, (1983).

103. Kiehard, J.H., Synopsis of Lift, Drag and Vortex Frequency Data for Rigid Cylinders, Washington State University, College of Engineering Research Div., Bulletin 300 (1966).

104. Tatone, O.S., and Pathania, R.S., Steam-Generator Tube Failures, World Experience in Water-Cooled Nuclear Power Reactors in (1976), Nuclear Safety, 19, 6, 1978, pp. 748-760.

105. Paidoussis, M.P., Flow-Induced Vibration in Nuclear Reactors and Heat Exchangers, Practical Experiences and State of Knowledge, Practical Experiences with Flow-Induced Vibration, Eds. Naudascher, E. and Rockwell, D., Springer-Verlas, Berlin, (1980), pp. 1-81.

106. Reisch, F. Technical Note, New Type of Steam Generator Fails in First Year of Operation, Nuclear Safety 23, 3, (1982), pp. 355-358.

107. Christopher, J., 'Shake and Break' Plagues Pressure-Water Reactor, New Scientist, May 27, (1982).

108. Chen, S.S., Cross-Flow-Induced Instabilities of Circular Cylinders, The Shock and Vibration Digest, 12, 5, (1980), pp. 21-34.

109. Tanaka, H., A Study on Fluid Elastic Vibration of a

Circular Cylinder Array, Trans. of Japan Society of Mechanical Engineers, Section B, 46, (408), (1980), pp. 1398-1407.

110. Tanaka, H., and Takahara, S., Unsteady Fluid Dynamic Force on Tube Bundle and its Dynamic Effect on Vibration, Flow-Induced Vibration of Power Plant Components, Eds. Au-Yang, M.K., ASME, New York, (1980),pp. 77-92.

111. Tanaka, H., and Takahara, S., Fluid Elastic Vibration of Tube Array in Crossflow, J. of Sound and Vibration 77, 1, (1981), pp. 19-37.

112. Chen, S.S., Instability of Mechanisms and Stability Criteria of a Group of Circular Cylinders Subjected to Crossflow, Part I, Theory, J. of Vibration, Acoustics, Stress and Reliability in Design, 105, 1, (1983), pp. 51-58.

113. Chen, S.S., Instability Mechanisms and Stability Criteria of a Group of Circular Cylinders Subjected to Crossflow, Part II, Numerical Results and Discussion, ASME, Paper No.81-DET-22, To appear in J. of Vibration Acoustics, Stress and Reliability in Design.

114. Gibert, R.S., Sagner, M., and Doyen, R., Vibration of Tube Arrays in Transversal Flow Proc. 6th SMiRT, Paris, France, Paper B6/7, (1981).

115. Chen, S.S., Experiments in Fluid Elastic Instability in Tube Banks Subjected to Liquid Crossflow, J. of Sound and Vibration, 78, 3, (1981), pp. 355-381.

116. Heilker, W.J., and Vincent, R.Q., Vibration in Nuclear Heat Exchangers due to Liquid and Two-Phase Flow, J. of Engineering for Power 103, (1981), pp. 358-366.

117. Yeung, H.C., and Weaver, D.S., The Effect of Approach Velocity Direction on Flow-Induced Vibrations of a Triangular Tube Array, J. of Vibration, Acoustics, Stress and Reliability in Design, 105, 1, (1983), pp. 76-82.

118. Chen, S.S., and Jendrzejczyk, J.A., Experiment and Analysis of Instability of Tube Rows Subject to Liquid Crossflow, J. of Applied Mechanics 49, 4, (1982), pp. 704-709.

119. Zdravkovich, M.M., and Namork, J.E., Structures of Interstitial Flow Between Closely Spaced Tubes in Staggered Array, Flow-Induced Vibrations, Eds. Chen, S.S., and Bernstein, M.D., (1979), pp. 41-46.

120. Blevins, R.D., Flow Induced Vibrations, Van Nostrand Reinhold, 1977.

121. Sarpkaya, T., Vortex Induced Oscillations: A Selective Review, J. Applied Mathematics 46, 1979, PP.241-258.

122. Haribut, S.E., Spaulding, M.L., and White, F.H., Numerical Solution for Laminar Two Dimensional Flow about a Cylinder Osillating in a Uniform Stream, 104, 1982, PP. 214-222.

123. Zdravokvich, M.M., Review of the Interface between Two Circular Cylinders in Various Arrangements, J. of Fluids Engng., 99, 1977, PP. 618-633.

124. Fitz-Hugh, J.S., Flow-Induced Vibration in Heat Exchangers, Proc. Int. Sym. on Vibration Problems in Industry, Keswick, U.K., Paper No. 427, 1973.

125. King, R., A Review of Vortex Shedding Research and its Applications, Ocean Engng. 4, 1977, PP. 141-171.

126. Bishop, R.E.D., and Hassan, A.Y., The Lift and Drag Forces on a Circular Cylinder in a Flowing Field, Proc. Roy. Soc., London, SER.A, 277, 1964, PP. 51-75.

127. Koopman, G.H., The Vortex Wakes of Vibrating Cylinder at Low Reynolds Numbers, J. of Fluid Mechs., 28, 1967, PP. 501-512.

128. Griffin, O.M., and Ranbers, S.E., The Vortex Street Wake of Vibrating Cylinders, J. of Fluid Mechs., 66, 1974, PP.

553-576.

129. Naudascher, E., Proc. ASCE, HY 4, July 1967.

130. Chen, Y.N., Excitation Sources of the Flow-Induced Vibrations and Noise in Tube Bank Heat-Exchangers, Noise and Fluid Engineering, ASME, edited by Hickling, R., 1977, PP. 239-246.

131. Yu, I. W. and Vanburen, W., Dynamic Analysis of a Tube in a Fluid, Trans. of the 7th Int. Conf. on Structural Mechs. in Reactor Tech. (SMiRT), Vol. B, Aug.1983, Illinois, U.S.A.